Morphology of Circumnuclear Accreting Gas in Active Galactic Nuclei

Author: **Tathagata Saha**
M.Sc., Presidency University, Kolkata, 2019

Supervisor: **dr hab. Alex G. Markowitz**

A thesis submitted in fulfillment of the requirements
for the degree of Doctor of Philosophy

Nicolaus Copernicus Astronomical Centre
of the Polish Academy of Sciences
ul. Bartycka 18, 00-716 Warszawa, Poland

October 2023

Declaration of Authorship

I, Tathagata Saha, declare that this thesis titled, "Morphology of Circumnuclear Accreting Gas in Active Galactic Nuclei" and the work presented in it are my own. I confirm that:

- This work was done wholly while in candidature for a research degree at Nicolaus Copernicus Astronomical Center of the Polish Academy of Sciences.
- Where any part of this thesis has previously been submitted for a degree or any other qualification at this University or any other institution, this has been clearly stated.
- Where I have consulted the published work of others, this is always clearly attributed.
- Where I have quoted from the work of others, the source is always given.
- With the exception of such quotations, this scientific analysis of in the thesis is mainly my own.
- I have acknowledged all main sources of help.
- Where the thesis is based on work done by myself jointly with others, I have made clear exactly what was done by others and what I have contributed myself.

Signed:

_____

Abstract

The centers of all galaxies host a supermassive black hole. In many of the galaxies, the central black holes are persistently accreting matter from the surroundings, resulting in the continuous generation of high-luminosity electromagnetic radiation across the electromagnetic spectrum. The centers of these galaxies are known as Active Galactic Nuclei (AGN). The accretion process in AGNs is connected to the formation of various substructures around the supermassive black hole; these structures span a range of length scales from the accretion disk and hot corona out to the pc-scale dusty torus. The spectral and temporal study of AGN emission has broadly revealed the physical properties of these structures and how they interact. However, open questions remain. For example, the morphology of the distant parsec-scale, geometrically thick, dusty AGN torus remains unclear. The torus serves as the reservoir of the accreting gas and a source of obscuration of emission originating from the central regions of an AGN. Current research on AGN tori focuses on understanding the level of its clumpiness, the distribution of clumps, the shape and density profile of individual clumps, and the physical mechanisms connected to the formation and kinematics of these clumps. Meanwhile, over the past decades, extreme variability (greater than a factor of 10) events, wherein the X-ray and/or optical wavebands vary more than expected from normal variability in AGNs (a few percent to a factor of few), have been detected in large numbers. Many of these events have been linked to major variations in the global and/or local accretion rates. A multi-wavelength study of extreme-variability transient events in AGNs can help understand the morphological properties of substructures like the accretion disk, the X-ray emitting corona, the broad line region, or the distant dust distribution in these sources and in particular their evolution in response to major changes in accretion rate. In this thesis, I address the statistical challenges associated with determining the structure of the AGN obscuring torus given the current X-ray data quality, study the mechanism driving extreme variability in a flaring AGN and the properties of its inner accretion flow and geometry of its broad line region, and partially develop and initiate the development of and test a pipeline for detecting variable obscuration using X-ray spectrum from the eROSITA telescope.

In the first project, we tested the reliability of the AGN torus X-ray spectral models used by the community in X-ray spectroscopic studies of obscured AGNs. Several models of the X-ray reprocessing of the AGN torus have been recently developed. They span a range of assumed torus geometries and morphologies, e.g., smooth or clumpy. A few examples of such models are UXCLUMPY, CTORUS, MYTORUS, etc. We hypothesize that given the available data quality of the current X-ray instruments, various model parameters returned from a spectral fit are poorly constrained. The degeneracies in these models can limit reliable constraints of parameters of interest, such as the intrinsic photon index and parameters determining torus morphology. To investigate the effects of data quality on parameter constraints, we simulate synthetic data under XMM-Newton and NuSTAR response files based on six different models. We use the Bayesian Nested Sampling method implemented through the Bayesian X-ray Analysis package to analyze the simulated datasets with the same set of models. For exposure times and fluxes typical of nearby Compton-thick AGN, several morphological parameters of the torus remain unconstrained. In addition, a distinction of model or morphology using Bayesian methods is possible only if we have a high intrinsic value of flux for a typical exposure time. Our project aims to guide the X-ray community both in terms of the accuracy in applying the correct torus model with the implications for conclusions on the torus geometry and morphology and the robustness of estimation of model parameters with implications for limitations on precision of those parameters.

In the second project, we perform a multi-wavelength campaign on a flaring and changing-look AGN transient to investigate the flaring mechanism and study the time-dependent responses

of the various accretion substructures – disk, corona, BLR, and torus. In 2020, the Zwicky Transient Facility detected a transient flaring event in the type-1.9 AGN 6dFGS gJ042838.8-000040, wherein a sharp peak of $\sim$0.55 and $\sim$0.29 magnitudes in g- and r-bands, respectively, occurred over $\sim$ 40 days. Spectrum Roentgen Gamma (SRG)/eROSITA also observed the object in X-rays as a part of its all-sky scans, but after the flare had started decaying. We performed a three-year, multiwavelength follow-up campaign of the source to track the evolution of its spectral and temporal characteristics. This campaign included multiple ground-based facilities for optical spectroscopic monitoring and space-based observatories including *XMM-Newton* and *Swift* for X-ray and UV observations. An optical spectrum taken immediately after the peak revealed a changing-look event wherein the source had transitioned from type 1.9 to 1, with the appearance of a double-peaked broad Hβ line and a blue continuum, both absent in an archival spectrum from 2005. The X-ray emission exhibits dramatic flux variation: a factor of $\sim$ 17, but with no spectral evolution. There is also no evidence of a soft X-ray excess which is commonly seen in multiple persistently-accreting Seyferts. After the event, the optical continuum evolves from being a blue continuum-dominated spectrum in 2020 to a galaxy-dominated spectrum after three years. Our detailed spectral and temporal study finds no apparent signatures of a tidal disruption event. Thus, we propose that the extreme multi-wavelength variability is triggered by an instability in the inner accretion disk. Our study of this source demonstrated how the disk instability drove extreme flaring emission originating from the accretion disk, which in turn drove the observed extreme variability in continuum and line emission emanating from the X-ray corona, BLR, and dusty torus.

In the third project, we exploit the large numbers of AGN monitored by eROSITA to search for changing-obscuring AGN events, which occur rarely on a per-object basis. Specifically, I am developing and testing a pipeline to detect changing obscuration events in the eROSITA archive. In this project, we adopt an X-ray hardness ratio-based methodology to detect changing obscuration AGNs. I tested the code using eROSITA responses, assuming simplistic models of obscured AGNs. We find that the detection of changes in line of sight absorption can be made only in nearby Compton-thin and mildly obscured sources having a flux above 1 mCrab in the 2–10 keV band. The pipeline will be effective in detecting the bright COAGN sources both in the eROSITA archive and subsequently for real-time detection of COAGN sources when eROSITA scans resume. The accumulation of such events supports our long-term objective of statistically deriving constraints on cloud properties and distributions to support clumpy-torus models. Additionally, when future real-time detections occur, this pipeline can yield alert triggers to initiate dense spectral and temporal follow-up campaigns that can enable us to measure the profile and distribution of matter in a cloud involved in a given occultation event while it is in-progress.

Abstract (in Polish)

Centra wszystkich galaktyk zawierają supermasywne czarne dziury. W wielu galaktykach centralne czarne dziury stale gromadzą materię z otoczenia, co skutkuje ciągłym generowaniem promieniowania elektromagnetycznego o wysokiej jasności w całym zakresie widma elektromagnetycznego. Centra tych galaktyk znane są jako aktywne jądra galaktyczne (AGN-y). Proces akrecji w AGN-ach związany jest z tworzeniem się rozmaitych struktur wokół supermasywnej czarnej dziury; struktury te obejmują dyski akrecyjne, gorące korony oraz torusy pyłowe. Widmowe i czasowe badania emisji AGN-ów w szerokim zakresie długości fali ujawniły fizyczne właściwości tych struktur i ich wzajemne oddziaływanie. Pozostają jednak otwarte pytania. Na przykład morfologia odległego, geometrycznie grubego, pyłowego torusa o skali parseków pozostaje niejasna. Torus służy jako zbiornik akreującego gazu oraz pochłaniacz emisji pochodzącej z centralnych obszarów AGN-u. Obecne badania nad torusami AGN-ów koncentrują się na zrozumieniu ich struktury modelowanej jako zbiór tzw. kłaczków, ich rozmieszczenia, kształtu i profilu gęstości, oraz mechanizmów fizycznych związanych z ich tworzeniem się i kinematyką. W międzyczasie, w ciągu ostatnich dziesięcioleci, wykryto dużą liczbę przypadków ekstremalnej zmienności (o czynnik 10 lub więcej), w których jasności rentgenowskie i/lub optyczne różnią się bardziej niż oczekuje się od normalnej zmienności w AGN-ach (od kilku do kilkuset procent). Wiele z tych zdarzeń zostało powiązanych z dużymi zmianami w globalnym lub lokalnym tempie akrecji. Badanie zjawisk przejściowych o ekstremalnej wielozakresowej zmienności w AGN-ach może pomóc zrozumieć morfologiczne właściwości struktur takich jak dysk akrecyjny, korona emitująca promieniowanie rentgenowskie, obszar szerokich linii (BLR) lub rozkład pyłu w tych źródłach, a w szczególności ich ewolucję w reakcji na duże zmiany tempa akrecji. W niniejszej rozprawie zajmuję się wyzwaniami statystycznymi związanymi z określeniem struktury torusa przesłaniającego AGN-y, biorąc pod uwagę obecną jakość danych rentgenowskich; badam mechanizm napędzający ekstremalną zmienność w rozbłysku AGN-u oraz właściwości jego wewnętrznego przepływu akrecyjnego i geometrię obszaru BLR, a także rozwijam i testuję oprogramowanie do wykrywania zmiennej absorpcji w widmach rentgenowskich z teleskopu eROSITA.

W pierwszym projekcie przetestowaliśmy wiarygodność modeli widm rentgenowskich torusów w AGN-ach wykorzystywanych w badaniach spektroskopii rentgenowskiej zaabsorbowanych AGN-ów. W ostatnim czasie opracowano kilka modeli przetwarzania promieni rentgenowskich w torusie AGN-u. Obejmują one szereg zakładanych geometrii i morfologii torusa, np. gładkie lub kłaczkowate. Kilka przykładów takich modeli to UXCLUMPY, CTORUS, MYTORUS, itp. Stawiamy hipotezę, że biorąc pod uwagę dostępną jakość danych z obecnych instrumentów rentgenowskich, różne parametry modelu uzyskane poprzez modelowanie widm są słabo ograniczone. Degeneracje w tych modelach mogą ograniczać wiarygodność oszacowań istotnych parametrów, takich jak wewnętrzny indeks fotonowy czy parametry określające morfologię torusa. Aby zbadać wpływ jakości danych na ograniczenia parametrów, symulujemy wyniki obserwacji teleskopami XMM-Newton i NuSTAR oparte na sześciu różnych modelach torusa. Używamy metody "Bayesian Nested Sampling" zaimplementowanej w pakiecie „Bayesian X-ray Analysis" do analizy symulowanych zestawów danych z tym samym zestawem modeli torusa. Dla czasów ekspozycji i strumieni typowych dla pobliskich komptonowsko grubych AGN-ów, kilka parametrów morfologicznych torusa pozostaje nieograniczonych. Ponadto, rozróżnienie modelu lub morfologii przy użyciu metod bayesowskich jest możliwe tylko wtedy, gdy mamy wysoką wewnętrzną wartość strumienia dla typowego czasu ekspozycji. Nasz projekt ma na celu wskazanie społeczności rentgenowskiej z jaką dokładnością można stosować poszczególne modele torusa, jakie wnioski można wyciągnąć co do geometrii i morfologii torusa, oraz jak solidne są oszacowania parametrów modelu z implikacjami dla precyzji ograniczeń tych parametrów.

W drugim projekcie przedstawiamy wyniki wielozakresowej kampanii obserwacyjnej rozbłysku

oraz przejścia stanowego AGN-u, mającej na celu zbadanie mechanizmu rozbłysku oraz zależnych od czasu reakcji poszczególnych struktur akrecyjnych - dysku, korony, BLR-u i torusa. W 2020 r. Zwicky Transient Facility wykrył przejściowy rozbłysk w AGN-ie 6dFGS gJ042838.8-000040 typu widmowego 1.9, w którym ostre maximum o amplitudach $\sim$0,55 i $\sim$0,29 magnitudo, odpowiednio w pasmach g i r, wystąpiło w ciągu $\sim$40 dni. Teleskop eROSITA na kosmicznym obserwatorium Spectrum Roentgen Gamma (SRG) również obserwował ten obiekt w promieniowaniu rentgenowskim w ramach przeglądu całego nieba, ale dopiero po tym, jak rozbłysk zaczął zanikać. Przeprowadziliśmy trzyletnią wielozakresową kampanię obserwacyjną tego źródła, aby śledzić ewolucję jego charakterystyki widmowej i czasowej. Kampania ta obejmowała wiele naziemnych teleskopów z możliwością monitorowania spektroskopowego w zakresie optycznym, oraz obserwatoria kosmiczne, w tym XMM-Newton i Swift, do obserwacji w zakresie rentgenowskim i UV. Widmo optyczne wykonane bezpośrednio po maksimum ujawniło zmianę typu widmowego z 1.9 do 1, wraz z pojawieniem się szerokiej linii Hβ o podwójnym maksimum, oraz niebieskiego kontinuum, nieobecnych w widmie archiwalnym z 2005 roku. Emisja promieniowania rentgenowskiego wykazuje dramatyczną zmienność strumienia: o czynnik $\sim$17, ale bez ewolucji widmowej. Nie ma również dowodów na nadmiar miękkiego promieniowania rentgenowskiego, który jest powszechnie obserwowany w wielu Seyfertach o stałej emisji. Po tym zdarzeniu widmo optyczne ewoluowało od stanu zdominowanego przez niebieskie kontinuum w 2020 roku do stanu zdominowanego przez galaktykę 3 lata później. Nasze szczegółowe badania widmowe i czasowe nie wykazały żadnych widocznych śladów zaburzeń pływowych. W związku z tym proponujemy, że ekstremalna wielozakresowa zmienność została wywołana niestabilnością wewnętrznego dysku akrecyjnego. Nasze badania tego źródła wykazały, w jaki sposób niestabilność dysku spowodowała ekstremalny rozbłysk pochodzący z dysku akrecyjnego, który z kolei spowodował obserwowaną ekstremalną zmienność w kontinuum oraz w liniach widmowych pochodzących z korony rentgenowskiej, BLR-u i pyłowego torusa.

W trzecim projekcie wykorzystujemy dużą liczbę AGN-ów monitorowanych przez teleskop eROSITA do wyszukiwania zdarzeń zmiany stanu absorpcyjnego w AGN-ach (COAGN), które występują rzadko w odniesieniu do pojedynczego obiektu. W szczególności opracowuję i testuję oprogramowanie do wykrywania zdarzeń zmian absorpcji w danych archiwalnych z eROSITy. W tym projekcie stosujemy metodologię opartą na współczynniku twardości promieniowania rentgenowskiego do wykrywania zmieniającej się absorpcji AGN-u. Przetestowałem ten kod przy użyciu symulacji obserwacji eROSIT-ą, zakładając uproszczone modele zaabsorbowanych AGN-ów. Okazało się, że zmiany absorpcji na linii widzenia można wykryć tylko w pobliskich, lekko absorbowanych, komptonowsko cienkich źródłach o strumieniu powyżej 1 mCrab w zakresie 2–10 keV. Oprogramowanie to będzie skuteczne w wykrywaniu jasnych źródeł COAGN zarówno w danych archiwalnych eROSITA, jak i w czasie rzeczywistym po wznowieniu przez eROSIT-ę przeglądu nieba. Nagromadzenie takich zdarzeń wspiera nasz długoterminowy cel, jakim jest statystyczne wyprowadzenie ograniczeń dotyczących właściwości i rozkładów chmur w celu weryfikacji modeli kłaczkowatego torusa. Dodatkowo, gdy w przyszłości pojawią się detekcje w czasie rzeczywistym, oprogramowanie to może generować alerty, aby inicjować intensywne widmowe i czasowe kampanie obserwacyjne, które mogą umożliwić nam pomiar rozkładu materii w obłoku zaangażowanym w trwające zdarzenie absorpcyjne.

Acknowledgements

I extend my heartfelt gratitude to dr hab. Alex G. Markowitz for providing me the opportunity to collaborate and work with him on multiple intriguing projects. Under his mentorship, I learned the physics of AGN, the techniques of observation, and the statistical methods employed in astrophysical data analysis. I am deeply thankful for his availability for advice regarding the projects connected to my Ph.D. and for always being patient and supportive during my studies. I will always be indebted to the knowledge, guidance, and, teaching that Prof. Markowitz provided during my Ph.D. studies. I am immensely grateful to Dr. Johannes Buchner for guiding me through the concepts of the powerful Nested Sampling algorithm and providing guidance in applying the BXA package to X-ray data. I sincerely thank Dr. David Homan for guiding me through the techniques of optical spectroscopy. I am grateful for his availability on short notice when the extended group/myself needed to clarify a conceptual or technical doubt. I thank Dr. Mirko Krumpe for sponsoring and supporting my participation in the multiwavelength follow-up campaign of eROSITA detected sources and providing me the invaluable opportunity to work in collaboration with the eROSITA_DE group. I sincerely thank Prof. dr hab Agata Rozanska for organizing enriching group meetings regularly, which consisted of useful discussions related to X-ray astronomy. I would like to express my gratitude to all the professors who taught multiple courses as a part of the Ph.D. curriculum. I am deeply grateful to CAMK secretaries and the IT department for their assistance in solving administrative and technical problems, specifically those that involved the extensive use of the Polish language. I extend my heartfelt thanks to Pani Kasia Morawska for patiently explaining procedures related to health insurance, residency permit application, and other significant issues related to life in Poland. I thank my juniors, seniors, and batch mates Ankan, Chandra, Ruchi, Samaresh, Raj, Rajeev, Gonzalo, Abinash, Sumeet, Sudhagar, Parikshit, and Biswaraj for their companionship and insightful conversations during the difficult years of my Ph.D. studies. I thank my senior Dr. Saikruba Krishnan for being available for support in matters related to my thesis and providing guidance on multiple issues related to life in Poland. I express my heartfelt gratitude to Dr. Mohammad Hassan Naddaf Moghaddam for all the intellectually stimulating and emotionally reassuring conversations. His friendship and guidance during moments of stress and hardship have been a source of great comfort and support. I thank Prof. Ritaban Chatterjee and Prof. Suchetana Chatterjee for teaching me physics, astronomy, cosmology, and laboratory as a part of undergraduate and postgraduate courses at Presidency University. They have always been available for extensive and stimulating discussions related to academia, mental health, society, and politics. I am immensely grateful to the late Prof. Murari Kundu, who taught me not only the fundamental concepts of Physics when I was in high school but also critical problem-solving skills in physics and mathematics. The knowledge, concepts, and techniques of scientific thinking that I have practiced and utilized in the subsequent years are fundamentally the result of Prof. Kundu's mentorship. The contributions of my family towards my generic growth and well-being are immense and cannot be expressed in words. Their support, love, and encouragement have always been instrumental in navigating through life.

Contents

List of Abbreviations

ADAF	Advection-Dominated Accretion Flow
AGN	Active Galactic Nucleus
BHXRB	Black Hole X-ray Binary
BLR	Broad Line Region
BXA	Bayesian X-ray Analysis
CLAGN	Changing-Obscuration Active Galactic Nuclei
COAGN	Changing-Look Active Galactic Nuclei
eROSITA	Extended ROentgen Survey with an Imaging Telescope Array
EPIC	European Photon Imaging Camera
FWHM	Full Width at Half Maximum
HEASOFT	High Energy Astrophysics Software
IR	Infrared
ISIS	Interactive Spectral Interpretation System
JWST	James Webb Space Telescope
MRI	Magneto-Rotational Instability
NIRCam	Near Infrared Camera
NLR	Narrow Line Region
NuSTAR	Nuclear Spectroscopic Telescope Array
RGS	Reflection Grating Spectrometer
SMBH	Supermassive Black Holes
SRG	Spectrum-Roentgen-Gamma
TDE	Tidal Disruption Event
UV	UltraViolet
XMM-Newton	X-ray Multi-Mirror Mission

Physical Constants

Speed of Light	$c = 2.997\,924\,58 \times 10^{8}\ \mathrm{m\,s^{-1}}$
Constant of gravitation	$G = 6.67430 \times 10^{-11}\ \mathrm{Nm^{-2}kg^{-2}}$
Boltzmann constant	$k_B = 1.380649 \times 10^{-23}\ \mathrm{JK^{-1}}$
Mass of proton	$m_{\mathrm{p}} = 1.67262192 \times 10^{-27}\ \mathrm{kg}$
Mass of electron	$m_{\mathrm{e}} = 9.1093837 \times 10^{-31}\ \mathrm{kg}$
Thompson cross section	$\sigma_{\mathrm{T}} = 6.65245873 \times 10^{-29}\ \mathrm{m^2}$

Chapter 1

Introduction

Active Galactic Nuclei (AGNs) are the brightest 'persistent' objects in the universe. They are powered by the accretion of matter onto supermassive black holes (SMBH). The distribution of circumnuclear matter around the central SMBH is the result of the multitude of physical processes related to accretion. This distribution strongly affects the spectral and temporal properties of the source as viewed by the observer. In this thesis, we aim to understand the systematic challenges associated with determining the geometry of the parsec-scale structure in an AGN using X-ray spectra. Additionally, we study how the sub-structures in the accretion flow respond to the extreme variability that originates in the inner accretion flow.

1.1 Active galactic nucleus: History of discovery

Optical spectroscopy has proved instrumental in the discovery and understanding of AGNs. Fath (1909) observed the first optical spectrum of the galaxy NGC 1068, which exhibited strong emission lines, similar to that of nebulae. Studies of multiple galaxies undertaken by Hubble (1926) also reported planetary nebula-type spectrum from their center. Subsequent spectroscopic analysis of six galaxies by Carl Seyfert (Seyfert, 1943) revealed a combination of intense narrow forbidden and broad (FWHM > 1000 km s^{-1}) emission lines in their spectra. The broadening of these lines was attributed to the Doppler effect. Subsequently, galaxies with strong forbidden lines and broad emission lines from their nuclear region were termed Seyfert galaxies.

Subsequently, quasars were discovered and their optical spectroscopy revealed a unique nature in that they exhibit both forbidden emission lines of [O III] and a hydrogen Balmer series (e.g. in 3C 273) which was systematically redshifted (Schmidt, 1963). This high redshift was found to be related to Hubble expansion. This also established that these objects have a very high intrinsic luminosity. Additionally, the presence of forbidden emission lines set an upper limit to the gas density of two sources, 3C 273 and 3C 48 (Greenstein and Schmidt, 1964), indicating a mass of $\sim 10^{11} M_{\odot}$ confined to within less than a parsec.

Subsequently, there were questions regarding the energy generation mechanism of quasars and Seyfert galaxies, given their high intrinsic luminosity. Initially, the idea of thermonuclear fusion in a supermassive star (up to $\sim 10^{8} M_{\odot}$) was proposed by Hoyle and Fowler (1963a) and Hoyle and Fowler (1963b). However, subsequent studies (e.g. Salpeter, 1964) proposed that quasar energy production can be a consequence of accretion of matter onto a supermassive black hole. The material that is spiraling into the black hole through the innermost stable orbit of the accretion disk results in energy emitted at a very high efficiency – $\sim 0.06c^2$ per unit mass – higher than the typical efficiency of nuclear fusion. Lynden-Bell (1969) argued for the inevitability of an inactive supermassive black hole at the center of all galaxies, in addition to the fact that accretion onto supermassive black holes can explain multiple high-energy phenomena including cosmic rays, or forbidden or broad lines in Seyfert galaxies. Soltan (1982) also argued that

the observed efficiency of mass-to-energy conversion in quasars is consistent with supermassive black hole accretion yielding growth to masses similar to the observed range. Subsequent observation-based studies of the motion of the masers in the AGN NGC 4258 (Miyoshi et al., 1995; Herrnstein et al., 1999) required the presence of a supermassive object confined to subparsec scales. The continuous monitoring of the motion of the stars in the Galactic center (Ghez et al., 2005) has provided convincing evidence in favor of a massive object ($\sim 10^6 M_\odot$) at the center of our own Galaxy. Additionally, recent studies of the center of the Milky Way galaxy – the radio source Sagittarius A* (Event Horizon Telescope Collaboration et al., 2022) – and the center of the active galaxy M87 (Event Horizon Telescope Collaboration et al., 2019) by the Event Horizon Telescope Collaboration have yielded direct images of the center of both galaxies in the radio band, revealing a 'silhouette' of a black hole consistent with the theories of general relativity. In summary, observations of motion of stars and gas around massive objects in galactic centers, direct observation of the 'silhouette' of a black hole at the galactic centers of the Milky Way and M87, and the high efficiency of energy generation in quasars collectively support accretion onto supermassive black hole as the mechanism powering active galactic nuclei (AGN).

1.2 Accretion processes in supermassive black holes

Other than persistent accretion which powers AGNs, there can be short phases of relatively fast accretion onto an SMBH triggered by a tidal disruption event (TDE). A TDE occurs when a star gets tidally stripped by a black hole and subsequently, the debris gets accreted (Rees, 1988). Both AGNs and TDEs involve the emission of high-luminosity electromagnetic radiation. However, TDEs exhibit a burst of luminosity for a relatively short duration, while AGNs have been seen to sustain it over an extended period. In this section, we discuss some terminologies related to accretion processes.

Over the last century, theories of accretion have been developed and explored in the context of several astrophysical sources including AGNs and black hole X-ray binaries (BHXRB). The simplest configuration of accretion is Bondi accretion (Bondi, 1952), where matter falls spherically onto the central object black hole. The accreting matter is considered to have no angular momentum with respect to the central object. A problem posed by the simple adiabatic Bondi accretion is its inability to sustain high bolometric luminosities for long durations. In a more realistic scenario, Bondi accretion would require more effective ways of dissipation of gravitational energy for example turbulence, magnetic re-connection, and shock acceleration (Frank, King, and Raine, 2002) to reach desired efficiencies.

A more straightforward way of dissipation of gravitational potential energy is disk accretion. In disk accretion, the dissipation of gravitational potential energy is facilitated through viscosity alongside the outward transportation of angular momentum. This naturally increases both the timescale and efficiency of energy generation in accreting sources, making disk accretion a more viable model for accretion-powered sources like AGNs.

The rate of accretion determines the luminosity of accretion powered sources. However, there exists an upper limit on the the emitted power which is referred to as the Eddington luminosity. At Eddington luminosity ($L_{\rm Edd}$), the corresponding radiation pressure on the accreting gas balances the gravitational attraction between the gas and the black hole. The mathematical expression of $L_{\rm Edd}$ is:

$$L_{\rm Edd} = \frac{4\pi G M_{\rm BH} m_{\rm p} c}{\sigma_T} \tag{1.1}$$

where m_p is the mass of a proton, and σ_T is the Thompson cross section. It is convenient to express the total (bolometric) luminosity (L_{bol}) of an accreting system as a fraction of L_{edd}:

$$\lambda_{Edd} \equiv \frac{L_{bol}}{L_{Edd}} \tag{1.2}$$

The widely-used theory of a geometrically-thin, optically-thick, thermally-emitting accretion disk was developed by Shakura and Sunyaev (1973). The underlying process that drives the viscosity in these disks is thought to be magneto-rotational instability (MRI; Balbus and Hawley, 1992), which is parameterized by the α parameter, first introduced in Shakura and Sunyaev (1973). These thin disks are also a dominant model of the thermal X-ray emission from accretion disks around stellar-mass black holes in BHXRBs in their bright (high/soft) states, for high values of λ_{Edd} (Remillard and McClintock, 2006). Additionally, they work well in describing the emission of highly-accreting AGNs, wherein, a major fraction of electromagnetic radiation is dominated by thermally-emitted optical/UV radiation.

However, when the accretion rate is low ($\lambda_{Edd} \lesssim 0.01$) geometrically-thick and radiatively-inefficient accretion disks dominate the inner accretion flows of AGNs and BHXRBs. These can be is in the form of an advection-dominated accretion flow (ADAF; Narayan and Yi, 1994). These advection-dominated disks are hot and less luminous because of their lower radiative efficiencies. Meanwhile, for the high accretion rate regime, 'slim' disk solutions were proposed by (Abramowicz et al., 1988). With the advances in computation and several GRMHD codes, the nature of accretion flows has been studied much more extensively. Contemporary literature on accretion disks has demonstrated the different solutions for a 'steady' accretion flow: puffy disks (Lančová et al., 2019; Wielgus et al., 2022), and magnetized thin disks (Mishra et al., 2020). However, given the current data quality challenges on the observation front, comprehensive observational testing and confirmation of these theories are challenging.

AGNs emit in multiple wavelengths starting from radio to gamma rays. Despite the ambiguity in the detailed nature of an accretion flow, accretion being at the heart of the overall power generated by AGNs is the dominant theory. The subsequent subsections describe the substructures of AGNs and how they are connected to the multi-wavelength emission in AGN and the core accretion processes.

1.3 Substructures in an AGN

The process of 'persistent' accretion onto a supermassive black hole results in the formation of multiple sub-structures. Observational studies over several decades have inferred the presence of certain common substructures in AGNs. Each of these has its contribution to the broadband spectrum of an AGN. We describe each of the components and sub-structures briefly in this section:

- **The black hole:** Theoretically, black holes are considered to be a consequence of Einstein's theory of general relativity (Misner, Thorne, and Wheeler, 1973). These are singularities in space-time which are enclosed by an event horizon – a spherical surface of radius R_{eh} such that for r<R_{eh} the escape velocity is higher than the speed of light (c). A black hole is characterized by its mass, charge, and angular momentum. The event horizon for a non-rotating black hole is given by;

  $$R_s = 2GM/c^2 \tag{1.3}$$

  Astrophysically, such a black hole can result from the gravitational collapse of a massive object. Stellar-mass black holes result from the collapse of massive stars with mass

ranging from a few $M_\odot$ to a few $10M_\odot$. However, in AGNs, the central black hole is supermassive with masses ranging from $10^5 M_\odot$ to $10^{10} M_\odot$. Several proposed channels lead to the formation of the SMBH, but the processes are still debated. Typical sub-Eddington accretion processes result in the growth of a black hole but are not adequate to evolve a non-SMBH seed black hole to an SMBH over cosmic timescales. Super-Eddington accretion under certain conditions can result in rapid black hole growth and can be important in the seed-to-SMBH evolution (e.g. Volonteri and Rees, 2005). However, other channels like mergers (e.g. Hopkins et al., 2005) can also trigger rapid black hole growth, as they can lead to direct black hole coalescence and trigger rapid accretion – an AGN ignition. Thus, accretion triggered by galaxy mergers can accelerate the formation and growth of SMBHs, making AGNs an important phenomena to study black hole growth and galaxy evolution. With the discovery of gravitational wave signals, the community is exploring the multi-messenger aspect of the formation and evolution of astrophysical black holes, via multiple compact object mergers (e.g. Abbott et al., 2016).

- **Accretion disk:** The accretion disk is made up of in-falling matter surrounding the black hole. The disk structure is generally assumed to be the geometrically-thin, optically-thick Shakura and Sunyaev (1973) disk in most studies of typical highly-accreting AGNs ($\lambda_{\rm Edd} \gtrsim 0.01$) The optical spectrum of an AGN, commonly referred to as the big blue bump (e.g. Malkan and Sargent, 1982; Czerny and Elvis, 1987), is thought to have strong optically-thick thermal emission. The geometrically-thin accretion disk in general successfully models the optical-UV emission in AGNs and is generally adopted as a simple model for the observed spectral shape in the optical waveband. The flux thermally emitted from an annulus at radius r is given by

$$F(r) = \frac{3GM\dot{M}}{8\pi r^3}(1 - \sqrt{r_{\rm in}/r}) \tag{1.4}$$

  where $\dot{M}$ is the accretion rate. When the radius in the above expression is scaled with gravitational radius ($R_{\rm g}$), the maximum temperature of a thin disk is found to inversely vary with black hole mass – $T_{\rm max} \propto M^{-1/4}$ – and the scaled radius – $T_{\rm max} \propto r^{-3/4}$. Thus, the maximum temperature of a thin accretion disk assuming a range of supermassive black hole of $10^6 - 10^9 M_\odot$ is $T_{\rm max} < 10^6$ K.

  Models of radiatively-inefficient, geometrically-thick, optically-thin accretion disks like ADAFs (e.g. Narayan and Yi, 1994) are also invoked in the low accretion regimes, as discussed above.

- **The hot corona:** AGNs emit a moderate fraction of their total power in X-rays (1-10%; Duras et al., 2020). However, the thermal emission from a geometrically-thin disk proves inadequate to explain the high luminosity output of AGNs in X-rays and the shape of their X-ray spectra. It is thus hypothesized that there exists a hot ($T \sim 10^9$ K) and tenuous distribution of electrons (or positrons) in the inner region of the system close to the black hole, up-scattering low energy photons (ultraviolet and optical), via inverse-Compton scattering (e.g. Haardt and Maraschi, 1993; Maraschi and Haardt, 1997; Zdziarski et al., 2020). The primary X-ray spectra of a corona can generally resemble a power law with a high-energy cutoff $\gtrsim$ 20 keV to a few 100 keV (e.g. Tortosa et al., 2018). The geometry of the corona is uncertain, and several models fit into the theoretically proposed physical properties of the corona – high temperature, low optical depth, and physical location in the accretion flow. The corona could be the accretion flow transformed into an ADAF in the inner regions (e.g. Ichimaru, 1977; Esin, McClintock, and Narayan, 1997). Additionally, it can also be the base of a jet (e.g. Henri and Pelletier, 1991; Markoff, Nowak, and Wilms, 2005). Several studies involving reverberation of the 'reflected' X-ray spectrum from the

inner accretion disk (de Marco et al., 2011) and spectroscopic studies of the broad Fe Kα emission line (Fabian et al., 2009) estimate that the corona has a small size (3–10 R_g) and is compact (Fabian et al., 2015).

- **Broad line region:** Many AGNs exhibit broad emission lines with FWHM of $\gtrsim 1000$ km s^{-1} (e.g. Boroson and Green, 1992). The most common broad emission lines are hydrogen Balmer lines – Hα, Hβ, Hγ, Hδ. This line emitting gas is assumed to be in photo-ionization equilibrium (e.g., Beckmann and Shrader, 2012). The line emitter is located farther away from the accretion disk, typically a few light weeks to light months from the black hole. Correlations between the continuum and Hβ variability help constrain the average distances of the broad line emitter from the central emission (Pancoast, Brewer, and Treu, 2014). Additionally, the spectroscopic study of line profiles reveals the kinematics and structure of BLRs, (Pancoast et al., 2014; Villafaña et al., 2022) involving circular motion, inflows, and outflows. Recent observations by the GRAVITY collaboration have confirmed the structure of the BLR inferred from the line fitting studies (e.g. Gravity Collaboration et al., 2018). On the theoretical modeling front, a few physical models have been developed. For example, the Failed Radiatively Accelerated Dusty Outflow model (FRADO; Czerny and Hryniewicz, 2011; Naddaf and Czerny, 2022) invokes the motion of the dusty gas due to radiation pressure to explain the formation, kinematics, and the morphology of the BLR.

- **Narrow line region:** AGN spectra exhibit narrow forbidden emission lines, which result from transitions with low probabilities. Commonly observed forbidden emission lines are the [O III]$\lambda\lambda$4959,5007-doublet, the [N II]$\lambda\lambda$6548,6585-doublet, and the [S II]$\lambda\lambda$6717,6732-doublet. It is thought that NLR clouds are comprised of clouds driven to kiloparsec-scale distances as a part of AGN outflows (Müller-Sánchez et al., 2011; Leung et al., 2019), where their densities reach low enough values – $\sim 10^{3-5}$ cm^{-3} (Netzer, 2013) – to favor forbidden-line emission.

- **Torus:** A dusty structure exists a few parsecs away from the central black hole. This is the region where dust can survive due to a lower temperature ($T \sim 10^3$ K), and the thermal emission is dominant in the infrared band. The torus lies at the heart of the optical spectral classification in AGN (Section 1.4), where depending on whether the line of sight passes through the obscuring torus, quasars are classified into Type-1 or Type-2. Initially, the torus was pictured as a dusty static structure (e.g., Urry and Padovani, 1995); however, our picture has evolved thanks to multi-wavelength studies in infrared and X-ray over the last decade. The static continuous picture is now superseded by a dynamic structure, which is clumpy, and is connected to inflow and outflows in the central engine (Ramos Almeida and Ricci, 2017). The torus is discussed in more detail in Section 1.5.

- **Jet:** A small fraction of AGNs exhibit collimated relativistic jets, which originate from the core of the central engine. The dominant model for launching a relativistic jet is the Blanford-Znajek mechanism (Blandford and Znajek, 1977). In this model, the spin of the black hole and the magnetic fields play an important role. Poloidal magnetic field lines under the effects of a black hole's frame dragging develop a toroidal component, which increases the magnetic pressure, leading to the launching of the jet (Tchekhovskoy, McKinney, and Narayan, 2012). The process can accelerate electrons to large distances, explaining the presence of mega-parsec scale jets seen in some sources. The jets are bright in radio frequencies and jetted AGNs constitute the radio-loud AGN class (Section 1.4.3).

1.4 Unification, classification, and observational/spectral properties of various sub-classes of AGN

The different components of the AGN central engine, along with their spectral signatures and morphology, are at the heart of AGN classification. AGNs are broadly classified into different types according to their optical spectra, X-ray spectra, and radio luminosity.

1.4.1 Optical classification

Quasars and their scaled-down version – Seyfert galaxies – are classified into Type-1 and Type-2 based on the nature of the emission lines in their optical spectra (Khachikian and Weedman, 1974). This classification is based on the apparent presence of broad emission lines in their optical spectra. As described in Section 1.1, all Seyferts exhibit narrow forbidden emission lines of [OIII]$\lambda\lambda$4959,5007 doublet, [NII]$\lambda\lambda$6548,6584 doublet, [SII]$\lambda\lambda$6716,6731 etc. with narrow Balmer lines of Hβ and Hα. However, only Type-1s exhibit broadened Balmer emission lines ($>$ 1000 km s^{-1}) and other lines of Helium (e.g., HeIIλ4686Å, HeIλ5876Å), in addition to the narrow lines. Type-2 AGNs exhibit only narrow emission lines.

Type-1

The broad Balmer lines in Type-1 AGNs have FWHM $\gtrsim 10^3$ km s^{-1} originating in the broad line region corresponds to densities $\gtrsim 10^9$ cm^{-3} (e.g. Netzer, 2013; Ilić et al., 2010; Boroson and Green, 1992). This observation implies that, in a Type-1 AGN, the observer has an unhindered view of the sub-parsec central engine that corresponds to higher Keplerian speeds, temperature, and density. The broad emission lines seen commonly in Type-1 AGNs are the Balmer recombination lines of Hα, Hβ, Hγ, and Hδ.

Another significant feature in the spectra of Type-1 AGNs is a featureless optical-UV continuum originating from the central engine–referred to as the big blue bump. This component is optically thick and thought to be the thermal emission from the accretion disk (e.g. Shields, 1978; Kishimoto, Antonucci, and Blaes, 2003). The simplest model invoked to explain this continuum is optically-thick 'multi-colored black body' emission – integrated emission from annular blackbodies at different temperatures – from the geometrically-thin accretion disk (Shakura and Sunyaev, 1973) . Studies by Malkan and Sargent (1982) and Malkan (1983) have demonstrated that the optical–UV spectrum can be broadly modeled by a thermal optically-thick blackbody. However, the inadequacies of the geometrically-thin accretion disk emission were realized with the discovery of the UV excess (Zheng et al., 1997) and it was argued that the features of the UV continuum required Comptonization of the accretion disk spectrum in an optically-thick, warm accretion flow. Kubota and Done (2018) developed a model in which the warm Comptonization that can potentially explain the ultraviolet excess (alongside the soft X-ray excess seen in many AGNs; Section 1.4.2). Finally, apart from the continuum emitted by the central engine, there is an extrinsic contribution from host galaxy starlight with varied degrees of strength in nearby Seyferts.

Type-1 AGNs occasionally exhibit significant contributions of multiple line complexes originating in the BLR clouds. FeII multiplets constitute one of the main components in the line complex (e.g. Osterbrock, 1977; Bruhweiler and Verner, 2008). This complex of blended lines – occasionally referred to as a pseudo-continuum, depending on the amounts of Doppler broadening and blending – was first theoretically modeled by (Verner et al., 1999). Accounting for the FeII blended emission in the spectrum is required to estimate broad emission line properties of the Hβ and Hα emission lines. In addition to iron emission lines, calcium is also present in the BLR medium (e.g. Martínez-Aldama et al., 2015; Panda et al., 2020). The properties of the

emission lines of Fe and Ca emission are instrumental in estimating the properties of the lower ionization region of the BLR (e.g. Panda et al., 2020; Panda, 2021).

In addition to the commonly-observed Balmer recombination lines, emission lines of Helium (HeIIλ 4686, HeIIλ5876, etc.; Kollatschny et al., 2001; Grier et al., 2012) have also been observed in many Type-1 Seyferts. Photo-ionized species also manifest themselves in the UV via CIVλ1549 and MgIIλ2798, etc. Theoretical study by e.g., Korista et al. (1997) and Korista, Ferland, and Baldwin (1997) using the code CLOUDY (Ferland et al., 1996) estimate the intensities of a multitude of these emission lines for given properties of broad line region gas and a given incident radiation field.

Overall, the unobstructed view of the central engine offered by Type-1 AGNs posits them as suitable sources for studying the properties of radiation originating from, the atomic processes dominant in, and the nature of the accretion flow in the inner sub-parsec region of an AGN.

Type-2

Type-2 AGNs exhibit only the narrow forbidden emission lines. The line widths indicate that they originate from material located at kiloparsec length scales from the central engine (e.g. Netzer, 2013). This kiloparsec-scale matter distribution emitting the narrow forbidden lines is the narrow line region (NLR). The strength of the forbidden lines indicates that the NLR has densities in the $\sim 10^3$–10^4 cm^{-3} range, which is much lower than that of the BLR ($\sim 10^9$ cm^{-3}).

The continua of Type-2 AGNs are mostly dominated by the host galaxy (e.g., spectra of sources studied in Antonucci and Miller, 1985; Miller and Goodrich, 1990). This feature makes it occasionally challenging to distinguish between active and non-active star-forming galaxies based on their continuum. However, one of the indicators used to distinguish Type-2 galaxies with active centers from star-forming galaxies is the line ratios of the forbidden emission lines, represented as a BPT diagram (Baldwin, Phillips, and Terlevich, 1981). In BPT diagrams, a plot of the line ratios of [OIII]λ5007/Hβ vs. [NII]λ6583/Hα and [OIII]λ5007/Hβ vs. [SII]λ6716/Hα are made. A higher ratio indicates a higher level of excitation of the electrons to a higher energy state, resulting from a higher level of photo-ionizing radiation. The ionizing radiation from an AGN is expected to be more intense compared to stellar processes, thus creating the difference between a Type-2 AGN and a star-forming galaxy.

Spectropolarimetric study of the Type-2 AGN NGC 1068 (Miller and Antonucci, 1983; Antonucci and Miller, 1985) revealed that the optical spectrum of the source has a significant fraction ($\sim$ 10%) of polarized emission. The polarized spectrum was found to exhibit a 'featureless' AGN continuum (distinct from starlight/galaxy flux) and a broad Balmer emission line, resembling a Type-1 AGN. Miller and Goodrich (1990) have also reported multiple sources that exhibit similar hidden broad line regions. It is thus argued that, in these sources, a hidden Type-1 AGN provides the initial radiation field to be scattered by free electrons (e.g. Antonucci and Miller, 1985) resulting in the otherwise hidden polarized component. It was thus inferred by these studies (Antonucci and Miller, 1985; Miller and Goodrich, 1990; Antonucci, 1993), that Type-2 AGNs are generally the consequence of a Type-1 AGN that has been obscured by a geometrically-thick dusty obscurer (the putative AGN torus), thus formulating the orientation-dependent unification model of Seyfert AGNs.

However, there are 'True' Type-2 sources where spectro-polarimetric observations did not find evidence of an obscured BLR, thus challenging the obscuration-dependent Type-2 phenomena. One example of such a source is NGC 3147, where optical, X-ray spectroscopy (Bianchi et al., 2008) and spectro-polarimetric studies (Shi et al., 2010) have revealed no obscuration or polarized broad emission lines. Several sources reported in (Brightman and Nandra, 2008) also exhibit the 'true' Type-2 phenomena. Studies like Tran (2003) and Elitzur and Ho (2009) have

linked the absence of a broad line emitter and the intrinsic accretion rate. In the context of the BLR being formed as a wind from the disk, sources with lower accretion rates ($\lambda_{\rm Edd} <\sim 10^{-3}$) are thought to be unable to transfer matter from the disk into the BLR, thus explaining the 'true' type-2 phenomena.

Further studies such as Elitzur, Ho, and Trump (2014) attempt to explain the multiple kinematic components observed in broad emission line profiles (broadly: a Keplerian component + a vertical outflow). The relative contributions of each component depends on the accretion rate, indicating the evolution of BLR sub-structures with accretion rate (e.g. Temple et al., 2023). In summary, the phenomenon of 'true' Type-2 AGN, along with the luminosity dependence of BLR emission and morphology, challenges orientation/obscuration as being the sole criteria for classification of Seyferts, and links extreme variability in accretion rates to evolution in broad emission lines – a phenomenon known as changing-look AGNs (CLAGN, Section 1.6.4).

Intermediate types

The optical classification broadly defines two sub-classes. However, the boundary between them is not discrete; some objects can display weak broad Hβ lines. For instance, Osterbrock and Koski (1976) discussed the intermediate nature of the objects NGC 4151 and Markarian 6. Subsequently, Osterbrock (1981) introduced the Seyfert types 1.5, 1.8, and 1.9 terminologies for intermediate type Seyferts depending on the relative strength of the broad Balmer lines. For example, a Type-1.9 has a broad Hα but no Hβ, whereas a Type-1.8 exhibits both weak Balmer components. Type-1.5 has both Balmer lines with the Hβ broad line being equally strong as the Hβ narrow component. Type-1.2 are typically Type-1 objects where the Hβ FWHM is lower than that of the Hα line. The phenomenon can be attributed to the effect of obscuration, or differences in strength of the ionizing continuum (Elitzur, Ho, and Trump, 2014).

1.4.2 X-ray classification

Here, we describe AGN classification in the X-ray band, with the spectral properties of each subclass. The Galaxy contributes a certain level of line of sight absorption to all extragalactic sources. AGNs that exhibit line of sight absorption in excess of the Galactic absorption are referred to as absorbed sources. The source of X-ray absorption can be either intrinsic and extrinsic to the AGN (e.g. Figure 3 of Matt, 2000; Laha et al., 2020). An intrinsic origin involves obscuration by the circumnuclear gas at pc scales or smaller, e.g., the BLR or torus. Extrinsic absorption might originate from the host galaxy: kpc-scale dust lanes (Malkan, Gorjian, and Tam, 1998). This absorption is measured by the quantity $N_{\rm H}$, which is the column density of hydrogen at the line of sight. Sources exhibit different levels of absorption in the X-ray ranging from very mild or practically no absorption ($N_{\rm H} \lesssim 10^{20}$ cm^{-2}), mild absorption ($N_{\rm H} < 10^{22}$ cm^{-2}), Compton-thin absorption ($10^{22} \lesssim N_{\rm H} \lesssim 10^{24}$ cm^{-2}) to Compton-thick absorption ($N_{\rm H} \gtrsim 10^{24}$ cm^{-2}). As argued by e.g., Matt (2000), the level of absorption might depend on the source of obscuration, e.g., host galaxies might tend to contribute absorption columns up to $N_{\rm H} \lesssim 10^{22}$ cm^{-2}, whereas intrinsic absorption can typically be associated with higher (Compton-thick) values of $N_{\rm H}$ ($\sim 10^{24}$ cm^{-2}). A recent JWST/NIRCam based study by Silverman et al. (2023) of distant ($z > 1$) X-ray obscured AGNs ($\gtrsim 10^{22}$ cm^{-2}) demonstrated that a significant level of obscuration (up to $\sim 10^{22.5}$ cm^{-2}) can originate in the host galaxy, however, heavier obscuration ($\gtrsim 10^{23}$ cm^{-2}) requires a contribution from the circumnuclear matter intrinsic to the AGN. As a caveat, a mid-infrared spectral study by Goulding et al. (2012) found that silicate absorption has poor correlation with heavy absorbing columns ($N_{\rm H} \sim 10^{24}$ cm^{-2}) and sources exhibiting strong silicate absorption have host galaxies with disturbed morphologies. Thus it was argued that this observation may be consistent with the fact that heavy obscuration to the central engine is often provided by host galaxy dust lanes. In this thesis, for the sake of simplicity, we discuss

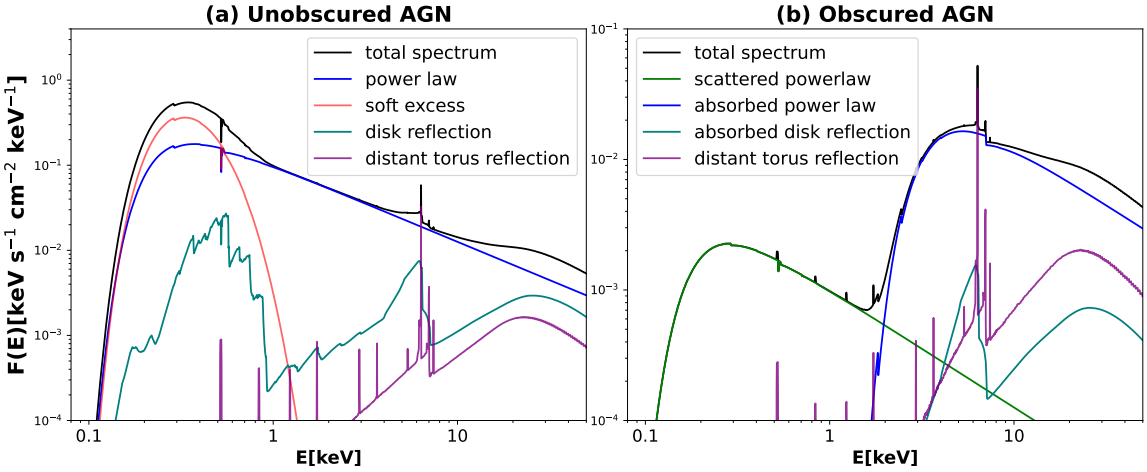

FIGURE 1.1: Model X-ray spectra of (a) Unobscured Seyfert: The power law from the corona (blue) is superposed by a soft excess (red), disk reflection component (teal) with a broad iron line, a distant torus reflection with the narrow iron line (magenta). (b) Obscured Seyfert: The components originating in the central engine are strongly absorbed by the torus. The soft excess is completely absorbed and can be considered absent. The power-law (blue) and the disk-reflection components (teal) are strongly absorbed. The torus reflection is the only direct component that reaches the observer. As a caveat, it should be noted that the contribution from the photo-ionized emission lines originating in a distant gas distribution (potentially the NLR) is not present in the above figures, however they are seen in well-resolved (gratings) X-ray spectra of obscured sources (e.g. Bianchi, Guainazzi, and Chiaberge, 2006).

the situation where strong absorption originates intrinsically in the circumnuclear material, in the vicinity of the AGN (parsec-scale gas).

The X-ray absorption has implications for optical emission. Akiyama et al. (2003) studied the optical properties of absorbed sources, wherein they observed that sources with X-ray columns $N_{\rm H} > 10^{22}$ cm^{-2} tend to be correlated with the absence of a broad Hβ emission line due to obscuration by dust. Over the years, the following general correlation between X-ray absorption and optical properties has emerged: mildly-absorbed AGNs in X-rays are typically Type-1 or Type-1.2 in optical (with the exceptions of 'true' type-2 sources, Section 1.4.1), and highly-absorbed AGNs in the X-rays tend to be type 1.8, 1.9 or type 2 in the optical (Beckmann and Shrader, 2012). Classically, considering the correlation between high absorption in X-ray and disappearance of broad emission lines, $N_{\rm H} = 10^{22}$ cm^{-2} is generally accepted as the boundary above which all sources are referred to as obscured (e.g., Hickox and Alexander, 2018, and references therein). For simplicity, we refer to all the mildly-obscured sources ($N_{\rm H} < 10^{22}$ cm^{-2}) as 'unobscured'. In the following sections, we discuss the properties of the X-ray unobscured and obscured sources.

Unobscured AGNs

Following the definition above, these sources have a line of sight absorption lower than $N_{\rm H} = 10^{22}$ cm^{-2}. Consequently, the direct power law originating from the corona (Section 1.3) and other spectral signatures (e.g. the soft excess as described below) originating near the black hole are mostly transmitted directly to the observer. The emission components of an unobscured AGN X-ray spectrum are:

1. **Primary continuum:** The primary X-ray spectrum is a power law with a high-energy cut-off: $f_{\rm PL}(E) \sim E^{-\Gamma} e^{-E/k_{\rm B}T_{\rm e}}$. This component originates from the hot corona due to inverse-Compton scattering of low-energy (optical–UV) radiation from the accretion disk (Haardt

and Maraschi, 1993; Maraschi and Haardt, 1997). Here, $k_B T_e$ denotes the electron temperature, and is typically ∼20–200 keV (Tortosa et al., 2018); Γ is referred to as the photon index.

2. **Soft excess:** In most unobscured AGNs, there exists an emission component, in excess of the primary power-law component, below 1–2 keV (Halpern, 1984; Turner and Pounds, 1989), which is referred to as the soft excess. There are two dominant models for this component. It can originate from the thermal Comptonization of low-energy photons from the accretion disk in an optically-thick ($\tau \gtrsim 10$), warm corona with temperature $k_B T_e \sim 1$ keV (Mehdipour et al., 2011; Petrucci et al., 2018; Done et al., 2012; Kubota and Done, 2018). The emission from the warm corona can also extend to the far ultraviolet band and contribute significantly there (Zheng et al., 1997). Another possible explanation for the soft excess comes from relativistic blurring of ionized soft X-ray emission lines originating in the inner accretion disk (Crummy et al., 2006; García et al., 2013).

3. **Compton reflection hump (CRH):** In the hard X-rays, a signature of Compton reflection or scattering is observed as an excess flux contribution in the form of a hump peaking around the rest-frame energy of ∼20-30 keV. This feature is accompanied by fluorescent emission lines from multiple species including iron, silicon, argon, calcium, etc. However, the iron Kα emission line at 6.4 keV is the brightest and hence the most frequently-detected line in Type-1 Seyferts. The Compton hump is continuum emission resulting from Compton scattering and reprocessing of a fraction of the coronal power law in colder, X-ray-optically-thick media (Magdziarz and Zdziarski, 1995; García et al., 2013; Dauser et al., 2010; Murphy and Yaqoob, 2009), namely the accretion disk and the torus (e.g. Ghisellini, Haardt, and Matt, 1994; Ogawa et al., 2021). The shape and intensity of the Compton reflection hump is dependent on the thermal, kinematic, and geometric properties of the scatterer. In addition, the CRH originating from the disk is modified by special relativistic effects associated with the disk's fast rotation, and by general relativistic effects associated with the extreme gravity and the spin of the black hole (Dauser et al., 2014; García et al., 2014). In contrast, the shape and intensity of the torus CRH is affected mostly by the morphology of the gas and dust distribution.

4. **Iron line:** A CRH is always accompanied by multiple fluorescent emission lines, the strongest of which is Fe Kα. The Fe Kα line at 6.4 keV originates from the cold matter, e.g., the accretion disk (García et al., 2013; Dauser et al., 2010) and/or the torus (e.g. Awaki et al., 1991a; Awaki et al., 1991b), and it is also evidence for reflection and reprocessing of the primary power law in these structures. The emission lines originating from the torus and the accretion disk can have different profiles. When originating from the accretion disk, the Fe Kα line is strongly affected by the kinematics of the accretion disk, and the special and general relativistic effects of the geodesic around the black hole and its spin, thus producing a broadened and smeared line profile (Fabian et al., 1989; Fabian, 2006). In the case of the torus, no such effects are seen and thus the Fe Kα line is typically narrow, with minimal Doppler broadening (few hundred km s^{-1}).

In summary, X-ray unobscured AGN spectra are dominated by components originating in the central engine, thus providing insight into the physics of the corona and the inner disk, and the measurement of black hole spin.

Obscured AGNs

The emission generated by the central engine of obscured AGNs has similar emission properties to those of the unobscured AGNs. However, this emission is absorbed by intervening matter along the line of sight and with a column density in excess of the Galactic column. Following the definition above, we consider obscured AGNs as those containing column densities $N_H > 10^{22}$

cm^{-2}. Heavy line of sight absorption ($N_{\rm H} > 10^{23}$ cm^{-2}) along with an iron Fe Kα line with large equivalent width seen in X-ray observations of NGC 4507 required a large covering factor (Awaki et al., 1991b), as indicated by Monte Carlo simulations (Awaki et al., 1991a). Such a large covering factor was argued to be consistent with a geometrically thick torus. A multiwavelength study involving X-ray and UV continuua and the optical narrow lines by Mulchaey et al. (1994) observed that X-ray and UV continuua are underluminous and the narrow emission line and the continuum luminosities are uncorrelated in the Type-2 AGNs. This observation also supports a line of sight absorption resulting from the dusty torus. All these studies are consistent with the AGN unification paradigm proposed by (Antonucci, 1993).

Studies of variable absorption have also revealed the intrinsic nature of X-ray obscuration in AGN. Such observations support obscuring material composed of discontinuous gaseous clumps. Some studies of variable absorption resulting from clumps of matter transiting across the line of sight suggest that the distances and the size of the clumps are commensurate with the inner broad line region (Risaliti et al., 2007; Maiolino et al., 2010; Beuchert et al., 2015). Other detections of discrete clumps by (Rivers, Markowitz, and Rothschild, 2011; Markowitz, Krumpe, and Nikutta, 2014) yield distance estimates consistent with the outer broad line region or the inner dusty torus.

The attenuation of the X-rays in obscured AGN is mainly via photoelectric absorption (e.g. Murphy and Yaqoob, 2009). The absorption is stronger in the soft X-ray bands, leading to attenuation of the soft excess otherwise seen in unobscured cases. The spectra of obscured AGNs also has a reflection component – the CRH along with the ubiquitous Fe Kα – which likely originates in the AGN torus (e.g. Awaki et al., 1991a; Awaki et al., 1991b; Bianchi et al., 2005). Depending on the level of absorption obscured AGNs are classified as either Compton thin or Compton thick. Compton-thin AGNs exhibit low absorption columns ($N_{\rm H} \lesssim 10^{24}$cm^{-2}), and their spectrum is dominated by the absorbed power law. The more heavily-obscured AGNs, with $N_{\rm H} \gtrsim 10^{24}$cm^{-2} are Compton-thick AGNs (Section 1.5.2); their X-ray spectrum is dominated by the torus Compton reflection component (Matt et al., 1996; Bianchi et al., 2005) (Section 1.5.2). All obscured AGNs exhibit an additional scattered component in photoionized gas resembling a power law in softer energies (Bianchi et al., 2005; Brightman et al., 2014; Buchner et al., 2019, e.g.) originating in Compton scattering of the intrinsic power law in optically-thin material distant from the central engine, e.g., the NLR. In unobscured AGNs, this component is generally overwhelmed by the direct power-law component. Furthermore, studies using the RGS high-resolution grating instrument onboard XMM-Newton have revealed that multiple obscured AGNs exhibit numerous emission lines of neon, iron, oxygen, etc. in the soft X-ray band (<1 keV) superposed on the soft-X-ray scattered component, which is consistent with originating from a photo-ionized NLR (e.g. Bianchi, Guainazzi, and Chiaberge, 2006). Figure 1.1b shows the typical continuum X-ray spectral model with the dominant components of an obscured AGN generated using spectral model components available in `XSPEC`. However, this figure does not feature the soft-X-ray emission lines from the distant photoionized NLR.

In summary, the study of obscured AGNs in the X-ray waveband contributes to our understanding of the dynamic nature of the circumnuclear gas in AGN, mainly the torus (Section 1.3). The properties of the AGN torus and the evolution in our understanding of the torus are discussed further in Section 1.5.

1.4.3 Radio classification

AGNs can also be classified as radio-loud and radio-quiet depending on their radio intensity. Radio-loud galaxies are commonly observed as two extended structures or lobes originating

from a central point source, the formation of which is driven by a strong jet (Section 1.3 Blandford and Rees, 1974). Radio-quiet AGNs do not exhibit such a structure. The dominant mechanism of radio emission is synchrotron emission in the jets, generated from the electrons accelerated in the presence of the magnetic field in the jet. Based on the jet morphology these sources can be classified into class-I or Fanaroff-Riley-I (FR-I) and class-II or Fanaroff-Riley-II (FR-II) (Fanaroff and Riley, 1974). The FR classification is thought to be at the heart of the radio galaxy evolution. Sources with higher accretion rates tend to exhibit an FR-II morphology, whereas lower accretion rate sources tend to have an FR-I morphology (e.g. Baum, Zirbel, and O'Dea, 1995). The power generated in radio wavebands over a time scale of decades is also dependent on accretion rate as suggested the recent study of sources that transitioned from radio-quiet to loud by Wołowska et al. (2021), where, they suggest that an enhancement in accretion rate can launch of a radio jet.

Blazars

The micro-physics and emission processes in jets are better understood through the multi-wavelength study of a special class of radio galaxies called blazars. In blazars, the observer sees the system along the jet axis, and the emission from the central engine (e.g. accretion disk, corona, etc.) is overwhelmed by this jet emission. In the leptonic model of the jet, the primary jet emission is generated via synchrotron emission, when the electrons are accelerated in the magnetic fields of the jet. The synchrotron emission also undergoes inverse-Compton scattering in the same electron distribution: this Synchrotron self-Compton (SSC) process generates high-energy radiation in X-rays and gamma rays (e.g. Arbeiter, Pohl, and Schlickeiser, 2005). However, 'isotropic' emission from other substructures (e.g. BLR or the torus) can also be up-scattered in the jet (External Compton process Sikora, Begelman, and Rees, 1994).

1.5 The AGN torus

In the previous sections, we discussed the importance of the AGN torus in our current understanding of the AGN classification scheme. In this section, we discuss the contemporary understanding of the AGN torus and how the paradigm evolved from a static continuous dusty structure to a more dynamic structure connected to the accretion processes in an AGN.

1.5.1 Geometry and morphology of the torus

The AGN torus is the geometrically-thick circumnuclear matter distribution where dust has survived, due to low flux or heating from the radiation incident from the central engine. The radius ($R_{\rm sub}$) beyond which dust can survive is called the dust sublimation radius (e.g. Netzer, 2015). $R_{\rm sub}$ depends on the intrinsic bolometric luminosity ($L_{\rm bol}$) of the central engine, the composition of the dust, and the level of anisotropy of the incident radiation field. The most significant composition of dust in the torus is silicon in the form of silicate compounds of metals (e.g. $Mg_{2x}Fe_{2(1-x)}SiO_4$, Draine, 2003; Ricci and Paltani, 2023) and carbon in the form of graphite (Draine, 2003). The sublimation temperatures of silicate and carbonaceous grains are $T_{\rm sub} \sim 1500$ K and $T_{\rm sub} \sim 1800$ K, respectively (Barvainis, 1987; Netzer, 2015). Assuming a standard luminosity of $L_{\rm bol} = 10^{44}$ erg s^{-1}, the torus is found to sustain beyond a radius of ~ 0.1 pc. While the dust sublimation radius is effective in estimating the region where dust can survive, from the observational and theoretical point of view the situation is more complex.

The torus has a strong thermal continuum signature in the infrared band (Barvainis, 1987). In the process of radiative transfer of the central engine emission, the dusty material of the torus produces signatures of absorption or emission. One such signature is the pair of $\sim$9.7 μm and $\sim$18 μm silicate lines (e.g., Netzer, 2015; Pier and Krolik, 1993). A continuous distribution of dust

and gas was assumed in the community's initial modeling of the infrared emission of the torus (e.g. Pier and Krolik, 1992), for simplicity of calculations. However, models wherein the torus consists solely of a continuous gas and dust distribution are disfavored on both theoretically and observational grounds. We discuss some arguments against a simple smooth torus in the following bullet points:

- Theoretically, the smooth continuous torus model poses a challenge to the existence of dust. Krolik and Begelman (1988) argued against the smooth obscurer model by invoking the argument that a high covering fraction for a smooth torus requires relatively high vertical velocity dispersion ($\sim \frac{\Delta v_z}{v_{\rm orb}}$), which is possible when the temperature is as high as $\sim 10^6$ K. In such high temperatures, the dust sublimates.
- The observations in the mid-infrared also provide evidence against a smooth and continuous torus. The 9.7μm silicate feature broadly seen as absorption in sources classified as Type-1 and as emission in sources classified as Type-2 (e.g. Ramos Almeida and Ricci, 2017) is dependent on torus matter distribution. However, divergence from the above correlation is reported for many sources, with Type-1s exhibiting both silicate emission and weak absorption and Type-2s exhibiting weak absorption (Hao et al., 2007), challenging the simple orientation dependent obscuration scenario. Ramos Almeida et al. (2011) has demonstrated that clumpy spectral models are consistent in general with the divergent mid-infrared spectral features seen in multiple Type-1, Type-2, and intermediate sources. Overall, a continuous torus distribution is expected to exhibit a high optical depth leading to a deep absorption feature, which is in contrast to the shallower feature observed in obscured sources (Nenkova et al., 2008; Netzer, 2015). Clumpiness in the torus potentially explains both the shallowness in the shape of the silicate feature, and the prevalence of both absorption and emission features in a given Seyfert type (Hatziminaoglou et al., 2015). This is broadly because: (a) the radiation can transport in between the clumps without attenuation (b) there exists a gradient in temperature between the illuminated and non-illuminated side of each clump which comprises the torus, with each clump emitting in multiple temperature (Netzer, 2015).
- In the X-rays, photoelectric absorption affects the emission from the inner corona. Several sources have exhibited a change in the line of sight absorption, indicated by variable column density at the line of sight ($N_{\rm H}$, e.g. Elvis et al., 2004; Markowitz, Krumpe, and Nikutta, 2014; Mehdipour et al., 2017; Marchesi et al., 2022). However, as a caveat, it should be noted there have been cases where the line of sight obscurer is consistent with clouds or winds residing in the broad line region, not only in the dusty torus.

The observations and theory, thus, support a more complex, and clumpy geometry of the torus. The physical processes that sustain the torus matter distribution are still debated. Traditionally, it has been regarded as the source of material that fuels the accretion flow. However, spectral studies in the mid-infrared band, interferometry, and imaging of some obscured or Type-II AGNs (e.g. NGC 424 and the Circinus galaxy, Tristram et al., 2007; Stalevski, Asmus, and Tristram, 2017) have argued that the torus is potentially connected to dusty outflows. Hönig et al. (2012) also argued the presence of a dusty outflow, originating from the inner wall of the cold dust and gas distribution, which can effectively be part of the torus. The existence of dusty outflows is also theoretically supported by hydrodynamic simulations. Wada (2012) has demonstrated that the radiative pressure or feedback from the central engine can potentially drive such outflows, which can function as a dusty obscurer with a large covering fraction, consistent with a geometrically thick torus.

1.5.2 Compton-thick AGN: X-ray signatures of the AGN torus morphology

In this thesis, we focus mainly on the heavily obscured Compton-thick AGNs. Compton-thick AGNs by definition have a line of sight column density $N_{\rm H} \gtrsim 1/\sigma_{\rm T} = 10^{24}{\rm cm}^{-2}$ (e.g. Comastri, 2004), where $\sigma_{\rm T}$ is the Thompson cross section. A sample study of X-ray spectra of local intermediate and Seyfert type-2 AGNs indicate a large fraction of heavily obscured type-2 AGNs are potentially Compton thick (Risaliti, Maiolino, and Salvati, 1999). The study indicates that the strong Compton-thick absorption originates strictly through the absorption and reflection in Type-2 AGN tori. A BeppoSAX (Boella et al., 1997) based sample study by Maiolino et al. (1998) demonstrates that the intrinsic X-ray spectra of the heavily obscured AGNs are frequently dominated by a Compton-scattered component since the intrinsic components are heavily attenuated by the torus (Section 1.4.2). Thus, the Compton-thick AGNs are characterized by the dominant Compton reflection hump and a narrow iron line, with Compton shoulders which are indications of Compton scattering (Risaliti, Maiolino, and Salvati, 1999). The reflection-dominated X-ray spectrum of Compton-thick AGNs bear the signatures of the torus morphology, e.g., covering fraction CF = $\Omega/4\pi$ of the torus, the distribution of the matter, etc.

Only a few Compton-thick AGNs are known in the local Universe which have significant X-ray flux to enable highly detailed X-ray spectral and/or imaging studies, e.g., the Circinus galaxy, NGC 1068, NGC 424, Markarian 3, etc. The limited number of sources stems from the fact that these sources have low flux below ∼10 keV due to heavy obscuration. A few benchmark objects with high observed fluxes are the nearby Circinus galaxy ($z = 0.0014$) and NGC 1068 ($z = 0.0037$), which have been extensively studied in the infrared, radio, and X-ray bands to understand the nature of the torus. X-ray spectral analysis of the two sources (e.g. Arévalo et al., 2014; Zaino et al., 2020; Kayal et al., 2023) indicate that their tori have very high column densities, $N_{\rm H} \gtrsim 2 \times 10^{24}{\rm cm}^{-2}$. The upper limit on the dynamical mass (virialized mass of the stellar distribution and the Seyfert core, Thatte et al., 1997) of the obscuring Compton-thick gas estimated from the covering fraction and line of sight absorption ($N_{\rm H}$), puts a bound on the radial extent ($\lesssim$ 10–100 pc) of the gas (Risaliti, Maiolino, and Salvati, 1999) offering the absorption. Additionally, subsequent X-ray spectroscopic and imaging studies that mapped the Doppler broadening and spatial extent, respectively, of the narrow Fe Kα core indicated that the line originates in an extended ($\lesssim$ 100 pc) and distant parsec-scale structure (Bauer et al., 2015; Marinucci et al., 2013; Andonie et al., 2022). Additionally, a spectroscopic study by Liu et al. (2019) argues that the low Fe Kα/Si Kα line ratio in the Circinus galaxy and the blue-shifted component in the Si Kα emission line is consistent with polar out-flowing gas. Spectroscopic and imaging studies in the infrared (e.g. Stalevski, Asmus, and Tristram, 2017; Stalevski, Tristram, and Asmus, 2019) and imaging, and interferometric studies (e.g. Tristram et al., 2014; García-Burillo et al., 2019; Imanishi et al., 2020; Gámez Rosas et al., 2022) indicate that the torus structure can be decomposed into disk-type and polar emission components. Therefore, with the multi-wavelength studies of the individual nearby Compton-thick Seyferts and sample studies of obscured sources, an estimate on the geometrical extent and the complicated nature of the AGN torus has emerged.

Compton-thick AGNs contribute significantly to the cosmic X-ray background (XRB Setti and Woltjer, 1989). The observed spectrum of the XRB exhibits a flux excess at $\sim$ 20 keV, which has a qualitative resemblance with the Compton hump. Obscured, mostly unresolved, and 'hidden' Compton-thick AGNs (e.g. Gilli, Salvati, and Hasinger, 2001; Ananna et al., 2019) are thought to contribute a significant fraction of flux to the hard X-ray ($\sim 20\ keV$) part of the XRB. The synthesis of the XRB requires spectral energy distributions evaluated for distribution of parameters such as $N_{\rm H}$, photon index (Γ), and other parameters governing morphology. Thus, evaluation of the composite X-ray background requires proper evaluation of the X-ray luminosity functions and space distributions of the sources, and modeling of the torus/obscurer of the obscured

sources. Thus, proper modeling of the obscured AGN sources and understanding the reliability of the currently available X-ray spectra models are necessary.

Thus for X-ray studies, careful modeling of the data is required to retrieve both the parameters of the torus morphology and the central engine. The currently available X-ray models and the radiative transfer/ray-tracing code infrastructures can be used by the community for this purpose. However, because of the low observed flux of most of these objects, such detailed modeling is not always feasible at high accuracy and precision, as discussed in Chapter 2.

Compton-thick torus models

Following these observational studies of the Compton-thick AGNs, a range of torus models were developed to model the X-ray spectrum of the torus. These models assume a range of torus geometries to simulate the X-ray spectrum of the torus by implementing the physics of radiative transfer. Continuous-torus spectral models assuming simple geometries were developed e.g. simple doughnut (e.g. MYTORUS, RXTORUS: Murphy and Yaqoob, 2009; Paltani and Ricci, 2017) and bi-conically cutout (e.g., ETORUS, BORUS; Ikeda, Awaki, and Terashima, 2009; Baloković et al., 2018) gas distributions. More complicated and clumpy models were also developed in-parallel to account for the clumpy nature of the torus e.g. CTORUS (Liu and Li, 2014), XCLUMPY (Tanimoto et al., 2019), and UXCLUMPY (Buchner et al., 2019). However, the assumed morphology is not always the only difference between these models. There are differences in the assumed micro-physics e.g. the cross sections of scattering used (Thopmson vs Klein-Nishina), the types of scattering processes considered (Paltani and Ricci, 2017) (Rayleigh scattering in addition to Compton scattering), the accounting of dust in the spectral simulations (Ricci and Paltani, 2023), iron abundance (Baloković et al., 2018), etc.

Several of these X-ray spectral models are calculated using generic Monte Carlo radiative transfer or ray-tracing codes. Some of the generic radiative transfer and ray tracing codes are SKIRT (Vander Meulen et al., 2023), XARS (Buchner et al., 2019) and REFLEX (Paltani and Ricci, 2017; Ricci and Paltani, 2023). A prime advantage of these codes is the ability of the community to build complicated and physically motivated torus models for arbitrary geometries.

Modeling the X-ray spectra; challenges

XMM-Newton (Jansen et al., 2001), *Chandra* (Weisskopf et al., 2000), and the *NuSTAR* (Harrison et al., 2013) missions have been obtaining X-ray spectral data on multiple Compton-thick AGNs to study their emission and absorption spectral components. The energy ranges of *XMM-Newton* and *Chandra* are limited to below 10 keV, enabling us to characterize this relatively softer energy band. In contrast, *NuSTAR* covers a relatively harder X-ray range, 4.0 keV $\lesssim E \lesssim$ 78 keV, and is effective in observationally constraining the Compton reflection hump. Combining these instruments for simultaneous observations can help us obtain spectra covering the entire relevant energy range of Compton-thick AGNs, and minimize ambiguity associated with modeling limited-bandpass spectra.

Kammoun, Nardini, and Risaliti (2018) performed a reliability study on the status of recovery of the black hole spin parameter from the reflected spectra for unobscured AGNs. Synthetic datasets were simulated based on the model of AGNs with warm and partial covering neutral absorption using *XMM-Newton* and *NuSTAR* responses. Fitting of the same dataset was performed to check the status of recovery of the input parameters. The study thus demonstrated the complex parameter space associated with the fitting models given the quality of the simulated datasets, consequently pointing out the limitations related to spin measurement from the reflection spectrum.

It is suspected that similar degeneracies can exist when heavily obscured spectra are modeled using the torus models. For the available X-ray torus models, we conducted a similar study (Chapter 2 and Saha, Markowitz, and Buchner, 2022) which explores parameter degeneracies as well as distinguishability between the currently available torus models, given the currently available best X-ray spectral data quality.

1.6 Temporal variability in Seyfert AGNs

AGNs exhibit variability in all timescales and wavelengths. However, the underlying processes resulting in the observed variability can be different depending on the variability mechanism, the object type, and the waveband studied. In this section, we discuss the processes associated with normal stochastic and extreme variability in Seyfert AGNs.

1.6.1 Normal variability

AGNs exhibit stochastic variability in all wavebands. The variability can occur on timescales of hours to decades (e.g. Mushotzky, Done, and Pounds, 1993; Markowitz, Edelson, and Vaughan, 2003, and references therein). A typical Seyfert or quasar exhibits stochastic variability of up to a factor of $\sim 10-20$ in X-rays (e.g. Markowitz and Edelson, 2004) and by factors of $\sim$ a few in the optical (e.g. Uttley et al., 2003) on timescales up to months–years. The leading model explaining normal stochastic variability in Seyfert-type AGNs is the fluctuating-propagation model (Lyubarskii, 1997; Ingram and Done, 2011). In this model, local stochastic variations originating in a given annulus of the accretion disk propagate inwards and modulate the variability originating from relatively more-inner radii. The local mass accretion rate variations are generated due to variations in the local magneto-rotational instability (MRI; Balbus and Hawley, 1991).

This resultant variability from these propagating fluctuations can broadly explain the observed trends in the optical-to-X-ray regime wherein emission at relatively shorter wavelengths is more variable. Under this model, emission from the inner accretion flow is more strongly modulated by local short-timescale fluctuations in the inner regions of the accretion flow. Thus, since X-rays are emitted from a compact region that is located close to the black hole ($\sim$3-10R_g; Fabian et al., 2015), they exhibit more short-timescale variations than optical emission, which is emitted from an extended region of the accretion disk.

1.6.2 Extreme variability

The intrinsic accretion rate in otherwise persistently accreting AGNs has been seen to drop or increase rapidly in excess of the normal stochastic variability in many sources. Multiple intrinsic phenomena related to changes in the accretion flow can lead to such extreme variability, and these phenomena may be connected to the episodic increase/decrease in accretion rate (e.g. Shen, 2021). Additionally, extreme variability can also result from extrinsic factors leading to changing levels of absorption, due to eclipse of the central engine by material from the broad line region (e.g. Mehdipour et al., 2017; Mehdipour et al., 2021) or the torus.

Both intrinsic and extrinsic changes might result in observational signatures in the optical/X-ray spectrum, e.g., changes in the broad emission line properties. In the optical spectra, extreme variability can result in a significant change in the relative strength of the broad emission lines – the Balmer decrement (Hα/Hβ) – or complete appearance or disappearance of the broad emission lines (e.g. Shappee et al., 2014). X-ray spectra can be affected in two ways–if driven by intrinsic factors, central engine parameters like the photon index and the X-ray flux may vary, if driven by an extrinsic change in obscuration then a spectral shape change (e.g. Mehdipour et al., 2017) is seen in the X-ray spectrum.

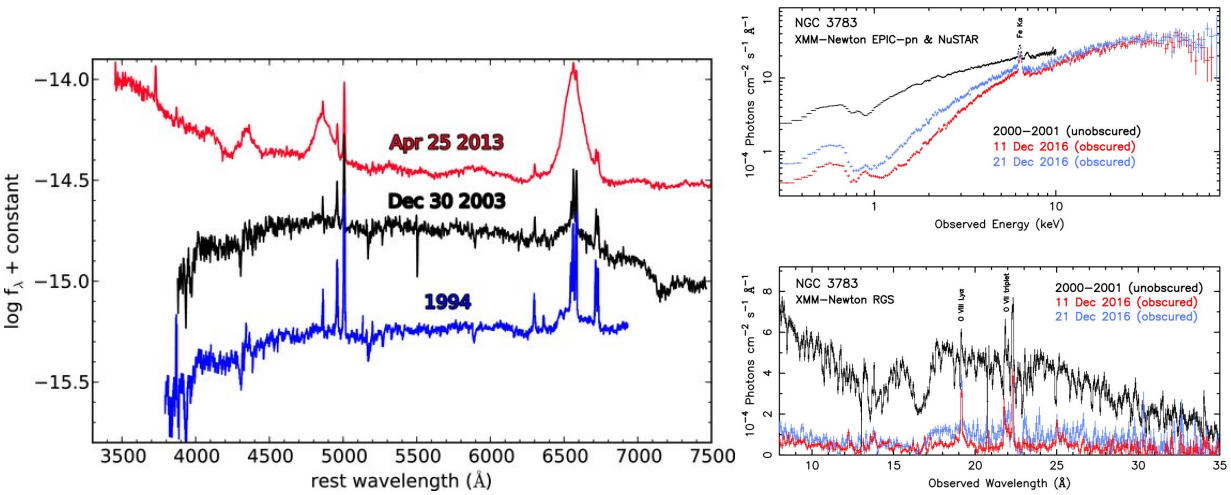

(a) (b)

FIGURE 1.2: Spectral change in an (a) optical changing-look AGN, NGC 2617, with change in broad emission line intensity (Shappee et al., 2014)(b) X-ray changing-obscuration AGN in NGC 3783 (Mehdipour et al., 2017) with variation in soft-X-ray emission. The figures shown here are published in the following articles: (a) Figure-2 of Shappee et al. (2024) ApJ, 788, 48 "The Man behind the Curtain: X-Rays Drive the UV through NIR Variability in the 2013 Active Galactic Nucleus Outburst in NGC 2617", DOI: https://doi.org/10.1088/0004-637X/788/1/48 (b) Figure 2 of Mehdipour et al. (2017) A&A "Chasing obscuration in type-I AGN: discovery of an eclipsing clumpy wind at the outer broad-line region of NGC 3783," DOI: https://doi.org/10.1051/0004-6361/201731175

1.6.3 Changing obscuration AGNs

As discussed in Section 1.4.2, some sources have been seen to exhibit time-variable absorption as distinctly indicated by their X-ray spectral change. Long-term X-ray light curves can discern distinct eclipse events, accompanied by systematic variation in the X-ray hardness ratio resulting from the spectral change, assisting detection of these events in X-ray archives.

Cloud eclipses have been detected across roughly two dozen Type-1 and Type-2 Seyferts. In general, the duration, ionization, and column density of a cloud eclipse event can yields constraints on the cloud's location. The absorption variability of multiple sources exhibiting perpetual full-covering or partial-covering of the X-ray source by a central absorber studied by Laha et al. (2020) indicated that Compton-thin $N_{\rm H}$ variability can originate from the circumnuclear torus. A detailed study of changing obscuration events based on a sample of 55 Seyferts in the *Rossi X-ray Timing Explorer* archive was conducted by Markowitz, Krumpe, and Nikutta (2014), where X-ray hardness ratio was used to identify eclipse events. The dense time sampling of a few cases allowed the estimation of the transverse density profile of some eclipsing clouds. Additionally, distances of the eclipsing clouds from the central black hole were constrained to be $\sim 3 - 10\times10^4\ R_{\rm g}$. This distance estimate is consistent with the inner torus or the outer broad line region. Importantly, Markowitz, Krumpe, and Nikutta (2014) demonstrated that continuous and systematic X-ray monitoring of a large sample of Seyferts is key for not just detecting new eclipse events in large numbers but for providing statistical constraints for the clump properties. Other cases of COAGN events have been reported in e.g., Miniutti et al. (2014), Mehdipour et al. (2021), Marchesi et al. (2022), and Torres-Albà et al. (2023), just to name a few. Another unique obscuration event was reported by (Mehdipour et al., 2017) in the source NGC 3783 (Figure 1.2b). Here, the evolution was found to affect the broad emission line properties along with imparting changes to the broad blue-shifted absorption components. The cause of the changing obscuration event was found to be triggered by a clumpy outflowing wind driven from the disk or the BLR.

In summary, the motion of the matter in the vicinity of the black hole can lead to extreme variability distinct from normal stochastic variation, and these cases of extreme variation are called changing obscuration AGNs (COAGN). Detection and follow-up studies of these sources in large numbers can lead to the understanding of the origins, kinematics, and physical properties of the obscuring gas in AGNs.

1.6.4 Changing look AGNs

In multiple AGNs, extreme variability by a factor of $\gtrsim$10 in the X-ray and/or significant changes in optical magnitude ($|g| > 1$; MacLeod et al., 2016) has been observed. Extreme variability is frequently connected to significant changes in the optical spectra which involves dramatic changes (appearance or disappearance) in the continuum and emission lines, e.g., the broad Hydrogen Balmer lines (Figure 1.2a) and consequently, a Seyfert type change (Shappee et al., 2014). These sources with extreme variability tied to optical spectral changes are referred to as changing look AGN (CLAGNs). LaMassa et al. (2015) reported a changing look transition in the quasar SDSS J015957.64 + 003310.5. The object changed from type-1 to type-1.9 within a decade. Denney et al. (2014) reported the Sy 1.5 to 1.0 to 2.0 transformation in Mkn 509 while the source's continuum gradually dimmed. Frederick et al. (2019), Frederick et al. (2021) and MacLeod et al. (2016) report multiple such cases of flaring AGNs with CLAGN phenomena detected with transient surveys by the Zwicky Transient Facility (ZTF) and using the SDSS archive. A study of Mkn 1018 by Noda and Done (2018) and a small sample of quasars by Ruan et al. (2019) reported CLAGN transitions alongside a spectral hardening over many years and argued that these transitions are analogous to state changes seen in BHXRBs. The appearance/disappearance of the broad emission lines alongside the increase/decrease of the continuum flux and broad spectral hardening/softening could not be explained by obscuration or dust reddening. Additionally, where X-ray spectra were available signatures of changing obscuration were not detected (e.g. Fig. 5 of LaMassa et al., 2015). Thus, the most plausible mechanism of the extreme variability in these sources is argued to be intrinsic changes in the accretion flow, analogous to the changes of state in X-ray binaries.

Mechanisms driving extreme variability CLAGNs

AGN accretion, which is otherwise persistent, can undergo phases of episodic cutoff and reignition. Shen (2021) argued for a paradigm that included a cumulative period of quasar activity divided into multiple shorter timescale episodes of accretion. CLAGN transitions can be a part of the proposed episodic phases of accretion.

The hardening of the broadband spectrum of Mkn 1018 (Noda and Done, 2018) and the relation of the broadband spectral shape change reported in Ruan et al. (2019) is attributed to structural changes in the accretion flow as it varied with the accretion rate. The accretion flow was thought to change from a thin accretion disk extending close to the black hole during a high accretion rate to a truncated thin disk with an inner ADAF at low accretion rates (e.g., Fig. 5 of Ruan et al., 2019). The measured accretion rate fluctuations in both the above works were much higher than expected in normal AGN variability. In the following paragraphs, we discuss the possible mechanisms.

An overall major drop or increase in accretion rate as a driving mechanism would require changes to happen in viscous timescales (Krolik, 1999), which for a standard geometrically-thin disk are longer by a few orders of magnitude than what has been observed. For a major change in global accretion rate, the infall velocity needs to be shortened considerably, thus requiring different mechanisms of angular momentum loss, e.g., large-scale waves in inner disks or MHD winds as argued by LaMassa et al. (2015).

Disk instabilities have often been invoked to explain the extreme variability CLAGN phenomenon. Accretion disks in AGNs, because of low gas densities, might have regions dominated by radiation pressure, resulting in instabilities (Lightman and Eardley, 1974) and consequently limit-cycle behavior (Lin and Shields, 1986) and outbursts (e.g. Sniegowska et al., 2020). Other instability mechanisms involve the thermal instability (MacLeod et al., 2019; Jiang, Davis, and Stone, 2016) where disk metallicity and atomic physics, e.g., the presence of iron in the accretion disks (Jiang, Davis, and Stone, 2016), can drive outbursts. To explain the variability in SDSS J110057.70-005304.5, (Ross et al., 2018) proposed the propagation of a cooling front near the innermost stable orbit or ISCO, induced by a magneto-hydrodynamical instability in the accretion flow which drives a heating/cooling front in the accretion disk. Rapid accretion changes might also involve magnetic flux inversion in magnetically arrested disks (MAD) (Sikora and Begelman, 2013; Scepi, Begelman, and Dexter, 2021), which has been invoked to explain the variability in the CLAGN event in 1ES 1927+654 initially reported by Trakhtenbrot et al. (2019). All these studies indicate that a multitude of processes intrinsic to the already-existing accretion flow can trigger extreme variability, leading to a CLAGN event.

TDEs can also induce significant increase in the accretion rate in AGNs. In this case, the star disrupts the accretion flow affecting the emission spectrum. The 'TDE in an AGN' phenomenon has been invoked to explain the variability in the CLAGN event in 1ES 1927+654 as an alternative to the magnetic flux inversion (as described in the previous paragraph). The anti-correlation of the X-rays with respect to the optical band alongside X-ray spectral softening was explained by the destruction of the corona due to the event (Ricci et al., 2020). Another source, eRASSt J234402.9−352640, detected by X-ray monitoring with eROSITA, was reported by Homan et al. (2023). This source exhibited TDE-type variability properties along with broad emission lines appearing during its ignition phase. This source also exhibited narrow emission lines and exhibited properties of a low-luminosity AGN in which TDE flaring occurred.

Overall, the AGN community has been discovering multiple changing-look AGN events. These sources, with their increasing number and diversity in physical properties, e.g., different types of line profiles and varied degrees of responses to extreme variability, are currently helping the community understand the physics of the accretion flow around supermassive black holes. However, questions remain on issues such as the diverse timescales seen in these events, the frequency of their occurrence, and the possible cause(s) of their trigger.

1.7 Detection of extreme variability events

Most of the the extreme-variability supermassive black hole transient sources that have been detected over the last few decades were detected serendipitously. However, with several optical monitoring and time domain surveys like ASAS-SN and the ZTF (Bellm et al., 2019) being operational, the search and detection of these sources in optical wavebands have become efficient. In parallel, with the periodic all-sky X-ray surveys with eROSITA, (Predehl et al., 2021) the soft X-ray telescope on the Spektrum Roentgen Gamma spacecraft, the search for extragalactic transients in X-rays has become more systematic. With the eROSITA all-sky scans, it is now possible to identify extreme brightening/dimming in X-ray flux in compact sources in any part of the sky. The community is thus entering the era of "big data," wherein it is possible to detect extreme variability trends in SMBH transients in large numbers as they are occurring, hence providing an opportunity to perform follow-up studies of these changes while they are happening.

1.8 Thesis overview

In this section, I summarize the projects that were undertaken as a part of the thesis.

Chapter 2 is focused on testing the accuracy of torus modeling using X-ray spectroscopy, given the currently available data quality and model of the AGN torus. For this purpose, we use the torus X-ray spectral models that have been developed over the last decade: MYTORUS, CTORUS, UXCLUMPY, etc. They span a range of geometries, from a simple doughnut to a distribution of clumps. However, due to limitations in current data quality, potential degeneracies can exist between these models. These degeneracies can limit reliable constraints on the intrinsic photon index, line of sight absorption, and parameters of torus morphology in the case of a Compton-thick AGN. In this project, we answered the following questions: [1] How accurately are the torus parameters recovered? [2] What is the role of systematics (fitting the data with a potentially 'wrong' model) in determining various torus parameters? [3] Are the models effectively distinguished, given a value of observed flux? To investigate these effects, we simulated X-ray spectra with some of the torus models and used Bayesian nested sampling methods through the BXA package to fit the datasets using the same set of models. The study answers the above questions by performing the fits to the simulated data using the models same as that were used during simulations and those different from the simulations. The details of the work can be found in the published paper Saha, Markowitz, and Buchner (2022): "Inferring the morphology of AGN torus using X-ray spectra: a reliability study".

Chapter 3 describes the multi-wavelength study of a flaring supermassive black hole transient event detected with eROSITA and ZTF. The Seyfert-1.9 galaxy LEDA 1154204 (6dFGS gJ042838.8-000040) went into a flaring state in early 2020. The flaring was found to be tied to a change in Seyfert type from 1.9 to 1, with the appearance of a broad Hβ emission line. We performed a multi-wavelength follow-up campaign on the source using space- and ground-based observatories for three years, to track the evolution of the broad emission lines, the accretion disk, and the X-ray emitting corona. We observe an evolving optical spectrum that transformed from being dominated by a blue quasar continuum to being dominated by a galaxy as the flare subsides. The broad emission lines of Hβ and Hα were found to be double-peaked, and their flux broadly tracks the X-ray continuum. The X-ray spectrum was found to be best explained by a simple power law and missing the near-ubiquitous soft excess. We aim to establish the plausible cause of the trigger of the extreme flaring variability (disk instability or TDE in an AGN), and the nature and geometry of the accretion disk and the broad line emitter. The details of the work can be found in the article submitted to Astronomy & Astrophysics Saha et al. (2023): "Multi-wavelength study of extreme variability in LEDA 1154204: A changing-look event in a type 1.9 Seyfert".

Chapter 4 focuses on the development of a pipeline to detect changing-obscuration AGN events using eROSITA. In this project, we initiate the development of a code to detect changing- obscuration events detected in successive eROSITA all-sky surveys. We test the feasibility of using the X-ray hardness ratio, defined by the ratio of photon counts in two given X-ray bands, to detect a transition in line-of-sight absorption in nearbySeyferts. We simulate eROSITA data under simple obscured AGN models to estimate the count-based hardness ratio for each of these models. The simulations are performed for different levels of the flux. We crudely estimate the likelihood of detecting the transitions using standard parameters of successive eROSITA all-sky scans, for different levels of flux. We find that the detection of changes in line-of-sight absorption can be made only in nearby Compton-thin and mildly obscured sources having a flux above 1 mCrab in the 2—10 keV band. The pipeline will detect new COAGN sources in the eROSITA archive and can also assist real-time detection of sources upon resumption of the eROSITA all-sky survey. The detection of new sources in large numbers will enable us to statistically study

the properties of the clumpy torus in the case of archival detection and constrain the properties of the clumps causing the obscuration in case of dense follow-up of real-time detections.

Chapter 5 contains the overall conclusion derived from the three projects undertaken in this thesis.

1.9 Chapterwise co-authorship contributions:

- **Chapter 2:**
  - Alex Markowitz: Guidance on the X-ray spectral fitting, torus models, statistical methods, and comments and feedback on the development of the manuscript.
  - Johannes Buchner: Guidance on usage of Bayesian X-ray Analysis (BXA), the torus model UXCLUMPY, and comments on manuscript.
- **Chapter 3:**
  - Alex Markowitz: Guidance on the X-ray spectral fitting and on X-ray physics of AGN, and comments and feedback while development of manuscript. Obtaining spectroscopic data from Southern African Large Telescope (SALT) as principal investigator.
  - David Homan: Guidance on the optical spectral fits and reducing data from TNG, NOT, and VLT-FORS2, and providing comments on the development of the manuscript.
  - Mirko Krumpe: Sponsoring participation in the follow-up campaign of eROSITA detected sources. Obtaining the XMM-Newton spectra as principal investigator, and providing feedback on the development of the manuscript.
  - Steven Hammerich: Development of the eROSITA pipeline, spectral data reduction from eROSITA pipeline, and comments on the development of manuscript.
  - Bozena Czerny: Providing comments on the FRADO model and extreme flaring variability in the context of disk-instability models.
  - Matthew Graham: Obtaining immediate follow-up spectral data from the Keck telescope.
  - Suvi Gezari, Sara Frederick: Obtaining the spectral data and performing reduction of the LDT datasets. Obtaining the Swift data.
  - Mariusz Gromadzki: Reducing data obtained from the SALT telescope.
  - Mohammad Hassan Naddaf: Providing the FRADO profiles for fitting the data.
  - Hartmut Winkler: Obtaining optical spectroscopic data from SAAO
  - David Buckley, Jaco Brink: Obtaining and reducing spectroscopic some of the data from SALT.
  - Joern Wilms, Andrea Gokus, Arne Rau, Zhu Liu, Iulia Grotova: Involved in the development of eROSITA software pipelines.
- **Chapter-4:**
  - Alex Markowitz: Guidance on X-ray spectral analysis, estimation of hardness ratios, and physics of obscured AGNs.

– Steven Hammerich: Providing eROSITA responses files for simulations and assistance with coding with the Interactive Sspectral Interpretation System.

– Mirko Krumpe: Providing assistance regarding the future follow-up strategies of eROSITA-detected COAGN.

Chapter 2

Article I: Inferring the morphology of AGN torus using X-ray spectra: a reliability study

In this chapter, I present the published paper, which comprises of the first part of the thesis. All the text, tables, and figures presented in this chapter have been published in the Monthly Notices of the Royal Astronomical Society in 2022 Volume 509, page 5485 with the DoI: https://doi.org/10.1093/mnras/stab3250.

2.1 Published article

Monthly Notices of the ROYAL ASTRONOMICAL SOCIETY

MNRAS **509,** 5485–5510 (2022) https://doi.org/10.1093/mnras/stab3250
Advance Access publication 2021 November 27

Inferring the morphology of AGN torus using X-ray spectra: a reliability study

Tathagata Saha [1]★ Alex G. Markowitz[1,2] and Johannes Buchner [3]

[1]*Nicolaus Copernicus Astronomical Center of the Polish Academy of Sciences, Bartycka 18, PL-00-716 Warszawa, Poland*
[2]*Center for Astrophysics and Space Sciences, University of California, San Diego, 9500 Gilman Drive, La Jolla, CA 92093-0424, USA*
[3]*Max Planck Institute for Extraterrestrial Physics, Giessenbachstrasse, D-85741 Garching, Germany*

Accepted 2021 November 4. Received 2021 October 25; in original form 2021 June 9

ABSTRACT

Numerous X-ray spectral models have been developed to model emission reprocessed by the torus of an active galactic nucleus (AGN), e.g. UXCLUMPY, CTORUS, and MYTORUS. They span a range of assumed torus geometries and morphologies – some posit smooth gas distributions, and others posit distributions of clouds. It is suspected that given the quality of currently available data, certain model parameters, such as coronal power-law photon index and parameters determining the morphology of the AGN torus, may be poorly constrained due to model degeneracies. In this work, we test the reliability of these models in terms of recovery of parameters and the ability to discern the morphology of the torus using *XMM–Newton* and *NuSTAR* spectral data. We perform extensive simulations of X-ray spectra of Compton-thick AGNs under six X-ray spectral models of the torus. We use Bayesian methods to investigate degeneracy between model parameters, distinguish models and determine the dependence of the parameter constraints on the instruments used. For typical exposure times and fluxes for nearby Compton-thick AGN, we find that several parameters across the models used here cannot be well constrained, e.g. the distribution of clouds, the number of clouds in the radial direction, even when the applied model is correct. We also find that Bayesian evidence values can robustly distinguish between a correct and a wrong model only if there is sufficient energy coverage and only if the intrinsic flux of the object is above a particular value determined by the instrument combination and the model considered.

Key words: methods: statistical – galaxies: active – X-rays: galaxies.

1 INTRODUCTION

The optical spectra of quasars and Seyfert galaxies are subject to broad classification: only Type 1 active galactic nuclei (AGN) display Doppler-broadened lines (Balmer lines, etc.), while both types exhibit narrow emission lines. A gaseous and dusty 'torus' was hypothesized to explain this diversity: under an orientation-dependent unification scheme, it blocks the line of sight (LOS) to the central engine and the broad line emission region (Antonucci 1993) in the type 2 objects. For example, one simple depiction of the morphology of the AGN torus was visualized in Urry & Padovani (1995) where it was approximated to be a contiguous axis-symmetric dusty doughnut. In the X-rays, optical type 2s (and a few type 1s) exhibit strong line-of-sight absorption (e.g. Awaki et al. 1991b) which can be attributable to a circumnuclear obscuring torus. This finding implied that the X-ray spectral properties of the AGN were dependent on whether and at which angle the observer's LOS intersected the torus. Physically such an obscuring torus can be a matter reservoir which feeds the AGN over its duty cycle and additionally can have links to radiatively driven outflows (Hönig et al. 2012). The outflows driving matter away from the central black hole into the galactic environment (Hönig 2019) thus are a potential source of AGN feedback, limiting the mass of the central black hole (Murray, Quataert & Thompson 2005). Thus the different roles the torus plays in the AGN or galactic environment can be correlated with the complexities in its structure. Hence, studying the morphology and nature of the torus is important not just for understanding AGN/Seyfert orientation-dependent unification schemes, but also for luminosity-dependent unification schemes (Ricci et al. 2013), contributions of obscured AGN to the cosmic X-ray background (CXB; Comastri et al. 1995; Risaliti, Maiolino & Salvati 1999; Gilli, Salvati & Hasinger 2001; Treister & Urry 2005; Gilli, Comastri & Hasinger 2007) and potential anisotropic radiative effects on host galaxy processes, such as star formation (Murray et al. 2005; Fabian, Celotti & Erlund 2006) or ionization of diffuse plasma (e.g. Yang, Wilson & Ferruit 2001).

Several studies in IR and X-rays have shed light on the possible structure of the AGN torus. The X-ray study by Awaki et al. (1991a) showed that the iron line Fe K edge could be reproduced sufficiently by a torus model where viewing angle is the only parameter. The sufficiency of a one parameter torus model in Awaki et al. (1991a) could be the result of poor quality of data (in terms of signal-to-noise ratio and degrees of freedom available) analysed. A subsequent study by Alonso-Herrero et al. (2003) discovered that a simplistic torus model with a higher optical depth towards the equator was unable to explain the absence of predicted dichotomy in the steepness in the IR spectra for type 1 and type 2 AGNs. Lutz et al. (2004) and Horst et al. (2006) demonstrated that infrared (IR) emission from dust structures is relatively more isotropic than predicted from

★ E-mail: tathagata@camk.edu.pl

a simple continuous-doughnut shape; additionally the ratio of X-ray and mid-infrared (MIR) luminosities is similar for both type-1 and type-2 Seyferts. All these results provide observational evidence against the orientation-only classification of type-1 and type-2 AGN. Also, X-ray eclipse events (e.g. Risaliti, Elvis & Nicastro 2002; Markowitz, Krumpe & Nikutta 2014) produced strong evidence that the obscurer is clumpy, thus challenging the pure orientation-dependent paradigm of AGN classification. Additional evidence for clumpiness in the circumnuclear material comes from MIR spectral fits (Ramos Almeida et al. 2011). It has thus been established that it is not just the orientation but also the nature of the obscurer that determines whether an AGN is seen as type-1 or 2 in optical or obscured or unobscured in X-rays (e.g. Ramos Almeida & Ricci 2017). Elitzur (2008) summarized the observational signatures which indicated the presence of the clumpiness of the torus. An even further complication is a likely dependence of covering fraction on intrinsic luminosity (e.g. Burlon et al. 2011; Ricci et al. 2015).

In this work, our attention is focused towards Compton-thick X-ray obscured AGN and we investigate how accurately the properties of the torus and the central engine can be discerned from their X-ray spectra. The X-ray spectrum of a Compton-thick obscured AGN is comprised of two components viz. the photoelectrically absorbed (zeroth-order continuum) and Compton scattered component (reflection component) of the direct power-law originating in the AGN corona. In addition to the continuum, there are several distinct emission lines from the most abundant elements, notably the 6.4 keV iron line, accompanied by their Compton shoulders (e.g. Ghisellini, Haardt & Matt 1994; Done, Madejski & Smith 1996; Matt 2002; Yaqoob & Murphy 2011). The zeroth-order continuum and the scattered power law has information about the torus morphology and the obscured central engine. Previously in X-ray spectral data fits (e.g. Bianchi et al. 2005), the assumed model for the zeroth-order continuum was an absorbed power law and the model for the scattered component was approximated by using simplistic models viz. reflection from infinite slab (Magdziarz & Zdziarski 1995). Reflection models incorporating a semi-infinite slab are more consistent with an accretion disc rather than a torus. Hence, no physically important parameters corresponding to the torus morphology can be derived when a geometrically inconsistent model (e.g. Murphy & Yaqoob 2009) is used for data analysis. Thus in an attempt to study the physics of the X-ray obscurer, numerous physically motivated models simulating the reprocessed X-ray spectral emission from the AGN torus have been developed over the past decade. These models use complex radiative transfer codes to calculate the X-ray spectrum of a Compton-thick AGN. Some assume a contiguous dust and gas structure; others assume clumpy distribution of dust and gas. Other than the differences in the morphology, the models also assume different aspects of radiative physics like different scattering cross-sections and consideration of some different radiative components. The differences in morphology and/or radiative physics introduce different features in the scattered spectra of the AGN torus e.g. like different nature of the Compton-Reflection Hump (hereafter 'CRH'), different shape of the iron lines, and Compton shoulders. Most of the simulated models are available as FITS tables and can be used for fitting to real data to estimate the model parameters via spectral analysis software like XSPEC and ISIS.

Spectral model fits, including those involving torus models, can be potentially misleading in two different ways. First, some parameters in the given model are degenerate with some other parameters and these degeneracies can affect the quality of simple spectral model fits. From the statistical point of view in complex parameter space, simple χ^2-fit algorithms can get stuck and falsely return wrong values of parameter and uncertainties. Secondly, it might be possible to fit a given data set with different models and obtain good measure of goodness of fit (χ^2/dof), but with differing value of fit parameters (Guainazzi et al. 2016) for different models assuming different geometry. Ogawa et al. (2019) have demonstrated similar cases of model degeneracy for un-obscured cases, where both relativistic reflection from the accretion disc, modelled using `xillver` and the scattered continuum from the AGN torus, modelled using `XCLUMPY` (Tanimoto et al. 2019) could fit the same data set. This problem of model degeneracy will aggravate as we descend down to low data quality shorter exposures or lower fluxes where the signal-to-noise ratio is poor. The data-model residuals alone can become ineffective in determining the best model for a given data. This brings challenges in measurement of quantities derived from fit parameters; e.g. Eddington ratio (λ_{edd}) or bolometric luminosity (L_{bol}) calculated from Γ (e.g. Brightman et al. 2013). So from the viewpoint of data analysis, X-ray astronomers must be informed about which parameters from the models can be constrained correctly, which parameters have the potential to mislead and what are the signatures that can be helpful to realize that the fitting model is not appropriate.

In this paper, we investigate the problem from the viewpoint of an observational astronomer. The goal of our work partially mirrors that of González-Martín et al. (2019) in their testing reliability of AGN IR spectral model fits. We use data simulated using the torus models and the instrument functions of two X-ray satellites, *XMM–Newton* and *NuSTAR*, whose combined X-ray coverage spans 0.2–78 keV. We use Bayesian analysis to calculate posteriors and evidence value of a model given a simulated data set(s). The case where data are simulated under and analysed with the same torus model is referred to as the intramodel analysis. The case where data are analysed using a torus model different from the one that has been used to simulate it, is referred to as cross-model analysis. We analyse the behaviour of parameter posteriors and the values of Bayesian evidence for both intra- and cross-model analyses in different conditions to understand their implications on model distinction and parameter determination.

The remainder of this paper is organized as follows: In Section 2, we introduce the spectral models and each of their geometries and parameters, we introduce the Compton-thick model used to test them, and we describe aspects of data simulation and the Bayesian spectral fitting method used. In Sections 3 and 4, we present the results of our model fits, for intra- and cross-model analyses, respectively. In Section 5, we briefly discuss feasibility of detection of a broad discline component in these spectra. In Section 6, we present considerations for exposure time requirements. In Section 7, we discuss our results, including guidelines to the X-ray community regarding making conclusions about the original obscurer morphology and the values of parameter that are estimated from the fits, and caveats associated with our analysis. We summarize our findings in Section 8.

2 METHODOLOGY

In this section, we discuss the models we test, their morphology and the parameters. We also discuss the methodology of our data simulation using the models and our data analysis. This section also contains important abbreviations that we use throughout the work in the subsequent sections.

2.1 Description of models used

In this subsection, we summarize the key features of the different models we tested here.

(i) MYTORUS: Murphy & Yaqoob (2009) assumes an axi-symmetric doughnut geometry. The model thus implements the classic orientation dependent AGN classification paradigm. The size of the torus is determined by the ratio c/a where c is the distance from the point X-ray source and a is the radius of the torus cross-section. The ratio is $c/a = 0.5$ (fixed) in the published model. The gas density is uniform throughout the torus. The column density at the equator ($N_{\rm H,\,eq}$) is a variable parameter; the LOS column density ($N_{\rm H,\,los}$) is derived from the ratio c/a and angle of inclination ($\theta_{\rm i}$). Here and throughout the paper, we refer $\theta_i = 0^\circ$ or 90° as face-on or edge-on, respectively. The mathematical relation between $N_{\rm H,\,eq}$ and $N_{\rm H,\,los}$ is given by

$$N_{\rm H,los} = N_{\rm H,eq}\sqrt{1-\left(\frac{c}{a}\right)^2\cos^2\theta_{\rm i}}. \quad (1)$$

The primary radiative processes that reprocesses the input radiation are photoelectric absorption, Compton scattering, and fluorescent line emission. The published model in its most recent version has three separate FITS files: each for the zeroth -order continuum, the scattered continuum and the iron fluorescent lines with their Compton shoulders. The input to the torus is assumed to be a simple power law.

(ii) RXTORUS: This model is based on the radiative transfer code REFLEX (Paltani & Ricci 2017). The geometry assumed is an axi-symmetric doughnut. However, there are important additions to the radiative physics of the model, where photon scattering from electrons bound to the metallic atoms are also taken into account. The scattering cross-sections of bound electrons are modified by binding corrections, which decrease the Compton scattering cross-section and the Rayleigh scattering dominates, mainly at the low energies. This is manifested as excess soft band emission, when compared to the corresponding spectra for MYTORUS. Additionally, c/a is a variable parameter (unlike in MYTORUS). $N_{\rm H,\,los}$ is a derived parameter calculated from equation (1).

(iii) ETORUS: Ikeda, Awaki & Terashima (2009) assume a continuous torus. This model has a spherical geometry with a biconical cutout at the poles; the cone vertices lie above/below the central point on the symmetry axis. The X-ray source is a point source at the sphere's center. The ratio of the inner to the outer radius of the torus ($r = r_{\rm in}/r_{\rm out}$) is kept fixed at 0.01 in the published model. The opening angle ($\theta_{\rm o}$) is variable and for obscured AGN, the angle of inclination ($\theta_{\rm i}$) has to be greater ($\theta_{\rm i} > \theta_{\rm o}$). The density of the torus is constant all throughout the volume. The model uses $N_{\rm H,\,eq}$ as a parameter in data-model fits and the LOS absorption is a function of r, $N_{\rm H,\,eq}$, $\theta_{\rm i}$, and $\theta_{\rm o}$ and is given by

$$N_{\rm H,los} = N_{\rm H,eq}\frac{r(\cos\theta_{\rm i}-\cos\theta_{\rm o})+\sin(\theta_{\rm i}-\theta_{\rm o})}{(1-r)(r\cos\theta_{\rm i}+\sin(\theta_{\rm i}-\theta_{\rm o}))}. \quad (2)$$

However for our analysis we only test the case where $\theta_{\rm i}$ and $\theta_{\rm o}$ are such that $N_{\rm H,\,los} \simeq N_{\rm H,\,eq}$. The model assumes a Thompson scattering cross-section to calculate the scattered continuum. The published model has only the reflected continuum. The zeroth-order continuum is modelled by a simple `zTBABS×CABS×CUTOFFPL` in `XSPEC` notation, where `zTBABS` models the direct photoelectric absorption and `CABS` models the Compton scattering losses. `ZGAUSS` is used to estimate emission lines.

(iv) BORUS: BORUS (Baloković et al. 2018) assumes a continuous torus with a biconically cutout spherical geometry. Qualitatively, similar to ETORUS but the with the cone vertices coincide with the central point X-ray source. The free parameters and model setup are similar to that of ETORUS. Similar to ETORUS the zeroth order continuum is modelled with a power-law attenuated `zTBABS` × `CABS`. BORUS allows for the iron abundance ($A_{\rm Fe}$) to be a free parameter in the torus, thus simulating the iron line consistently with the scattered continuum.

(v) CTORUS: The model (Liu & Li 2014) is based on `Geant4` biconical cut-out geometry except the gas distribution is clumpy. The clumps are distributed uniformly between the inner radius $R_{\rm in}$ and the outer radius $R_{\rm out}$, effectively forming a thick shell filled with clouds. The angular limitation of the clump distribution is put by a conical surface for which σ (Liu & Li 2014) is 60°. σ is not a variable parameter here.

(vi) UXCLUMPY: UXCLUMPY (Buchner et al. 2019) uses the radiative transfer code `XARS` and cloud distribution used in (Nenkova et al. 2008) given by the mathematical formula:

$$\mathcal{N}(\beta) = \mathcal{N}_0 e^{-\left(\frac{\beta}{\sigma_{\rm o}}\right)^m}, \quad (3)$$

where β is the latitude angle. The value of m is set to 2. σ_o sets the width of the torus cloud distribution about the equator. The radial distribution of the cloud is uniform (Nenkova et al. 2008). `UXCLUMPY` uses such a cloud distribution with an additional optional inner Compton-thick gaseous ring. The Compton-thick ring results in additional absorption in the 7 keV to $\sim$ 20 keV band, thus increasing the curvature of the CRH. UXCLUMPY uses $N_{\rm H,\,los}$ as a free parameter and it assumes that the line of sight always intersects with at least one clump irrespective of the inclination ($\theta_{\rm i}$). However, the distribution of the clouds imply that, as $\theta_{\rm i}$ tends towards the edge or equator (90°), the number of clumps and hence the probability of obscuration increases.

In Table 1, we summarize the models and their most important features and parameters.

2.2 The implemented model

We simulated the data while implementing the same basic model components across all the torus models. For simplicity, we choose one representative model, typical for X-ray obscured Seyferts in the nearby Universe. The model contains the following components:

(i) Zeroth-order continuum: The intrisic spectrum of the corona is assumed to be a simple power law or a cutoff power law (ICPL hereafter). In case of an obscured AGNs, the ICPL from the AGN corona is attenuated by the column of the AGN torus, by the process of photoelectric absorption. This absorbed ICPL is referred to as the zeroth-order continuum (Murphy & Yaqoob 2009) ($I_{\rm tor,\,t}(E,\ N_{\rm H,\,tor},\ \Gamma,\ \theta_{\rm i},\ R,\ x_1,\ x_2,..)$, where x_1, x_2,.. are morphological parameters of the torus). The parameters that directly affect the zeroth-order continuum involve the parameters of the ICPL viz. Γ, $E_{\rm cut}$ and the $N_{\rm H,\,los}$ column of the torus. *Throughout the paper* $N_{\rm H,\,los}$ and $N_{\rm H,\,eq}$ *are expressed in units of* 10^{22} cm^{-2} *unless stated otherwise.* For the models MYTORUS, RXTORUS, CTORUS, and UXCLUMPY, the zeroth-order continuum is published as FITS tables, whereas models like BORUS and ETORUS do not have a published FITS table for the same and hence one uses `ZTBABS` × `CABS`[1] × `ZPOWERLAW` to simulate it.

(ii) Scattered/reflected continuum: In addition to photoelectric absorption, the incident X-ray photons undergoes Compton scattering (once or multiple times) in the torus material. This modifies the ICPL to give rise to the scattered continuum, $I_{\rm tor,\,R}(E,\ N_{\rm H,\,tor},\ \Gamma,\ \theta_{\rm i},\ R,\ x_1,\ x_2,..)$, with distinct features like the CRH, fluorescent

[1] https://heasarc.gsfc.nasa.gov/xanadu/xspec/manual/node234.html

Table 1. In this table we summarize: the models names, abbreviations that we occasionally use in the parentheses and the corresponding papers (Col. 1), the type of torus and the morphology of gas or clump distribution (Col. 2), energy range set by the upper limit of *NuSTAR* (Col. 3), their corresponding parameter and the prior range we use in our work for Bayesian analysis (Col. 4), the input values of these parameters we used in our data simulations (Col. 5).

Models (1)	Gas distribution and morphology (2)	Energy range (keV) (3)	Free parameters and ranges (4)	Parameter input (5)
MYTORUS (MYT) (Murphy & Yaqoob 2009)	Continuous: Classic Doughnut	0.6–78	$N_{\rm H,eq}(10^{22}{\rm cm}^{-2}) = [1, 10^3]$	150(MCT), 680(HCT)
			$\Gamma = [1.6, 2.5]$	1.9
			$\theta_{\rm i}(^\circ) = [0, 90](\theta_i < 60^\circ)$	70
			$C_{\rm sc\text{-}pl} = [10^{-7}, 1]$	10^{-3}
			$T/R = [0.5, 5.0]$	1, 1.8
RXTORUS (RXT) (Paltani & Ricci 2017)	Continuous: Classic Doughnut	0.6–78	$N_{\rm H,eq}(10^{22}{\rm cm}^{-2}) = [1, 10^3]$	150
			$\Gamma = [1.6, 2.5]$	1.9
			$\theta_{\rm i}(^\circ) = [0, 90](\theta_i < 60^\circ)$	70
			$c/a = [0.1, 1]$	0.5
			$C_{\rm sc\text{-}pl} = [10^{-7}, 1]$	10^{-3}
			$T/R = [0.5, 5.0]$	1, 1.8
ETORUS (ETOR) (Ikeda et al. 2009)	Continuous: Sphere with biconical cutout cone vertex above/below the axis X-ray source on the symmetry	1–78	$N_{\rm H,eq} \simeq N_{\rm H,los}(10^{22}{\rm cm}^{-2}) = [1, 10^3]$	150, 500
			$\Gamma = [1.6, 2.5]$	1.9
			$\theta_{\rm o}(^\circ) = [0, 70]$	45
			$\theta_{\rm i}(^\circ) = [0, 90](\theta_i > \theta_{\rm o})$	60
			$C_{\rm sc\text{-}pl} = [10^{-7}, 1]$	$1E-3$
			$T/R = [0.5, 5.0]$	1
BORUS (BOR) (Baloković et al. 2018)	Continuous: Sphere with biconical cutout cone vertex co-incident with the X-ray source	1-78	$N_{\rm H,los}(10^{22}{\rm cm}^{-2}) = [1, 10^3]$	100(MCT), 500(HCT)
			$\Gamma = [1.6, 2.5]$	1.9
			$E_{\rm cut}({\rm keV}) = [60, 500]$	400
			$C_{\rm frac,tor} = \cos\theta_{\rm o} = [0, 1]$	0.58
			$\cos\theta_{\rm i} = [0, 1]\ (\cos\theta_{\rm i} < \cos\theta_{\rm o})$	0.48
			$A_{\rm Fe} = [0.1, 10]$	1.0
			$C_{\rm sc\text{-}pl} = [10^{-7}, 1]$	1e−3
			$T/R = [0.5, 5.0]$	1
CTORUS (CTOR) (Liu & Li 2014)	Clumpy: Uniformly distributed clouds in a thick spherical shell	1.2-78	$N_{\rm H,los}(10^{22}{\rm cm}^{-2}) = [1, 10^3]$	100(MCT), 500(HCT)
			$\Gamma = [1.4, 2.5]$	1.9
			$N_{\rm cloud} = [2, 10]$	4
			$\cos\theta_{\rm i} = [0.05, 0.95](\theta_i > 30^\circ)$	0.35
			$C_{\rm sc\text{-}pl} = [10^{-7}, 1]$	10^{-3}
			$T/R = [0.5, 5.0]$	1,1.8
UXCLUMPY (UXCL) (Buchner et al. 2019)	Clumpy: Distribution proposed in (Nenkova et al. 2008)	0.3-78	$N_{\rm H,los}(10^{22}{\rm cm}^{-2}) = [1, 10^4]$	100(MCT), 500(HCT)
			$\Gamma = [1.4, 2.5]$	1.9
			$E_{\rm cut}({\rm keV}) = [60, 500]$	200,400
			$\sigma_{\rm o}(^\circ) = [6, 84]$	45
			$C_{\rm frac} = [0.0, 0.6]$(inner ring)	0.4
			$C_{\rm sc\text{-}pl} = [10^{-7}, 1]$	10^{-2}(MCT)
				$3.5E-3$(HCT)
			$\theta_{\rm i}(^\circ) = [0, 90]$	60

emission lines and a softer tail ($E < 6$ keV) which are discussed below. For all the models the scattered component are published FITS tables. The scattered continuum contains the information about torus morphology. One aspect of the application of a torus model is the value relative normalization (denoted as T/R hereafter) of the zeroth-order continuum with respect to the scattered continuum. The user has the freedom to either set $T/R = 1$ or let T/R vary. In a real scenario the scattered component is delayed with respect to the zeroth-order continuum due to light traveltime. Thus, in such a case if the ICPL exhibits significant variability $T/R \neq 1$ (see MYTORUS online manual[2]) and should be kept free in the analysis.

(iii) Emission lines: The spectra also contains several fluorescent emission lines, of which the most notable is the iron emission line

[2]http://mytorus.com/mytorus-instructions.html

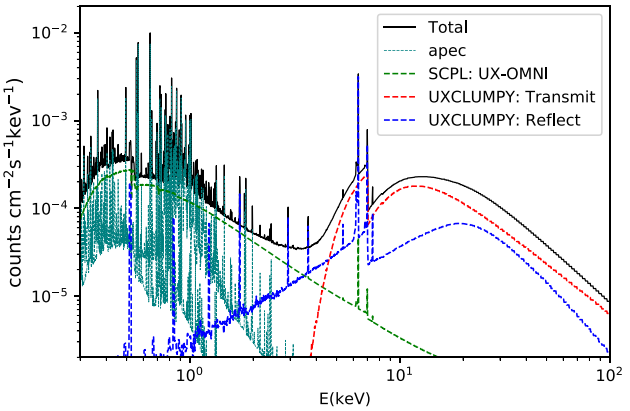

Figure 1. The plot illustrates the model components and how they contribute to the total spectrum. The plot is generated under UXCLUMPY with $N_{\rm H,\,los}$ = 100, which implies a medium Compton-thick (MCT) regime, and it is clear that the zeroth-order continuum component has a higher flux contribution in the $E > 5$ keV band.

complex. The lines are accompanied by their corresponding Compton shoulders, which is the resultant of higher order down-scatterings. The treatment of lines are different in different models, e.g. MYTORUS provides only two emission lines, whereas UXCLUMPY, CTORUS, RXTORUS, BORUS provides numerous emission lines. ETORUS does not provide any lines, so the user needs to add an external model e.g. `zgauss` to simulate them.

(iv) Scattered power-law/warm mirror reflection: Many heavily absorbed AGNs show a significant excess emission component in the soft band. This component might be the scattered component from diffuse gas which cannot be obscured by the torus (e.g. Bianchi, Guainazzi & Chiaberge 2006; Brightman et al. 2014; Buchner et al. 2014, 2019) or the scattered component from the volume filling interclump medium of a clumpy torus (Buchner et al. 2019). For simulation of data using MYTORUS, RXTORUS, BORUS, ETORUS, and CTORUS the scattered power law or warm mirror (both referred as SCPL hereafter) was assumed to be a simple or cutoff power law. UXCLUMPY allows two setups for data simulation and fitting. In one setup, the user can use a simple `zcutoffpl` for the SCPL. We call this setup UX-ZCPL hereafter in the paper. In another setup, where the SCPL is the scattered emission from the interclump medium of a clumpy torus where scatterings of several orders are considered (Buchner et al. 2019), the user can use the published UXCLUMPY model component, `uxclumpy-cutoff-omni`. As a result, this component contributes its own weak reflection hump and Fe Kα line. We call this setup UX-OMNI hereafter in this paper. The warm mirror spectrum thus emits its own mild CRH and a weak iron line. The ratio of the normalization ($C_{\rm sc\text{-}pl}$) of the SCPL with respect to the scattered component ranges from 10^{-3} to 10^{-2} times that of the scattered component for all simulations. In this work, we refer to the ratio of the scattered power-law normalization to the torus normalization as $C_{\rm sc\text{-}pl}$.

(v) Soft X-ray thermal emission: We can expect that X-ray spectra will almost always contain some potential contamination from host galaxy structures such as star-forming regions and point sources such as ULXs or XRBs, or cluster gas if one is studying an AGN in a cluster or X-ray-emitting shocks for radio-loud objects. To encorporate such soft contamination by significant emission lines caused by photonization (Kinkhabwala et al. 2002), we introduce two components of ionized gas emission. Correct modelling of the component would involve use of e.g. PHOTEMIS[3] from the package XTARDB. This is however computationally prohibitive for the simulations we produce. Instead, we use collisionally ionized plasmas (APEC;(AtomDB version 3.0.9 [4]). The different shape has no impact on how torus models are fit.

(vi) Galactic absorption: We use `TBABS` (Wilms, Allen & McCray 2000) to simulate the Galactic absorption. We assume a value of $N_{\rm H,\,Gal}$ of 10^{21} cm^{-2} for all the simulated data.

The generic model of Seyfert-2 (see Fig. 1) implemented for all the available torus geometries and morphologies is

$$\begin{aligned} f(E) = e^{-\tau(N_{\rm H,Gal},E)}[&f_{\rm apec}(E,T_1) + f_{\rm apec}(E,T_2) + I_{\rm sc-pl}(E,\Gamma) \\ &+ I_{\rm tor,T}(E, N_{\rm H,tor}, \Gamma, \theta_{\rm i}, T, x_1, x_2, ..) \\ &+ I_{\rm tor,R}(E, N_{\rm H,tor}, \Gamma, \theta_{\rm i}, R, x_1, x_2, ..) \\ &+ I_{\rm tor,lines}(E, N_{\rm H,tor}, \Gamma, \theta_{\rm i}, R, x_1, x_2, ..)]. \end{aligned} \quad (4)$$

The regime of Compton-thick AGNs practically starts from $N_{\rm H,\,los} \simeq 100$ where the scattered continuum contributes a significant amount of flux to the spectra in addition to the zeroth-order continuum. If we move to higher values of the LOS column density, the zeroth-order continuum drops drastically and the scattered continuum starts dominating. At regime where $N_{\rm H,\,los} < 200$ the zeroth-order continuum is dominant in the $E > 4$ keV band compared to the scattered continuum. In the regime of $N_{\rm H,\,los} > 200$ the scattered continuum starts overwhelming the zeroth-order continuum. So in context of this work, we phrase the regime with $N_{\rm H,\,los} <= 200$ as medium Compton-thick (MCT) and $N_{\rm H,\,los} > 200$ as heavy Compton-thick (HCT) regime. In the heavy Compton-thick regime we analyse two different classes of spectra for two models (CTORUS and BORUS). The classes are referred to as HCT0 and HCT1. The scattered power law (SCPL) is comparatively stronger in the HCT0 class compared to the HCT1 class in the 2–10 keV energy range (see Fig. 2d and f). Its contribution is weaker with respect to the total flux ($F_{2-10,\rm torus}/F_{2-10,\rm total} \leq 70$ per cent) in the HCT0 case and the same ratio being stronger (> 70 per cent) in HCT1 case for each of two models, CTORUS and BORUS.

2.3 Data simulation

Data were simulated with the FAKEIT command in XSPEC for *XMM–Newton* EPIC-pn (Jansen et al. 2001) and *NuSTAR* focus plane modules (FPM) A and B (Harrison et al. 2013) based on the instrument responses. For our primary analysis, we assume joint simultaneous observations with both missions, simulating good exposure times after screening of 100 ks for *XMM–Newton* (t_{XMM}) and 50 ks per *NuSTAR* FPM module (t_{NuSTAR}); later, we explore the effects of using only one mission on the model fits. In our primary analysis, the 2–10 keV flux (f_{2-10}) of observed and absorbed flux for all models/instruments was ∼0.5 mCrb. However, if specific cases require us to analyse a spectrum where 2–10 keV flux is significantly different from 0.5 mCrab i.e. $|f - 0.5| \geq 0.09$ we specify the values of flux explicitly. For our primary analysis, we simulated data for 100 ks (t_{XMM}) and 50 ks (t_{NuSTAR}) on the *XMM–Newton* EPIC-pn and *NuSTAR* instruments, respectively, when the analysis concerned the behaviour of the parameters. In a separate study (the results of which are presented in Section 3.3), we intend to understand the distribution of statistical properties (e.g. the 90 per cent confidence region) of the parameters posteriors. To study the distribution of

[3] https://heasarc.gsfc.nasa.gov/xstar/docs/html/node106.html
[4] http://atomdb.org/

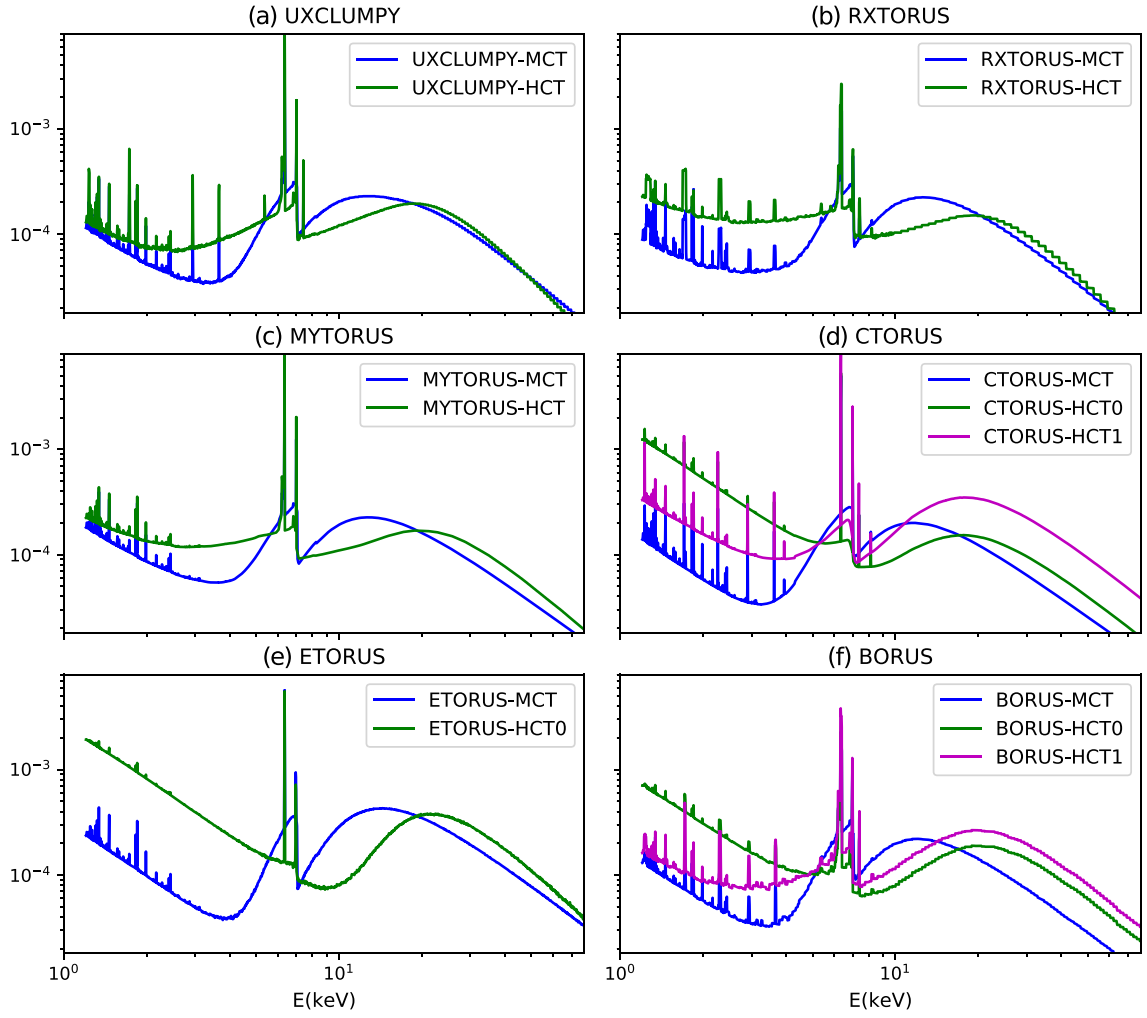

Figure 2. We plot overplot the spectrum of the input models for both the MCT and the HCT regime. HCT0 refers to the spectra where the CRH is comparatively weaker compared to the HCT1. For HCT0, the quantity $r = F_{2-10,\mathrm{torus}}/F_{2-10,\mathrm{total}} < 70$ per cent whereas, for HCT1 it is < 70 per cent. In our cases CTORUS and BORUS, $r_{\mathrm{HCT1}} \simeq 90$ per cent for both and $r_{\mathrm{HCT0}} \simeq 65$ per cent and 45 per cent for BORUS and CTORUS, respectively.

posterior properties we simulate 100 different spectral data sets under a select model for independent fitting using BXA.

For the purpose of studying the dependence of the Bayesian evidence (Z) on intrinsic flux of the object (see Section 6 below), we simulated 10 spectra with the 2–10 keV flux set to be $f = 0.83/n$ mCrb, where n runs from 1 to 10 with the exposure fixed at $t_{XMM} = 100$ ks and $t_{NuSTAR} = 50$ ks.

2.4 Fitting methods

We carry out Bayesian analysis on the simulated data sets for a given torus model to calculate the parameter posterior distribution. In this paper, we will frequently use common terminology used in simple (e.g. least squares) data-model fitting, but it should be clear to the reader, that despite using the terms that may also apply to simple data-model fitting, the process is Bayesian analysis unless explicitly mentioned otherwise. Specifically, we use nested sampling using MULTINEST (Skilling 2004; Feroz, Hobson & Bridges 2009) implemented via BXA and PyMultinest packages (Buchner et al. 2014) for X-spec version 12.10.1f (Arnaud 1996) for posterior calculation. The issues related to convergence e.g. getting trapped in a local maximum of the likelihood, in standard Goodman–Weare Markov Chain Monte Carlo (GW-MCMC) calculations are not present in nested sampling algorithms. Another convergence problem we have with MCMC is assumption on the length of the chain, which might not be enough for convergence and might require multiple burn-ins and several sequential runs. Nested sampling algorithms, including MULTINEST, attempt to map out all of the most probable regions of parameter sub-space: it maintains a set of parameter vectors of fixed length, and removes the least-likely point, replacing it with a point with a higher likelihood, and thus shrinking the volume of parameter space in each calculation. The convergence of a MULTINEST run is automatic and does not require any initial assumption like the chain length or burn-in. MULTINEST calculates a parameter called evidence Z which is the probability of data (D) given a hypothesis (H), $P(D|H)$, mathematically expressed as

$$Z = \int \mathcal{L}(D|\Theta, H)\pi(\Theta|H)d^{N}\Theta. \quad (5)$$

From a probalistic point of view the evidence (Z) is the probalility of data given the hypothesis, $P(D|H)$. There are two contributors to

the final value of evidence (Z) or $P(D|H)$ namely, the likelihood function ($\mathcal{L}$) and the final posterior (π) (see equation 5). The likelihood probability here quantifies the deviation of the data from the model and the posterior distribution $\pi(\Theta|H)$ quantifies the volume of the parameter space which signifies the effective implementation of Occam's razor criterion. The evidence value is a combined effect of these data-model deviations and Occam's razor. We use MULTINEST version 3.10 with default arguments (400 live points, sampling efficiency of 0.8) set in BXA version 3.31. For all model fits we use uniform or log-uniform as our initial prior parameter distribution. We use `cstat` (Cash 1979) in XSPEC as the likelihood function for all model fits. The `cstat` likelihood is mathematically expressed as $\mathcal{L}(\Theta, D|H) = \prod_i \frac{(f_i(\Theta)t_{\rm exp})^{D_i}}{D_i!} e^{-f_i(\Theta)t_{\rm exp}}$, where $t_{\rm exp}$ is the exposure time for a given instrument, $f_i(\Theta)$ is the theoretical count rate for a model H folded with instrument response, and D_i the count rate at the ith channel or energy bin.

We consider the best-fitting value of the parameters to be the median or 0.5th quantile of the posterior distribution and the lower and upper bound of errors are the 0.05th and 0.95th quantile of the distribution, unless stated otherwise. Our prescription of best-fitting value and bound on the error works best when th posterior distribution is a monomodal distribution. Interpretation of the results for the posteriors which show multiple maxima i.e. having multiple solutions, depend on the specific situation concerning the model and the data set. Posterior distributions which are strongly non-Gaussian (i.e. has a minima, are uniform or those that converge towards the edge of the prior range or any other 'irregularities') will be termed in general as *irregular* posteriors hereafter. Interpretation of *irregular* posteriors will be contextual. Our prescription of best-fitting value and the errors might will be less reliable in such cases and a separate treatment might be required. To quantitatively express the goodness of the recovery of the parameters, we define some simple mathematical parameters to quantify constraints, discrepancy, and the quantitative estimate on the accuracy of the returned values of the parameters.

$$R_{90} = q_{0.95} - q_{0.05} \tag{6}$$

$$\delta = \frac{0.5R_{90}}{q_{0.5}} \tag{7}$$

$$\Delta q = |q_{0.5} - q_{\rm input}| \tag{8}$$

$$r_{\rm q} = \frac{2\Delta q}{R_{90}}. \tag{9}$$

Here q_r is the r-th quantile of the posterior[5] distribution and thus R_{90} quantifies the spread of the posteriors in the 90 per cent confidence region. δ is the proportional error about the median, thus the lesser the value of δ the lesser the spread of the 90 per cent confidence region about the median. Δq quantifies the deviation of the median value of the posterior distribution from the input. r is the ratio of the deviation (Δ) to the 90 per cent confidence range (R_{90}). $r = 0$ indicates no discrepancy, whereas $r \sim 1$ indicates that the discrepancy is almost equal to the average statistical error. If $r > 1$ then the discrepancy is more than the average statistical error. In this work, we take 1.5 to be the critical value for r, thus we term a parameter recovered if $0 \leq r \leq 1.5$.

[5]The 2D posterior figures are produced using the package `corner` (Foreman-Mackey 2016). All other plots are made using the package `matplotlib` (Hunter 2007).

3 RESULTS: INTRAMODEL FITS

In this section, we present the results for the intramodel fits (IM-fits hereafter) for joint *XMM–Newton* EPIC-pn and *NuSTAR* FPM-A and B data. We grouped all simulated spectra to 30 cts bin^{-1} for our primary analysis.

3.1 Medium Compton-thick regime (MCT)

In this subsection, we discuss the results of intramodel fits to the simulated data in the MCT regime. Some models adopt LOS column density ($N_{\rm H,\,los}$) like BORUS, UXCLMPY, and CTORUS. Other models adopt column density at equator ($N_{\rm H,\,eq}$) like MYTORUS, RXTORUS, and ETORUS. During simulation of the data, for the models which adopt $N_{\rm H,\,los}$ as a parameter, we have set $N_{\rm H,\,los} = 100$. For the models that use $N_{\rm H,\,eq}$ as a parameter, we have set $N_{\rm H,\,eq} = 150$ where the implied value of $N_{\rm H,\,los}$ will be lower than 150, for $\theta_{\rm i}$ situations where the LOS interferes with the torus dust structure (e.g. $\theta_{\rm i} > \theta_{\rm o}$).

(i) Column density ($N_{\rm H}$): Both LOS column delsity ($N_{\rm H,\,los}$) in the models BORUS, CTORUS, and UXCLUMPY and equatorial ($N_{\rm H,\,eq}$) column density in MYTORUS, RXTORUS, and ETORUS are recovered with very tight constraints for all models. Over all the tested cases and models, $N_{\rm H,\,los}$ is recovered, with maximum value of $\delta = 0.032$ and the average values of $\delta = 0.023$. In this regime, the zeroth-order continuum contributes to the total observed flux more significantly than the CRH ($\left[\frac{F_{\rm T}}{F_{\rm R}}\right]_{3-100{\rm keV}} \sim 1.8$–$5.0$). The Fe K absorption edge and the rollover at $E < 5$ keV are the distinct features of a zeroth-order continuum determining $N_{\rm H,\,los}$. The geometry of the system does not play a very significant role in determining the $N_{\rm H,\,los}$ in the MCT regime, both in terms of tightness of the posteriors and parameter recovery. This holds in the cases where the spectrum is dominated by the zeroth-order continuum.

(ii) Photon index (Γ)**:** We have simulated the data with SCPL-Γ (scattered power law) and ICPL-Γ (coronal power law) set to the same value ($\Gamma = 1.9$) for all input models. When fit with the SCPL and ICPL Γ tied, Γ was recovered for all models with values of R_{90}, δ, and $r_{\rm q}$ never exceeding 0.12, 0.03, and 0.92, respectively. Despite the degeneracy or correlation between Γ and $E_{\rm cut}$ for (BORUS and UXCLUMPY), the constraints on Γ are tight. We also test the case where the values of SCPL- and ICPL-Γ were not tied for three models. The trends were model dependent in this case. For models CTORUS and MYTORUS (no $E_{\rm cut}$) constraints on ICPL-Γ were unchanged. However, the behaviour of SCPL-Γ worsened in both the cases as posteriors widened ($R_{90} = 0.27$ for CTORUS, $R_{90} = 0.11$ for MYTORUS). In UXCLUMPY for data simulated in the UX-OMNI setup, R_{90} value of ICPL-Γ worsened for both the UX-OMNI and UX-ZCPL setup due absence of leverage from the SCPL and a simultaneous varying $E_{\rm cut}$, in the uncoupled configuration. The trends in SCPL-Γ remained unchanged in the UX-OMNI setup. In the UX-ZCPL setup, the recovered value of SCPL-Γ was flatter (1.83 ± 0.05) and was just barely recovered ($R_{90} = 0.1$, $r_q = 1.4$). For this case, the SCPL-Γ lowered to account for the excess flux (noticeable in the $2 < E < 5$ keV band) in the data (simulated in the UX-OMNI setup). Thus it can be concluded that the behaviour of SCPL-Γ can affect constraints on ICPL-Γ when they are tied, more so when they have dissimilar values.

(iii) High-energy cutoff ($E_{\rm cut}$)**:** For most of the cases, we simulated the data sets with $E_{\rm cut}$ set to the highest possible limit allowed by the models, to have a minimum influence of $E_{\rm cut}$ on the other

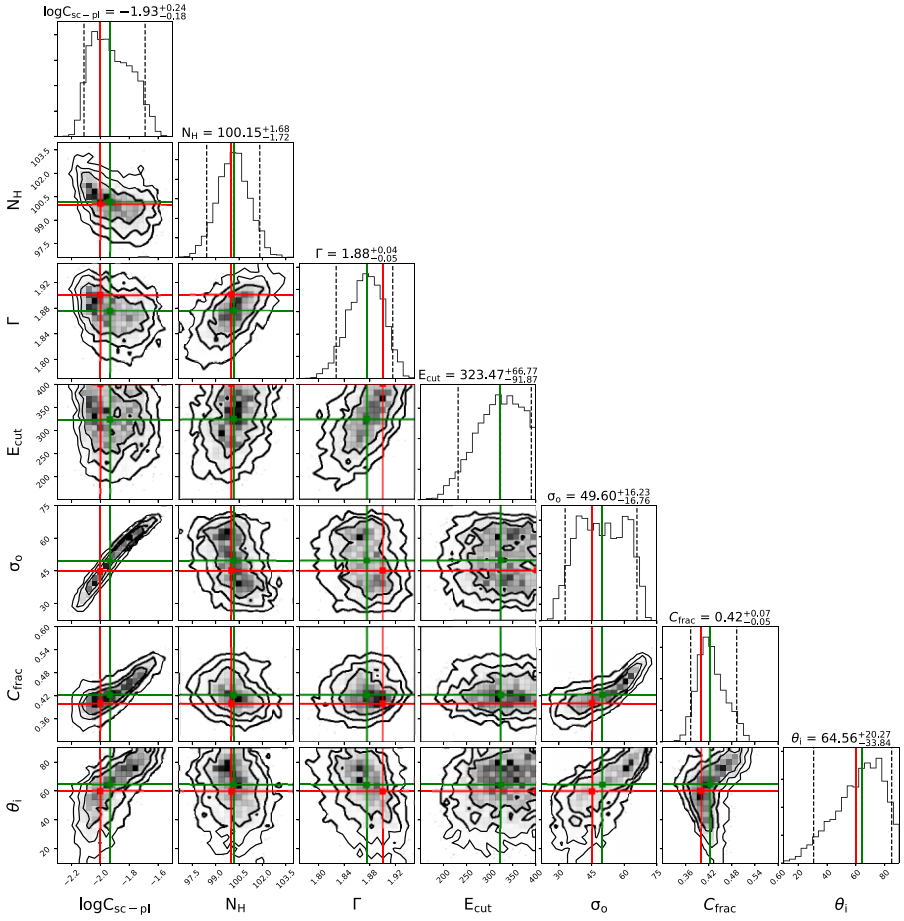

Figure 3. Contours for UXCLUMPY IM analysis in the MCT regime, with $N_{\rm H,\,los} = 100$ as input. The degeneracy or correlation between the parameters (log$C_{\rm sc\text{-}pl}$–$\sigma_{\rm o}$–$C_{\rm frac}$) with extremely skewed contours can be noticed. The lines or cross-hairs coloured red denote the input value and those coloured green denote the median value calculated from the posterior distribution.

features (e.g. CRH) in the $E < 78$ keV band. When we keep $E_{\rm cut}$ free, the posteriors of $E_{\rm cut}$ are broad and the constraints are wide in both BORUS and UXCLUMPY. We also simulated two data sets in BORUS and UXCLUMPY with $E_{\rm cut,\,input}$ for the simulated data set to a value of 200 keV. In this case, the constraints on $E_{\rm cut}$ are recovered with regular monomodal posteriors.

Γ–$E_{\rm cut}$ dependence: For models which have $E_{\rm cut}$, Γ shows a dependency on $E_{\rm cut}$ when it is kept free, this is clear from the skewness in Γ-distribution when $E_{\rm cut}$ is a variable parameter in the fits. For BORUS when SCPL-ICPL are uncoupled, posteriors of Γ in the case of $E_{\rm cut}$ frozen fits are more asymmetric and have higher values of R_{90} and δ. For UXCLUMPY, the same situation holds, but the availability and dependence on SCPL down to 0.3 keV in *XMM–Newton*, diminishes the effect of the $E_{\rm cut}$ in the fit where SCPL and ICPL are coupled. The overall trends suggest that $E_{\rm cut}$ might influence constraints on ICPL-Γ.

(iv) Angle of Inclination ($\theta_{\rm i}$)**:** The angle of inclination ($\theta_{\rm i}$) to the torus axis is determined the flux and the shape of the scattered continuum reaching the observer. Thus, the models will use the CRH and/or the low energy ($E < 6.0$ keV) tail of the scattered continuum, to estimate $\theta_{\rm i}$. For UXCLUMPY, in the UX-OMNI setup, in the *XMM–Newton*+*NuSTAR* joint fits, the value of δ for $\theta_{\rm i}$ is 0.41, indicating that it is not a well constrained parameter. For CTORUS, θ_i is skewed towards the higher angles. This is an artefact of the correlation of $\theta_{\rm i}$ with $N_{\rm cloud}$ (Fig. 6a). The $N_{\rm cloud}$ posterior which covers the whole allowed range (see pt. vii) causes the $\theta_{\rm i}$ posteriors to get skewed to higher angles. In models based on bi-conical cutouts like BORUS and ETORUS $\theta_{\rm i}$ is constrained well if the torus opening angle (cos$\theta_{\rm o}$ or equivalently $C_{\rm F,tor}$ of BORUS) constrained well. For cases when $\theta_{\rm o}$ shows trends of wider posteriors or bimodality $\theta_{\rm i}$ shows the same trend. Additionally bimodality in $\theta_{\rm i}$ was seen if $\theta_{\rm o}$ shows bimodality. In doughnut-based models like MYTORUS and RXTORUS, $N_{\rm H,\,eq}$ is the input parameter and $N_{\rm H,\,los} = f(N_{\rm H,\,eq}, \theta_i, c/a)$. Because of the dependence $N_{\rm H,\,los}$ is a well constrained parameter in this regime and thus can help narrow down the favourable $\theta_{\rm i}$ region in the parameter space. Further localization and limiting the $N_{\rm H,\,eq} - c/a - \theta_i$ degeneracy is provided by features of the scattered continuum. We find that the $N_{\rm H,\,eq} - \theta_{\rm i}$ correlation is strong when c/a is frozen. However, when c/a is kept free (in RXTORUS), the $N_{\rm H,\,eq}$–θ_i correlation weakens and the $c/a - \theta_i$ correlation strengthens.

(v) Relative normalization between the transmitted and the reflected components (T/R)**:** In many models, the normalization of the zeroth-order continuum and the scattered continuum can was kept equal i.e. $T/R = 1$ or kept free as discussed in Section 2.2. We simulated data for two cases, (A) $T/R > 1$ for CTORUS ($T/R = 1.8$) and MYTORUS ($T/R = 1.5$) (B) $T/R = 1$ for all models. We kept T/R free for only MYTORUS, CTORUS, and ETORUS. For all these models, in both case-A and case-B the parameters were recovered. For MYTORUS, CTORUS, and ETORUS (r, δ) were

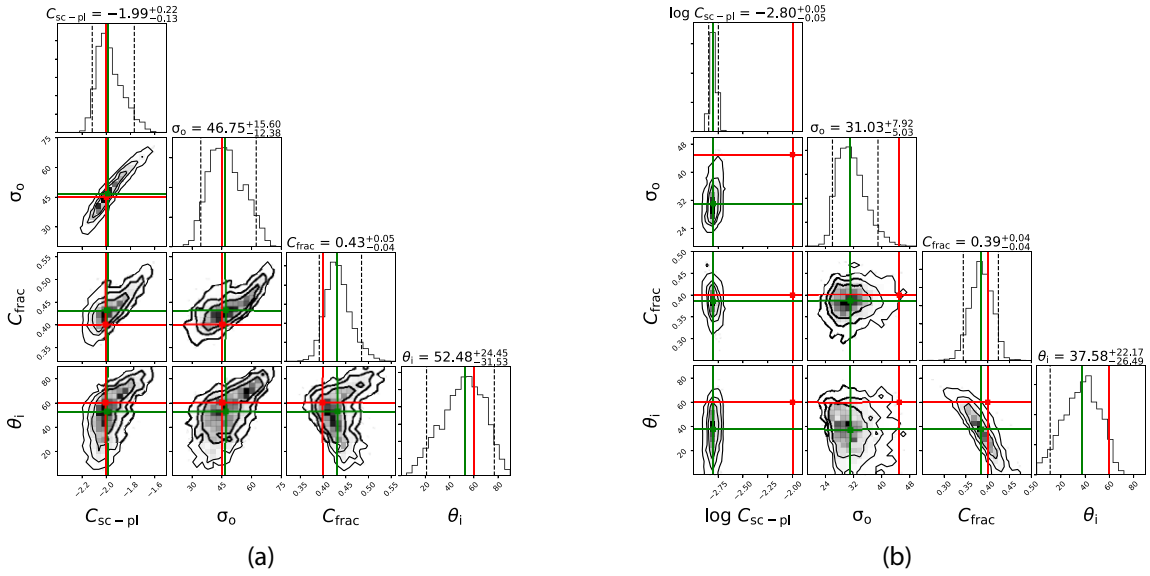

Figure 4. Contour plots indicating the correlation of the parameters $C_{\rm sc\text{-}pl}$ (relative normalization of warm-mirror or scattered power law), $\sigma_{\rm o}$, $C_{\rm frac}$, and $\theta_{\rm i}$ of UXCLUMPY, when data simulated under UX-OMNI is fit with the (a) UX-OMNI (b) UX-ZCPL setup. The red and the green lines in the histograms and cross-hairs in the contour plots mark the input and the median values calculated from the distributions, respectively. The nature of the correlation between the parameters changes depending on the SCPL model. In this case we keep the temperatures and normalizations of the apec components and the instrumental constants frozen at their input values.

found to be [A:(0.77, 0.08), B:(0.12, 0.06)], [A:(8×10^{-3}, 0.154), B:(0.09, 0.17)], [B:(0.9, 0.29)], respectively.

(vi) Relative Normalization of the SCPL ($C_{\rm sc\text{-}pl}$): For the models MYTORUS, RXTORUS, BORUS, ETORUS, and CTORUS $C_{\rm sc\text{-}pl}$ are recovered with $\delta \sim 0.067$–0.54. For UXCLUMPY, in the UX-OMNI, $C_{\rm sc\text{-}pl}$ posteriors were recovered with values of δ and r equal to 0.54 and 0.28, respectively. $C_{\rm sc\text{-}pl}$ is strongly correlated with $\sigma_{\rm o}$, $\theta_{\rm i}$, and $C_{\rm frac}$ of the inner ring. In the UX-ZCPL setup the torus $C_{\rm sc\text{-}pl}$ is recovered with $\delta \simeq 0.1$, $C_{\rm sc\text{-}pl}$ is correlated with σ_o and $\theta_{\rm i}$, but not with $C_{\rm frac}$.

(vii) Parameters of Torus morphology**:**

(a) *c*/*a* of RXTORUS**:** The posteriors returned from the fits are regular monomodal distributions. The *c*/*a*-parameter shows strong correlation with the posteriors of $N_{\rm H,\,eq}$ and $\theta_{\rm i}$. *c*/*a* in RXTORUS determines the opening angle of the doughnut, hence the $c/a - \theta_{\rm i}$ correlation. The constraints on *c*/*a* are tight as $\delta \simeq 0.086$ and $r \simeq 0.024$.

(b) Opening angle ($\theta_{\rm o}$)**:** For ETORUS $\theta_{\rm o}$ is a direct input. However, in BORUS the opening angle is given by $\theta_{\rm o} = \cos^{-1} C_{\rm F,\,tor}$ for a contiguous torus. $\theta_{\rm o}$ shows different trends in ETORUS and BORUS. For ETORUS, $\theta_{\rm o}$ returned very broad posteriors with $\delta = 0.2$ when T/R was frozen to the input value ($T/R = 1$) and worsened to 0.35 when T/R was free, with strong $\theta_{\rm o}$–T/R correlation. For BORUS ($T/R = 1$ frozen in all cases) however the constraints are better with $\delta \simeq 0.02$. The parameter constraints are determined from the shape of the lower energy ($E < 6.0$ keV) tail of the reflected continuum and the shape of the CRH.

(c) Tor-sigma ($\sigma_{\rm o}$) of UXCLUMPY: When data simulated in the UX-OMNI setup and was fit it with the same, $\sigma_{\rm o}$ is recovered with $\delta \simeq 0.33$. The 90 per cent confidence region was spread over almost ~ 65 per cent of the prior range for the given flux level (see Fig. 3). The most distinct influence σ_o and has is the soft band tail of the reflection component. σ_o along with $C_{\rm frac}$ also affects the relative height of the CRH to the FeKα absorption edge. Additionally, the zeroth-order continuum is strongly present in the 7–25 keV band and dominates the reflection component. This invokes a strong $\sigma_{\rm o}$–$C_{\rm frac}$–$C_{\rm scpl}$ correlation and a large spread in the posteriors of $\sigma_{\rm o}$ (see Fig. 4 or 3). When the UX-OMNI data set is fit with the UX-ZCPL setup, σ_o was not recovered. While we get a lower value of $\delta \simeq 0.2$, the value of r increases to 2.2, indicating a discrepancy. The SCPL excess was adjusted by decreasing σ_o, which increased the amount of the scattered component to make up for the comparatively higher contribution from the warm mirror. Fig. 4 shows the comparison of the UXCLUMPY morphological parameters, for the UX-OMNI and UX-ZCPL cases.

(d) Covering fraction ($C_{\rm frac}$) of inner ring of UXCLUMPY: In the UX-OMNI setup, there exists a strong $C_{\rm frac}$–σ_o degeneracy (see Fig. 3). The posteriors were recovered with $\delta \simeq 0.14$. But strong degeneracy with $\sigma_{\rm o}$ can result in discrepancy with the input. The constraints on the $C_{\rm frac}$ are derived from the energy band of the scattered continuum between 7 and 25 keV. In the MCT regime, the dominance of the zeroth-order continuum over the scattered continuum in the 7–30 keV energy band results in poor constraints on $C_{\rm frac}$. In the UX-ZCPL setup, $C_{\rm frac}$ was recovered with $\delta \simeq 0.08$. From the contour plots (see Fig. 4), it can be seen that the nature of σ_o–$C_{\rm frac}$ correlation is different for the two setups. UX-OMNI shows a σ_o–$C_{\rm frac}$ Pearson's correlation coefficient of 0.75 ($N_{\rm samples} \simeq 3718$), whereas for UX-ZCPL setup we get σ_o–$C_{\rm frac}$ correlation of $\sim$0.14 ($N_{\rm samples} \simeq 2682$) with a confidence of greater than 99.99 per cent.

(e) $N_{\rm cloud}$ of CTORUS: The input value of $N_{\rm cloud}$ of data simulated with CTORUS was set to 4. We simulated the data sets for $T/R = 1.0$ and 1.8, respectively (see point no. iv). The values of R_{90} and δ for both the spectra with $T/R = 1.8$ and T/R

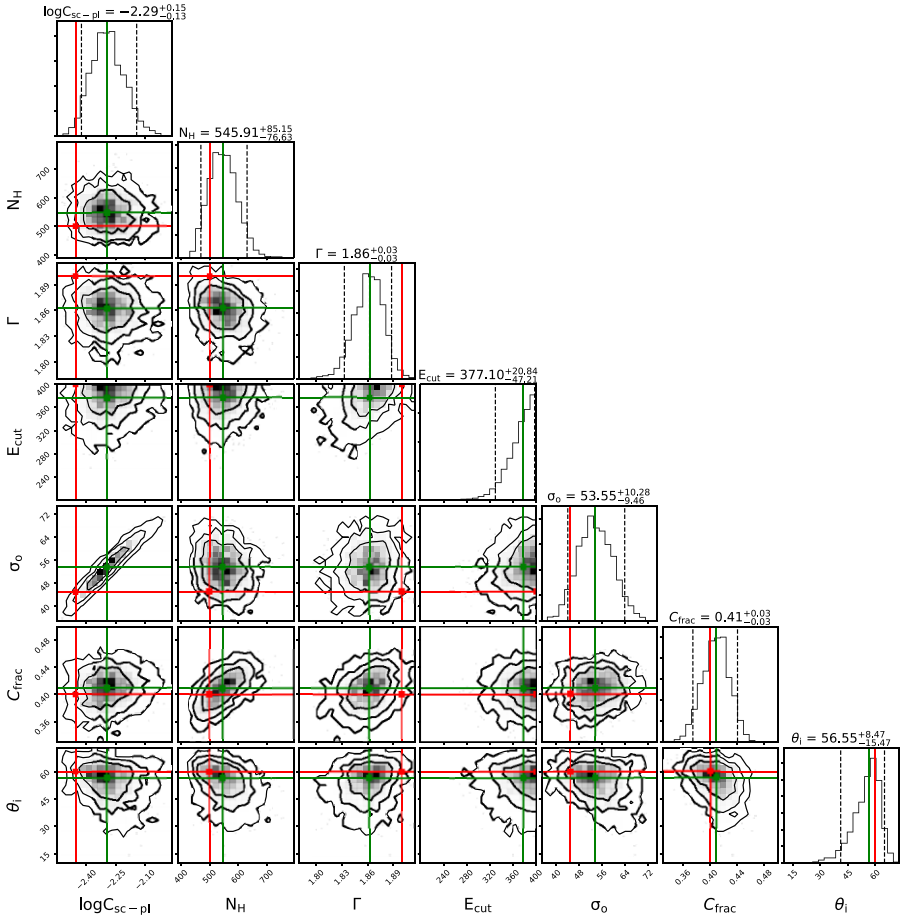

Figure 5. Contour plot for UXCLUMPY IM analysis in the HCT regime, with $N_{\rm H,\,los} = 500$ as the input. A noticeable difference exists in the parameter posteriors in terms of (1) better posterior localization/constraints on parameters of morphology and (2) lesser level of parameter degeneracy exhibited by the nature of the 2D contours compared to the MCT regime (Fig. 3). The lines or cross-hairs coloured red denote the input value and those coloured green denote the median value calculated from the posterior distribution.

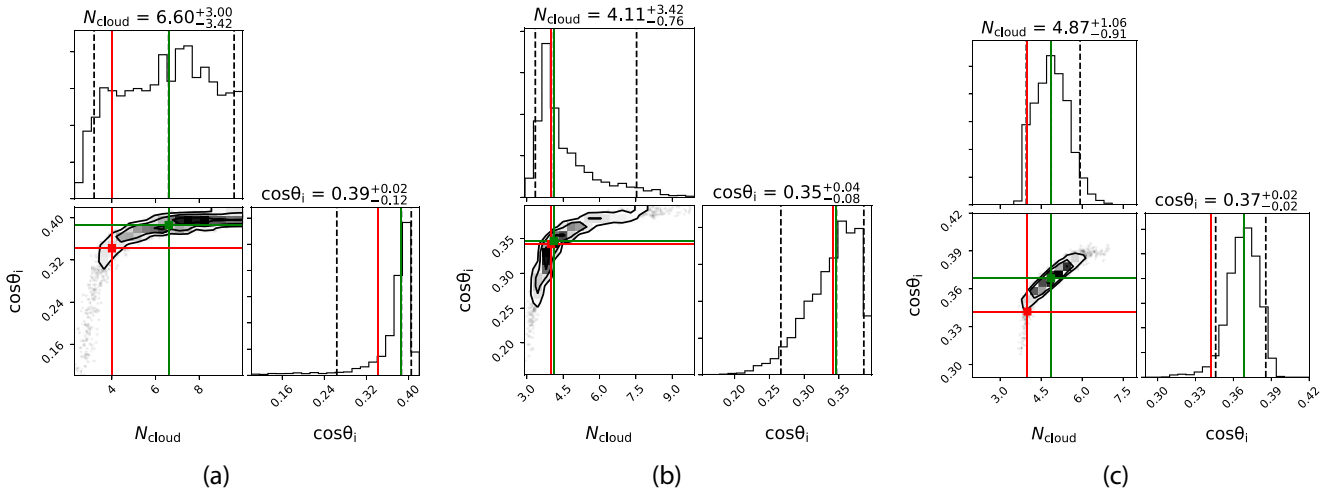

Figure 6. Contours for CTORUS IM analysis in the (a) MCT: input $N_{\rm H,\,los} = 100$, (b) HCT0: input $N_{\rm H} = 500$, (b) HCT1: input $N_{\rm H,\,los} = 500$. The lines or cross-hairs coloured red denote the input value and those coloured green denote the median value calculated from the posterior distribution. The influence on $N_{\rm cloud}$ posterior on $\theta_{\rm i}$ due to its poor localization is noticeable in (a). But constraints improve considerably in (b).

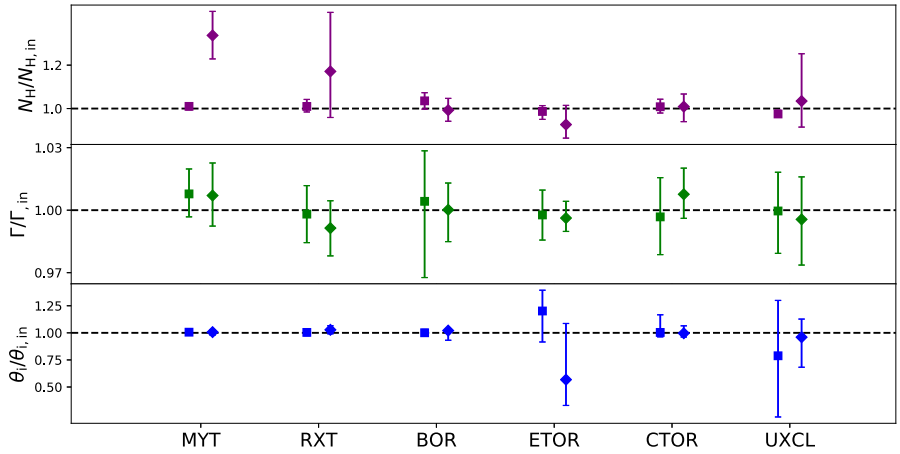

Figure 7. We plot the posterior medians and 90 per cent confidence ranges for the parameters that are common across all the models. The diamond markers are for the HCT regime and the square markers for MCT. Noticeable difference in the trends of parameters across regimes for different models can be seen e.g. $N_{\rm H,\,los}$ is well constrained in the MCT regime for all models. However, the extent of worsening of the constraints on $N_{\rm H,\,los}$ in the HCT regime is different for different models.

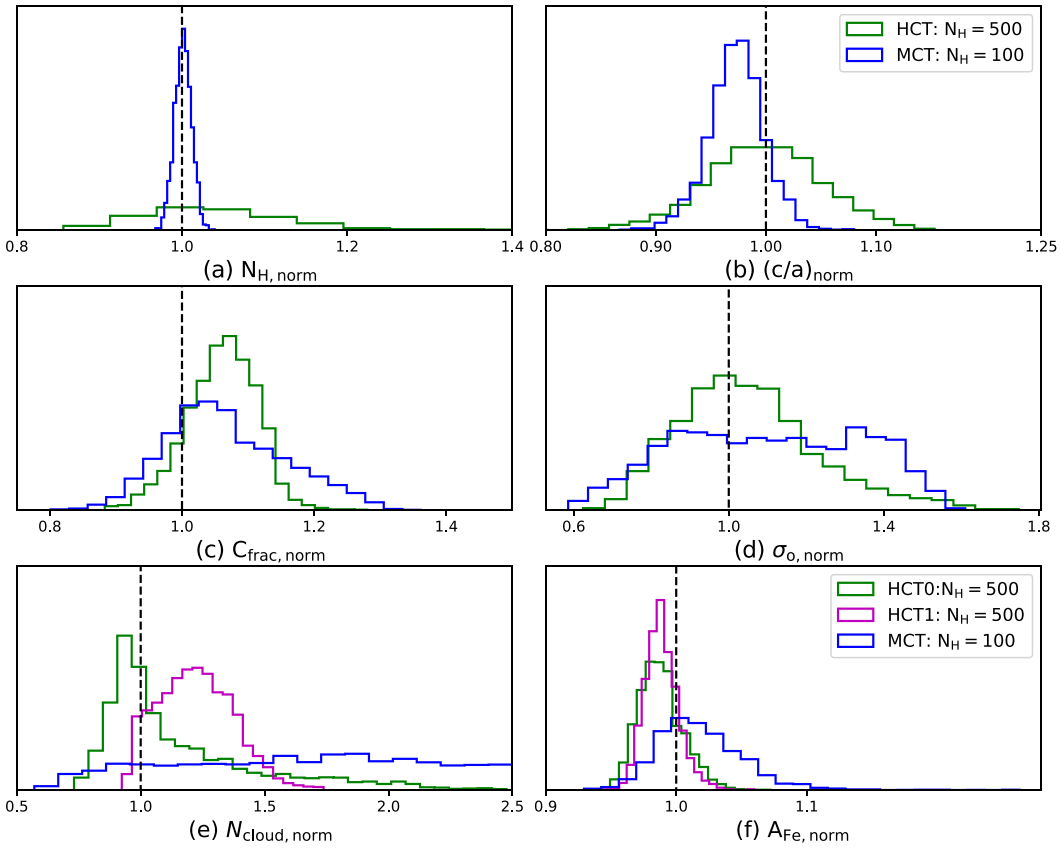

Figure 8. Overplot of the distributions of $X_{\rm norm} = X_{\rm posterior}/X_{\rm input}$ for MCT and HCT regime, where $X_{\rm posterior}$ represents the point corresponding to the posterior distribution and $X_{\rm input}$ is the input value used for data simulation. Noticeable differences exist in the distribution of the selected parameters in the MCT and HCT regimes. e.g. subplot (a) shows that the probability distribution of $N_{\rm H}$ (note: in linear space) is more localized in the MCT regime. Posterior distribution of other parameters get more localized in the HCT regime by virtue of higher flux contribution from the scattered continuum, as shown in subplots (b)–(f).

$= 1.0$ are similar ($R_{90} \sim 5$ and $\delta \sim 0.6$). The constraints on $N_{\rm cloud}$ are determined from two features of the reflected continuum: the $E < 6$ keV tail and the CRH. The reflected continuum has lower flux by a factor of $\sim$1/5 ($T/R = 1.8$) to $\sim$1/3 ($T/R = 1$) than the zeroth-order continuum in the 3–100 keV band in this regime; constraints from CRH become overwhelmed, leading to flattened posteriors of $N_{\rm cloud}$. Additionally, the soft tail ($E <$ 6 keV) of the scattered component is weaker compared to other models, leading the SCPL to be more dominant in this band, weakening the constraints on $N_{\rm cloud}$.

Table 2. In this table, we compare the average values of δ and r_q for selected parameters in the MCT and HCT regimes. The averages are taken over all analysed sub cases of all intramodel fits of the models that have the given parameter. For most parameters of morphology, we get a better constraints except θ_o of ETORUS which worsens and $\cos\theta_o$ of BORUS which does not show any significant improvement in the HCT regime.

Parameter	δ		r_q	
	MCT	HCT	MCT	HCT
$N_{H,\,los}$	0.02	0.09	0.44	0.51
Γ	0.018	0.014	0.35	0.46
θ_i	0.18	0.13	0.60	0.49
$\cos\theta_o$ of BORUS	0.035	0.021	0.84	0.23
θ_o of ETORUS	0.31	0.47	0.5	0.67
σ_o of UXCLUMPY	0.32	0.2	0.37	0.37
C_{frac} of UXCLUMPY ring	0.13	0.08	0.51	0.84
N_{cloud} of CTORUS	0.64	0.26	0.47	0.8
A_{Fe} of BORUS	0.059	0.026	0.41	0.49
c/a of RXTORUS	0.086	0.043	0.024	0.63

(f) Iron abundance (A_{Fe}) of BORUS: The zeroth-order continuum is simulated using the cutoff power law absorbed through `zTBABS×CABS` and abundance is fixed at 1. Thus, technically there is no way to consistently simulate a generic spectrum with any value of A_{Fe} by linking the zeroth-order continuum-A_{Fe} to the scattered component-A_{Fe}. Thus, to make the spectrum consistent, for the data simulated under BORUS: $A_{Fe} = 1.0$ for the scattered component. A_{Fe} was recovered ($r_q \simeq 0.2$) with $\delta \simeq 0.05$ by measuring the features e.g. depth of the Fe K absorption edge, the height of the FeKα line of only the reflected component.

(viii) APEC components: APEC parameters were genereally recovered when the lowest energy bin of the data is lower than the APEC temperature included in the spectrum. Thus with this knowledge we kept the APEC temperatures and normalizations frozen at the input values, except for a medium Compton-thick fit of UXCLUMPY where all the APEC parameters are kept free.

3.2 Heavy Compton-thick regime

The photon-index Γ did not show significant changes in the constraints. However several other parameters showed a significant change in terms of recovery, degeneracy, and constraints in the HCT regime compared to the MCT regime. We summarize the list of values of δ and r for all parameters and models for the MCT and HCT regime in Table 2. We discuss the results of fits for data simulated in the HCT regime, with $N_{H,\,los} \simeq 500$ and 2–10 keV flux values similar to that of the MCT for all models. The most significant difference of this regime is the zeroth-order continuum gets overwhelmed by the scattered continuum ($\left[\frac{F_T}{F_R}\right]_{3-100\,keV} \simeq 0.1$). We discuss the results from the HCT regime in this subsection.

(i) Column density (N_H)**:** The constraints on $N_{H,\,los}$ worsen (top panel of Figs 7 and 8a) in this regime because of the decrement of $\left[\frac{F_T}{F_R}\right]_{3-100\,keV}$ by an order of magnitude. δ ranges between 0.03 and 0.21 (average $\delta \simeq 0.09$, table 2) in the HCT-regime for IM fits of all models. For estimating the constraints on $N_{H,\,los}$ in the HCT regime (in the absence of the zeroth-order continuum) the features of the scattered continuum e.g. the relative height of the CRH to the Fe K-edge, the $E < 5$ keV tail and the shape of the Compton hump play the most significant role.

(ii) Angle of inclination (θ_i)**:** In all cases (except ETORUS), the constraints in θ_i either improved or remained same as the MCT in the HCT regime. This improvement can be attributed to the improved prominence of the scattered continuum resulting in better constraints in the morphological parameters which affects θ_i posteriors. For example in CTORUS, posteriors of N_{cloud} in the HCT1 case improved, thus improving δ for θ_i to 0.05 (Fig. 6). For UXCLUMPY the parameter posteriors of $\sigma_\circ$ and C_{frac} improved, leading to an improvement in the value of δ for θ_i. Although for the case of RXTORUS and MYTORUS, the constraints do not improve but remained almost the same as that of the MCT regime. However, ETORUS showed worse constraints on θ_i, when T/R is free but better when T/R if frozen (see next bullet point on θ_o). In the HCT regime, as an average generic trend posterior on θ_i are better constrained, with an average value of δ lower than the MCT regime for the respective models (Table 2).

(iii) Parameters of morphology:

(a) c/a of RXTORUS: The constraints on c/a improved (Fig. 8b) in this regime. The parameter was recovered, with $\delta \simeq 0.04$ which is nearly half of that calculated in the MCT regime. The value of r_q on the other hand became worse (increased to 0.63 from 0.02 in the MCT regime), (see Table 2) compared to the MCT regime. One reason for this change is the decrease in the spread of 90 per cent confidence region (R_{90}) in the HCT regime, thus increasing the ratio ($\Delta q/R_{90}$).

(b) Opening angle (θ_o) or $\cos\theta_o$**:** For ETORUS the values of δ improved mildly to 0.14 (from 0.2 in the MCT) when T/R is kept frozen at input in the HCT regime. When T/R is kept free, the constraints worsen ($\delta \simeq 0.8$) compared to MCT and are spread over the whole prior range. The soft tail ($E < 6$ keV) of the scattered continuum of ETORUS is considerably lower compared to the other models in the HCT regime. For BORUS we observe bimodality, with two disjoint peaks in the posteriors. The major peak corresponds to the input and the minor peak is significantly discrepant from the input. We can evaluate the quantiles independently for each peaks. When compared to the MCT regime the values of R_{90} and δ are similar. R_{90}=1.51 and 2.12 for the major and minor peak, respectively. The ratio of the number of samples corresponding to major and minor is $N_M/N_m \simeq 17$. It may be possible to reject the minor peak as it corresponds to lower probalility. The bimodality in θ_o induces bimodality in θ_i and $C_{sc\text{-}pl}$.

(c) **Tor-sigma** (σ_o) of UXCLUMPY: Because improved prominance of the scattered-continuum in the HCT regime, the influence of the effects of $\sigma_\circ$ on 6–40 keV becomes evident unlike in MCT. In the HCT when the σ_o decreases, it increases the level of the soft band ($E < 6$ keV) tail, it increase the warm-mirror component if the spectra are simulated in the UXOMNI setup and it approaches the Compton-thick ring and that introduces a mild depression in the 7 and 30 keV band similar to that of the Compton-thick inner ring. When $\sigma_\circ$ approaches 90° the system approaches an almost 4π covered system, diminishing the soft band significantly. These features can potentially establish stronger constraints as observed (comparison of Fig. 5 with 3 and posterior overplot in Fig. 8d) in the HCT compared to MCT as the scattered continuum is the dominant part of the spectrum.

(d) Covering fraction (C_{frac}) of inner ring of UXCLUMPY: The constraints improve (Fig. 8c) because of improved prominance of the features of the scattered continuum. This improved the posteriors of $\sigma_\circ$ and $C_{sc\text{-}pl}$, leading to elimination of the

heavy correlation seen otherwise in the MCT regime. We found that δ for $C_{\rm frac}$ improves from 0.14 in the MCT regime to 0.08 in the HCT regime.

(e) $N_{\rm cloud}$ of CTORUS**:** For the HCT regime we test two cases:

(1) The SCPL is stronger and contributes much more flux (HCT0) than the scattered continuum from the torus (green curve in Fig. 2d) in the 2–50 keV band $[f_{\rm torus}/f_{\rm total}]_{2-10} = 0.45$. This case represents objects with higher diffused/scattered emission. For this case, we get $\delta = 0.5$ and $R_{90} \simeq 4.18$.

(2) The SCPL is weaker than the soft tail of the scattered continuum from the torus (HCT1, magenta curve in Fig. 2d): $[f_{\rm torus}/f_{\rm total}]_{2-10} \simeq 0.90$. In this case, the CRH is much stronger and represents cases where the diffused or scattered emission is weak but the torus continuum is strong. For this case we get $\delta = 0.2$ and $R_{90} \simeq 1.97$. This is because of the presence of the strong soft-tail from the torus scattered continuum.

For both cases, the posteriors of $N_{\rm cloud}$ (Figs 6b and 8e) improve in the HCT regime, as the CRH and $E < 4$ keV tail become dominant over the zeroth-order continuum.

(f) Iron abundance ($A_{\rm Fe}$) of BORUS**:** The constraints of BORUS improved in the HCT regime (Fig. 8f), $\delta \simeq 0.02$. The problems introduced because of the inconsistency of the iron abundance in the zeroth-order continuum and the scattered continuum would be minimal or absent in the HCT regime, because of the low value of $\left[\frac{F_T}{F_R}\right]_{3-100\,\rm keV}$, which almost eliminates the zeroth-order continuum, thus enabling us to calculate $A_{\rm Fe}$ from the features of the dominant scattered continuum only. We found that δ improves to 0.02 in the HCT-regime from 0.07 in the MCT regime (see Table 2).

3.3 Bulk simulations

The properties of the posterior distributions e.g. R_{90}, δ, and r_q are affected by statistical processes involved in data generation. This implies that for a given theoretical spectral model, the data sets generated in each case will be different and Bayesian analysis performed on these data sets will return posteriors of parameters with median values, R_{90}, δ, and r_q different from each other. However these distributions will follow a characteristic distribution for each parameter. To verify this we perform bulk simulations of spectra for the UXCLUMPY in the MCT and HCT regime. We limit ourselves to simulating 100 spectrum for each case, due to the limits of computational power and time. We perform intramodel fits on each of these spectra and calculate posteriors in each case.

We calculate the distribution of certain properties of the posteriors (e.g. R_{90}) of different regimes. We find several properties of the distribution which are consistent with our observations from the single fits. $N_{\rm H,\,los}$ remains well constrained in the MCT regime compared to the HCT regime. The distributions of R_{90} and δ determined from the bulk fitting of the spectra of the torus-morphological parameters are localized to the lower values for the HCT regime compared to those of the MCT regime which is spread towards comparatively higher values. However, the distribution of R_{90} from the two regimes shows overlap with each other as shown in Table 3. Thus the values of R_{90} and δ estimated in the single spectral fit in the previous sections are parts of these distributions of respective parameters. That is for a given parameter the probability that the value of R_{90} (or δ) calculated from a single fit will remain enclosed in the respective values and the errorbar on the parameter quoted in Table 3 is 90 per cent. The implies that δ values quoted in Table 2 which reflect the statistical errors, should not be considered as absolute, as they can be affected by the statistical process involved in the data generation, implying a chance of getting slightly different values of R_{90} and δ for data sets simulated for the same model under same conditions. The extent of variation in the R_{90} and δ depends on the regime and the parameter of interest. Additionally, Table 4 shows that a decrease in R_{90} or δ values results in a decrease in the uncertainty on the same. In the context of intramodel fits, this means, as a parameter becomes better constrained, the statistical error on that parameter becomes less influenced by statistical processes involved in data simulation or generation.

Finally, as a test of validation of the errors for individual fits, we compare the average value of R_{90} ($\langle R_{90}\rangle = \Sigma_i(q_{0.95} - q_{0.05})$) over all the individual fits (given a parameter) and compare it with the extent of 90 per cent confidence region of the distribution of median values of the posteriors ($R_{90,\,\rm med}$). We find that values of $\langle R_{90}\rangle$ and values of $R_{90,\,\rm med}$ are very similar for both regimes. For example, values of $\langle R_{90}\rangle$ and $R_{90,\,\rm med}$ for Γ are $\sim$0.81 and 0.60 for MCT regime and 0.81 and 0.64 for HCT regime, respectively. The values of $\langle R_{90}\rangle$ and $R_{90,\,\rm med}$ for $\sigma_{\rm o}$ are, respectively, 26.14 and 20.55 for the MCT regime, and 20.04 and 18.68 for the HCT regime. These similarities indicate the properties fo the uncertainties obtained from individual fits are valid in that they are representative of the distributions of medians.

3.4 Instrument dependence of model parameters

In this section, we seek to understand which parameter constraints are leveraged by which instrument, and hence understand the required energy band coverage for measurement of a particular parameter. We fitted either *XMM–Newton* data only, or *NuSTAR* data only, and compare the results with those obtained above from joint fits. This was done for both MCT and HCT scenarios. We summarize our primary findings as follows:

(i) Column density ($N_{\rm H,\,los}$): In the MCT regime $N_{\rm H,\,los}$ parameter is more reliably determined with the *XMM–Newton* data which facilitates the better constraints compared to *NuSTAR* because of better energy resolution, thus facilitating better measurement of the Fe K absorption edge and the rollover at $E < 5$ keV. In the HCT regime the scattered component is dominant and the strong attenuation of the transmitted component does not allow the measurement of a rollover or edge of the transmitted component. Both the instruments individually do not provide reliable measurement in the HCT regime. However joint fits in all cases are more reliable in terms of values returned and in terms of low statistical errors, which makes joint observation preferable when proper measurement of $N_{\rm H,\,los}$ is concerned.

(ii) σ_o of UXCLUMPY: σ_o of the cloud distribution is not a well constrained parameter in any case, with values of δ as large as $\sim$0.30. The posteriors are wider (Fig. 9d) for *NuSTAR* compared to *XMM–Newton* only, as the $E < 4$ keV tail of the scattered component is absent in *NuSTAR* only data.

(iii) Covering fraction ($C_{\rm frac}$) of inner ring of UXCLUMPY: The constraints are generally drawn from the shape of the CRH, that is, $7 < E \lesssim 30$ keV band. We found that fitting only *XMM–Newton* data returns very wide irregular posterior, whereas *NuSTAR* only returns regular monomodal distribution, with stronger constraints. The constraints improved only by a small amount in the joint analysis. Thus, data from *NuSTAR* are a compulsory requirement to constrain the covering fraction ($C_{\rm frac}$) of such a ring if present.

Table 3. In this table, we show the distribution of the parameters characterizing posteriors distributions, calculated from the bulk fitting of 100 spectrum. The 'overlap percentage' (abbreviated as per cent-overlap) is the fraction of the values of R_{90} or δ from the wider distribution that overlaps with values lesser than the 0.95th quantile of the narrower distribution. The narrower which for the Γ and $N_{\rm H,\,los}$ is MCT regime and for $\sigma_{\rm o}$, $C_{\rm frac}$, and $\theta_{\rm i}$ is the HCT regime. These values give an idea about how much the statistical errors (R_{90}, δ, and r_q) might vary due to random process associated with the data generation.

Parameter	R_{90}			δ			r_q	
	MCT	HCT	Per cent-overlap	MCT	HCT	Per cent-overlap	MCT	HCT
Γ	$0.080^{+0.013}_{-0.015}$	$0.081^{+0.018}_{-0.017}$	$\sim$100 per cent	$0.021^{+0.004}_{-0.004}$	$0.022^{+0.005}_{-0.005}$	$\sim$100 per cent	$0.40^{+0.85}_{-0.38}$	$0.63^{+0.86}_{-0.50}$
$N_{\rm H,\,los}$	$3.24^{+0.29}_{-0.31}$	143^{+251}_{-57}	$\sim$0 per cent	$0.016^{+0.0016}_{-0.0017}$	$0.138^{+0.211}_{-0.048}$	$\sim$0 per cent	$0.56^{+0.69}_{-0.52}$	$0.32^{+0.76}_{-0.28}$
$\sigma_{\rm o}$	26^{+8}_{-6}	20^{+5}_{-4}	43 per cent	$0.27^{+0.09}_{-0.08}$	$0.22^{+0.03}_{-0.03}$	38 per cent	$0.38^{+0.91}_{-0.34}$	$0.49^{+0.82}_{-0.43}$
$C_{\rm frac}$								
of UXCLUMPY ring	$0.094^{+0.039}_{-0.016}$	$0.07^{+0.008}_{-0.013}$	10 per cent	$0.11^{+0.04}_{-0.02}$	$0.09^{+0.01}_{-0.02}$	32 per cent	$0.53^{+0.66}_{-0.48}$	$0.47^{-0.44}_{+0.73}$
$\theta_{\rm i}$	52^{+13}_{-14}	29^{+9}_{-7}	6 per cent	$0.47^{+0.60}_{-0.19}$	$0.28^{+0.2}_{-0.1}$	53 per cent	$0.41^{+0.78}_{-0.40}$	$0.53^{+0.90}_{-0.45}$

Table 4. We summarize the input parameters that are used for data simulation under UXCLUMPY and the median values and errors calculated from the parameter posteriors in this table, for the cases $M_{\rm j} \rightarrow D_{\rm UXCL}$, where j = UXCL, MYT, RXT, CTOR, and BOR in the MCT regime. For parameter estimation the full energy range allowed by a model has been taken into consideration and the χ^2/dof value is also calculated over the entire energy range. The values of evidence and Bayes-Factor are quoted for the case when all the energy range of the data used for analysis is 1.2–78.0 keV for all models.

Parameters	Input	Fitting model				
	Input for $D_{\rm UXCL}$	$M_{\rm UXCL}$	$M_{\rm MYT}$	$M_{\rm CTOR}$	$M_{\rm RXT}$	$M_{\rm BOR}$ (coupled)
$C_{\rm sc\text{-}pl}$	-2	$-1.93^{+0.24}_{-0.18}$	$-2.28^{+0.04}_{-0.04}$	$-2.19^{+0.05}_{-0.09}$	$-2.24^{+0.05}_{-0.05}$	$-2.49^{+0.03}_{-0.04}$
$N_{\rm H,\,eq}$	–	–	211^{+40}_{-34}	–	218^{+20}_{-25}	–
$N_{\rm H,\,los}$	100	$100^{+1.7}_{-1.7}$	92	$104.5^{+0.24}_{-0.29}$	92	$91.83^{+1.5}_{-1.6}$
Γ	1.9	$1.88^{+0.04}_{-0.05}$	$1.72^{+0.03}_{-0.03}$	$1.71^{+0.03}_{-0.03}$	$1.8^{+0.03}_{-0.03}$	$1.60^{+0.02}_{-0.02}$
$E_{\rm cut}$	400	323^{+67}_{92}	–	–	–	500 (frozen)
$\sigma_{\rm o}$	45	49^{+16}_{-17}	–	–	–	–
$C_{\rm frac}$	0.4	$0.42^{+0.07}_{-0.05}$	–	–	–	–
$N_{\rm cloud}$	–	–	–	$3.36^{+3.95}_{-1.2}$	–	–
T/R	1 (frozen)	1 (frozen)	$1.90^{+0.10}_{-0.10}$	$3.03^{+0.53}_{-0.44}$	$2.42^{+0.16}_{-0.15}$	$6.38^{+0.73}_{-0.73}$
c/a	–	–	–	–	$0.88^{+0.03}_{+0.02}$	–
$C_{\rm Frac,\,tor}$ or $\cos\theta_{\rm o}$	–	–	–	–	–	$0.85^{+0.06}_{-0.12}$
$\theta_{\rm i}$ or $\cos\theta_{\rm i}$ (for BOR and CTOR)	60.0	64.56^{+20}_{-33}	$63.25^{+1.43}_{-0.92}$	$0.53^{+0.29}_{-0.04}$	$36.85^{+3.48}_{-2.62}$	$0.88^{+0.05}_{-0.14}$
$A_{\rm Fe}$ (for BOR)	–	–	–	–	–	$0.96^{+0.06}_{-0.09}$
$L_{7\text{–}50}/L_{\rm in,\,7\text{–}50}$ of coronal power law	1.0	1.04 ± 0.04	0.87 ± 0.02	1.08 ± 0.04	0.89 ± 0.02	0.96 ± 0.03
χ^2/dof	–	1.004	1.14	1.09	1.11	1.34
For evidence estimates: $1.2 \leq E \leq$ 78 keV						
log$Z$	–	-592.96	-626.01	-654.60	-625.09	-800.12
log$\rm BF = \log Z_j - \log Z_{UXCL}$	–	0	-33.06	-61.64	-32.13	-207.16

(iv) c/a of RXTORUS: The values of δ are similar for both the instruments. But the median value of *NuSTAR* fit is discrepant compared to the input and posteriors are wider whereas the *XMM–Newton* fit is not. On the other hand, the constraints on the lower limit, are stronger in the *XMM–Newton* fit, whereas constraints on the higher limit are stronger for *NuSTAR* fit. The constraints on the joint fits, thus depend strongly on data from both the *XMM–Newton* and *NuSTAR* instruments. The median value of *NuSTAR* posteriors differ from the input by nearly 24 per cent, due to unavailability of the $E < 4$ keV tail of the scattered component.

(v) $N_{\rm cloud}$ of CTORUS: *XMM–Newton*-only fits provides tighter constraints compared to *NuSTAR* as shown in the figure (e.g.$R_{90,\,\rm Nu} = 6.48$ and $R_{90,\,XMM} = 4.35$ for HCT). The joint posteriors improve significantly (e.g. $R_{90,\,\rm joint} = 1.97$ for HCT) under the influence of *XMM–Newton*. Thus, for a more localized posterior on $N_{\rm cloud}$, joint fits with *XMM–Newton* data is a requirement.

(vi) $A_{\rm Fe}$ of BORUS: Both the *XMM–Newton* and *NuSTAR* parameters have values quite different from the joint fits and the input. The posteriors of *NuSTAR* are wider. We would require both *NuSTAR* and *XMM* data to constrain the posteriors better accuracy.

Our analysis of the data from the instruments separately, also shows that simultaneous coverage of $0.3 < E < 78$ keV band improves the posteriors significantly, compared to separate $E \sim 10$ keV through *XMM–Newton* or $E > 4$ keV only through *NuSTAR* coverages. We jointly show the 1D posterior plots of *XMM–Newton*

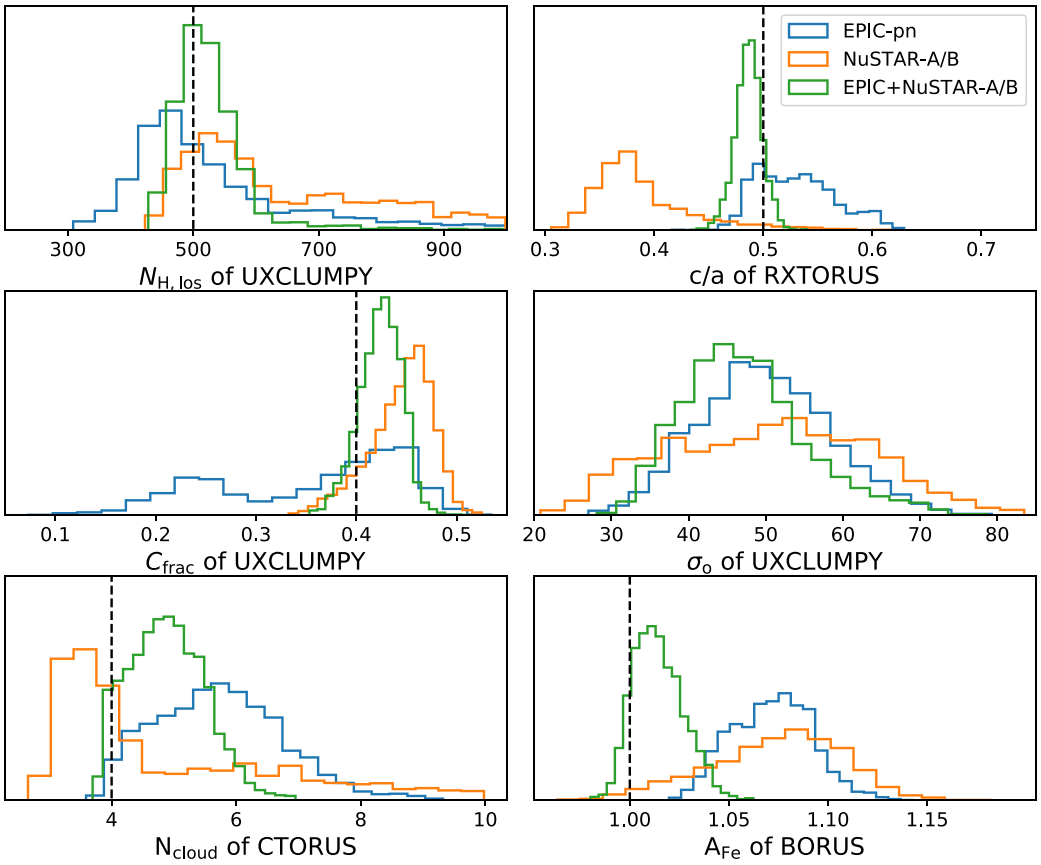

Figure 9. We compare the 1D posterior distributions calculated from *XMM–Newton*, *NuSTAR*, and joint *XMM–Newton* + *NuSTAR* fits in this figure. We notice significant dependence in the nature of the posterior distributions on the instrument and their combinations. These posteriors prove that for decent constraints on some parameters e.g. C_{frac} of the inner ring of UXCLUMPY, *NuSTAR* data is a requirement, whereas for N_{cloud} in the HCT regime joint data from *XMM–Newton* and *NuSTAR* is required.

only, *NuSTAR* only and *XMM–Newton* plus *NuSTAR* joint fits for a few parameters in Fig. 9.

4 RESULTS: CROSS-MODEL FITS

In this section, we discuss the results of cross-model fits (CM-fits hereafter). We use the notation $M_j \rightarrow D_i$ to denote that the model j is fit to data simulated under model i. The indices i and j are the abbreviations for the model of which the reflection component is featured in the data simulations or fits. The abbreviations for the torus models are summarized in Table 1. For example, when the fitting model is UXCLUMPY, the notation would be $M_{\rm UXCL} \rightarrow D_{\rm MYT}$. For other cases, the abbreviations for model combinations are defined locally. The CM fits will identify and estimate the level of degeneracy between the models, show which parameters adjust themselves to fit a given data set when the assumed morphology is wrong. We do not test all possible model combinations; instead, we concentrate on only the following cases:

(i) $M_{\rm MYT} \rightarrow D_{\rm j}$, j = RXT, UXCL: spectral change due to difference only in radiative process and how well a simple smooth doughnut can represent complex arrangements.
(ii) $M_{\rm RXT} \rightarrow D_{\rm j}$, j = MYT, UXCL: similar to MYT but for the variable doughnut parameter (c/a).
(iii) $M_{\rm BOR} \rightarrow D_{\rm j}$, j = CTOR, UXCL: what happens when a model with a simplified contiguous cut-out geometry is applied to clumpy morphologies.
(iv) $M_{\rm CTOR} \rightarrow D_{\rm j}$, j = MYT, UXCL, BOR: how a clumpy torus model with an estimate on the number of clouds in the radial direction acts when applied to data simulated under other contiguous and clumpy models.
(v) $M_{\rm UXCL} \rightarrow D_{\rm j}$, j = MYT, RXT, BOR, CTOR: same as CTOR but UXCLUMPY has a more complex cloud distribution.

Different models treat and make predictions for the shape/intensities of the emission complex of Fe Kα and other fluorescent emission lines due to different scattering geometries and different physical processes in their radiative transfer codes e.g. MYTORUS contains Fe-lines with Compton shoulders only and other models contain a wider range of species. To account for such discrepancy between models, one can perform cross-model fitting ignoring certain narrow energy ranges thus focusing more on constraints from the continuum (see Section 4.2). We can expect that there may be narrow ranges of data-model residuals corresponding to differently modelled Fe Kα and other line complexes. Future work on model comparison can be done when models offer a more consistent treatment of narrow features like fluorescent lines and Compton shoulders.

4.1 Medium Compton-thick regime

(i) Column density ($N_{\rm H,\,los}$): Across all models tested in the MCT regime, LOS column density ($N_{\rm H,\,los}$) is the only parameter that was practically recovered. The dominance of the zeroth-order continuum in this regime is the reason for the well-determined constraint and values consistent with the input for $N_{\rm H,\,los}$ irrespective of the model. The maximum discrepancy was observed for $M_{\rm CTOR} \rightarrow M_{\rm BOR}$, where the percentage discrepancy corresponds to 31.8 per cent and $r_{\rm q}$ corresponds to 8.2. With regard to specific trends we find that the clumpy torus models returned higher values of $N_{\rm H,\,los}$ when fit to contiguous torus and the converse also holds true. The values of $r_{\rm q}$ correspond to the variation of $N_{\rm H,\,los}$ by 30 per cent. In order to check the discrepancy statistically we also perform bulk CM-fits of the case $M_{\rm MYT} \rightarrow D_{\rm UXCL}$ to 100 spectra simulated under UXCLUMPY. The minimum and maximum discrepancy in $N_{\rm H,\,los}$ in the bulk fits were found to be 1.7 and 8.6 per cent, respectively. This discrepancy in the values of $N_{\rm H,\,los}$ will not create profound physical inconsistencies and will not significantly change the scientific implications in terms of the spectral shape and the components present. Thus, we conclude that $N_{\rm H,\,los}$ returned from the fits were mostly consistent with the input in the MCT regime.

(ii) Photon-index (Γ)**:** Both the CRH and zeroth-order continuum determine the value of Γ. The values of $r_{\rm q}$ that we observed for Γ in the CM-fits range from 0.67 to 15 with $\Gamma_{\rm in} = 1.90$ for all tested cases. The best value was for the case $M_{\rm MYT} \rightarrow D_{\rm RXT}$ ($\Gamma_{\rm out} = 1.91$) and the worst value was obtained for $M_{\rm BOR} \rightarrow D_{\rm UXCL}$. In the MCT regime, for a specific case $M_{\rm j} \rightarrow D_{\rm UXCL}$, where j = MYT, RXT, BOR, and CTOR, the fits systematically returned flatter values of Γ, $1.60 \lesssim \Gamma_{\rm out} \lesssim 1.75$ (see Table 4). In the converse case viz. $M_{\rm UXCL} \rightarrow D_{\rm j}$, where j = MYT, RXT, BOR, and CTOR, the estimated values of Γ were in the range $2.02 \lesssim \Gamma_{\rm out} \lesssim 2.17$. The high discrepancy (quantified by r_q) in values of Γ is a direct implication of low statistical errors, caused by the intrinsic difference in the CRH shape for different models. Therefore, we can conclude that the retrieved value of Γ is thus strongly model dependent (see Fig. 13).

(iii) Angle of inclination ($\theta_{\rm i}$): The values of $\theta_{\rm i}$ returned from the CM fits are dependent on the torus morphology. However, there might be cases where interpretation of the values can be contextual and is dependent on morphology. We observed specific trends for certain models in the CM-fits. We list these in the following bullet points:

- (A) In CTORUS the zeroth-order continuum is independent of $\theta_{\rm i}$. The information about the only parameters of morphology ($N_{\rm cloud}$) and geometry ($\theta_{\rm i}$) is in the scattered component. In CTORUS, the obscuring clouds are located in a hypothetical biconically cutout thick shell between 60° and 90° (Liu & Li 2014) with respect to the symmetry axis. In the $M_{\rm CTOR} \rightarrow D_{\rm UXCL}$ fit when we assume a prior [0°, 90°], we get an inconsistent value of $\theta_{\rm i} < 60°$ according to the geometry proposed in Liu & Li (2014). However, a possible misinterpretation is the existence of a stray clump(s) or obscurer at $\theta = \theta_{\rm i} < 60°$ which is outside the hypothetical shell enclosure of CTORUS. This stray clump or obscurer can be thought to be contributing to $N_{\rm H,\,los}$. This is just a result of spectral or model difference and hence an artefact of fitting (also see the similar discussion for $\cos\theta_{\rm o}$ for BORUS). When we limit the prior range to [60°, 90°], the posterior monotonically increases towards the 60° edge.
- (B) For the CM-fits, $M_{\rm UXCL} \rightarrow D_{\rm j}$ where j = CTOR, MYT, BOR, $\theta_{\rm i}$ assumes an edge-on configuration with monotonically increasing posteriors consistent with 90°. The only exception is $M_{\rm UXCL} \rightarrow D_{\rm RXT}$, where the median value calculated from the posterior is $\simeq 66°$ for an input $\theta_{\rm i} = 70°$; we suspect that the excess contribution in the softer bands from Rayleigh scattering might be the result of the lower values of $\theta_{\rm i}$. The input value of $\theta_{\rm i}$ and the value returned from fit $M_{\rm UXCL} \rightarrow D_{\rm RXT}$ value might agree by chance.

We discuss the case of $\theta_{\rm i}$ for the $M_{\rm RXT} \rightarrow D_{\rm MYT}$ case along with *c/a* in the fifth bullet point.

(iv) Relative normalization between the transmit and the reflect component (*T/R*): We first discuss the results from the case: $M_{\rm j} \rightarrow D_{\rm UXCL}$ (j = RXT, MYT, CTOR, BOR). We find that $T/R \neq 1$ (input). For the case $M_{\rm BOR} \rightarrow D_{\rm UXCL}$, we get an exceptionally high value of $T/R \simeq 6.38$. Physically, the zeroth-order continuum across all models has the same shape for given a $N_{\rm H,\,los}$ ($A_{\rm Fe} = 1$), whereas the scattered continuum is very different for different models. The tendency of $T/R > 1$ in CM-fits may be an attempt to get a better fit. Physically if the value of T/R is inconsistent with 1, it would imply variability of the coronal power law, however as demonstrated here this effect might be an artefact of model difference.

(v) Parameters of Torus Morphology**:**

- (a) Opening angle ($\cos\theta_{\rm o}$ or $C_{\rm frac,\,tor}$) **:** For $M_{\rm BOR} \rightarrow D_{\rm CTOR}$ we get $\cos\theta_o \simeq 0.4$ ($\theta_{\rm o} \simeq 67°$) with corresponding $\theta_i \simeq 69.6°$. However in CTORUS the obscuring clumps are distributed in the region $\theta \geq 60°$. This can be due to the difference in the total covering fraction of between the two torus. For the case $M_{\rm BOR} \rightarrow D_{\rm UXCL}$ in the coupled configuration ($N_{\rm H,\,los} = N_{\rm H,\,eq}$ in this case, (Baloković et al. 2018)), we get a case where $\cos\theta_{\rm o} < \cos\theta_{\rm i}$ which implies the line of sight does not intersect the main gas distribution of the torus, but returns a non-zero LOS absorption ($N_{\rm H,los} \simeq 92$). This dichotomy can be misinterpreted as a different matter distribution (e.g. a stray clump, same $N_{\rm H,\,los}$ as the main gas distribution) lying along the LOS. In the uncoupled configuration of $M_{\rm BOR} \rightarrow D_{\rm UXCL}$, the $\cos\theta_{\rm o} > \cos\theta_{\rm i}$, but the $N_{\rm H,\,los} \simeq 97$ and $N_{\rm H,\,eq} \simeq 1300$ heavily discrepant and becomes inconsistent with respect to the defined morphology. However, a physical interpretation for this case can be made, if the torus is clumpy, in which case $\cos\theta$ loses its meaning and hence can be interpreted as covering fraction, $C_{\rm frac,\,tor}$.
- (b) *c/a* of RXTORUS**:** For $M_{\rm RXT} \rightarrow D_{\rm MYT}$, $c/a = 0.62 \pm 0.03$ (Fig. 11) which is discrepant with the fixed assumed value of 0.5 (effective $\theta_{\rm o} = 60°$) in MYTORUS despite the fact that both are doughnut models. Given a set of parameters the scattered continuum of MYTORUS and RXTORUS have different shapes because of the radiative difference. The scattered continuum has more photon counts due to the presence of Rayleigh scattering in the $E < 6$ keV band and lesser photon counts at the CRH because of having $E_{\rm cut}$ fixed at 200 keV (Fig. 11). The parameter *c/a* thus adjusts itself to a higher value decreasing the effective $\theta_{\rm o}$ to 51.7°. Γ and θ_i were also reduced to 1.83 and 65°, respectively (Fig. 11). For the $M_{\rm RXT} \rightarrow D_{\rm UXCL}$ case $c/a \simeq 0.88$, which can be considered consistent with the extended and random cloud distribution. This also led to $\theta_{\rm i}$ for this case to take a comparatively low value, ∼37°.
- (c) $\sigma_{\rm o}$ of UXCLUMPY**:** The value of $\sigma_{\rm o}$ follows different trends for data sets simulated with different models. For all the cases of $M_{\rm UXCL} \rightarrow D_{\rm j}$, j = MYT, RXT, BOR, and CTOR, values of $\sigma_{\rm o}$ were systematically found to be ≤30° (Fig. 12) which means most of the clouds aggregate closer to the equator. For all the fits $\delta < 0.1$, which is lower compared to the IM fits. In order to confirm that this trend is due to the effect of systematics (model difference) we performed an additional spectrum of MYTORUS spectrum for an exposure of $t_{XMM} =$

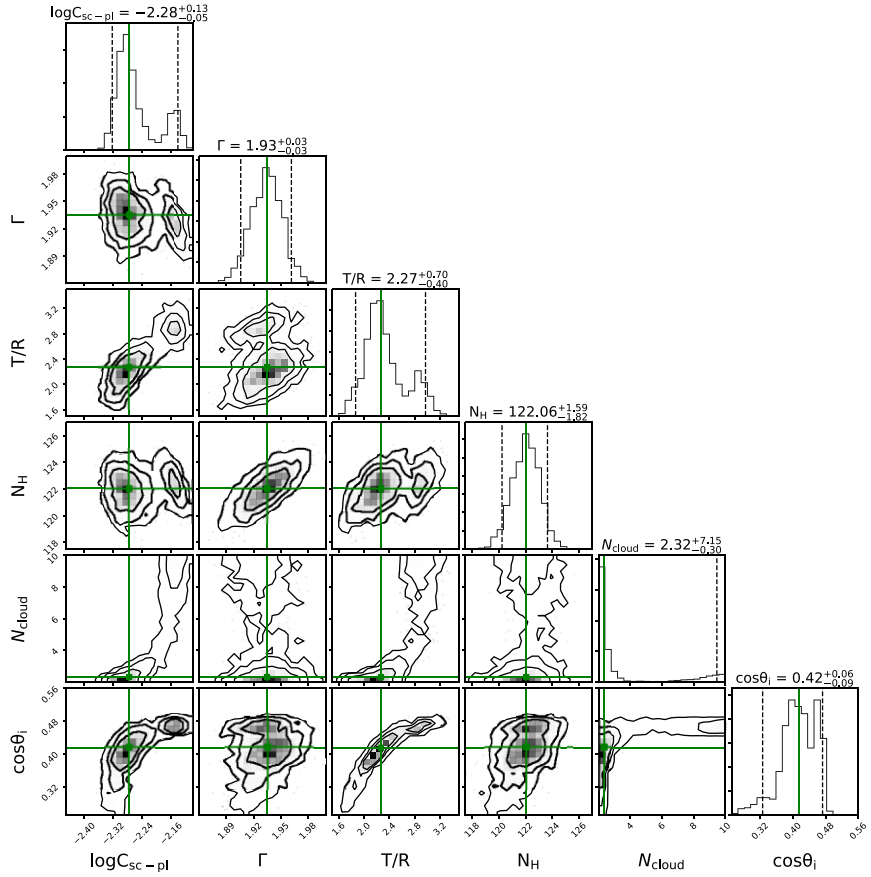

Figure 10. Contour plot results for the analysis $M_{\rm CTOR} \rightarrow D_{\rm MYT}$ in MCT regime. The posterior of $N_{\rm cloud}$ is irregular as there exists no maxima in the allowed prior range, but a minima, with ridges at the prior edges. This 'bifurcation' in the PDF of $N_{\rm cloud}$ gives rise to bimodality in the other parameters.

1.0 Ms and $t_{NuSTAR} = 0.5$ Ms and fit with UXCLUMPY ($M_{\rm UXCL} \rightarrow D_{\rm MYT}$). We find that the median values and the errorbars (the diamond and circular markers in 12) are consistent with each other. This indicates that the trends for the high exposure simulations are similar to that of the typical exposure case of $M_{\rm UXCL} \rightarrow D_{\rm MYT}$. This proves that the trends are systematic. We simulate data under UXCLUMPY using the best-fitting parameters obtained from $M_{\rm UXCL} \rightarrow D_{\rm MYT}$ and perform an IM fit. This is partially similar to the 'surrogate' method (Press et al. 2002). However, our analysis differs from Press et al. (2002), as we use a single 'surrogate' data set and our analysis of it is purely Bayesian. Consequently, the objective is comparison of the properties of the IM-posteriors obtained from the 'surrogate' data set with that of the CM-posteriors obtained from the real data set. We find that when the $M_{\rm UXCL} \rightarrow D_{\rm MYT}$ CM-fit returned $\delta \simeq 0.07$ for $\sigma_{\rm o}$, the IM fit for the 'surrogate' data set returned are wider with (Table 5) $\delta \simeq 0.46$ for $\sigma_{\rm o}$, which is ∼6 times higher.

(d) Covering fraction ($C_{\rm frac}$) of the inner ring of UXCLUMPY**:** The $C_{\rm frac}$ of the inner ring in the MCT regime returned posteriors with median values of $C_{\rm frac} < 0.1$ ($M_{\rm UXCL} \rightarrow D_{\rm j}$) or *irregular* posterior converging at the lower bound of the prior range implying $C_{\rm frac} \sim 0$ (Fig. 12) (all the other cases). We compare the posterior of $C_{\rm frac}$ from the CM-fit $M_{\rm UXCL} \rightarrow D_{\rm MYT}$ and the posterior obtained from IM-fit of the 'surrogate' data set. The posterior of $C_{\rm frac}$ in the CM-fit is irregular as it converges towards the lower edge (see Fig. 12). Similar to the σ_o the high exposure spectral fit ($M_{\rm UXCL} \rightarrow D_{\rm MYT}$), returns trends consistent with the typical exposure spectrum, implying a systematic trend. The median is ∼0.01. However, the $C_{\rm frac}$-posterior obtained from the same UXCLUMPY IM-fit of the 'surrogate' data set does not show irregularity. We find that $C_{\rm frac,\,median} \sim 0.19$ with $\delta \simeq 1$ and $R_{90} \simeq 0.1$ range is significantly large compared to that from $M_{\rm UXCL} \rightarrow D_{\rm MYT}$.

(e) $N_{\rm cloud}$ of CTORUS: The posteriors of the $N_{\rm cloud}$ for all the CM-fits, are *irregular* in the sense that the probability function has a minimum or is a monotonically increasing or decreasing function in the allowed prior range. The best values are either consistent with 2 or 10 or both (e.g. Fig. 10) all cases. In a real scenario, this can be an indication that CTORUS is a *wrong* model to apply in this case.

4.2 Heavy Compton-thick regime

In the HCT regime we do not get good fits (compared to the MCT regime) for a lot of cases when models are applied in their consistent form. So in many cases we had to apply the fits with the zeroth-order continuum and the scattered continuum uncoupled and or ignoring the data where there is an emission line (one can alternatively add Gaussian lines), to get a good fit. We ignored the energy ranges connected with difference in the emission lines in the following specific cases: $M_{\rm MYT} \rightarrow D_{\rm UXCL}$(1.16–1.31, 1.68–1.78, 3.5–3.61 keV), $M_{\rm BOR} \rightarrow D_{\rm UXCL}$ (2.15–3.26, 1.64–1.75 keV), $M_{\rm RXT}$

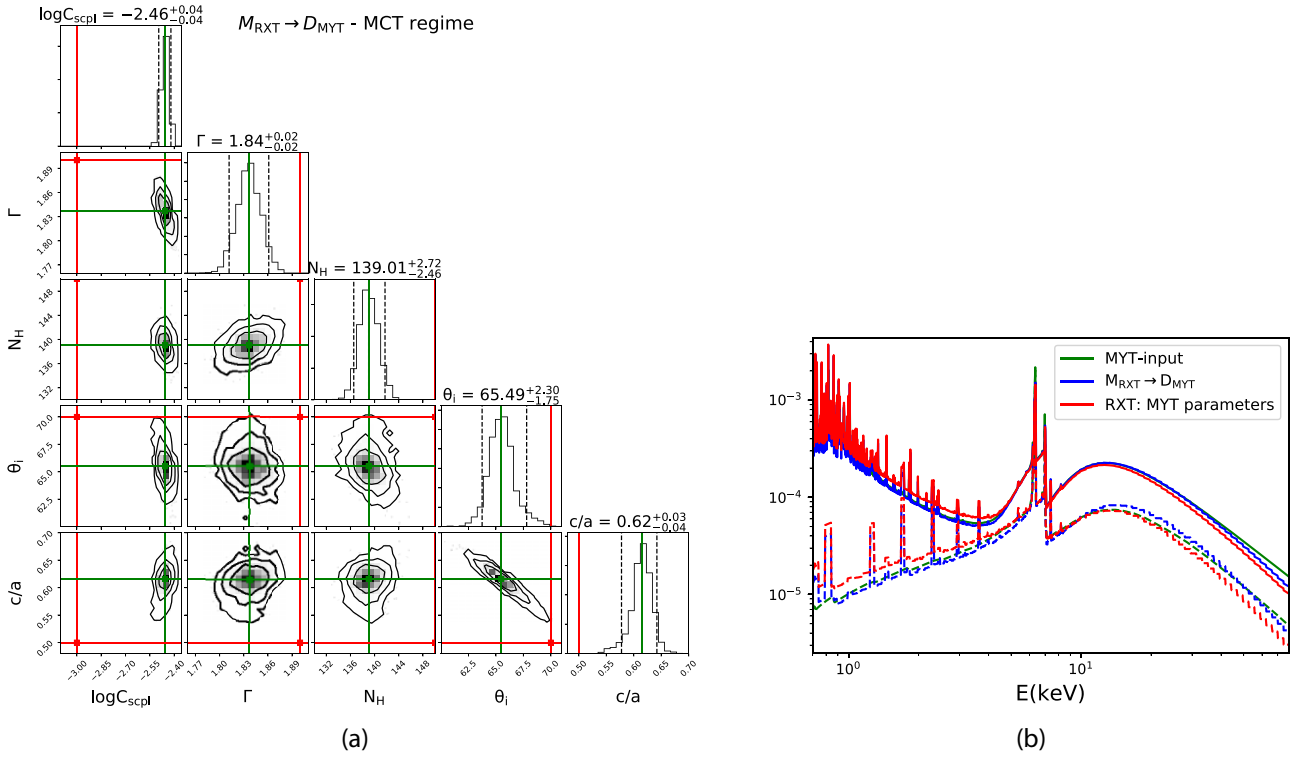

Figure 11. (a) Contour plot results for the analysis $M_{\rm RXT} \rightarrow D_{\rm MYT}$ in MCT regime. The noticeable discrepancy can be seen in the parameter c/a which in turn influences the constraints on $\log C_{\rm SCPL}$, $\theta_{\rm i}$ posteriors. (b) spectral overplot of the input model (green), the best-fitting spectrum from $M_{\rm RXT} \rightarrow D_{\rm MYT}$ (blue) and the RXTORUS model under MYTORUS input parameters (red). The dashed spectra are the scattered continua of the respective model spectra. The scattered components of RXTORUS and MYTORUS spectra under same parameters are different because of the difference in radiative process assumptions. χ^2/dof = 1.11 for the best-fitting parameters.

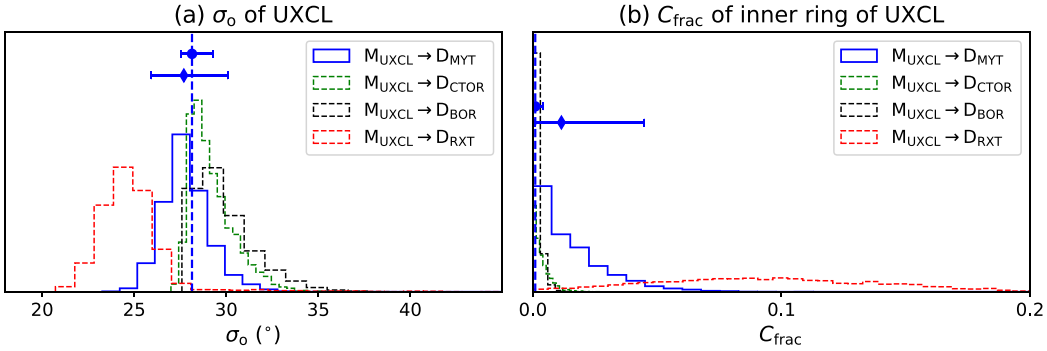

Figure 12. We show the behaviour of morphological parameters of UXCLUMPY for $M_{\rm UXCL} \rightarrow D_{\rm j}$-fits in the MCT regime(a)$\sigma_{\rm o}$ and (b)$C_{\rm frac}$ of the inner ring. $\sigma_{\rm o}$ is always $\leq 30^{\circ}$ and $C_{\rm frac}$ in most cases have irregular posteriors consistent with 0 and a regular posterior with median value consistent $\simeq 0.1$. The blue markers with errorbars represent the median values and uncertainty on σ_o and $C_{\rm frac}$ for typical of exposure (diamond marker: $t_{XMM} = 100$ ks, $t_{NuSTAR} = 50$ ks) and a deeper observation (circle marker: $t_{XMM} = 1.0$ Ms, $t_{NuStar} = 0.5$ Ms) for $M_{\rm UXCL} \rightarrow D_{\rm MYT}$. The dashed vertical lines mark the median values obtained from the spectrum with high exposure. The median values and the errors obtained from the typical and deeper observations show that trends are systematic and occurring due to model difference. See discussion in Section 4.1.

$\rightarrow D_{\rm UXCL}$ (2.15–3.26, 1.64–1.75 keV), $M_{\rm CTOR} \rightarrow D_{\rm UXCL}$ (2.15–3.26, 1.64–1.75 keV), and $M_{\rm MYT} \rightarrow D_{\rm RXT}$ (1.6–1.9, 2.2–2.4 keV).

(i) Column density ($N_{\rm H,\,los}$)**:** The values of $N_{\rm H,\,los}$ were not consistently retrieved (e.g. Fig. 14b) for the CM-fits in the HCT regime. In the context of the input model, the strong extinction on the transmitted component worsens the recovery of $N_{\rm H,\,los}$ when wrong models are fit. For the HCT regime all models were simulated with $N_{\rm H,\,los} \simeq 500$ and $T/R = 1$. The dissimilarity in the shapes of the CRH lead to bad fits in many cases when $T/R = 1$ (frozen) in the coupled configuration. So, T/R is kept free in most of the cases. We fit the doughnut (MYTORUS, RXTORUS) and biconical cut-out model (BORUS) to UXCLUMPY, in both coupled ($N_{\rm H,\,los} = f(N_{\rm H,\,eq})$) and the uncoupled configuration (where $N_{\rm H,\,los} \neq f(N_{\rm H,\,eq})$). The doughnut fits were always significantly better in the uncoupled configuration but the $N_{\rm H,\,los}$ values are discrepant in all cases. The fits using BORUS seems practically uneffected in the uncoupled configuration. However, severe discrepancy and *irregular* posteriors

Table 5. Parameter comparison for the cross-model fits ($M_{\rm UXCL} \rightarrow D_{\rm j}$, j = MYT-MCT, CTOR-HCT, and BOR-HCT) and surrogate data sets simulated under the fitting model (UXCLUMPY) for the best-fitting parameters. $\theta_{\rm i}$ and the parameters of morphology exhibit lower value R_{90} compared to the intramodel-surrogate fit for UXCLUMPY.

Model parameters of $M_{\rm UXCL}$	MYT-MCT regime		CTOR-HCT regime		BOR-HCT regime	
	R_{90} values for CM-fit and surrogate data set					
	$D_{\rm MYT}$	$D_{\rm UXCL}$ (surrogate)	$D_{\rm CTOR}$	$D_{\rm UXCL}$(surrogate)	$D_{\rm BOR}$	$D_{\rm UXCL}$ (surrogate)
$\sigma_{\rm o}$(in $^\circ$)	4.13	28.95	1.42	2.50	1.57	2.68
$C_{\rm frac}$ of inner ring	0.04	0.26	0.004	0.027	0.008	0.034
$\theta_{\rm i}$	3.63	9.47	0.15	1.31	0.26	1.08

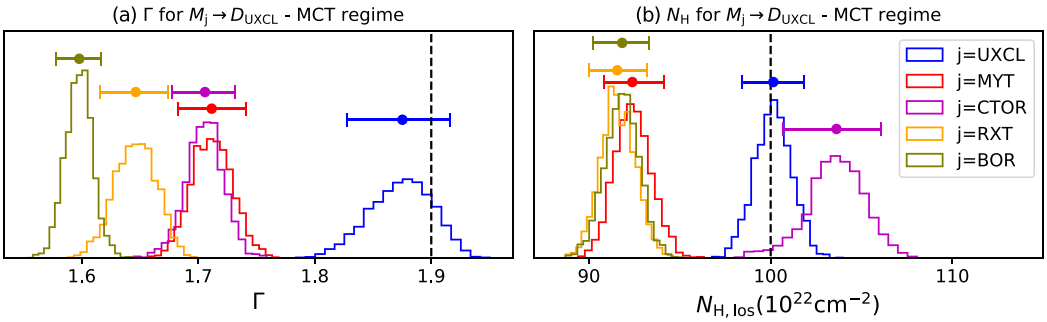

Figure 13. Cross- and intra-model fits for the case $M_{\rm j} \rightarrow D_{\rm UXCL}$ in the MCT regime, j = MYT, RXT, CTOR, and BOR models. The discrepancies in Γ are typically rather large, with a flattening by 0.2–0.3, and potentially impacting conclusions about the coronal power law. In contrast, discrepancies in $N_{\rm H,\,los}$ are much smaller, at only ∼ 10 per cent which does not significantly impact the spectral fit.

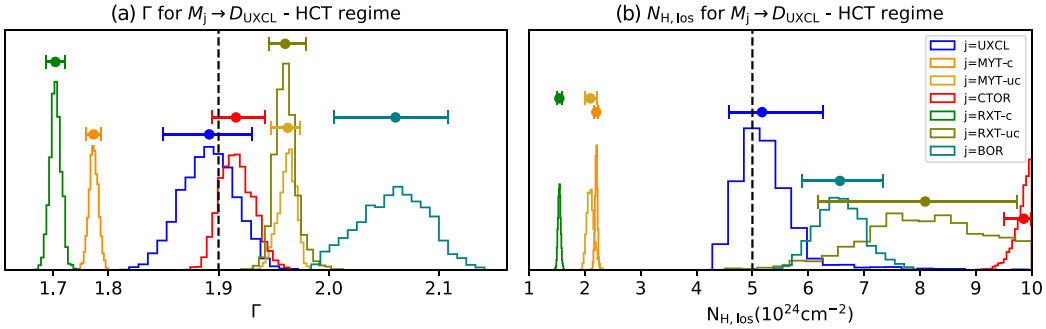

Figure 14. Cross- and intramodel fits for the case $M_{\rm j} \rightarrow D_{\rm UXCL}$, j = MYT, RXT, CTOR, and BOR models. The labels: -c and -uc refers to coupled and uncoupled configuration, respectively. The discrepancies in Γ are due to both flattening and steepening of Γ. The discrepancies in $N_{\rm H,\,los}$ are also large amounting to a maximum of ∼ 100 per cent.

in $N_{\rm H,\,los}$ are seen many cases ($0.88 \leq r_q \leq 27.0$, for the cases with *regular* $N_{\rm H,\,los}$ posteriors). There exist no specific trend methodology by which we can discern a correct value of $N_{\rm H,\,los}$. *The fitting is based on the attempt to adjust* $N_{\rm H,\,los}$, Γ *and T/R such that it best mimics a CRH generated under a different morphology. This is unlike the MCT regime where the rollover and the FeK-edge from the zeroth order contunuum determines* $N_{\rm H,\,los}$ *and the effect of CRH on* $N_{\rm H,\,los}$ *relatively less.*

(ii) Photon-Index (Γ): Γ is discrepant (e.g. Fig. 14a) in most cases due to the varying shapes of the CRH. For all models the input value of Γ was 1.9. From the fits we find $0.67 < r_q < 21$ holds for all tested model. The best value of r_q was obtained for $r_q = 0.67$ for $M_{\rm RXT} \rightarrow D_{\rm UXCL}$ (at $\Gamma_{\rm out} = 1.91$) and the worse is obtained for $M_{\rm CTOR} \rightarrow D_{\rm BOR}$ (at $\Gamma_{\rm out} = 1.69$). Thus in general it can be concluded that the recovered value of Γ is strongly model dependent.

(iii) Relative normalization between the transmitted and the reflected component (*T*/*R*)**:** When *T*/*R* was kept free, we find irregular posteriors and or severe discrepancy with the input value ($[T/R]_{\rm input} =$ 1 for all spectral simulations). One particular example case is $M_{\rm RXT} \rightarrow D_{\rm UXCL}$ where $[T/R]_{\rm out} = 4.92$ in the uncoupled configuration. This results in stronger zeroth-order continuum in the fit (originally much weaker in the $D_{\rm UXCL}$). The ∼ 5-fold increase in *T*/*R* effectively tries to fit the $E > 10$ keV region of the data. (Fig. 15). In other cases, *T*/*R* is reduced to very low values, thus arbitrarily decreasing the zeroth-order continuum (which is otherwise attenuated by $N_{\rm H,\,los}$). This results relatively lower values of $N_{\rm H,\,los}$ (e.g. $M_{\rm MYT} \rightarrow D_{\rm UXCL}$: $[T/R]_{\rm out}$ ∼ 0.5, $N_{\rm H,\,los} \simeq 200$). Several other cases where inconsistency in *T*/*R* occur are: $M_{\rm BOR} \rightarrow D_{\rm UXCL}$, $M_{\rm CTOR} \rightarrow D_{\rm UXCL}$, $M_{\rm CTOR} \rightarrow D_{\rm BOR}$ etc. Physically, $T/R \neq 1$ would imply variability of the coronal power-law; however as demonstrated here *this can arise due to morphological difference resulting in varying shape of a CRH*. The large discrepancy of *T*/*R* can result in heavy discrepancy in the intrinsic luminosity of the corona ($L_{\rm corona}$).

(iv) Parameters of morphology**:**

(a) *c*/*a* of RXTORUS: For the case of $M_{\rm RXT} \rightarrow D_{\rm UXCL}$($C_{\rm frac}$ = 0) in the coupled configuration, *c*/*a* ≃ 0.11. The geometry

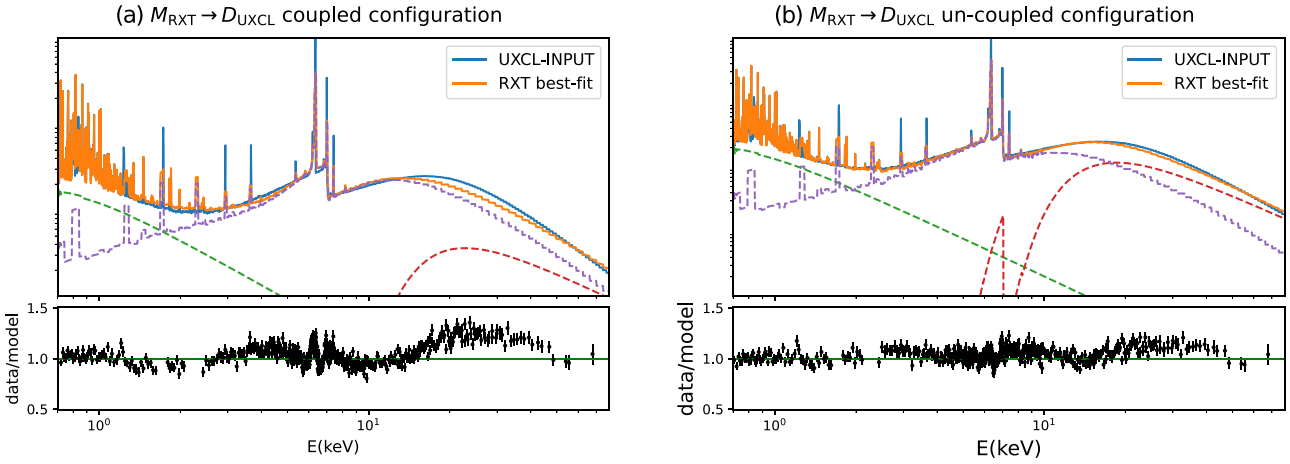

Figure 15. $M_{RXT} \rightarrow D_{UXCL}$ fit for two cases: *Z–S* coupled with χ^2/dof $\simeq$ 1.4 and log BF $\simeq -364.99$; *Z–S* un-coupled: with χ^2/dof $\simeq$ 1.16 and log BF $\simeq -148.56$. The Bayes Factors are calculated using the log Z_{UXCL} value obtained from the UXCLUMPY intramodel fit. Most of the discrepancy in the spectra happens in the continuum.

was thus assumed to be more of an annulus than a doughnut but χ^2/dof = 1.6. For the uncoupled configuration *c*/*a* returned values much higher, ∼0.71. However, the interpretation of *c*/*a* at face value is not possible. The geometrical interpretation of the results: the absorption happens through a Compton-thick absorber placed close to the axis of symmetry ($\theta_i \simeq 3°$) which is independent of a separate ∼ medium Compton-thick ($N_{H,\,eq} \simeq 86$, point 1) doughnut shaped gas distribution. For $M_{RXT} \rightarrow D_{UXCL}(C_{frac} = 0)$, *c*/*a* posteriors were bimodal, which resulted in bimodality in other posteriors. For both coupled and uncoupled configuration $M_{RXT} \rightarrow D_{UXCL}(C_{frac} = 0.4)$ returned $c/a > 0.75$ indicating an increased covering fraction of the torus. $M_{RXT} \rightarrow D_{MYT}$ also returned bimodal *c*/*a*-posterior.

(b) cosθ_o or $C_{Frac,\,tor}$**:** In the case of $M_{BOR} \rightarrow D_{CTOR}$ we get cos$\theta_o \simeq 0.39$, which is consistent with cosθ_i. The implications are similar to that of the fit obtained from the MCT regime. In the case of $M_{BOR} \rightarrow D_{UXCL}$, the uncoupled configuration ($N_{H,\,los} \neq N_{H,\,eq}$) returns a bimodal cos$\theta_o$ or $C_{Frac,\,tor}$ (one major and one minor peak in the posterior), which leads to bimodality in θ_i, A_{Fe}, and C_{scpl}. For this case we find $\cos\theta_i < \cos\theta_o$. Adding this up with the fact that $N_{H,\,los} \neq N_{H,\,eq}$ it is evident the otherwise '$\cos\theta_o$'-parameter makes more sense when interpreted as covering fraction $C_{frac,\,tor}$ of a clumpy torus as described in the fifth point in Section 4.1.

(c) σ_o of UXCLUMPY: $M_{UXCL} \rightarrow D_{CTOR}$ returns $\sigma_o \simeq 14°$ with $\delta \simeq 0.1$ and $M_{UXCL} \rightarrow D_{BOR}$ returns $\sigma_o \simeq 12°$ and $\delta \simeq 0.1$. In both the cases the joint analysis of *XMM–Newton* and *NuSTAR* returned fits for which $1.2 \leq \chi^2$/dof ≤ 1.3 (mainly due to discrepancy in the emission lines). We simulate 'surrogate' data sets under the best-fitting parameters of UXCLUMPY under both $M_{UXCL} \rightarrow D_{CTOR}$ and $M_{UXCL} \rightarrow D_{BOR}$ best fits parameters and carry out IM-fits. We find that the IM-fits in the surrogate data sets return wider posteriors (Table 5). For σ_o, δ_{IM}/δ_{CM} is 1.75 for BORUS and 1.77 for CTORUS. Both the fits $M_{UXCL} \rightarrow D_{RXT}$ and $M_{UXCL} \rightarrow D_{RXT}$ returned very low values of $\sigma = 7°$.

(d) C_{frac} of the inner ring of UXCLUMPY**:** Unlike the MCT regime, values of C_{frac} returned from the $M_{UXCL} \rightarrow D_{CTOR}$ and $M_{UXCL} \rightarrow D_{BOR}$ were clearly non-zero and assumed significantly higher values ($C_{frac} \simeq 0.3$ for both) with tighter constraints $\delta \sim 0.01$ for $M_{UXCL} \rightarrow D_{BOR}$ and $\delta \sim 0.001$ for $M_{UXCL} \rightarrow D_{CTOR}$. For the *NuSTAR* only fits as described in the previous point, the values of C_{frac} and δ are similar to those of the joint fits for $M_{UXCL} \rightarrow D_{BOR}$. For the $M_{UXCL} \rightarrow D_{CTOR}$ fits the C_{frac} value decreased but the δ increased to 0.5. The 'surrogate' data sets under IM fits returned broader posteriors (Table 5). For C_{frac}, δ_{IM}/δ_{CM} is 4.04 for BORUS and 6.67 for CTORUS. For both the RXT and MYT fits the posteriors are similar in shape and the median values are similar.

(e) N_{cloud} of CTORUS**:** We carried out the CM fits $M_{CTOR} \rightarrow D_j$ where j = MYT, UXCL, and BOR. For $M_{CTOR} \rightarrow D_{UXCL}$ and D_{MYT} we do not get a good fit ($1.2 \leq \chi^2$/dof ≤ 2.0) mostly because of the difference in the emission line profiles between UXCLUMPY and CTORUS. We get an *irregular* posterior for N_{cloud} converging towards the higher extreme edge of the prior range for both cases. For $M_{CTOR} \rightarrow D_{BOR}$, the N_{cloud} posteriors are extremely narrow.

5 RESULTS: DETECTABILITY OF AN ADDITIONAL RELATIVISTIC DISC-REFLECTION COMPONENT

In a Compton-thick AGN, the transmitted and reprocessed emission of the torus is the dominant part of the spectrum. However, there may be an additional component present in the spectrum originating due to relativistic reflection from the inner accretion disc. The question thus is, would it be possible to detect such a component from spectral model fits? To answer the question, we simulate a data set that has both the CRH-dominated torus component and a relativistic disc-reflection component. We use UXCLUMPY to simulate the torus and RELXILL (García et al. 2014) to simulate the disc-reflection component ($D_{UXCL\,+\,RELXILL}$). Since the disc reflection component originates close to the ISCO, it should be heavily absorbed by the torus column. Thus the model expression in `xspec` terminology is:

`MODEL = TBABS×(APEC(1)+APEC(2)+ UXCLUMPY-SCPL + ZTBABS×CABS×RELXILL + UXCLUMPY)`

The `ZTBABS` and `CABS` $N_{H,\,los}$ was tied to UXCLUMPY as the obscurers are one or multiple torus clouds. The parameters of RELXILL like Γ and θ_i were tied to the UXCLUMPY as the torus and the disc are illuminated by the same coronal power law. In the

flux range of 4–50 keV, the ratio of the flux of the disc absorbed through the torus column with respect to the total torus emission $F_{4\text{–}50,\,\mathrm{Disc}}/(F_{4\text{–}50,\,\mathrm{trans}} + F_{4\text{–}50,\,\mathrm{refl}})_{\mathrm{Torus}}$ is 0.36–0.38, which makes the total torus emission (comprising of the torus CRH and the transmitted component) the dominant feature of the spectra. In the published UXCLUMPY model, the CRH from the torus is calculated assuming a power law. But when a disc reflection is present, the torus should reprocess both the power-law and disc-reflection component. It was not possible for us to implement this in the current UXCLUMPY setup. This will put some limitations on the accuracy of our test but we do not expect it to significantly change the results. When our fitting model has only torus component (UXCLUMPY) and the data has both the disc `RELXILL` and torus component the notation would be $M_{\mathrm{UXCL}} \rightarrow D_{\mathrm{UXCL+RELXILL}}$ and in the converse case, the disc is modelled with `KDBLUR(XILLVER)`, the notation is $M_{\mathrm{UXCL+KD\text{-}XIL}} \rightarrow D_{\mathrm{UXCL}}$. During analysis, the prior of the relative normalization of the disc-component $C_{\mathrm{KD\text{-}XILL}}$ was set to be a log-uniform prior extending from 10^{-10} to 1. All other parameters of the disc that were kept free (ionization parameter $\log\xi_{\mathrm{i}}$ and abundance A_{Fe}) were given uniform priors extending accross the entire prior range. The methodology of analysis of the data is described in the following bullet points:

(i) Torus component only**:** We fit the data with torus component only i.e. $M_{\mathrm{UXCL}} \rightarrow D_{\mathrm{UXCL+RELXILL}}$ to see if it is possible for only a torus modeled by UXCLUMPY to replicate the spectra. We keep the APEC components and E_{cut} frozen to their input values. We find that the spectral shape was replicated and there no significant model or data excess in the residuals for both MCT and HCT regime. The overplot of the input-model and fit model for the HCT regime is shown in Fig. 16. At the median values of the parameter posteriors, we obtain $\chi^2/\mathrm{dof} = 1.046$ for HCT and 0.978 for MCT. The parameters like Γ, C_{frac} of UXCLUMPY and θ_{i} showed large discrepancies with the input. σ_{o} was consistent with the input. The fit returned a lower value of Γ and a higher value of C_{frac} (see Table 6).

(ii) Torus and disc component**:** We fit the simulated data with UXCLUMPY and an attenuated disc component modelled by `ZTBABS × CABS × kdblur`[6] (`XILLVER`[7]). This produced a better fit compared to the previous case, with $\chi^2/\mathrm{dof} \simeq 1.035$ for HCT and 0.974 for MCT, with no significant residuals. The `XILLVER` parameters like A_{Fe} and χ_{i} show very broad posteriors, which is attributable to the heavy extinction through the torus column.

Detecting an additional relativistic disc reflection component which is heavily attenuated in the torus absorbing material with certainty is impossible with simple χ^2/dof values. In all the fits with only the torus model (UXCLUMPY), the model replicates the data with almost indistinguishable values of χ^2/dof. But the low Bayes factor (see Section 6 for definition), $\mathrm{BF} = Z_{\mathrm{torus}}/Z_{\mathrm{torus+disc}} \simeq 1.21 \times 10^{-19}$ for HCT and 9.25×10^{-8} for MCT clearly hints at the existence of a relativistic disc reflection component. We also test the possibility for false detection of a disc component in the HCT regime and carry out the $M_{\mathrm{UXCL+KD\text{-}XIL}} \rightarrow D_{\mathrm{UXCL}}$ fit. We found that the parameters of UXCLUMPY got recovered, but the parameters of XILLVER showed *irregular* posteriors. Specifically, the tendency of the $C_{\mathrm{KD\text{-}XILL}}$ posterior-distribution to converge towards the lower limit ($\sim 10^{-8}$) indicated the absence of the disc reflection component. The log-evidence values for the $M_{\mathrm{UXCL+KD\text{-}XIL}} \rightarrow D_{\mathrm{UXCL}}$ and $M_{\mathrm{UXCL}} \rightarrow D_{\mathrm{UXCL}}$ are $\log Z_{\mathrm{torus+disc}} \simeq -652.19$ and $\log Z_{\mathrm{torus}} \simeq -653.67$, respectively. Thus, the bayes factor is $\mathrm{BF} = Z_{\mathrm{torus}}/Z_{\mathrm{torus+disc}} \simeq 0.033$, the value being greater than our threshold of 0.01 (Section 6) for model distinction. Nevertheless, the results of $M_{\mathrm{UXCL+KD\text{-}XIL}} \rightarrow D_{\mathrm{UXCL}}$ is consistent with the absence of a relativistic disc refelction.

[6]Laor (1991).
[7]García et al. (2013).

6 RESULTS: DEPENDENCE OF EVIDENCE ON FLUX LEVELS

To study the effect of flux levels on model evidence, we simulate 10 spectra (S_n, n runs from 1 to 10) for 10 different flux levels under UXCLUMPY and CTORUS for an intrinsic 2–10 keV flux of $0.83/n$ mCrb in the HCT regime. The exposures on all the simulated spectra are 100 ks on *XMM–Newton* and 50 ks on *NuSTAR*. All spectra are grouped into 30 counts bin^{-1}. We run BXA sims on the simulated spectra for both: (A) joint *XMM–Newton* and *NuSTAR* (B) *NuSTAR* only cases. Our Bayesian fitting strategy can be summarized in the following representation: $M_{\mathrm{j}} \rightarrow D_{\mathrm{UXCL}}$ and $M_{\mathrm{j}} \rightarrow D_{\mathrm{CTOR}}$, where j = UXCL, CTOR, and BOR. In our work, Bayes factor is defined as the ratio of the Bayesian evidence of a fitting model ($Z_{\mathrm{fitting\ model}}$) to that obtained from an intramodel fit (Z_{input}): $\mathrm{BF} = \mathrm{Z_{fitting-model}/Z_{input}}$. We plot the Bayes factor values to the corresponding flux levels (Fig. 17). For effective distinguishing of models, we set the following condition on Bayes factor (BF): $\mathrm{BF} < 10^{-2}$, which practically means that the flux value below which the logBF *value rises above −2 for the first time* is considered as the lower limit on flux, below which effective distinguishing of *correct* from the *wrong* model is not possible. We expect that joint fits are more effective in distinguishing models. Our results confirm this from the fact that we can distinguish the models more effectively down to an intrinsic flux value of ∼0.1 mCrb for joint *XMM–Newton* plus *NuSTAR* fits. For the *NuSTAR* only fits, for which this lower threshold value was slightly higher than ∼0.1 mCrb (Fig. 17b and d). It is also worth noticing that systematically lower values of logBF and local fluctuations in logBF (e.g. as seen in the *NuSTAR*-only fits; Fig. 17) can push the threshold to higher limits (grey vertical line at flux level *f*/3 in Fig. 17d). These fluctuations which might have occurred during the data simulation or detection process are more likely to influence the evidence values at the lower flux regimes or lower bandwidth data, thus reducing the precision in evidence-based model distinction. Thus, it is safer to assume more conservative thresholds determined from synthetic data simulations, when applying Bayes factor for model distinction in case of real data. We discuss these aspects in detail in Section 7.

7 DISCUSSIONS

7.1 Guidelines to the X-ray community

7.1.1 Parameter estimates

We perform joint analysis of synthetic data simulated under *XMM–Newton* and *NuSTAR*. The baseline flux level for all the input models was ∼0.5 mCrb in the 2–10 keV band. The exposure times on *XMM–Newton* and *NuSTAR* were 100 and 50 ks, respectively. For *XMM–Newton* EPIC-pn, given the flux and exposure time in the 2–10 keV band, the average photon-count is $\sim 8.2 \times 10^4$. From the results of our analysis of the synthetic data, we assert the following prescriptions for the parameter posteriors:

(i) From the cross-model fits, it is quite clear that *the photon-index (Γ) cannot be determined with certainty when a wrong model is applied*. Almost all the posteriors are regular-monomodal distributions with very small statistical errors, but the discrepancy (represented by

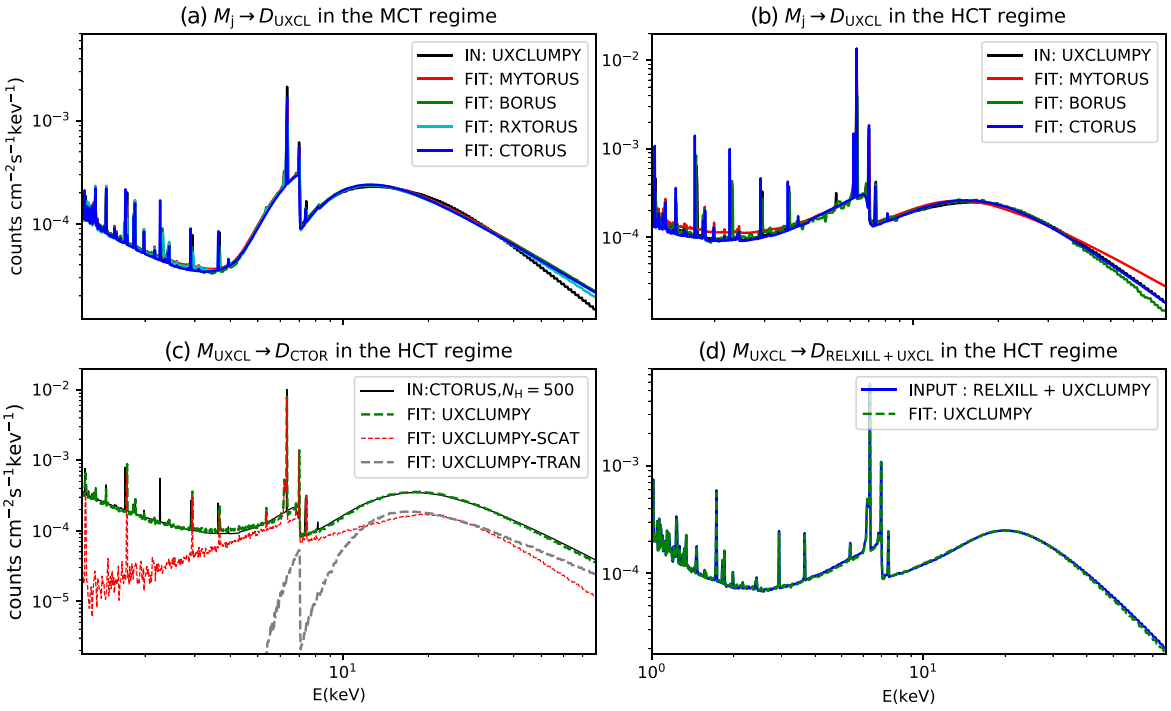

Figure 16. Cross model fits: overplot of UXCLUMPY input model and fitting models (a) in the MCT regime (b) for the HCT regime with the Compton-thick ring absent ($C_{frac} = 0$) (c) Overplot of CTORUS input and $M_{UXCL} \rightarrow D_{CTOR}$ best-fitting model. The zeroth-order continuum adjusts itself to replicate the CRH of CTORUS (d) Overplot of input model comprised on a weak disc component(RELXILL) and torus component(UXCLUMPY) and fitting model with only a torus model(UXCLUMPY).

Table 6. Table for input and the fit parameters for data simulated under torus and relativistic disc. Two cases are shown in this table. In the first case, only the torus (M_{UXCL}) is fit to the data where both the torus and disc components $D_{UXCL+RELXILL}$ are present. In another case, the fit was performed with both the relativistic disc and the torus.

Parameters	A_{Fe}	log ξ_i	$N_{H,los}$ (cm^{-2})	Γ	σ_o (°)	C_{frac}	θ_i (°)	χ^2/dof
Input								
MCT	1.0	1.0	100.0	1.9	45.0	0.4	60.0	–
HCT	1.0	1.0	500.0	1.9	45.0	0.4	60.0	–
$M_{UXCL} \rightarrow D_{UXCL+RELXILL}$								
MCT	–	–	102.0 ± 1.24	1.83 ± 0.03	$32.0^{+8.1}_{-4.4}$	$0.57^{+0.02}_{-0.04}$	$46.6^{+5.6}_{-4.3}$	0.978
HCT	–	–	547^{+58}_{-57}	1.72 ± 0.02	$32.8^{8.9}_{-4.6}$	$0.47^{+0.01}_{-0.01}$	$24.0^{9.7}_{-14}$	1.046
$M_{UXCL+KD-XIL} \rightarrow D_{UXCL+RELXILL}$								
MCT	$0.61^{+0.14}_{-0.09}$	$0.62^{+0.64}_{-0.54}$	97 ± 2	1.86 ± 0.03	$48.6^{+11.5}_{-14}$	$0.34^{0.09}_{-0.1}$	$77^{+6.5}_{-14}$	0.974
HCT	$3.36^{+5.6}_{-2.41}$	$2.31^{+1.5}_{-2.0}$	516^{+106}_{55}	$1.9^{+0.04}_{-0.03}$	51^{+12}_{-11}	$0.44^{+0.06}_{-0.08}$	$50.6^{+11.4}_{-25}$	1.035

the r_q values) between the input and fit values are extraordinarily high ($\Delta\Gamma \simeq 0.3$ and r_q as high as 16). This discrepancy in Γ for different models is also reported by Buchner et al. (2021). Even multiple models returning similar values of Γ should not be taken at face value (as discussed in Section 4). *Our results indicate that precision in the value* Γ *is no guarantee for its correctness.* In such a scenario, where the systematic discrepancies originating due to model-difference cannot be corrected, we recommend that users apply caution in the interpretation of Γ (e.g. when used to estimate intrinsic luminosity or accretion rate relative to Eddington), particularly if very low values of Γ are obtained. Alternate, indirect methods to determine the value of Γ may be preferred. For example, Brightman et al. (2013) noted an empirical relation between Γ and FWHM of optical broad emission lines in X-ray selected, broad-line radio-quiet AGN. However, such a sample is biased to be X-ray-unobscured, and this relationship might not hold in X-ray obscured AGNs. *The community would thus benefit from exploration into whether any empirical relation between* Γ *and other measurable properties of Compton-thick AGN exists.*

(ii) Consistent values of LOS column density ($N_{H,los}$) were returned in the medium Compton thick (MCT) regime, because of the strong zeroth-order continuum. In the heavy Compton thick (HCT) regime, the values of $N_{H,los}$ were recovered but were less constrained as seen from most of the intramodel fits (IM-fits). However, when *wrong* models were applied (CM-fits) many cases returned discrepant values and irregular posteriors. The determination of the precise value of $N_{H,los}$ starts to become difficult in the HCT regime, because the suppression of a zeroth-order continuum by the scattered continuum. However also in the HCT regime, in the CM-fits there are cases when the intensity of the zeroth-order continuum is modulated by the *T*/*R*-parameter (arbitrarily taking values $>$ or $<$ 1) to adjust the shape

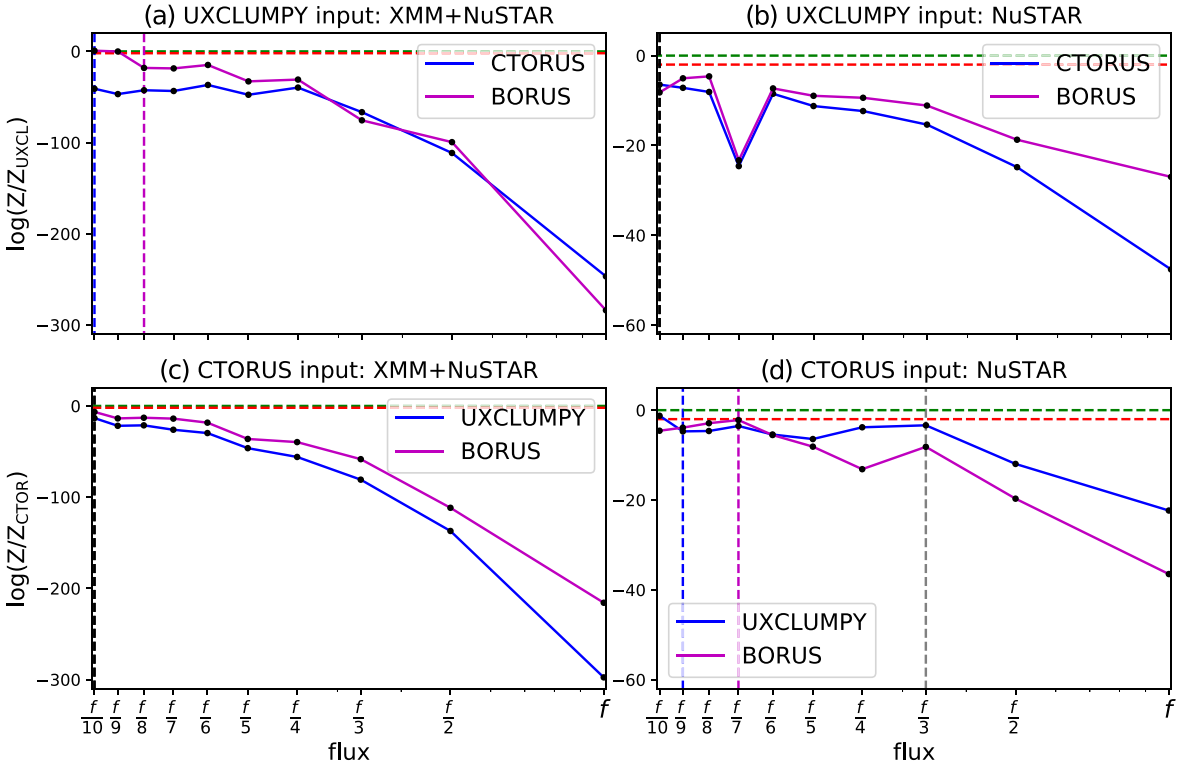

Figure 17. log Bayes Factor versus flux level plot: Spectra simulated for *XMM–Newton* and *NuSTAR* exposures of 100 and 50 ks, respectively, with an intrinsic flux level of $f_n = 0.83/n$ mCrb. (a) and (c) demonstrate the variation of evidence values with flux when both *XMM–Newton* and *NuSTAR* data are used. (b) and (d) demonstrate the same, but considering *NuSTAR* only data. The blue and magenta dashed lines denote the flux level at which the relation $\log Z_{\rm input} - \log Z_{\rm fit} \geq 2$ holds for the wrong model. The black and green dashed lines marks the logBF = 2 and logBF = 0 level, respectively.

of the CRH (Fig. 15). *The large discrepancy of T/R can result in an equally sized mis-estimation of the intrinsic accretion luminosity* ($L_{\rm corona}$). ($L_{\rm X,\ corona}$), *which can be severely discrepant* ($L_{\rm corona,\ fit}$ *upto* $\sim$ *10 times* $L_{\rm corona,\ input}$ in our simulations).

(iii) The IM-fits returned comparatively narrower posteriors (Fig. 8) in the HCT regime for most parameters of torus morphology. The constraints on the parameters of morphology are drawn from the $E < 6$ keV tail, Fe K edge, and CRH of the scattered continuum which are dominant in the HCT regime. *However, these comparative levels of improvements in the constraints in the HCT regime w.r.t. to MCT can be dependent on the exact spectral shape.* However, it can be inferred that under the *correct* model assumption parameters of morphology on average can be better constrained in the HCT regime, as the HCT regime has lower 'contamination' from the zeroth-order continuum. However, the behaviour of the posteriors of the morphological parameters shows different trends for different models for intramodel fits and cross-model and are open to interpretation:

(a) Continuous torus: In the continuous torus model there are only two morphological parameters: *c/a* for doughnuts and $\theta_{\rm o}$ or $\cos\theta_{\rm o}$ or $C_{\rm frac,\ tor}$ in the biconical cutouts. The doughnut thickness parameter *c/a* (of RXTORUS) shows *regular* posteriors (Section 2.4 for definition) in all cases. However, low values of *c/a* (e.g. *c/a* < 0.2) were observed for the baseline (coupled) configuration, which indicates an annular geometry rather than a doughnut. *Meanwhile for the uncoupled configuration one interpretation of the value of c/a can indicate the reflector geometry generating the scattered component (see Section 4.2).* Several other interpretations with different setups for an otherwise doughnut model are explained in Yaqoob (2012). $\cos\theta_{\rm o}$ or $C_{\rm frac,\ tor}$ of BORUS returns posteriors which are regular for most cases. However for some fits to *wrong* models in the coupled configuration ($N_{\rm H,\ los} = N_{\rm H,\ eq}$) we get $\theta_{\rm o} > \theta_{\rm i}$. This suggests an unobscured configuration. However these cases returned a $N_{\rm H,\ los}$ consistent with a Compton thick obscured case. For our case, we know that the applied model is incorrect. However in real situation where the input spectrum is unknown and these class of solutions are encountered there may a create potential chance of misinterpretation of an otherwise wrong solution (see the point on $\cos\theta$ or $C_{\rm frac,\ tor}$ in the Section 4.1).

(b) Clumpy torus: In the clumpy torus models there are three morphological parameters: $\sigma_{\rm o}$ and $C_{\rm frac}$ of inner ring of UXCLUMPY and $N_{\rm cloud}$ of CTORUS. When UXCLUMPY is the wrong model (CM-fits) $\sigma_{\rm o}$ systematically showed narrower posteriors (lower values of R_{90} and δ) compared to the case when it is the correct model (IM-fits) at the same flux levels. The covering fraction ($C_{\rm frac}$) of the inner C-thick ring of UXCLUMPY returned *irregular* posteriors (Section 2.4 for definition) with $C_{\rm frac} \sim 0$ for majority of the tested cases in the MCT regime. However in the HCT regime the posteriors of $C_{\rm frac}$ were monomodal with comparatively higher values ($C_{\rm frac} > 0.1$). *This could be interpreted as the tendency of the UXCLUMPY geometry to adjust the overall covering fraction of the clump distribution to match the shape of the data generated under another morphology.* $N_{\rm cloud}$ of CTORUS returned mostly *irregular* posteriors when CTORUS is the *wrong* fitting model, which had either a minimum or converged at one of the extreme edges of the priors. For the intramodel fits, however, the $N_{\rm cloud}$ posteriors are wide but mostly *regular*.

Although it might not be a generic trend there might exist differences in the nature of the posteriors for a *wrong* and *correct* model. Thus in real data analysis a rigorous test of the behaviour of the parameters of the fitting model becomes a necessity. *This can be done by simulating synthetic data under the fitting model for the values of the best-fitting parameters and then performing an intramodel fit. The posteriors properties (e.g. δ, R_{90}) for the real data and the intramodel fit can then be compared.*

(iv) Posteriors of θ_i are generally regular monomodal in case of application of the correct model (IM fits). However, in several cases the proportional errors are large. In general, the constraints on θ_i are dependent on the constraints on other morphological parameters, which are better determined in the HCT regime with a dominant scattered continuum allowing better constraints. However, when the applied model is wrong (CM-fits), in several cases we got *irregular* posteriors (converging at the edge) especially those involving the fitting of UXCLUMPY. In general, θ_i remains a parameter dependent on morphological assumptions and hence *should not always be accepted at face value*.

(v) As described before a significant fraction of cases where a *wrong* model is applied (CM fits), returned *irregular* posteriors for some of the parameters [e.g. θ_i, N_{cloud}, C_{frac} etc. (see Table 1) for a summary of the parameters]. However, for a significant number of fitting models, the best value (typically the median) derived from the posteriors of the cross-model fits returned $\chi^2/dof < 1.2$, which is otherwise acceptable. Also in most of these cases, it is possible to improve the value of χ^2/dof significantly by adding emission lines or by decoupling the zeroth-order and the scattered continuum (see Section 4.2), etc. This might return meaningful values of certain parameters (e.g. $N_{H,\,los}$), but the morphological and radiative aspects remain open to (mis-)interpretation (e.g. point-3 of Sections 4.1 and 4.2). *The danger of misinterpretation is less in the case for* MULTINEST *as in addition to χ^2/dof estimates we can apply Bayes-Factor to weigh up the model preferences and explore the nature of intramodel posteriors.*

We thus strongly recommend that the users perform their data simulations and use global Bayesian algorithms for data analysis. The methodology used here and the exercise undertaken in this work can be treated as an example. We advocate simulating data under selected models of choice to understand potential limitations both in cases of preparing observing proposals and when modeling already obtained data. We leave it to the readers to use the responses/ARFs of the selected instrument(s) as appropriate, and perform intramodel and/or cross-model fits as needed to understand the behaviour of the posteriors for the given models, instrument, exposure time, etc.

7.1.2 Limitations of using Bayes Factor values

From the results in Section 6, it is clear that values of log-evidence (logZ) and log-Bayes factor (log BF) are strongly affected by the number of degrees of freedom, which is a strong function of the number of data bins, and availability (or lack thereof) of certain instruments and bandpasses. For a given flux/exposure time, maximizing the energy bandpass used by, for example, performing joint *NuSTAR* and *XMM–Newton* fits instead of fitting just one instrument maximizes the ability to distinguish between models based on Bayes Factor. In the case of joint *NuSTAR* and *XMM–Newton* fits to the synthetic Compton-thick AGN spectra (simulated under the selected models; Section 6), adopting a threshold log-Bayes factor of $\gtrsim$2 was effective in model distinction for cases with 2–10 keV fluxes brighter than ∼0.08 mCrb (Fig. 17), for 50/100 ks exposures with *NuSTAR/XMM–Newton,* respectively. For the *NuSTAR*-only fits the availability of fewer channels (data points) brings the logBF (Bayes factor) value closer to 0 (1), for a given intrinsic flux value. Additionally, as demonstrated in Section 6, 'local' random fluctuations in values of logBF occur (Fig. 17), but whether these fluctuations will impact distinction of a *wrong* model from a *correct* model depends flux or availability of data in a certain band. For our examples (Section 6 and Fig. 17), for the joint fits, the values of logBF are more negative and lie comfortably below the selected threshold (up to a flux range of *f*9 or 0.09 mCrb) despite random fluctuations. Meanwhile, for the *NuSTAR*-only fits the values of logBF are closer to the threshold and thus run more into the risk of crossing into the logBF > 0 zone under the influence of random fluctuations leading to a false inference on the morphology. The grey and vertical dashed line in Fig. 17(d) marks the flux value where logBF for $M_{UXCL} \rightarrow D_{CTOR}$ comes dangerously close to the logBF-threshold (but does not cross it) for a *NuSTAR*-only fit. Thus, there exists a possibility that for a given threshold on logBF, the threshold on flux required for an effective model distinction can get pushed to a higher value in the absence of a certain band/instrument and or presence of random fluctuations in values of logBF. Hence, these threshold values are approximate estimates and should not be considered as absolute. It should also be noted that these results from our examples are based on the assumption that the soft band emission (e.g. emission modelled with APEC) is modelled perfectly, which might not be the case in real situations(see Section 7.2). This is because of the involvement of several complicated factors related to measurement, contamination from other sources in the field of view and physical modelling of the system, *we advocate that the readers perform their simulations setting a reasonable limiting value of logBF, to estimate the appropriate threshold on intrinsic flux necessary for model distinction.*

7.2 Limitations of our analysis

(i) The spectral shape can determine counts in a band and various input parameters used for data simulation. For example, different values of $N_{H,\,los}$, different levels of contribution from the scattered power law, etc. can contribute to enhancement or suppression of torus features in the 2–10 keV band. This might also affect the relative spectral counts collected by *XMM–Newton* and *NuSTAR* given an exposure time, thus resulting in variation in the constraints. Effects of variation in spectral shape on parameter constraints were shown for a few parameters like N_{cloud} (Fig. 6). Comprehensive testing of all possible cases of spectral shapes for all models is out of the scope of this work. However, in the case of real data analysis, these spectral shapes should be taken into consideration.

(ii) In real data reduction, the given spectrum has unknown parameters and we model it as best we can. But there will always be some discrepancy between the modelled parameters and the real spectral parameters. This consequently results in statistical and systematic variations in the location estimates (e.g. median) of the parameter posteriors during the data generation process. A similar situation is encountered for simulated data. To undertake such a study one can simulate a very large number of spectra (of order 10^4) (e.g. González-Martín et al. 2019) using FAKEIT in XSPEC (e.g. Markowitz, Reeves & Braito 2006) and then carry out Bayesian analysis in bulk. We performed such a study on a smaller scale in Section 3.3, wherein we simulated and fit 100 spectra. Given the heavy computational requirements for the study, we limit ourselves to only 100 spectral fits. The distributions of the posterior properties can be studied better with a much larger number of simulated data sets.

(iii) The models used here differ in two aspects namely, the assumed morphology and the assumptions on radiative physics. The results of our simulations have been limited by the simultaneous occurrence of both radiative and morphological differences between the models. Thus, we could not effectively differentiate between the effects of the radiative and the morphological differences in our current study. To test solely the effect of the morphological difference of the torus, it is necessary to set the radiative properties across different morphologies to be constant, so that the various properties of the CRH are just the effect of torus morphology only. Therefore, only one radiative transfer code e.g. XARS should be used to simulate different spectra for different morphology which in turn should be used for model testing. Conversely, to test the variation that radiative physics, different radiative transfer codes like `XARS`, `REFLEX`, `GEANT`, etc. could be used to simulate the spectra for a fixed morphology.

(iv) In our analysis, we assumed only simplistic situations while modelling the emitted radiation from a Compton-thick obscured AGNs. More specifically we did not take into account any additional emission from other X-ray bright sources which might be present in the host galaxy. In a real scenario, there might exist significant contamination from other X-ray bright sources like ULXs, X-ray binaries, etc. This has been demonstrated in Arévalo et al. (2014) for the case of the Circinus galaxy, where several X-ray bright sources contaminate different energy bands at different levels. In our work, we have demonstrated the energy/band dependence of certain parameters. Thus, contamination can lead to wrong estimates of the parameter. It is thus required that the contaminants are accounted for and are modelled correctly.

(v) In the future, it is expected that more physically self-consistent torus models and complex-torus models (shown schematically in e.g. Esparza Arredondo et al. 2021) will be developed, incorporating additional morphologies, cloud distributions, and physical processes. In addition, the community can look forward to data from new X-ray missions, including *XRISM* and *ATHENA*: each of these missions will feature a calorimeter that can resolve subtle features in fluorescent emission line complexes such as the Compton shoulder (e.g. Yaqoob & Murphy 2011; Tanimoto et al. 2019). Even presently, data from currently active missions other than *XMM–Newton* and *NuSTAR* can be used for analysis. Thus, performing additional tests similar to that performed in this work is a necessity, when one uses a model and data from an instrument not been tested here.

8 SUMMARY

In this project we test the reliability of the estimates of the model parameters for an X-ray obscured Compton-thick AGNs. We simulate synthetic data under six models with the instrument functions of *XMM–Newton* and *NuSTAR* at a flux level of ∼0.5 mCrb in the 2–10 keV band. The exposure times were 100 ks on *XMM–Newton* and 50 ks on *NuSTAR*. Using Bayesian analysis techniques we perform intramodel (IM) and cross-model fits on the synthetic data using these models. We investigate the level of degeneracy between the parameters, the ability to distinguish models and the different ways a wrong model fitting results in incorrect interpretation of the morphological and central engine parameters (e.g. photon index). We point out the challenges and limitations concerning the analysis of single epoch spectra.

In the intramodel fits, we find that the parameters are mostly recovered. However many morphological parameters showed very wide posteriors covering more than 30 per cent of the prior range in the medium Compton-thick regime ($N_{\rm H,\,los} < 2 \times 10^{24}$ cm^{-2}). Constraints on $N_{\rm H,\,los}$ worsen and the constraints on the morphological parameters improve in the heavy Compton-thick regime ($N_{\rm H,\,los} > 2 \times 10^{24}$ cm^{-2}). We also demonstrated the effect of a particular energy band (or instrument) which is necessary for determining reasonably good constraints on the parameters.

We also discuss a few ways in which a wrong model can fit a given data set and lead to false conclusions on the morphology along with other properties (e.g. $N_{\rm H,\,los}/N_{\rm H,\,eq}$) of the obscurer and or reflector. When a wrong model is fit to a particular data set, the photon index (Γ) of the coronal power law (a common parameter across all models) in most of the cases returned posteriors showing that Γ is constrained with a proportional error of <3 per cent but with significant discrepancy with the input. However for wrong model fits in case of the parameters which are present in the fitting model but not in the model used for data simulation, a different method can be adopted. For a few cases involving fitting with UXCLUMPY viz. $M_{\rm UXCL} \rightarrow D_{\rm j}$ where j = MYTORUS, CTORUS, and BORUS, we compare the posteriors obtained from the CM-fit to an that obtained from and IM-fit to a 'surrogate' data set (simulated under fitting model with the median values obtained from the CM-fits). The analysis of the 'surrogate' data set returned broader posteriors compared to the CM-fits for the morphological parameters σ_o and $C_{\rm frac}$ of the inner ring (see model description). *It is thus established that the precision in the value obtained from a fit is no guarantee for its correctness and does not necessarily indicate the application of a model consistent with the real morphology.* Our results from the simulations thus indicate the dangers of accepting fit results at face value.

The parameter spaces of Compton-thick AGN with limited data are complicated and sometimes multimodal, and thus demand global parameter exploration algorithms. With the use of Bayes-factor from BXA/MULTINEST runs it is possible to rule out the least preferred models for a given data set, at least at the higher end the available data quality. However, the use of synthetic data (simulated under the models in use) to assess the possibility of random fluctuations in the values of Bayes factor, *which can potentially lead to false model conclusions* (Section 6, 7.1.2, and Fig. 17), is recommended given an instrument combination and or flux regime. We thus conclude that measuring the properties of Compton-thick obscurers or reflectors with single epoch data obtained jointly from *XMM–Newton* and *NuSTAR* bands is not straightforward, even without the complicated effects of contamination. However, a study with multiepoch data can help us study variability (to detect variations in $N_{\rm H,\,los}$) and thus partial conclusion on the morphology can be drawn (e.g. Markowitz et al. 2014; Baloković et al. 2018; Laha et al. 2020; Esparza Arredondo et al. 2021). Thus time-variability analysis coupled with spectral analysis can yield better constraints on morphology.

The results of all the analysis carried out in this work thus suggest the importance of performing synthetic data simulation and analysis alongside real data using the instruments and the models of interest. This will help understand the potential limitations of the analysis, the models and the instruments. Hence, it is recommended that the users of these models perform similar simulations considering this work as example and noting corresponding potential limitations.

ACKNOWLEDGEMENTS

The authors thank Prof. Dr. hab. Agata Różańska for her valuable feedback on the scientific results and their broader significance in the X-ray astronomy. The authors also thank the anomymous referee for the insightful comments. This research

has made use of data and software provided by the High Energy Astrophysics Science Archive Research Center (HEASARC), which is a service of the Astrophysics Science Division at NASA/GSFC. This work was financially supported by Polish National Science Center (NCN) grant number: 2018/31/G/ST9/03224. AM also acknowledges partial support from NCN grant number: 2016/23/B/ST9/03123.

DATA AVAILABILITY

The corner-plots of all the analysed cases can be found in https://users.camk.edu.pl/tathagata/tsaha1996.html. Any other data products will be made available on reasonable request.

REFERENCES

Alonso-Herrero A., Quillen A. C., Rieke G. H., Ivanov V. D., Efstathiou A., 2003, AJ, 126, 81
Antonucci R., 1993, ARA&A, 31, 473
Arévalo P. et al., 2014, ApJ, 791, 81
Arnaud K. A., 1996, in Jacoby G. H., Barnes J., eds, ASP Conf. Ser. Vol.101, Astronomical Data Analysis Software and Systems V. Astron. Soc. Pac., San Francisco, p. 17
Awaki H., Koyama K., Inoue H., Halpern J. P., 1991a, PASJ, 43, 195
Awaki H., Kunieda H., Tawara Y., Koyama K., 1991b, PASJ, 43, L37
Baloković M. et al., 2018, ApJ, 854, 42
Bianchi S., Miniutti G., Fabian A. C., Iwasawa K., 2005, MNRAS, 360, 380
Bianchi S., Guainazzi M., Chiaberge M., 2006, A&A, 448, 499
Brightman M. et al., 2013, MNRAS, 433, 2485
Brightman M., Nandra K., Salvato M., Hsu L.-T., Aird J., Rangel C., 2014, MNRAS, 443, 1999
Buchner J. et al., 2014, A&A, 564, A125
Buchner J., Brightman M., Nandra K., Nikutta R., Bauer F. E., 2019, A&A, 629, A16
Buchner J., Brightman M., Baloković M., Wada K., Bauer F. E., Nandra K., 2021, A&A, 651, A58
Burlon D., Ajello M., Greiner J., Comastri A., Merloni A., Gehrels N., 2011, ApJ, 728, 58
Cash W., 1979, ApJ, 228, 939
Comastri A., Setti G., Zamorani G., Hasinger G., 1995, A&A, 296, 1
Done C., Madejski G. M., Smith D. A., 1996, ApJ, 463, L63
Elitzur M., 2008, New Astron. Rev., 52, 274
Esparza Arredondo D., González Martín O., Dultzin D., Masegosa J., Ramos Almeida C., García Bernete I., Fritz J., Osorio Clavijo N., 2021, A&A, 651, A91
Fabian A. C., Celotti A., Erlund M. C., 2006, MNRAS, 373, L16
Feroz F., Hobson M. P., Bridges M., 2009, MNRAS, 398, 1601
Foreman-Mackey D., 2016, J. Open Source Softw., 1, 24
García J., Dauser T., Reynolds C. S., Kallman T. R., McClintock J. E., Wilms J., Eikmann W., 2013, ApJ, 768, 146
García J. et al., 2014, ApJ, 782, 76
Ghisellini G., Haardt F., Matt G., 1994, MNRAS, 267, 743
Gilli R., Salvati M., Hasinger G., 2001, A&A, 366, 407
Gilli R., Comastri A., Hasinger G., 2007, A&A, 463, 79
González-Martín O. et al., 2019, ApJ, 884, 10
Guainazzi M. et al., 2016, MNRAS, 460, 1954
Harrison F. A. et al., 2013, ApJ, 770, 103
Hönig S. F., 2019, ApJ, 884, 171
Hönig S. F., Kishimoto M., Antonucci R., Marconi A., Prieto M. A., Tristram K., Weigelt G., 2012, ApJ, 755, 149
Horst H., Smette A., Gandhi P., Duschl W. J., 2006, A&A, 457, L17
Hunter J. D., 2007, Comput. Sci. Eng., 9, 90
Ikeda S., Awaki H., Terashima Y., 2009, ApJ, 692, 608
Jansen F. et al., 2001, A&A, 365, L1
Kinkhabwala A. et al., 2002, ApJ, 575, 732
Laha S., Markowitz A. G., Krumpe M., Nikutta R., Rothschild R., Saha T., 2020, ApJ, 897, 66
Laor A., 1991, ApJ, 376, 90
Liu Y., Li X., 2014, ApJ, 787, 52
Lutz D., Maiolino R., Spoon H. W. W., Moorwood A. F. M., 2004, A&A, 418, 465
Magdziarz P., Zdziarski A. A., 1995, MNRAS, 273, 837
Markowitz A., Reeves J. N., Braito V., 2006, ApJ, 646, 783
Markowitz A. G., Krumpe M., Nikutta R., 2014, MNRAS, 439, 1403
Matt G., 2002, MNRAS, 337, 147
Murphy K. D., Yaqoob T., 2009, MNRAS, 397, 1549
Murray N., Quataert E., Thompson T. A., 2005, ApJ, 618, 569
Nenkova M., Sirocky M. M., Nikutta R., Ivezić Ž., Elitzur M., 2008, ApJ, 685, 160
Ogawa S., Ueda Y., Yamada S., Tanimoto A., Kawaguchi T., 2019, ApJ, 875, 115
Paltani S., Ricci C., 2017, A&A, 607, A31
Press W. H., Teukolsky S. A., Vetterling W. T., Flannery B. P., 2002, Numerical Recipes: the Art of Scientific Computing. Cambridge Univ. Press, Cambridge
Ramos Almeida C. et al., 2011, ApJ, 731, 92
Ramos Almeida C., Ricci C., 2017, Nat. Astron., 1, 679
Ricci C., Paltani S., Awaki H., Petrucci P. O., Ueda Y., Brightman M., 2013, A&A, 553, A29
Ricci C., Ueda Y., Koss M. J., Trakhtenbrot B., Bauer F. E., Gandhi P., 2015, ApJ, 815, L13
Risaliti G., Maiolino R., Salvati M., 1999, ApJ, 522, 157
Risaliti G., Elvis M., Nicastro F., 2002, ApJ, 571, 234
Skilling J., 2004, in Fischer R., Preuss R., Toussaint U. V., eds, AIP Conf. Ser. Vol. 735. p. 395
Tanimoto A., Ueda Y., Odaka H., Kawaguchi T., Fukazawa Y., Kawamuro T., 2019, ApJ, 877, 95
Treister E., Urry C. M., 2005, ApJ, 630, 115
Urry C. M., Padovani P., 1995, PASP, 107, 803
Wilms J., Allen A., McCray R., 2000, ApJ, 542, 914
Yang Y., Wilson A. S., Ferruit P., 2001, ApJ, 563, 124
Yaqoob T., 2012, MNRAS, 423, 3360
Yaqoob T., Murphy K. D., 2011, MNRAS, 412, 277

SUPPORTING INFORMATION

Supplementary data are available at *MNRAS* online.

Please note: Oxford University Press is not responsible for the content or functionality of any supporting materials supplied by the authors. Any queries (other than missing material) should be directed to the corresponding author for the article.

This paper has been typeset from a TEX/LATEX file prepared by the author.

Chapter 3

Article II: Multiwavelength study of extreme variability in LEDA 1154204: A changing-look event in a type 1.9 Seyfert

In this chapter, I present the results of the analysis of a flaring AGN source which comprises of the second part of the thesis. All text tables and figures here have been submitted to A&A published by EDP sciences and also appears on arxiv at https://arxiv.org/abs/2309.08956.

3.1 Submitted article

Astronomy & Astrophysics manuscript no. aanda
September 19, 2023

Multiwavelength study of extreme variability in LEDA 1154204: A changing-look event in a type 1.9 Seyfert

T. Saha[1], A. Markowitz[1,2], D. Homan[3], M. Krumpe[3], S. Haemmerich[4], B. Czerny[5], M. Graham[6], S. Frederick[7,8], M. Gromadzki[9], S. Gezari[10], H. Winkler[11], D. A. H. Buckley[12,13,14], J. Brink[13], M. H. Naddaf[1,5], A. Rau[15], J. Wilms[4], A. Gokus[16,4,17], Z. Liu[15], and I. Grotova[15]

[1] Nicolaus Copernicus Astronomical Center of the Polish Academy of Sciences, ul. Bartycka 18, 00-716 Warszawa, Poland
email: tathagata@camk.edu.pl
[2] Center for Astrophysics and Space Sciences, University of California, San Diego, 9500 Gilman Drive, La Jolla, CA 92093-0424, USA
[3] Leibniz-Institut für Astrophysik Potsdam, An der Sternwarte 16, 14482 Potsdam, Germany
[4] Dr. Karl Remeis-Observatory & ECAP, Friedrich-Alexander-Universität Erlangen-Nürnberg, Sternwartstr. 7, 96049 Bamberg, Germany
[5] Center for Theoretical Physics, Polish Academy of Sciences, Al. Lotników 32/46, 02-668, Warszawa, Poland
[6] Division of Physics, Mathematics, and Astronomy, California Institute of Technology, Pasadena, CA 91125, USA
[7] Department of Astronomy, University of Maryland, College Park, MD 20742, USA
[8] Department of Astronomy, Vanderbilt University, 6301 Stevenson Center, Nashville, TN 37235, USA
[9] Astronomical Observatory, University of Warsaw, Al. Ujazdowskie 4, 00-478 Warszawa, Poland
[10] Space Telescope Science Institute, 3700 San Martin Drive, Baltimore, MD 21218, USA
[11] Department of Physics, University of Johannesburg, Kingsway, 2006 Auckland Park, Johannesburg, South Africa
[12] South African Astronomical Observatory, PO Box 9, Observatory 7935, Cape Town, South Africa
[13] Department of Astronomy, University of Cape Town, Private Bag X3, Rondebosch 7701, South Africa
[14] Department of Physics, University of the Free State, PO Box 339, Bloemfontein 9300, South Africa
[15] Max Planck Institute for Extraterrestrial Physics, Giessenbachstrasse, D-85741 Garching, Germany
[16] Department of Physics & McDonnell Center for the Space Sciences, Washington University in St. Louis, 1 Brookings Drive, St. Louis, MO 63130, USA
[17] Lehrstuhl für Astronomie, Universität Würzburg, Emil-Fischer-Straße 31, 97074 Würzburg, Germany

Received; accepted

ABSTRACT

Context. Multiwavelength studies of transients in actively accreting supermassive black holes have revealed that large-amplitude variability is frequently linked to significant changes in the optical spectra – a phenomenon referred to as changing-look AGN (CLAGN).
Aims. In 2020, the Zwicky Transient Facility detected a transient flaring event in the type-1.9 AGN 6dFGS gJ042838.8-000040, wherein a sharp increase in magnitude of ∼0.55 and ∼0.3 in the *g*- and *r*-bands, respectively, occurred over ∼40 days. Spectrum Roentgen Gamma (SRG)/eROSITA also observed the object in X-rays as part of its all-sky survey, but only after the flare had started decaying.
Methods. We performed a three-year, multiwavelength follow-up campaign of the source to track its spectral and temporal characteristics. This campaign included multiple ground-based facilities for optical spectroscopic monitoring and space-based observatories including *XMM-Newton* and *Swift* for X-ray and UV observations.
Results. An optical spectrum taken immediately after the peak revealed a changing-look event wherein the source had transitioned from type 1.9 to 1, with the appearance of a double-peaked broad Hβ line and a blue continuum, both absent in an archival spectrum from 2005. The X-ray emission exhibits dramatic flux variation: a factor of ∼17, but with no spectral evolution, as the power-law photon index remained ∼1.9. There is no evidence of a soft X-ray excess. Overall the object exhibits no apparent signatures of a tidal disruption event.
Conclusions. The transient event was likely triggered by a disk instability in a pre-existing accretion flow, culminating in the observed multi-wavelength variability and CLAGN event.

Key words. galaxies:active–galaxies:Seyfert–X-rays:galaxies

1. Introduction

A supermassive black hole (SMBH) at the center of a galaxy grows from the accretion of matter (Sołtan 1982). However, it is not clear if accretion proceeds persistently over long timescales (∼10^6 to 10^7 yr), although there is evidence for episodic nuclear accretion activity (e.g. Shen 2021). An accreting black hole forms an Active Galactic Nucleus (AGN), emitting continuum radiation across the electromagnetic band. Such radiation varies stochastically on timescales from hours to decades (e.g. Mushotzky et al. 1993; Markowitz et al. 2003, and references therein). A typical Seyfert or quasar can exhibit stochastic variability of up to a factor of 10 – 20 in X-rays (e.g. Markowitz & Edelson 2004) and by factors of few in the optical (e.g. Uttley et al. 2003) on timescales up to months–years. One of the lead-

ing models explaining such variability trends is the existence of inward-propagating fluctuations in local mass accretion rate (e.g. Ingram & Done 2011), aided by local magneto-rotational instability (MRI; Balbus & Hawley 1991).

However, the community has been collecting observations of extreme, transient variability in AGN, which indicates major changes in the underlying accretion rate. Observed events include persistently-accreting AGNs that have exhibited extreme variability on timescales ranging from a few months to years, with amplitude significantly higher than that measured in the case of regular variability. Multiple sources that are otherwise classified as Type 1 (exhibiting broad emission lines), Type-2 (exhibiting only narrow emission lines, Antonucci 1993), or intermediate types (varying relative intensity of the broad emission lines; Osterbrock & Koski 1976), have exhibited optical spectral type changes tied to extreme flux variability. These spectral changes are broadly manifested as the appearance or disappearance of one or more broad Balmer emission lines (e.g., Hα, Hβ). Such events are referred to as changing-look events, and the sources as changing-look AGN (CLAGN). Changing-look events involve brightening of the source (turn-on) in the form of an outburst or dimming of the emission (shut-down). Several CLAGNs have been reported over the last decade (e.g., Gilli et al. 2000; Trippe et al. 2008; Denney et al. 2014; Shappee et al. 2014; LaMassa et al. 2015; MacLeod et al. 2016; Ruan et al. 2019). For instance, Shappee et al. (2014) reported an optical spectral type change from type 1.8 to 1 in NGC 2617, concurrent to a high-amplitude increase in X-ray and UV continuum output; this is considered to be a significant accretion turn-on event. LaMassa et al. (2015) reported a shut-down event in the quasar SDSS J015957.64+003310.5 where the dimming of the source is associated with the disappearance of broad emission lines leading to a transition from Type 1 to 1.9. All these studies have argued that an intrinsic change in the accretion rate and the properties of accretion substructures — sometimes referred to as a changing state event — is the strongest candidate for driving most CLAGN events. Variations in line-of-sight absorption (e.g. Miniutti et al. 2014; Mehdipour et al. 2017) are rarely responsible. The current sample of known CLAGN is growing, with well over one hundred known so far (e.g. Graham et al. 2020).

However, another example of a class of high-amplitude transients is a tidal disruption event (TDE) of a star by a quiescent black hole (Rees 1988; Evans & Kochanek 1989). Recent observations have been uncovering some very peculiar CLAGN cases for which TDE-type accretion may be relevant. One example is the case of 1ES 1927+654: Trakhtenbrot et al. (2019) reported this Seyfert's transition from a type 2 to a type 1. Surprisingly, an increase in optical continuum and broad emission line flux was associated with a decrease, then recovery, in X-ray flux. Two different interpretations for the event were proposed: (1) magnetic 'braking' of the flow in the inner disk (Sikora & Begelman 2013; Scepi et al. 2021), and (2) a TDE in an AGN (Ricci et al. 2020, 2021). Another peculiar example of an SMBH transient event is a TDE occurring in the low-luminosity AGN WISE J234402.95-352641.8, reported by Homan et al. (2023): the rapid rise and slower decay of the X-ray and optical continua suggested a TDE, although optical spectral features, including broad Balmer lines and narrow emission lines such as the [O III]$\lambda\lambda$4959,5007 doublet, indicated ongoing AGN activity. Finally, there are other examples of changing-look behavior associated with strong flares in AGNs' optical and/or UV continuua (e.g. Frederick et al. 2019, 2021). The origin of these flares is not clear, as some of these sources display observational similarities to TDEs.

Thus, the physics of AGN transients is still an open question. In summary, all these studies have a general agreement on the fact that extreme temporal variability in a significant number of changing-look SMBH transients is connected to major changes in the accretion rate or change in the structure of the accretion flow (e.g. Ross et al. 2018; Scepi et al. 2021; Brogan et al. 2023). However, there does not seem to be a single underlying mechanism, as some cases indicate changes in disk structure and accretion rate, others indicate TDE-like accretion, and some invoke a combination of both mechanisms. Since most reported transients have a multi-band response, systematic multi-wavelength follow-ups are an essential tool to determine the physics of SMBH transients in both active and quiescent galaxies and their connection to the structures that feed SMBHs.

In 2020, between January and March, the Zwicky Transient Facility (ZTF; Bellm et al. 2019) observed a strong optical flaring (flare timescale of ~80 days) in the type-1.9 Seyfert galaxy LEDA 1154204 = WISEA J042838.77−000038.9 (referred to as J0428−00 henceforth). In parallel, the Extended ROentgen Survey with an Imaging Telescope Array (eROSITA; Predehl et al. 2021), the soft X-ray telescope onboard the *Spectrum Roentgen/Gamma* (*SRG*) spacecraft (Sunyaev et al. 2021) observed decaying X-ray emission in J0428−00 through its four successive all-sky scans spanning 1.5 years. In response to the optical flaring, we triggered a multi-wavelength follow-up campaign to discern the nature of the flaring event and track the evolution of the accretion flow. We conducted X-ray follow-up observations with *Swift* X-ray Telescope (XRT) (Gehrels et al. 2004) and *XMM-Newton* European Photon Imaging Camera (Jansen et al. 2001) to track the corona, UV observations using *Swift* Ultraviolet/Optical Telescope, and the *XMM-Newton* optical monitor to track the thermal emission, and optical spectroscopy with multiple ground-based optical telescopes to track the broad-line emission. Optical follow-up spectra showed that the flaring in *g*- and *r*-wavebands was accompanied by an optical spectral change from type-1.9 to type-1 (Frederick et al. 2020). J0428−00 thus belongs to the class of nuclears transient with changing-look transitions. We also used public photometry from Asteroid Terrestrial-impact Last Alert System (ATLAS, Tonry et al. 2018) to analyze the nature of the long-term optical variability. Additionally, archival observations from the Wide-field Infrared Survey Explorer (*WISE*) in the *W*1 and *W*2 bands were used to constrain the physics associated with infrared variability.

This paper presents the results and conclusions of the multi-wavelength follow-up campaign of J0428−00. Section 2 discusses the historical observations of the object. In Section 3, we report all the follow-up data obtained from our campaign and data reduction. Section 4 describes the analysis of the long-term optical light curves. Sections 5, 6, and 7 describe the analysis of the X-ray, broadband SED, and optical emission line spectra, respectively. We discuss the implications of our results in the context of accretion processes, AGN emission, and extreme supermassive black hole transients in section 8. We summarise our conclusions in section 9.

2. Object detection and counterpart

The Zwicky Transient Facility detected the transient event in J0428−00 at the coordinates α = 04:28:38.79 and δ = −00:00:39.7, marked by a substantial change in optical magnitude (Frederick et al. 2020): ZTF *g*- and *r*-band reduced magnitudes changed by $\Delta g \simeq 0.55$ and $\Delta r \simeq 0.29$ in ~40 days. To calculate the average scatter of the light curves about the long-term variability, we first smoothed it over the timescale of ~10 days.

Table 1. X-ray and space-based optical/UV observations of J0428−00.

Instrument	ObsID	Date (MJD)	X-ray Exp. (in ks)	Optical & UV filters (exp. in ks)
Swift	00013199001	58886	2.0	V(0.17), B(0.17), U(0.17), W1(0.3), M2(0.37), W2(0.67)
Swift	00013199003	58895	1.4	V(0.1), B(0.1), U(0.1), W1(0.20), M2(0.35), W2(0.44)
Swift	00013199004	58899	0.7	B(0.09), U(0.09), W1(0.26), W2(0.2)
Swift	00013199005	58901	2.1	V(0.17), B(0.17), U(0.17), W1(0.3), M2(0.5), W2(0.7)
Swift	00013199006	58907	1.9	V(0.15), B(0.15), U(0.15), W1(0.3), M2(0.47), W2(0.61)
eROSITA	eRASS1	58911	0.3 (0.14)	NONE
Swift	00013199007	58912	1.2	V(0.11), B(0.11), U(0.11), W1(0.21), M2(0.22), W2(0.42)
Swift	00013199008	58914	1.7	V(0.13), B(0.13), U(0.13), W1(0.26), M2(0.42) ,W2(0.53)
Swift	00013199009	58916	1.7	V(0.14), B(0.14), U(0.14), W1(0.28), M2(0.42), W2(0.56)
Swift	00013199010	58919	1.7	V(0.14), B(0.14), U(0.14), W1(0.28), M2(0.42), W2(0.55)
eROSITA	eRASS2	59093	0.3 (0.14)	NONE
eROSITA	eRASS3	59263	0.3 (0.14)	NONE
eROSITA	eRASS4	59452	0.3 (0.14)	NONE
Swift	00014932001	59550	5.7	V(0.29), B(0.29), U(0.29), W1(0.85), M2(2.3), W2(1.4)
XMM-Newton	0903991001	59651	21.8	V(3.5),B(3.5), W1(4.4), M2(4.4), W2(4.4)
Swift	00015274001	59786	5.5	V(0.43), B(0.43), U(0.43), W1(0.87), M2(1.44), W2(1.74)
XMM-Newton	0903991101	60017	44.0	V(4.4), B(4.4), U(4.4), M2(4.4)

Notes. Log of space-based X-ray, optical, and ultraviolet observations with eROSITA, *Swift* (XRT and UVOT instruments), and *XMM-Newton* (EPIC-pn and the Optical Monitor). The exposure times listed in the table for *Swift* and *XMM-Newton* are good time intervals (GTI) after screening. For the eROSITA observations we report both the GTI and the vignetting-corrected exposure (in parentheses). In this table, W1, M2 and, W2 are abbreviations for the UVW1, UVM2, and UVW2 filters, respectively.

Table 2. Optical spectroscopic observations of J0428−00.

Time (MJD)	Instrument(Telescope)	Slit width (″)	Seeing (″)	Exposure (s)
58871	LRIS+LRISBLUE (Keck)	1.0	0.46	600
58905	DeVeny (LDT)	1.5	1.5	1800
59105	DeVeny (LDT)	1.5	1.5	1700
59189	DeVeny (LDT)	1.5	1.5	2400
59468	SpUpNIC (SAAO)	2.7	~2.5	2400
59586	RSS (SALT)	1.5	0.1-2.7	120
59660	FORS2 (VLT)	1.3	<1.3	900
59821	ALFOSC (NOT)	1.3	0.8-1.6	300
59828	DBSP	1.5	1.5	600
59853	DOLORES (TNG)	1.5	1.0-2.0	600
59881	RSS (SALT)	1.5	0.1-2.8	500
59883	RSS (SALT)	1.5	0.1-2.8	120
60018	FORS2 (VLT)	1.3	<1.3	900

Notes. The list of abbreviations for different instruments: LRIS: Low Resolution Imaging Spectrometer; RSS: Robert Stobie Spectrograph; DBSP: Double Spectrograph; ALFOSC: Alhambra Faint Object Spectrograph and Camera; SpUpNIC: Spectrograph Upgrade: Newly Improved Cassegrain, FORS2: FOcal Reducer/low dispersion Spectrograph 2, DOLORES: Device Optimised for Low Resolution.

We then estimated the root-mean-squared variability (σ_g and σ_r) of the g and r-band light curve points after subtracting the long-term trend. The average scatter of the light-curve points calculated over the entire available light-curve (from ~MJD 58250 to ~MJD 58750) was found to be σ_g and $\sigma_r \sim 0.06$. Thus Δg and Δr are an order higher than σ_g and σ_r, statistically confirming a significant flaring event. In parallel, eROSITA detected the flare in consecutive all-sky X-ray scans, at α= 04h28m38.58s and δ = −00:00:41.8, with a positional uncertainty of ~1″, in its decaying phase through 2020 and 2021. For optical and X-ray detections, the most likely counterpart is the nearby (z = 0.07; Jones et al. 2009) Seyfert galaxy WISEA J042838.77-000038.9 = 6dFGS J042838.8-000040 = LEDA 1154204, located at α = 04:28:38.77 and δ=−00:00:40[1]. LEDA 1154204 is part of the

[1] https://ned.ipac.caltech.edu/

catalog of LEDA galaxies reported by Paturel et al. (2005). An optical spectrum was taken in 2005 as part of the 6dFGRS survey (Jones et al. 2004): as reported by Jones et al. (2009), it shows a broad Hα emission line along with other prominent narrow emission lines of [O III], [N II], and [S II], but no broad Hβ line. The emission line properties exhibited in the archival spectrum classify the object as an Type-1.9 Seyfert.

3. Data acquisition and reduction

3.1. Public photometric data

We obtained optical and infrared long-term continuum photometry from several forced-photometry websites. We ran the online forced-photometry pipeline of the ATLAS [2] (Tonry et al. 2018) to generate the *c*- and *o*- band optical light curves. We obtained the ZTF magnitude light-curve reduced data from the Infrared Science Archive (IRSA) website[3]. For both ATLAS and ZTF, we ran the online forced-photometry pipelines starting from the earliest epoch possible. We also obtained the *WISE* $W1$ and $W2$ band magnitude data from the IRSA website[4]. The *WISE* zero magnitude attributes are reported in Jarrett et al. (2011).

3.2. SRG/eROSITA

eROSITA detected the object during its first four all-sky scans i.e. eRASS1-4. We combined data from all seven Telescope Modules. We used event data from processing version c020, and the eROSITA data analysis software eSASS version *eSASSuser 211214* (Brunner et al. 2022; Predehl et al. 2021) in High Energy Astrophysics Software (HEASOFT) version 6.29. For each dataset, a circle and an annulus were used for the source and background regions, respectively. The radii were selected based on source brightness, where larger regions correspond to the source being brighter. Source region sizes varied between 105″ (most bright) and 47″ (least bright). Neighboring sources detected were excluded from the background regions in order to avoid background contamination. We list the eROSITA observations in Table 1.

3.3. Swift

We observed J0428−00 twelve times using the *Neil Gehrels Swift Observatory* (*Swift*) (Gehrels et al. 2004). Ten pointings occurred during the initial flaring state between February and March 2020; the 11th observation occurred more than a year later, in December 2021; the final observation occurred in March 2023.

The X-ray Telescope (XRT) exposures varied from 0.5 to 5.7 ks (Table 1). We calibrated the event files using `xrtpipeline` in HEASOFT version 6.29 and the latest calibration files. All spectra were extracted with circular regions of 40″ for both the source and the background. We generated the ancillary response files using `xrtmkarf`, and the response matrix (RMF) was taken from the latest calibration database.

For the Ultraviolet/Optical Telescope (UVOT) data, we selected a circular region of 5″ for the source and a 25″ circular region for the background for images taken by each of the UVOT filters. We used the task `uvotsource` to perform photometry and estimate fluxes for each of the available filters for the given observation. We applied Galactic extinction correction externally following the extinction estimates from Schlafly & Finkbeiner (2011). We also used the task `uvot2pha` to generate XSPEC-readable spectral files for the purpose of modeling simultaneous optical/UV/X-ray SEDs. It should be noted that in this case the Galactic extinction is not implemented on the data but rather via the spectral model `redden` when fitting data in XSPEC.

3.4. XMM-Newton

Two *XMM-Newton* (Jansen et al. 2001) observations (PI: M. Krumpe) with total durations of 20 ks and 40 ks were taken on 23rd March 2022 and 14th March 2023 respectively (Table 1). The EPIC observations were taken in full window mode. A 40″ circular region centered around the source was used to extract the source spectrum. The background spectrum was extracted from a circular region of the same radius, but a few arcmin away from the source. We reduced the EPIC-pn data with the SAS package (19.1) and HEASOFT (v6.28) using the standard settings for point sources.

We reduced the optical monitor dataset in imaging mode using the `omichain` pipeline processing. This command applies flat fielding, source detection, and aperture photometry, and ultimately creates mosaiced images. The script corrects for detector dead time. In the images, we do not find any imaging artifacts near the source, and the source is always located at the center of the CCD. Using the generated combined source list file, we used the `om2pha` command to generate XSPEC-readable spectral files for all the available filters (Table 1). For the optical monitor data, we used the canned response files available on the ESA *XMM-Newton* website[5].

3.5. Optical Spectroscopy

We obtained 13 long-slit spectra from January 2020 to March 2023 as a part of our post-flare monitoring campaign. As listed in Table 2, the spectroscopic observations were performed using multiple instruments. The time interval between successive spectra varied between one day and ∼6 months. We obtained one spectrum at each of the following facilities: the 10 m class Keck telescope (Oke et al. 1995), which is a part of Mauna Kea observatories, Hawaii, United States; 2 m class Nordic Optical Telescope (NOT) at Tenerife, Spain; 3 m class Telescopio Nazionale Galileo (TNG)[6] at Canary islands in Spain; 5 m class Hale Telescope[7] which is part of the Caltech Optical Observatories located at Palomar, CA, United States; and the upgraded 1.9 m telescope (Crause et al. 2019) at South African Astronomical Observatory (SAAO) at Sutherland, South Africa. We also obtained two spectra from the 8 m class Very Large Telescope (VLT) at Paranal, Chile (Appenzeller et al. 1998), which is a part of the European Southern Observatory (ESO). We also obtained three spectra each using the 4 m class the Lowell Discovery Telescope (LDT)[8] at Lowell Observatory in Arizona, United States, and the 10 m class Southern African Large Telescope (SALT; Buckley et al. 2006) at Sutherland, South Africa. All optical spectra were

[2] https://fallingstar-data.com/forcedphot/
[3] https://irsa.ipac.caltech.edu/Missions/ztf.html
[4] https://irsa.ipac.caltech.edu/Missions/wise.html
[5] https://sasdev-xmm.esac.esa.int/pub/ccf/constituents/extras/responses/OM/
[6] https://www.iac.es/en/observatorios-de-canarias/telescopes-and-experiments/telescopio-nazionale-galileo
[7] http://sites.astro.caltech.edu/palomar/about/telescopes/hale.html
[8] https://lowell.edu/research/telescopes-and-facilities/ldt/

reduced using standard methods. We discuss the spectroscopic analysis process in Section 7.

4. Long term variability

In Fig. 1, we display the ATLAS and the ZTF long-term light curves. They exhibit a slow initial rise long before the 2020 flare occurs. The main flare from 2020 appears symmetric in the rise and decay phases. However the presence of the data gap between ~MJD 58960 to ~MJD 59050 limits our ability to comment on the variability of the source in that interval. After the data gap from ~MJD 58960 to ~MJD 59050, we find a slow decay until ~MJD 59440 after which a weaker but broader secondary flare appears.

To mathematically qualify these properties, we fit the long-term light curves from ATLAS (o- and c-bands) and ZTF (g- and r-bands) with simple piece-wise phenomenological models to statistically identify the distinct variability characteristics in the data. We used a linear model for the light-curve for $\lesssim$MJD 58810. A Gaussian model is used model the flare in the ~MJD 58810 to ~MJD 58913 region. A power law is used to model the region from ~MJD 58910 to ~MJD 59500. A second Gaussian to model the broad peak after ~MJD 59500. We smoothed the light curves by taking a simple moving average. For the o- and c-bands the smoothing times were four and five days, respectively. For ZTF-g and ZTF-r the smoothing times were two and four days respectively.

To verify the apparent linear rise (before ~MJD 58850) we fit two models: (1) a linear model: $f_{\rm lin}(t) = bt + a$, and (2) a constant model: $f_{\rm cons}(t) = c$. We find that the linear rise model returns a better fit compared to the constant model: we define $p_{12} = \exp[(\mathrm{AIC}_1 - \mathrm{AIC}_2)/2]$ where AIC_1 and AIC_2 are the Akaike Information Criteria (Akaike 1974) for the linear model and the constant model respectively. For all light curves from ATLAS and ZTF, we find that p_{12} is less than 10^{-2} indicating the preference for a steady and slow rise.

We fit a Gaussian function to the flaring portion of the light curves from MJD~58810 to ~58910. We find that the peak of the flare lies between MJD ~58884 to ~58890 for each waveband, and the standard deviation of each Gaussian profile is ~20 days for each waveband. We define the full duration timescale of the flare as $t_{\rm flare} = 4\sigma$, which is ~80 days.

The main flare is followed by a slow decay lasting around ~2 years. We model this decay using a power law of the form (van Velzen et al. 2021)

$$f_{\rm pl}(t) = C\left(\frac{t - t_0}{t_{\rm sc}} + 1\right)^{-p}. \quad (1)$$

For fitting the decay region, we fix t_0 to the value of $t_{\rm peak}$ obtained from the Gaussian fitting of the flare. We find that the power-law decay index varies between $\sim 0.06 \pm 0.01$ and $\sim 0.048 \pm 0.005$ for the ATLAS o- and c-band light curves respectively, and ~0.1–0.2±0.1 for the ZTF light curves. The average value of p across all light curves is ~0.1, significantly lower than the theoretical 5/3 decay index expected for a typical TDE (Evans & Kochanek 1989).

The slow decay is followed by a secondary flare around ~MJD 59640 which is broader than the primary flare from 2020. While its profile shape is not clear from visual inspection, a Gaussian fit returns a flare timescale (4σ) of ~370 days. This secondary flare is more visually pronounced in the o-band light curve than others. However, this is because of the fact that the c-band has low sampling. For the g-band and r-band light curves the data exhibit the rise; however, there exist no other data to encompass the complete flare.

We can thus characterize the variability as follows:

i. The slow rise (modeled using a linear function) prior to the main flare and the slow decay (modeled using a power law) posterior to the main flare extends for $\gtrsim$ a few years in total as seen from the light curves. These trends considered together (slow rise and slow decay) might be due to a contribution from underlying stochastic variability, some transient process, or a combination of both. We discuss these processes in detail in Section 8.9 and 8.10.
ii. Superimposed on the slow baseline trends is the sharp flare in 2020; its total duration is ~80 days in the given bands.
iii. Also superimposed on the slow baseline trends in a weaker but broader secondary flare in March 2022.

We now discuss the infrared photometric monitoring. We smoothed the NEOWISE $W1$ and $W2$ band light curves such that there was one photometric point every six months, and the long-term variability trend can be more easily discerned. As shown in Fig. 1b, the increasing trend in the infrared light curve started before the sharp 2020 flare in the optical. The IR also shows a flare, but it is much broader in time than the optical flare. By visual inspection, the peak of the IR is delayed with respect to the optical peak by of order ~200 days. We discuss the possible mechanisms at work behind the infrared behavior in the context of an infrared dust echo in Section 8.10.

5. X-ray spectral analysis

We now discuss the X-ray data, from which we derived fluxes and spectral information. We used the Bayesian X-ray Analysis[9] package (BXA, version 4.0.6) (Buchner et al. 2014), which implements the nested sampling algorithm Ultranest (version 3.5.5 Buchner 2021) in XSPEC (version 12.12.0) to fit the X-ray data. The fit statistic was set to `cstat`, given the low number of counts and a requirement of BXA. We set the Galactic absorption $N_{\rm H}$ to 5.77×10^{20} cm^{-2} (Willingale et al. 2013) and assumed a redshift of 0.07 for all fits.

Initially, visual inspection of the datasets reveals that the X-ray spectra are relatively flat, with no obvious apparent evidence of more than one emission component (Fig.2a). We thus fit a simple power-law model to all spectra, and acceptable fits were obtained in all cases. We find that Γ remains at relatively moderate values (~1.9, Table 3) over the entire campaign, with no systematic trend over time. We additionally tested two physically-motivated Comptonization models: (1) thcomp (Zdziarski et al. 2020) and (2) nthcomp (Zdziarski et al. 1996; Życki et al. 1999). Both models returned similar values of photon indices; however other parameters – the input black body seed temperature, the Comptonizing electron temperature, and the covering fraction – remained unconstrained.

We also tested for the presence of a soft X-ray excess (e.g. Turner & Pounds 1989) in all spectra, by adding a ZBBODY component, or the presence of line-of-sight absorption, by including an absorption zTBABS component in addition to the Galactic absorption. The posterior distributions for the model with an additional intrinsic absorption returned a line of sight column density of $N_{\rm H,los} \lesssim 10^{20}$ cm^{-2}. The fraction of flux contributed to the total spectrum in the 0.5–1.0 keV band by the soft-excess component modeled by the black body was $\lesssim 10^{-4}$.

[9] https://johannesbuchner.github.io/BXA/index.html

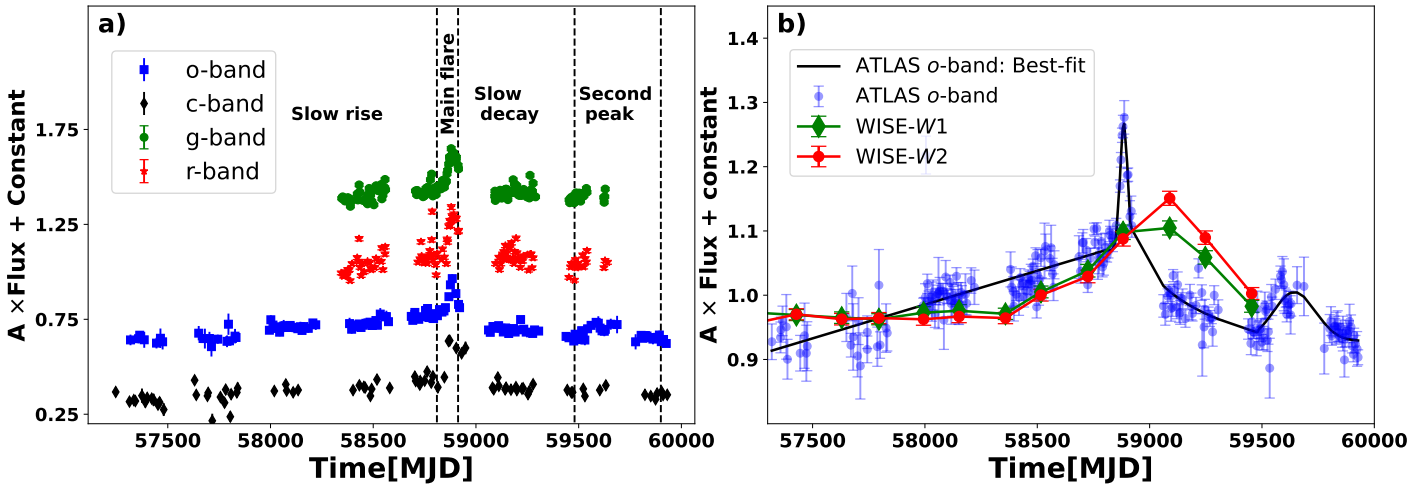

Fig. 1. Multiband light curves. Panel (a) shows the long-term optical light curves from ATLAS and ZTF. The vertical lines denote different time regions in the light curves, as discussed in the text. Panel (b) shows an overplot of the ATLAS *o*-band light curve, the best fit to the ATLAS *o*-band light curve, and the *WISE* light curves, illustrating the divergence in the optical and infrared continuum behaviour. In each figure, there are some data points for which the error bars are smaller than the data point marker.

We define Bayes Factor(BF) as: BF = Z_{other}/Z_{plaw} where Z_{plaw} and Z_{other} are the Bayesian evidence values of the simple power law and the other models respectively. Based on the Bayes Factors a simple power law model was marginally preferred, BF<1 holds for most cases. Overall from the posterior trends and the Bayes Factors, we thus conclude that the simple power law explains the data best and neither a soft X-ray excess nor an excess absorption above the Galactic column are required to model the spectra.

The X-ray flux exhibits variability on a shorter (∼day) timescale, as seen in the 0.2–5.0 keV light-curve (Fig. 2b) between MJD 58885 and MJD 58920.

6. Broad band SED analysis

All *Swift* and *XMM-Newton* observations in our campaign were accompanied by simultaneous optical and/or UV photometry, affording us the ability to assess broadband emission mechanisms via spectral energy distribution (SED) fitting. We used the AGNSED (Kubota & Done 2018) model for broadband SED fitting. Our model in XSPEC notation is `redden*tbabs*(galaxy + agnsed)`. Here, `galaxy` denotes the host-galaxy contribution; we used the galaxy-type Sb template from Mannucci et al. (2001) to model it. A luminosity distance (Wright 2006) of d_L = 317 Mpc, $E(B-V) = 0.064$[10] (Schlafly & Finkbeiner 2011), and $N_{H,Gal} = 5.77\times10^{20}$ cm^{-2} (Willingale et al. 2013) were assumed. The black hole mass (M_{BH}) for J0428−00 is poorly constrained (Section 8.4). We thus performed the broadband fitting for two extreme values of black hole mass: (a) $M_{BH} = 10^7\ M_\odot$ and (b) $M_{BH} = 4\times10^8\ M_\odot$. For all cases, we froze the value of the hard X-ray photon index (Γ_{hot}) to the value obtained from the corresponding X-ray analysis. We performed the broadband fits for two different cases for each of the assumed black hole masses, and bearing in mind the lack of observed soft-X-ray excess in the >0.2 keV spectra:

i. C1: This is a two-component model in which optical/UV emission is assumed to arise solely from the outer thin disk, and the X-ray emission from the inner hot corona. In the AGNSED model this is implemented by setting $R_{hot} = R_{warm}$.

ii. C2: This is the generic three-component AGNSED setup where a UV/soft X-ray emitting 'warm' corona bridges the outer thin disk and the hot inner corona (Kubota & Done 2018). In the AGNSED model, this is implemented by setting $R_{hot} < R_{warm}$.

We kept the temperature of the hot corona ($k_B T_{hot}$), the temperature of the warm corona ($k_B T_{warm}$), and the corona height frozen to 100 keV, 0.1 keV, and 10 R_g, respectively. The relevant values of the best fit parameters in the C1 and C2 setup are reported in Tables 4 and 5 respectively.

For $M_{BH} = 10^7\ M_\odot$, we get good fits for both the C1 and C2 configurations, indicating applicability of either configuration. The fits in the C1 configuration indicate that the sole contribution from the outer disk and hot corona adequately fit the optical-UV and X-ray flux in all spectra, indicating the adequacy of the two-component model. In the C2 configuration, the emission from a warm corona appears in the energy band attenuated by Galactic absorption, and does not extend to above 0.2 keV, thus imparting no significant effect in the observed bands, i.e., creating no soft-excess above 0.2 keV (Fig. 3a). The fit statistic is mildly better in most of the fits in the C2 configuration ($6 < (\Delta\chi^2)_{C1-C2} < 30$) due to the introduction of the additional warm Comptonization component with the bounds of the warm corona radius set in the range $16R_g < R_{warm} 500R_g$, which slightly improves the fit in the optical/UV part of the SED. However, this configuration also introduces large uncertainties in estimates of $\lambda_{edd} \equiv L_{bol}/L_{Edd}$ (Table 5) and R_{warm} remained unconstrained.

For $M_{BH} = 4\times10^8\ M_\odot$, we were unable to get a physical solution in the C1 setup. The problem is for two reasons. First, a consistent level of host-galaxy contribution was not obtained for all spectra. Second, the model did not generate enough flux to explain the given spectra in all bands. In the C2 setup, with the warm Comptonization present, we obtained a physical solution, with consistent values of host-galaxy contribution and AGN flux explaining the entire optical/UV waveband. In either case, there is no significant Comptonized flux reaching above 0.2 keV, as constrained by the lack of an observed soft X-ray excess (Fig. 3).

[10] https://irsa.ipac.caltech.edu/applications/DUST/

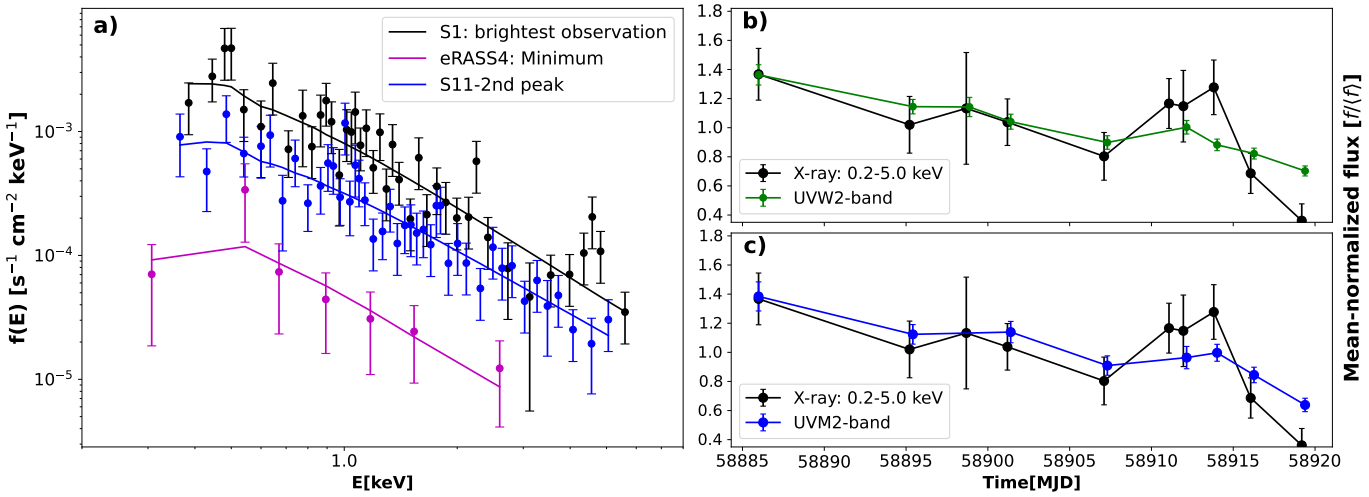

Fig. 2. X-ray spectra and light curves. Panel (a) shows the variation across three selected X-ray spectra taken during the brightest phase, the minimum flux, and during the second peak. There is no significant variation in spectral shape over time. Panels (b) and (c) show the short term variability in the decaying part of the flare, between MJD 58880 to 58920. The mean-normalized light curves for 0.2–5.0 keV X-rays and the UVM2 and UVW2 bands are plotted in panels (b) and (c), respectively. Both the X-ray and UV light curves exhibit short term variability. Furthermore, both X-ray and UV light curves show overall decreases in flux by roughly the same amount, though the X-rays decrease faster than the UV by the end of the campaign.

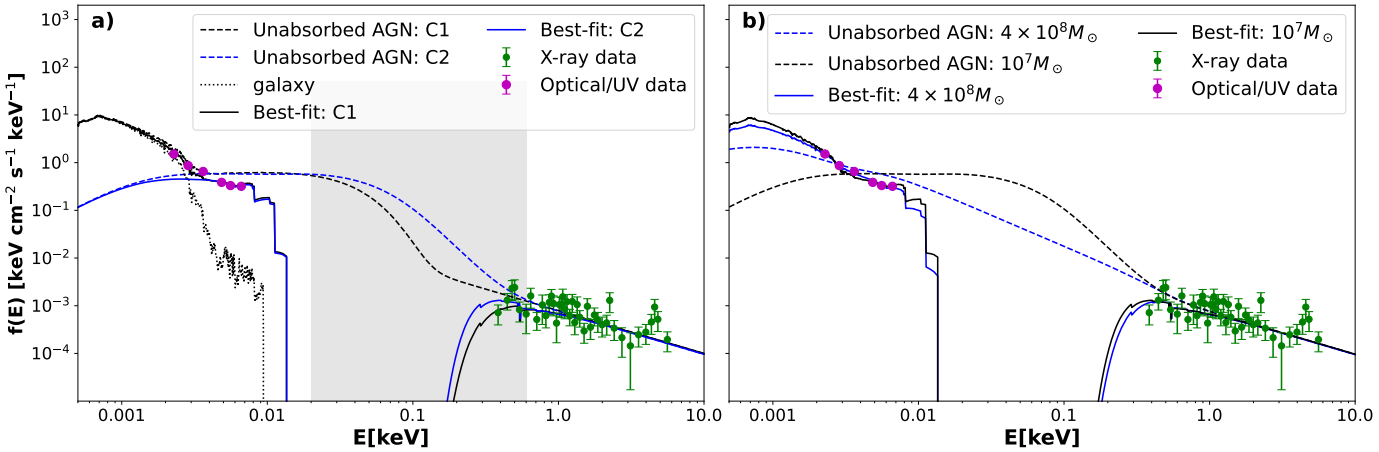

Fig. 3. Broadband SED fits for the brightest *Swift* spectrum (Section 6). (a) For given $M_{\rm BH} = 10^7\ M_\odot$, both the C1 (warm corona on) and C2 setups (warm corona off, Section 6) fit the data well. The difference exists in the unabsorbed AGN spectra, where the C2 setup generates excess flux from the warm corona in the ~0.02–0.6 keV band (the grey band). However, that fails to create significant differences in the absorbed spectra due to strong attenuation by our Galaxy, notably in the band where the soft X-ray excess is expected. (b) The best-fit spectra for two different black hole masses $M_{\rm BH}$) $10^7\ M_\odot$ and $4\times10^8\ M_\odot$ when the warm corona is present (C2 setup). The absorbed-model spectra for both cases fit the broad band datasets, even though the fit returned an underlying unabsorbed AGN spectra generated with different parameters. In each figure, there are some data points for which the error bars are smaller than the data point marker. marker.

7. Optical spectroscopic analysis

In this section, we discuss the details of the optical spectroscopic data obtained using ground-based telescopes during our three-year monitoring campaign. As a reminder: in Table 2 we report the instruments used in our optical spectroscopic observations. The evolution of the optical spectrum is plotted in Fig. 4.

7.1. Spectral scaling and extinction correction

We performed flux scaling for each spectrum by fitting the [O III]λ5007 line profiles using the method of van Groningen & Wanders (1992). This method corrects for the line centers and estimates a flux correction factor for the [O III]λ5007 line in each spectrum (see Appendix A for details). We used this factor to correct for each spectrum's emission line fluxes. We determined the redshift z of the object to be 0.0709 ± 0.0004 using the narrow [O III] emission line in the Keck spectrum; this value is consistent with the reported estimate from NED (Jones et al. 2009). We applied de-reddening correction to all optical spectra before the spectral fitting. We obtained the value of $E(B-V) = 0.064$ from Schlafly & Finkbeiner (2011) using the python package `sfdmap`[11], and thus calculated the extinction factor (A_λ) at each wavelength. We used the python package `extinction`[12] to apply extinction corrections.

[11] https://github.com/kbarbary/sfdmap
[12] https://extinction.readthedocs.io/en/

Table 3. X-ray photon indices and model flux from power-law fits to all X-ray spectra.

Date	Telescope	Γ	$F_{0.2-5.0\ \mathrm{keV}}$
(MJD)			(10^{-12} erg s^{-1} cm^{-2})
58886	*Swift*-XRT	1.90 ± 0.21	3.57 ± 0.48
58895	*Swift*-XRT	1.75 ± 0.36	2.66 ± 0.48
58899	*Swift*-XRT	1.91 ± 0.63	2.98 ± 1.00
58901	*Swift*-XRT	1.69 ± 0.24	2.69 ± 0.41
58907	*Swift*-XRT	1.76 ± 0.2	2.08 ± 0.42
58911	eROSITA	1.73 ± 0.34	3.06 ± 0.42
58912	*Swift*-XRT	1.99 ± 0.33	3.0 ± 0.62
58914	*Swift*-XRT	1.9 ± 0.25	3.34 ± 0.42
58916	*Swift*-XRT	1.82 ± 0.41	1.79 ± 0.38
58919	*Swift*-XRT	1.89 ± 0.69	0.96 ± 0.28
59093	eROSITA	2.07 ± 0.4	0.74 ± 0.21
59263	eROSITA	2.35 ± 0.55	0.52 ± 0.15
59452	eROSITA	2.61 ± 1.49	0.19 ± 0.12
59550	*Swift*-XRT	1.72 ± 0.19	1.54 ± 0.18
59651	*XMM-Newton* EPIC-pn	1.87 ± 0.06	0.48 ± 0.02
59786	*Swift*	1.56 ± 0.71	0.22 ± 0.09
60017	*XMM-Newton* EPIC-pn	1.81 ± 0.02	0.41 ± 0.01

Notes. Photon indices and values of 0.2–5.0 keV absorbed flux from the power-law fits to all X-ray spectra. All errors correspond to the 90% confidence limit of the BXA-Ultranest posteriors. The photon indices are mostly moderately flat, with Γ usually near 1.9.

Table 4. Parameters from broad SED fits assuming a black hole mass of $10^7 M_\odot$ in the configuration lacking a warm corona (C1).

Time (MJD)	Telescope	$\log \lambda_{\mathrm{Edd}}$	R_{hot} (R_{g})	χ^2/dof
58886	*Swift*	−0.31 ± 0.01	15.3 ± 0.7	1.74
58895	*Swift*	−0.43 ± 0.02	19.1 ± 1.7	1.06
58899	*Swift*	−0.37 ± 0.02	13.6 ± 1.5	2.51
58901	*Swift*	−0.43 ± 0.01	21.3 ± 1.8	2.03
58907	*Swift*	−0.52 ± 0.02	20.2 ± 1.9	2.54
58912	*Swift*	−0.50 ± 0.02	17.6 ± 1.6	1.53
58914	*Swift*	−0.55 ± 0.02	25.0 ± 2.6	1.43
58916	*Swift*	−0.60 ± 0.02	15.7 ± 1.3	2.61
58919	*Swift*	−0.72 ± 0.02	11.8 ± 1.2	2.75
59550	*Swift*	−0.98 ± 0.02	77.9 ± 8.0	1.36
59651	*XMM-Newton*	−1.34 ± 0.02	24.3 ± 1.2	1.32
59786	*Swift*	−1.55 ± 0.06	78.2 ± 13.8	1.88
60017	*XMM-Newton*	−1.57 ± 0.01	57.9 ± 3.3	5.21

7.2. Continuum fitting

A Seyfert's optical spectrum can typically contain the following emission components in its continuum: the blue continuum, which is thermal emission from the accretion disk and is typically modeled by a power law (Vanden Berk et al. 2001), $f \propto \lambda^{-\alpha}$; contribution from the host-galaxy; and the Fe II contribution. We used the galaxy templates from Mannucci et al. (2001) and the Fe II templates from Bruhweiler & Verner (2008). Thus the complete model (M0) can be represented as M0 = power law + host + Fe II.

We used least-square fitting implemented through the `PYTHON` module `lmfit` for fitting the optical spectra. We performed an initial global fit to the continuum of the best quality Keck spectrum with the M0 model, but we do not find any significant presence of Fe II in the spectrum. Thus for further fitting, we did not use the Fe II contribution; we denote this new model as M1.

Since the spectra were taken at different epochs, we can track how the continuum evolved from having a strong power law in early 2020 to being galaxy dominated in the later phases (Fig. 4). For most cases the template of an Sb type galaxy fit the spectra best, and we used it for the entire optical fitting exercise. Thus, the spectra from early 2020 required the presence of a power law (Fig. 5a) at varied degrees of strength, with the Keck and the first LDT spectra having the strongest contribution from it. However, for the spectra taken later, the host-galaxy template sufficed to describe the continua well (Table 6). Thus, our basic global continuum models are reduced to:

i. M1 = power law + host-galaxy
ii. M2 = host-galaxy only.

If we consider a wide range of different host-galaxy templates, it is possible for the fit to assume a weak continuum. However, the strength of such a continuum is expected to be quite weak as the spectra in the later phases are visually dominated by the galaxy component. Overall, we do not expect the selection of the galaxy template to have significant effects on the modeling of the emission line profiles nor on the physical interpretation of the changing-look event.

We explain the full details of the modeling in Appendix B. From the continuum power law, we estimate the parameters such as the broad line emission radius (R_{BLR}) and bolometric luminosity (Section 8.2). Reliable estimates could only be determined

Table 5. Parameters from broad SED fits assuming a black hole mass of $10^7 M_\odot$ in the configuration with a warm corona (C2)

Date (MJD)	Telescope	$\log \lambda_{\rm Edd}$	$\Gamma_{\rm warm}$	$R_{\rm hot}$ ($R_{\rm g}$)	χ^2/dof
58886	*Swift*	-0.16 ± 0.26	3.69 ± 0.62	12.2 ± 1.0	1.54
58895	*Swift*	-0.24 ± 0.20	3.45 ± 0.63	14.0 ± 4.6	0.88
58899	*Swift*	-0.15 ± 0.23	3.09 ± 0.46	9.7 ± 1.7	1.89
58901	*Swift*	-0.26 ± 0.16	3.56 ± 0.49	15.2 ± 3.6	1.83
58907	*Swift*	-0.31 ± 0.18	3.20 ± 0.44	13.6 ± 3.4	2.09
58912	*Swift*	-0.32 ± 0.23	3.48 ± 0.72	13.0 ± 2.8	1.41
58914	*Swift*	-0.32 ± 0.20	3.00 ± 0.48	14.6 ± 5.0	1.14
58916	*Swift*	-0.36 ± 0.20	3.03 ± 0.43	11.7 ± 3.5	2.18
58919	*Swift*	-0.50 ± 0.24	3.17 ± 0.46	9.0 ± 1.3	2.62
59550	*Swift*	-0.82 ± 0.13	2.75 ± 0.36	29.7 ± 12.8	1.60
59651	*XMM-Newton*	-1.21 ± 0.49	3.48 ± 1.29	18.1 ± 15.3	1.26
59786	*Swift*	-1.31 ± 0.32	2.15 ± 0.55	20.2 ± 14.2	2.91
60017	*XMM-Newton*	-1.42 ± 0.23	2.94 ± 0.61	27.2 ± 16.2	5.09

from the Keck and LDT spectrum since the power law component was distinctly visible only for these two spectra.

7.3. Line fitting

J0428−00 exhibits the narrow emission lines typically seen in Seyfert AGNs: the [O III]$\lambda\lambda$4959,5007 doublet, the [N II]$\lambda\lambda$6548,6584 doublet, and the [S II]$\lambda\lambda$6716,6731 doublet. Additionally, the source persistently exhibits a broad Hα emission line. However, the optical spectrum from the 6dF survey does not exhibit the broad Hβ emission line. We do not find any significant evidence of a broad He IIλ4686 emission line, nor Bowen fluorescence lines (e.g. [N II]λ4640) in any spectra.

We fit the Hβ and Hα line regions with a local continuum model (Appendix B) and Gaussian profiles. The basic method for all spectra is described below:

- Local continuum: The local continuum model for the broad-line regions was either taken to be M1 or M2 (the overall continuum models in 7.2). In some cases, however, it was not enough to always correctly account for the underlying local continuum around the broad emission lines. For those spectra where the line regions are not well fit by the overall continuum models, we added a linear continuum of the form $f = a\lambda + b$, to account for local deformations in the line regions (Appendix B).
- Narrow lines: In the Hβ line region, the most significant narrow lines are the [O III] doublet. For most spectra, we required one or two moderately broad blue-shifted components in addition to the narrow lines to fully model the [O III] profiles (Fig. 5b). We find an emission line feature at $\lambda \simeq 4893$ Å for the Keck spectrum from 23rd January 2020 and the LDT spectra from 26th February 2020 and 13th September 2020. We identify this line feature as the forbidden coronal line of [Fe VII]. For the Hα region, the most significant narrow lines are the [N II] doublet, Hα, and the [S II] doublet (Fig. 5c). The [S II] doublet usually has low line flux, and in some spectra are not well resolved. Thus, for the [S II] doublet, one or two Gaussians are required depending on the resolution (Appendix B) and blending of the two lines. The errors on the integrated narrow line flux are calculated from the least square fitting method.
- Broad lines: We fit the broad emission lines using a single Gaussian, or a double Gaussian. In most cases, a double Gaussian (Fig. 5a and 5b) profile fits the line profile better than a single Gaussian. This is inferred by comparing the AIC values, $\rm AIC_1$ and $\rm AIC_2$, for the single and double Gaussian broad emission line fits, respectively. The quantity $p_{21} = \exp[(\rm AIC_2 - AIC_1)/2]$, in general, was found to be lower than 10^{-2} (Table 6), which indicates a preference for the double Gaussian model. However, in some cases pertaining to the low signal-to-noise Hβ line, it was not possible to distinguish between a single and a double Gaussian fit. In such cases, we accepted the single Gaussian fit. The method for estimating the errors on the integrated broad emission lines is discussed in Appendix C.
- The archival 6dF spectrum: The 6dF spectrum is not flux calibrated, thus comparison of flux estimates with the recently-obtained spectra is not possible. However, we performed line fitting to roughly estimate the broad line properties. A broad Hβ emission line was not detected in the spectrum. We performed a fit on the broad Hα emission line with both a single peaked and a double peaked profile. The double Gaussian profile returned a better fit.

We thus statistically confirm that the broad Hα and Hβ emission lines in J0428−00 exhibit a double-peaked profile both recently, as well as in 2005; however, while Hα was present in all spectra, Hβ is absent in 2005.

7.4. Testing the physical diskline model

For the best-quality spectrum, that taken with Keck, we test if a double-peaked (Chen et al. 1989; Chen & Halpern 1989) profile from a disk emitter explains the observed Hα and Hβ profiles. This model (henceforth "diskline") assumes that the line-emitting matter is in Keplerian motion in a flattened geometry and it incorporates the effects of Doppler shifts and gravitational redshift. We use the diskline with local broadening (Chen & Halpern 1989) due to electron scattering in a photoionized atmosphere (Halpern 1984; Shields & McKee 1981). The local broadening is parameterized with the parameter σ_0 such that the local broadening at a given wavelength λ is given by $\sigma_\lambda = \sigma_0 \lambda$, where λ is the central rest-wavelength of the broad line (details of modeling are discussed in Chen & Halpern 1989). The emissivity profile is a radial function assuming isotropic illumination from the center: r^{-3}.

For fitting with diskline, we first subtracted the underlying continuum and best fit narrow profiles obtained from the phenomenological Gaussian fitting (Section 7.3). This process isolates the broad emission line profile. We fit the broad lines with (A) only a diskline component and (B) with a diskline + a broad Gaussian component. The limits on the inner ($R_{\rm in}$) and outer ($R_{\rm out}$) radii were set to $50\,R_{\rm g} < R_{\rm in} < 1000\,R_{\rm g}$ and $1010\,R_{\rm g} <$

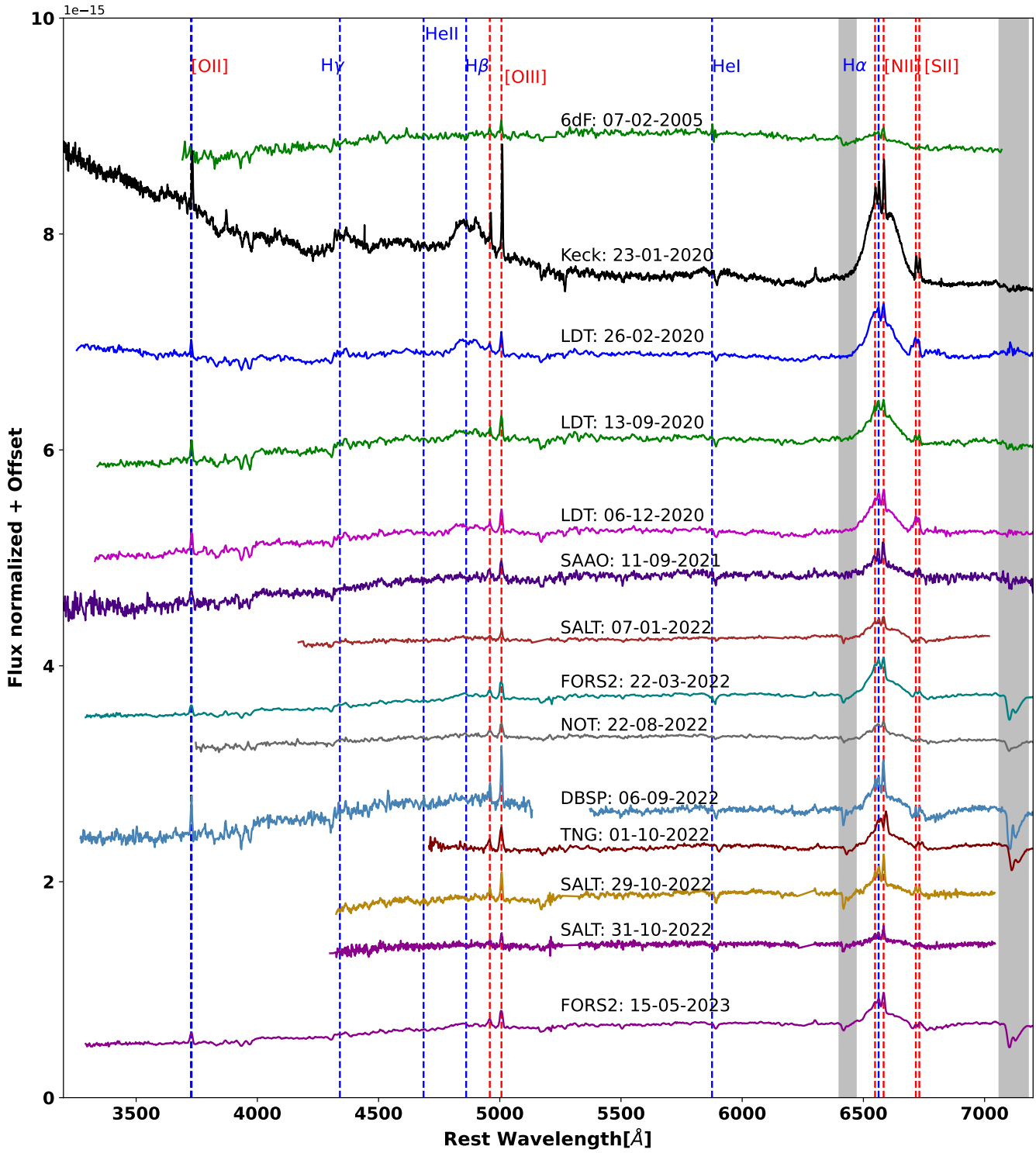

Fig. 4. The optical spectra obtained during our three years of monitoring J0428−00. The Keck spectrum from 2020 clearly shows the appearance of a broad Hβ profile which was absent in the 6dF spectrum from 2005, thus indicating a changing-look event. The source also exhibits a strong blue continuum initially in the Keck and the first LDT spectra, which fades over time. The broad Hβ emission line weakens considerably over time, such that it is difficult to distinguish over the continuum level by the end of the campaign. The Broad Hα follows a similar trend but is always detectable above the continuum level. The narrow emission lines of [O II], [O III], [N II], and [S II] are seen in the spectra. The grey bands mark telluric absorption bands.

$R_{\rm out} < 3 \times 10^4\, R_{\rm g}$ respectively. The limits on the viewing angle were $2.0^\circ < \theta_{\rm i} < 87^\circ$. To judge the quality of fit for case (A) and (B) we use the quantity $p_{\rm BA} = \exp[({\rm AIC_B} - {\rm AIC_A})/2]$, where $\rm AIC_A$ and $\rm AIC_B$ are the Akaike Information Criterion for case A and case B. If the condition $p_{\rm BA} < 10^{-2}$ holds, case (B) is a better fit. We describe the results below:

– Hα fit: For both cases, the wings of the broad Hα line were fit well. However, the data at the red and blue peaks and the

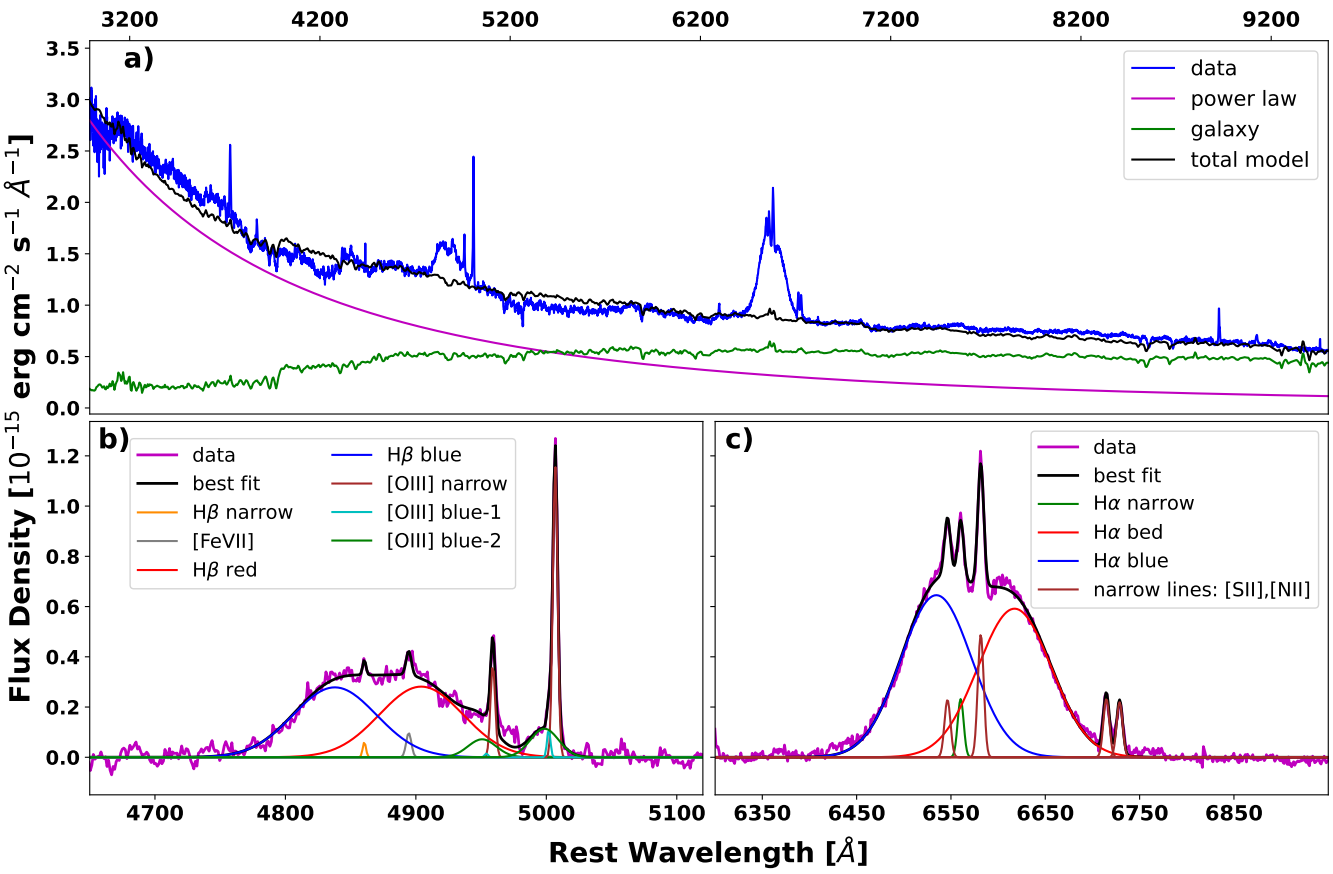

Fig. 5. Optical spectral decomposition for the Keck spectrum. (a) Continuum fit. We fit the continuum in the full spectrum using a power law + host-galaxy template. (b) The local continuum-subtracted Hβ line region. The best-fitting model consists of Gaussian profiles fit to the narrow [O III] doublet, including broader blue-shifted components, and red- and blue-shifted broad Gaussians to fit the broad Hβ emission profile. (c) The local continuum-subtracted Hα line region. The best-fitting model consists of Gaussian profiles fit to the doublets of [N II] and [S II] as well as to the narrow emission line of Hα, and red- and blue-shifted broad Gaussians to fit the broad Hα profile; as with Hβ.

valley between them (~6550–6600 Å) exhibit more curvature than the model (Fig. 6a). Consequently, resulting in significant residuals. For case B, the fit was carried out initially with the center of the Gaussian fixed to the rest wavelength of Hα (6562.81 Å). However, we obtained a better fit when the center was kept free (Fig. 6b). The center of the Gaussian was found to be displaced by 315 ± 79 km s^{-1} in the best fit (Table 7). For the Hα line profile, we obtain a $p_{\rm BA} = 10^{-266.26}$, indicating a preference for a diskline+Gaussian profile.

– Hβ fit: For case A, we initially kept, the parameters $R_{\rm in}$, $R_{\rm out}$, θ_i and σ_0 frozen to the values obtained from the Hα fit. In this setup, the blue wing of Hβ fits well, while the red wing leaves a substantial residual. Additionally, the peaks and the curvature of the valley between them are not accounted for fully by a single diskline model (Fig. 6c and 6e). The fits did not improve when we allowed the parameters to vary independently of the Hα fit. In general, we did not get a good fit with a single diskline. For case B, similarly, we checked if a good fit was obtained if the same parameter values obtained from the Hα fitting were used. In this case, we kept the morphological parameters of the diskline components frozen to the values obtained from the corresponding case B of the Hα fitting. Given the different rest wavelengths, we applied the following transformations for the shift in the line center and the standard deviation of the Gaussian component: (a) line-center shift: $\Delta\lambda_\beta = (\Delta\lambda_\alpha/\lambda_\alpha)\lambda_\beta$ (b) standard deviation: $\sigma_\beta = (\sigma_\alpha/\lambda_\alpha)\lambda_\beta$, based on the underlying assumption that the profiles of both lines result from identical kinematics. Here, λ_α and λ_β are the rest-wavelength of Hα and Hβ respectively. $\Delta\lambda_\alpha$ and σ_α are the deviation of the center from the rest wavelength of Hα and the standard deviation of the Gaussian component in the Hα fits respectively. This case also failed to fully account for the peaks and the valley in the Hβ profile (Fig. 6d). However, significant improvements in the fits were obtained when the parameter values were allowed to vary independently of those obtained for Hα (Fig. 6f). Thus, when the Hβ emission line is fit independently of Hα, the diskline+Gaussian is a better fit ($p_{\rm BA} = 10^{-79.58}$) to the data.

We summarize the parameters in Table 7. The fits involving the diskline model support the notion that J0428−00 has broad Balmer line profiles inconsistent with a typical single-peaked Gaussian profile. For both lines, a diskline component was required, although a single diskline component did not explain the line profiles optimally. The sum of a diskline and a broad Gaussian component returned a good fit for both profiles. For Hβ, the constraints on the diskline parameters are generally weak but consistent with those of Hα. This result can be a consequence of the lower S/N in the Hβ region. The Gaussian component has a flux contribution of ~40–50% to the total profile flux for both Hα and Hβ. Additionally, the broad Gaussian component also required different parameters between Hα and Hβ. Its displace-

ment in Hβ with respect to the rest-wavelength is ∼4 times that of Hα and its standard deviation is ∼700 km s^{-1} more than that of Hα (Table 7). However, all fits return a consistent value of inclination, $\theta_i \sim 15°$. The analysis indicates that the Hβ and Hα emission lines have broadly similar components. Speculatively, some differences in best-fitting model parameters might arise due to the two emission lines' preferentially originating in somewhat different regions of the same overall diskline-like distribution, thus sampling slightly different kinematics. We discuss the broader implication of the fits in Section 8.5.

7.5. Modeling of Balmer profiles using FRADO

The Failed Radiatively Accelerated Dusty Outflow (FRADO) model developed by Naddaf et al. (2021) and Naddaf & Czerny (2022) features a failed dusty outflow forming the broad line emitter. Gas containing dust rises up from the accretion disk, and gets accelerated outward by the radiation pressure on the dust until the dust sublimates due to the strong radiation from the central engine. The sublimation of the dust leads to a scenario where the radiation force is unable to provide the acceleration and the matter falls back onto the disk. The BLR is constantly being replenished by new outflowing clouds originating in the disk.

Currently, several line profiles are available in Naddaf & Czerny (2022) accounting only for the kinetic aspect of FRADO, i.e. the motion of matter (gas + dust/ gas only when dust evaporates) only due to the effect of the radiation and gravity. This does not include the local line broadening due to scattering or turbulence in the medium. We applied a phenomenological broadening term to the FRADO profiles to test if it explains the optical data of J0428−00. The broadening is given by the following expression:

$$f_\lambda = A \int f_{\lambda_0} \exp\left[-(\lambda - \lambda_0)^2 / 2\sigma^2\right] d\lambda_0. \quad (2)$$

Here, f_{λ_0} is a profile from Naddaf & Czerny (2022) and σ is the broadening at each wavelength. In its current setup, FRADO does not allow a continuous search across parameter space of mass, Eddington ratio, metallicity, and viewing angle for the least squares fitting. FRADO profiles are calculated on a coarse grid with black hole mass $\log(M_{\rm BH})$ = [6,7,8,9], inclination $\theta_{\rm i}$ = [15°,30°,45°], metallicity Z = [1.0,5.0], and accretion rate relative to Eddington or Eddington ratio $\lambda_{\rm Edd}$ of [0.01,0.1,1.0] (Naddaf & Czerny 2022). We tried fitting both Hβ and Hα with those FRADO models that yield double-peaked lines profiles with velocity widths comparable to that observed. The best-fit model profile in the pre-calculated grid from (Naddaf & Czerny 2022) is the one where $\lambda_{\rm Edd} = 0.01$, $M_{\rm BH} = 10^7 M_\odot$, an inclination of 15°, and $Z = 5$ (Appendix D). In the fits, σ and the central wavelength of the lines were kept free. We tested the model for the two cases: (A) a single FRADO and (B) a FRADO + Gaussian. The quantity, $p_{\rm BA}$, for these two cases are defined as $p_{\rm BA} = \exp[(\mathrm{AIC_B} - \mathrm{AIC_A})/2]$ similarly as the diskline model 7.4. For Hα, similar to the diskline fits, a single FRADO model is not adequate to explain the data (Fig. D.1a). The addition of a broad Gaussian component improves the fit (Fig. D.1b) as $p_{\rm BA} = 10^{-293.66}$. However, for the H$\beta$ line the profile was not well replicated in any case, as the broad Gaussian dominated the fit and the double-peaked profile from FRADO was too weak to fit the observed double horn profile (Appendix D). We do not claim that this particular FRADO profile is the best in terms of the best physical representation of the system. The values of $M_{\rm BH}$ and $\lambda_{\rm Edd}$ in this best-fit profile are not consistent with the estimates of the bolometric luminosity (Section 8.1). Other double-peaked FRADO profiles involving a black hole mass of $10^8 M_\odot$, $\lambda_{\rm Edd} = 0.01$, and $Z = 1$ exhibit line profiles with widths qualitatively similar to that observed. However, the line widths of FRADO are highly sensitive to the viewing angle. Thus, for the parameters corresponding to a $\sim 10^8 M_\odot$ black hole, the FWHM of the Hα line corresponding to $\theta_{\rm i} = 15°$ is narrow (∼5300 km s^{-1}) and the width of the line with a 30° inclination is broad (∼9300 km s^{-1}) compared to the observed profile (∼7300 km s^{-1}). Thus, there might exist some intermediate value of inclination, $15° < \theta_{\rm i} < 30°$ (consistent with the diskline model) for these values of $M_{\rm BH}$, $\lambda_{\rm Edd}$, and Z that could fit the observed profile. We discuss the implications for the FRADO fit in Section 8.5.

8. Discussions

8.1. Summary of the observed features of J0428−00

Our multiwavelength campaign tracked J0428−00 as it underwent rapid flaring in the X-ray, UV, optical, and infrared wavebands. The flaring is likely associated with a changing-look transition from type 1.9 to type 1, with the appearance of broad Hβ at some point between 2005 to 2020. We initiated a multiwavelength follow-up campaign to track the evolution of the source over three years (Fig. 4 and 7). We found in all observations that the X-ray spectrum is lacking the soft-excess component, visible in most Seyferts, and is fit adequately by a single component power law with a photon index typical for Seyferts (Section 8.6). The continuum in the optical spectrum evolves throughout the monitoring, with the blue power law continuum decreasing gradually as the main flare fades. The broad Hα and Hβ emission line fluxes evolve with time and track the long-term X-ray and optical continuum (Fig. 7). These line profiles are double-peaked and show apparent change in profile shape, with modest variations in the relative strengths of the red and blue peaks. The long-term optical continuum light curves do not exhibit the qualitative fast rise and slow decay typically seen in tidal disruption events (Section 4). Additionally, J0428−00 does not have the emission lines observed in the optical spectra of many TDEs (e.g., the broad He II line, the Bowen fluorescence lines, e.g. Gezari 2021). We discuss the implications of these observations in the following subsections.

8.2. Current and historical AGN activity in J0428−00

Throughout our three-year monitoring period, we find that the continuum evolved from having a strong blue component to a mostly galaxy-dominated spectrum from late 2020 to 2023 (Fig. 4). The reduction in AGN continuum emission indicates a decrease in accretion onto the central black hole.

We calculate the bolometric luminosity ($L_{\rm bol}$) during the flare from the Keck spectrum (MJD 58871) and the first LDT spectrum (MJD 58905). From the power-law fit, we estimate the continuum quasar flux contribution (f_λ) at $\lambda = 5100$ Å and subsequently $\lambda L_{5100} \equiv 4\pi D_{\rm L}^2 (1+z) f_{5100} \lambda$. Using the value of λL_{5100} and the expression from Runnoe et al. (2012), $\log L_{\rm bol} = 4.89 + 0.91 \times \log(\lambda L_{5100})$, we can calculate $L_{\rm bol}$.

From the Keck and the first LDT spectrum, we estimate the bolometric luminosity near the optical peak (around ∼ MJD 58900) to be $L_{\rm bol} \sim 2$–4×10^{44} erg s^{-1}. The estimates of $L_{\rm bol}$ from the optical-X-ray spectral index ($\alpha_{\rm OX}$; Lusso et al. 2010) and the model X-ray flux in the 2.0–10.0 keV band (Duras et al. 2020) around the same time were found to be consistent with

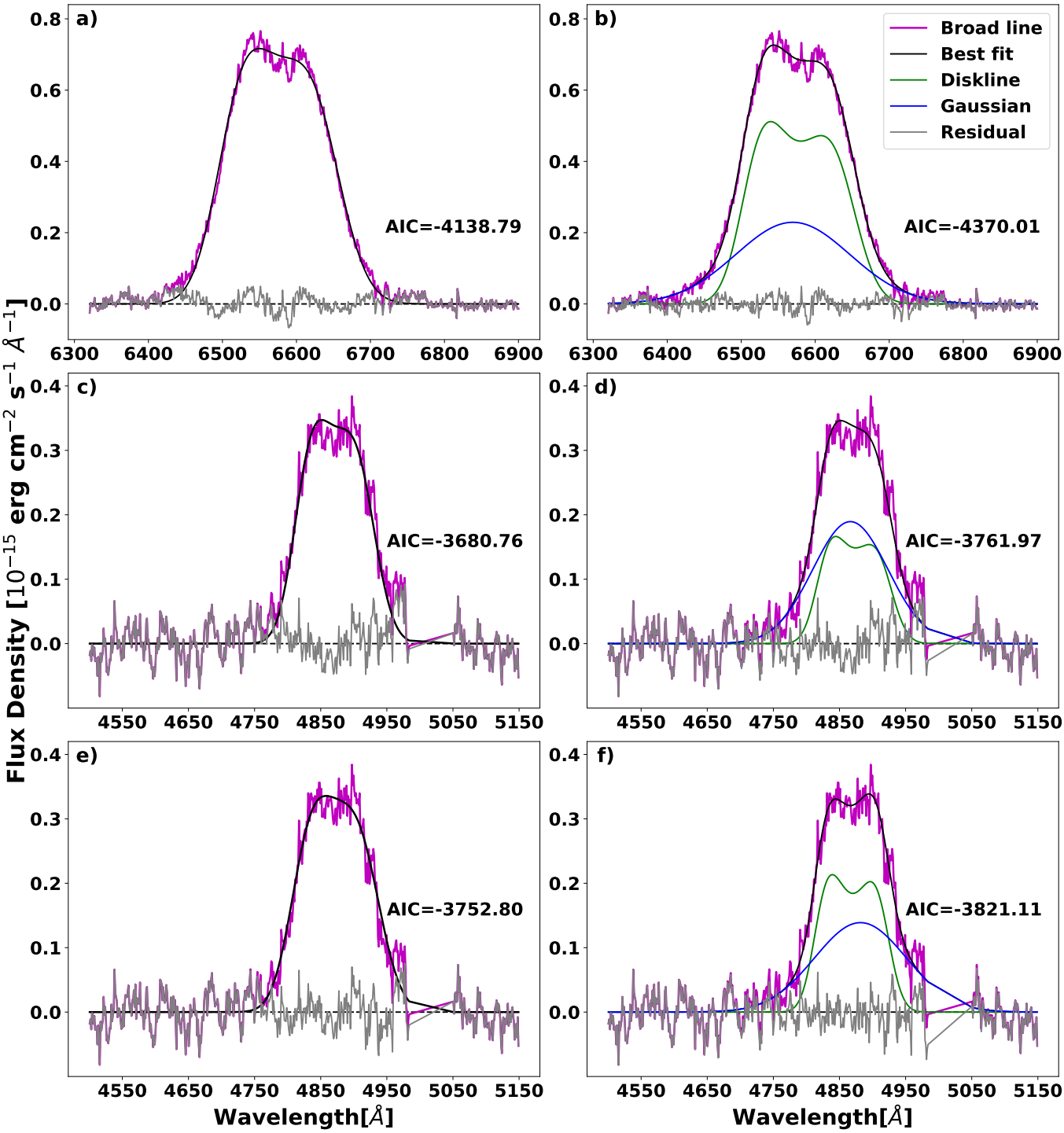

Fig. 6. Diskline model fits to the broad Hα and Hβ emission line profiles as described in Section 7.4. (a) A single diskline best fit to the Hα broad emission line. The residuals exhibit strong systematic variations in the ~6450 to 6700 Å wavelength range. (b) A diskline + broad Gaussian best fit to the broad Hα emission lines results in an overall improvement in the residuals. (c) Diskline best fit to the Hβ profile assuming the same morphological parameters as for the Hα line. (d) Same as (b), but for Hβ with the parameters of the Gaussian linked to the Hα parameters as described in Section 7.4. Both (c) and (d) show systematic residuals. (e) Diskline-only best fit for Hβ, with parameters independent of those for the Hα fit. (f) Diskline + Gaussian best fit to Hβ with parameters independent of those for the Hα. The Hα and Hβ profiles are broadly explained better by the combination of a diskline and a Gaussian compared to only a diskline.

that obtained from optical fitting, around ~4.0–5.5×10^{44} erg s^{-1} (Section 8.8). The optical spectra do not exhibit a reliably strong power-law component in the later phases of the observing campaign, precluding a reliable estimate of λL_{5100} (subsequently $L_{\rm bol}$). Thus based on the estimates of $\alpha_{\rm OX}$ and X-ray luminosity, we estimate that $L_{\rm bol}$ dropped by a factor of $\gtrsim$10 from the peak of the 2020 flare to ~3×10^{43} erg s^{-1} by three years after the flare.

The integrated flux of the [O III]λ5007 emission line can be used to estimate the historical luminosity of the source (Stern

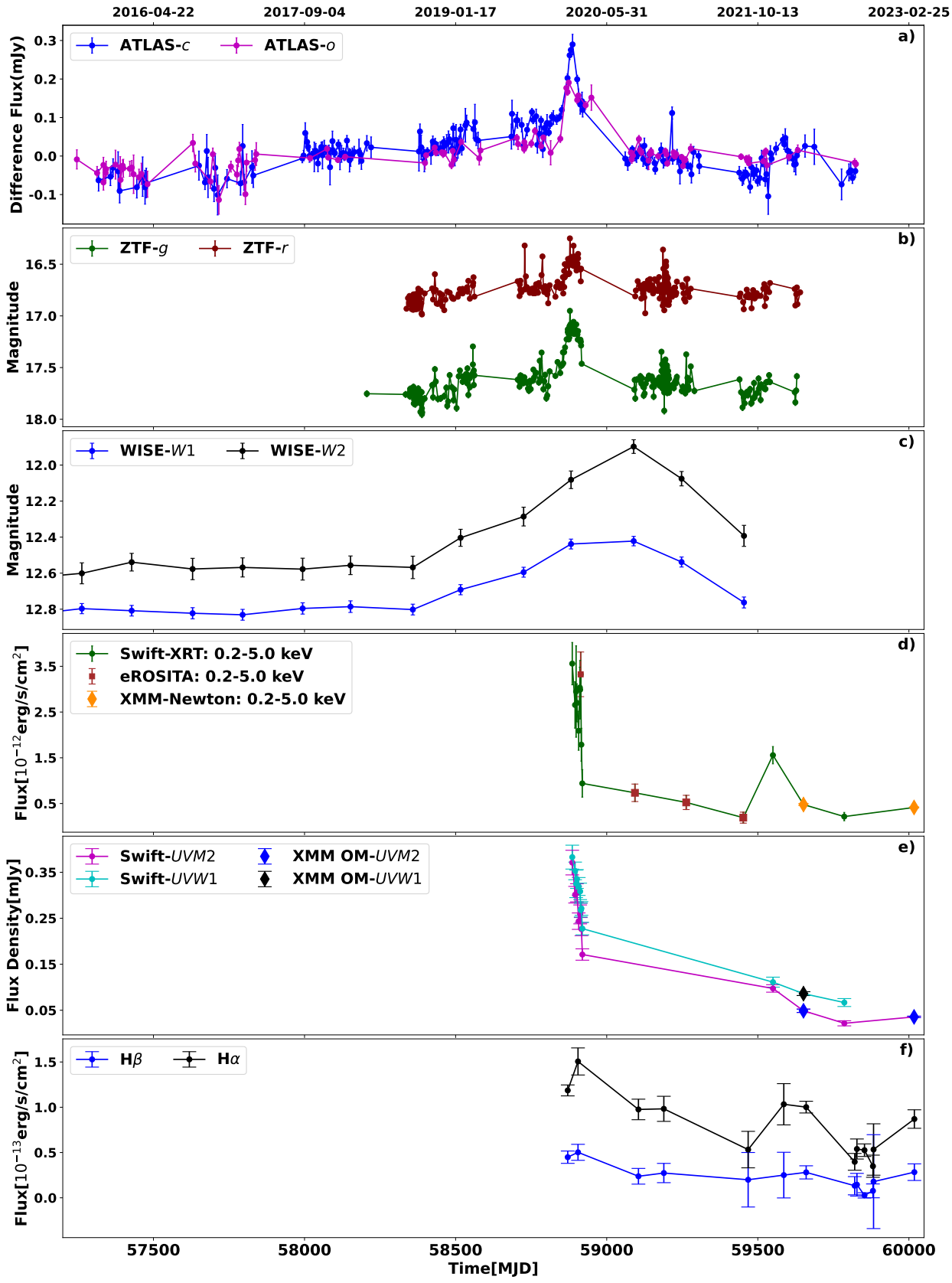

Fig. 7. Optical, UV, and X-ray light curves for the entire period of our monitoring. From the top to bottom panel are plotted: a) the *c*- and *o*-band difference light curves from ATLAS, b) the *g*- and *r*-band difference light curves from ZTF, c) the *W*1 and *W*2-bands from *WISE*, the X-ray light curves from *Swift*, d) *XMM-Newton* and eROSITA, e) the UV light curves from *Swift*-UVOT and *XMM-Newton* optical monitor, f) the Hβ and Hα light curves of the integrated line-flux from optical fitting. Two distinct peaks can be seen in the light curves for X-ray, the ATLAS, the emission line and the UV. In sub-plots b), d), and e), there are some data points for which the error bars are smaller than the data point marker.

Table 6. Summary of continuum and emission line fits

Date	Telescope	Overall continuum model		Line model		
(MJD)		Model	power law index (α)	linear continuum	$p_{21,\mathrm{H}\beta}$	$p_{21,\mathrm{H}\alpha}$
58871	Keck	M1	2.76	NO	$10^{-23.65}$	$10^{-309.76}$
58905	LDT	M1	3.96	YES	$10^{-22.35}$	$10^{-18.99}$
59105	LDT	M1	1.44	YES	$10^{-2.86}$	$10^{-21.82}$
59189	LDT	M1	1.23	YES	$10^{-8.43}$	$10^{-8.23}$
59468	SAAO	M2	–	YES	–	$10^{-12.99}$
59586	SALT	M2	–	YES	–	$10^{-97.55}$
59660	FORS2	M2	–	YES	$10^{-1.77}$	$10^{-9.36}$
59821	NOT	M2	–	YES	$10^{0.19}$	$10^{-13.77}$
59828	DBSP	M2	–	YES	–	$10^{-26.97}$
59853	TNG	M2	–	YES	–	$10^{-20.36}$
59881	SALT-2	M2	–	YES	$10^{-25.44}$	$10^{-9.19}$
59883	SALT-3	M2	–	YES	–	$10^{-5.10}$
60018	FORS2	M2	–	YES	$10^{-9.47}$	$10^{-28.91}$

Notes. The model M1 denotes a power-law continuum + host-galaxy emission, while M2 denotes just the host-galaxy. Column 5 notes whether a local linear continuum component is used to account for local deformation in either of the Hβ or Hα regions (Section 7, Tables 2 and B.1). The $p_{21} = \exp[(\mathrm{AIC}_2 - \mathrm{AIC}_1)/2]$ values indicate the preference for a double-peaked profile over the single peaked profile. In all cases, the Hα emission line is fit better with a double Gaussian profile than a single Gaussian as $p_{21,\mathrm{H}\alpha} < 10^{-2}$. The H$\beta$ line profiles are fit with a double- or single-Gaussian model depending on the data quality. Most cases with better data quality were adequate to distinguish models. In those cases, the double Gaussian profiles return a better fit with $p_{21,\mathrm{H}\beta} < 10^{-2}$, except for the NOT spectrum. Where S/N is too low, such that models are not distinguishable (SAAO, the first SALT spectrum, DBSP, TNG, and the third SALT spectrum), we do not fit a double Gaussian profile, thus the $p_{21,\mathrm{H}\beta}$ calculation in those cases are not applicable (marked by '–' in the $p_{21,\mathrm{H}\beta}$ column of the table).

Table 7. Parameters of Diskline fits to the Keck spectrum

Line	Model	R_{in}	R_{out}	Inclination (θ_{i})	σ_0	Gaussian component	
		(R_{g})	(R_{g})	(°)		$c\frac{\Delta\lambda}{\lambda}$(km s^{-1})	$c\frac{\sigma_\lambda}{\lambda}$(km s^{-1})
Hα	Diskline	507 ± 22	1256 ± 107	15.3 ± 0.14	$(4.96 \pm 0.06) \times 10^{-3}$	–	–
Hα	Diskline + Gauss	468 ± 16	1202 ± 95	14.3 ± 0.2	$(3.88 \pm 0.16) \times 10^{-3}$	315 ± 79	3513 ± 183
Hβ	Diskline	447 ± 74	$1010^{+8}_{-0^*}$	15.2 ± 0.4	$(5.85 \pm 0.22) \times 10^{-3}$	–	–
Hβ	Diskline + Gauss	$950^{+50^\dagger}_{-900^*}$	$1010^{+3500}_{-0^*}$	17.4 ± 1.23	$(3.80 \pm 0.49) \times 10^{-3}$	1253 ± 312	4261 ± 450

Notes. We report the parameter values of the diskline fits to the Hβ and Hα broad emission lines. Here we report the case when Hβ fit is independent of the parameters returned by the Hα fits. The inner radius R_{in} and R_{out} are in units of gravitational radius (R_{g}). The inclination angle (θ_{i}) is in degrees. The parameter σ_0 is the broadening parameter. The displacement of the peak ($c\frac{\Delta\lambda}{\lambda}$) with respect to the rest wavelength and the width of the additional Gaussian are each reported in km s^{-1}. The best-fitting geometrical parameters from Hα are roughly consistent with those obtained by Ward et al. (2023) using a similar diskline model. The error bounds marked with † and ∗ correspond to set upper and lower bounds (Section 7.4) respectively. The R_{out} values for Hβ fits peg at the respective lower limit. The R_{in} value in the diskline + Gaussian fit is practically unconstrained in the parameter bound set for the fitting.

& Laor 2012). Using the integrated flux from the Keck spectrum, $F_{[\mathrm{O\,III}]} \sim 8.77 \times 10^{-15}$ erg s^{-1} cm^{-2} (Table B.2), we obtain a historical bolometric luminosity of $L_{\mathrm{bol,hist}} \sim 4^{+12}_{-3} \times 10^{43}$ erg s^{-1}. The uncertainty in $L_{\mathrm{bol,hist}}$ originating from the expression (details are in Stern & Laor 2012) is quite large (∼100%). Nevertheless, these estimates indicate that the bolometric luminosity (L_{bol}) increased by factors of ∼2–40 above the historical rate during the CLAGN event of 2020.

We further diagnose the AGN activity in J0428−00 via Baldwin, Phillips, and Terlevich (BPT) diagrams (Baldwin et al. 1981b). For calculating the BPT diagrams, we use the best-fitting Gaussian parameters to the narrow lines to estimate the integrated line fluxes (Appendix E). We plot the flux ratios for both [O III]λ5007/Hβ versus [N II]λ6584/Hα and [O III]λ5007/Hβ versus [S II]λ6717/Hα along with classification curves from Schawinski et al. (2007), Kewley et al. (2001), and Kauffmann et al. (2003) in Fig. 8. We describe the details of the methodology in Appendix E. For most of the observations after the flare, the [O III]λ5007/Hβ line flux ratio is high enough to position the object in the 'AGN region' of the BPT diagram (the region above the solid blue curve in Fig. 8).

All these trends indicate that the nucleus of J0428−00 has been in a prolonged (∼10^3–10^4 years) persistently accreting state.

8.3. Characterization of the transient

The slow rise in the optical continuum preceding the main flare feature is not typical for a TDE. Additionally, we do not find distinct evidence of a slow decay seen usually in the light curves of TDEs (Section 4). The power law decay indices fit to the 'slow decay' light curve segment lie between ∼0.05 and ∼0.2, arguing against a TDE. However, a few TDE events have displayed relatively flat light curves with prolonged decays; in the case of 3XMM J150052.0+015452, for instance, the decay lasted over ∼10 years (Lin et al. 2022). We can also consider the emission lines: A variable He II broad emission line and/or Bowen fluorescence features have been found in a number of TDEs (Nicholl

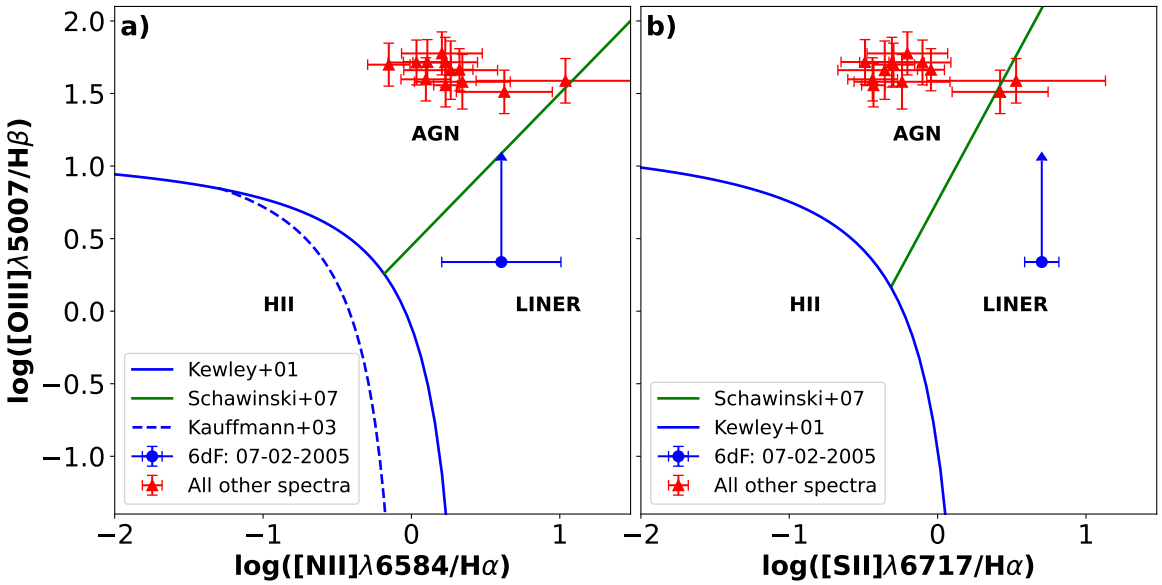

Fig. 8. The BPT diagrams (Baldwin et al. 1981a), with estimates for J0428−00. The line ratios (a) [N II]λ6583/Hα and (b) [S II]λ6717/Hα are plotted against the line ratio [O III]λ5007/Hβ. The classification curves are from Kewley et al. (2001) Kauffmann et al. (2003) and Schawinski et al. (2007). Most points for J0428−00 have clustered above the (Kewley et al. 2001) curve in the 'AGN' region of the diagram. The narrow line emission region is located at kpc scales and, hence is not expected to vary in timescales of $\sim 10^3$ years. Thus, the BPT diagram is consistent with persistent AGN activity.

et al. 2020; Gezari 2021). J0428−00 does not exhibit He II emission and Bowen fluorescence emission lines in any optical spectra taken during the period of our monitoring.

The observations instead support AGN-like accretion: A persistent broad Hα line was seen in both the archival 6dF spectra as well as during the recent campaign, indicative of AGN activity both in 2005 and during 2020–2023. Additionally, the narrow-line BPT diagnostics (Section 8.2) classify this source as an AGN.

The X-ray spectra of J0428−00 are Seyfert-like with a photon index of ∼1.9, and we do not observe any major systematic variation in photon index. This behavior is inconsistent with a thermal TDE, which typically exhibits a much softer X-ray spectrum with a typical photon index steeper than 3 (e.g. Gezari 2021). As a caveat, though, the photon index distribution of TDEs reported in Auchettl et al. (2018) shows that there exists a non-zero probability (∼0.3) for the X-ray spectrum of a TDE to have a hard photon index.

The ratio of the luminosity of the [O III] line to the hard X-ray luminosity, $L_{0.3-20\ \mathrm{keV}}/L_{[\mathrm{O\,III}]}$, is also an indicator of persistent AGN activity over the last $\sim 10^3$–10^4 years (Heckman et al. 2005). From a sample study of local AGNs, this ratio was found to be around $\sim 10^2$, while for TDEs, this ratio was reported to be $\sim 10^4$ (Sazonov et al. 2021). Physically, the discrepancy in these ratios arises from the fact that a persistently accreting Seyfert has a relatively higher [O III] luminosity. This is consistent with the fact that the [O III] line-emitting-region is continuously illuminated by persistent accretion over at least 10^3 to 10^4 years. In contrast, for a transient TDE, the increase in the X-ray luminosity is expected to be time-localized and transient relative to the time needed to illuminate the kiloparsec scale NLR. In the case, where nuclear activity is minimal and sustained only by occasional TDEs over a timescale of 10^3–10^4 years, the corresponding time-averaged amount of observed [O III] emission will be low.

For J0428−00, we estimate the ratio of $L_{0.2-6.0\ \mathrm{keV}}/L_{[\mathrm{O\,III}]}$ following Sazonov et al. (2021) both near the flare peak, at the highest X-ray luminosity recorded, and at a point ∼ three years after the peak. For the former case, the ratio is $\sim 10^{2.8}$, and for the latter case, this ratio is $\sim 10^{1.9}$. The value roughly three years after the peak is consistent with the expectations from AGN-type accretion. The high value of the ratio near the peak can be interpreted as being due to a rapid, temporary increase in X-ray flux during the outburst while the [O III] line flux remained non-variable. Thus, the value of the $L_{\mathrm{X-ray}}/L_{[\mathrm{OIII}]}$ ratio being low (10^2) during the baseline state but higher ($\sim 10^{2.8}$) during the X-ray flaring is consistent with extreme variability in a persistently-accreting AGN.

To summarize, the observed activity in J0428−00 seems more associated with accretion in an active galaxy than with a TDE. Below we consider possible cases for the flare in the context of AGN accretion.

8.4. Estimation of black hole mass and Eddington ratio

We calculate the black hole mass using three different methods: the [O III]λ5007 narrow line width, the K-band magnitude, and the combination of optical broad line width and the radius-luminosity relation for the BLR. All measures of line widths are are in the AGN rest frame. We describe the methods below:

i. **Narrow line [O III]λ5007 width:** The dispersion of stellar velocities (σ_*) scales with black hole mass (Nelson 2000). In an AGN the standard deviation of the narrow component of [O III] line (σ_{OIII}) can be used as a proxy for the velocity dispersion σ_* (Xiao et al. 2011). We thus use the standard deviation of the narrow [O III]λ5007 line, $\sigma_{\mathrm{OIII}} = 109 \pm 2$ km s^{-1} from the Keck dataset to determine the mass of the black hole using the relation from Tundo et al. (2007): $\log M_8 = 8.21 + 3.83 \log(\sigma_*/[200\ \mathrm{km\ s^{-1}}])$. We determine a mass of $\log M_{\mathrm{BH}}/M_\odot = 7.21 \pm 0.01$. We however note the fact that this method is designed for low-mass supermassive black holes such that the gravitational effect of the black hole does not significantly impact the width of the OIII lines.

ii. **K-band Magnitude:** Black hole mass has been found to scale with bulge stellar luminosity. The photometric observation taken in 2003 as a part of the 2MASS survey reported a K-band magnitude around $K_s \simeq 12.67$. Using the magnitude from NED reported by the Two Micron All Sky Survey Team as a proxy for bulge mass and the expression from Graham (2007), $\log(M_{BH}/M_\odot) = -0.37(M_K + 24) + 8.29$, we estimate $M_{BH} = 4.0 \times 10^8 M_\odot$. However, the AGN might have a significant contribution in addition to the host galaxy in the K_s band. Additionally, the aperture includes the entire galaxy. Hence we consider this magnitude value as a lower limit (upper limit on K_s band flux), and we treat the resulting black hole mass value as an upper limit.

iii. **BLR Radius-Luminosity-broad line FWHM relations:** In the Keck spectrum, for the estimation of FWHM for both the Hβ and Hα broad lines we consider the entire extent of the best fitting double Gaussian profile. We estimate a FWHM of ~8140 km s^{-1} for Hβ and ~7350 km s^{-1} for Hα. We use the following expressions from Vestergaard & Peterson (2006) and Greene et al. (2010) to calculate the black hole mass from the Hβ and Hα broad lines respectively:

$$M_{BH} = 10^{6.91} \left[\frac{\mathrm{FWHM(H}\beta)}{1000 \text{ km s}^{-1}}\right]^2 \left[\frac{\lambda L_{5100}}{10^{44} \text{ erg s}^{-1}}\right]^{0.5} M_\odot \quad (3)$$

and

$$M_{BH} = 9.7 \times 10^6 \left[\frac{\mathrm{FWHM(H}\alpha)}{1000 \text{ km s}^{-1}}\right]^{2.06} \left[\frac{\lambda L_{5100}}{10^{44} \text{ erg s}^{-1}}\right]^{0.519} M_\odot. \quad (4)$$

Using the Hβ and Hα broad emission lines we get black hole mass estimates of $M_{BH} = 3.28{\times}10^8 M_\odot$ and $3.54{\times}10^8 M_\odot$, respectively. The estimates are consistent with the upper limit set by the K-band magnitude estimates. Using the R_{BLR} vs λf_λ expression from Bentz et al. (2009) we obtain $R_{BLR} = 20$ light-days. This value of R_{BLR} is used directly in the black hole mass estimate from the Bentz et al. (2009) scaling relation:

$$M_{BH} = \frac{f_{vir} R_{BLR} \mathrm{FWHM}^2_{H\beta}}{G}. \quad (5)$$

Assuming a virial factor of 1.5, we obtain a black hole mass of $4 \times 10^8 M_\odot$.

Thus, from the above estimates we conclude that the black hole mass for J0428−00 is in the range $[10^7, 4 \times 10^8]$. However, as a caveat we mention that the Keck observation was taken near the peak of the transient flare. Thus, the application of the standard radius-luminosity relation, which is calibrated to the persistent phases of accretion, can result in systematic deviations.

In the previous section we calculated, 'historical' luminosity before the flare, the bolometric luminosity near the main optical flare peak, and three years after the main flare. We use those values to estimate the Eddington ratio ($\lambda_{edd} = L_{bol}/L_{edd}$) of the source. (a) For a black hole mass of $\sim 10^7$, λ_{edd} corresponding to the historical value of Eddington ratio is 0.03; the value near the optical peak (MJD 58900) is ~0.35–0.45, and the value three years after the peak is ~0.03. (b) For a black hole mass of $\sim 4 \times 10^8 M_\odot$, the value of λ_{Edd} at each of the above mentioned epochs is ~0.0008, ~0.009, and ~0.0007 respectively.

8.5. Broad emission lines and emitter geometry

Prior to the 2020 flare, J0428−00's optical spectrum, as observed during the 6dF survey, exhibited a double peaked Hα emission line, but no Hβ emission. During and after the 2020 flare, both Hβ and Hα emission lines in J0428−00 were visible and were double-peaked. We performed phenomenological modeling of the broad lines using Gaussian profiles for all spectra. Additionally, we explored more physically motivated models, namely diskline (Section 7.4, Chen & Halpern 1989; Chen et al. 1989) and FRADO (Section 7.5, Naddaf et al. 2021; Naddaf & Czerny 2022) when modeling only the (best quality) Keck spectrum. In this subsection, we discuss the physical implications of the results of the broad-line fitting.

From the phenomenological Gaussian fits (Section 7.3), we find that for most line profiles, a double Gaussian profile fits the data best. We evaluate the integrated broad-line flux for each spectrum to construct emission line light curves. The emission line light curves exhibit a steady decrease in line flux from around MJD 58900 until the second, smaller peak appears, between MJD 59500 and MJD 60000 (Fig. 7f). This behavior is consistent with the trend exhibited by the optical and the X-ray light curves.The similarity between continuum and line variability indicates that the broad line flux is a response to the varying ionizing continuum from the central engine.

We fit the Keck spectrum with a diskline model. We found that a diskline model fits the data reasonably well. However, the addition of a broad Gaussian component improves the fit (Fig. 6(b),(d),(f)). The Gaussian profiles for both the Hα and Hβ fits are substantially broad, with values of FWHM of 7000–9000 km s^{-1}, and they are redshifted: ~300 km s^{-1} for Hα and ~1200 km s^{-1} for Hβ (Table 7). These broad Gaussian components might suggest the presence of a wind type component in addition to a diskline, as BLR emission can potentially have contributions from both disk-type and wind-type components (Elitzur et al. 2014; Elitzur & Ho 2009). We also take into account the possibility that the Gaussian might be necessary because the diskline model is too simple to fully capture the complexity of the line profiles. However, for both cases, we can conclude that the broad line emitter is consistent with a rotating disk-type geometry extending from a few times 100 R_g to ~1000 R_g (Table 7) consistent with (Ward et al. 2023). This contributes a significant amount (~50–60%) to the total flux of the broad Balmer emission profiles.

For the FRADO model, a broad FRADO profile (Section 7.5) associated with black hole mass $M_{BH} = 10^7 M_\odot$, accretion rate relative to Eddington $\lambda_{Edd} = 0.01$ and abundance $Z = 5$, plus a broad Gaussian, can replicate a total model closest to the observed Balmer profiles. The accretion rate ($\lambda_{Edd} = 0.01$) and the black hole mass ($M_{BH} = 10^7 M_\odot$), yields a factor of ~10 mismatch with the theoretical values of the bolometric luminosity inferred from the FRADO model ($\sim 10^{43}$ ergs s^{-1}) with that observed during the peak ($\sim 4{\times}10^{44}$ ergs s^{-1}). Overall, our FRADO fits do not provide a precise determination of the properties of the broad line region, given that the model is still under development, and given the broad uncertainties regarding M_{BH} and λ_{Edd}. However, we argue in §7.5 that the FRADO model can potentially create profiles for $M_{BH} \sim 10^8 M_\odot$ that are qualitatively consistent with the width and shape of the observed Balmer profiles for values of inclination between 15° and 30°, which is consistent with the values obtained from the diskline fitting. Additionally, the vertical motion coupled with the circular motion of the gas for the proposed parameters of FRADO can potentially fit the profile, which would result in a rather flattened disk-type

structure with an aspect ratio: $z/R \lesssim 0.1$ (Figure 2 in Naddaf & Czerny 2022), which is qualitatively consistent with a diskline. Thus, both the diskline and FRADO fits indicate that the broad lines arise from a distribution of matter that is mostly undergoing a rotational motion.

We find that the profiles of the Hβ and Hα broad emission lines exhibit some modest variability in the relative heights of the red and blue peaks (Fig. 4 and Appendix B). Double-peaked profile with shapes different from typical diskline– e.g. red wing stronger than blue wing–has been observed in multiple sources (e.g. Schimoia et al. 2012) and (e.g. Storchi-Bergmann et al. 2017) These shapes have been interpreted by adopting a model where line-emitting matter is thought to be disk-like and its emissivity has both radial and azimuthal dependence, indicating the absence of axial symmetry. Schimoia et al. (2012) modeled the double-peaked line profile variability in NGC 1097 by adopting a time variable disk emissivity profile. In J0428−00, based on the similarity in line profiles, it is possible that a similar process can drive the variation in the line profiles as mentioned in Ward et al. (2023).

The broad Hα emission line is persistent in all stages. Hβ appeared during the 2020 transient event but has been slowly fading afterward. Both the broad lines exhibit a double-peaked profile. A significant number of intermediate type Seyferts exhibit double peaked broad lines (e.g. Elitzur et al. 2014). The type 1.9 stages of J0428−00 are consistent with such observations. We established via the X-ray spectrum that a varying level of obscuration is not connected to the transient event in J0428−00. Hence, it is unlikely that the appearance and the relative strengthening or weakening of the broad Hβ line (affecting the Balmer decrement) is due to the presence or absence of an external source of obscuration, for example, obscuration by a dusty torus cloud. J0428−00 in part resembles the transition in SDSS J015957.64+003310.5, a changing-look quasar (LaMassa et al. 2015) wherein a disappearance of only the Hβ broad line is reported, with no change in obscuration.

A theoretical study by Wu et al. (2023) has shown that such steep relative change in the Balmer lines (namely the Balmer decrement) can indeed be triggered due to a change in accretion rate affecting the strength of the ionizing flux (Q). A change in ionizing flux affects the responsivity of the Hβ emission line more than the Hα line due to the Q-dependent opacity in the emitter (details are given in Section 5 of Wu et al. 2023).

To summarize, a persistent (see arguments in Section 8.8) and flattened disk-type broad line emitter which existed in all stages of the source received more ionizing flux due to the transient event of early 2020, resulting in the appearance of a double-peaked broad Hβ emission line alongside the already-existing double-peaked Hα broad line.

8.6. Origin of the X-ray continuum

The photon index measured from our X-ray spectral fitting for J0428−00 is relatively flat, $\Gamma \sim 1.9$ (Section 5 and Table 3). This is similar to the values observed for normal (non-blazar) Seyferts where Comptonization of seed photons in a hot corona (Haardt & Maraschi 1991, 1993) is the most likely mechanism for X-ray production. We find no evidence for significant X-ray spectral variability over three years despite strong flux variability. It is therefore likely that the coronal parameters such as optical depth or geometry are stable over time as the flare decays. The spectra do not show any obscuration above the Galactic extinction level and consequently no evidence of changing obscuration.

A soft X-ray excess, manifested as a very steep power-law-like emission below ∼1–2 keV is near-ubiquitous in normal Seyferts (Halpern 1984; Turner & Pounds 1989). The absence of a soft-excess in the X-ray spectra of J0428−00 is puzzling. Its origin in normal Seyferts is debated (Sobolewska & Done 2007). The leading models are thermal Comptonization from a warm ($k_B T_e \sim 1$ keV) optically thick ($\tau \gtrsim 10$) medium (Mehdipour et al. 2011; Done et al. 2012; Petrucci et al. 2018) or blurred reflection from the innermost, ionized accretion disk (Crummy et al. 2006; García et al. 2013). In the former case, absence of the soft X-ray excess might simply mean that the warm medium is either radiatively weak in the X-rays (Section 8.7) or completely missing in J0428−00. In the latter case, a blurred reflection component might be absent due to a potentially truncated or radiatively-inefficient inner accretion disk as seen by, or a disk that is not efficiently illuminated by X-ray continuum photons.

8.7. Characteristics of the broad-band continuum

The broadband SED fitting of J0428−00 (Section 6) using the AGNSED model (Kubota & Done 2018) reveals that the SED, which is constructed from optical, UV, and X-ray spectral data, can be modeled successfully with a 'cold' disk and thermal Comptonization at all stages of the flare and decay. In addition, optical/UV and X-rays vary in concert. These findings are typical of non-blazar Seyferts where a thin accretion disk (Shakura & Sunyaev 1973) is thought to be the main contributor of the primary optical and partially the UV emission, with the X-rays generated via Comptonization of a fraction of the low-energy seed photons from the disk (Haardt & Maraschi 1991, 1993).

We performed the broad-band analysis assuming two different values of black hole masses, given that it is poorly constrained (Section 8.4). The emission components associated with a thin accretion disk and a hot corona are adequate to explain the entire broadband emission across all flux states of J0428−00 when we assume a black hole mass of $10^7 M_\odot$. However, when a black hole mass of $4 \times 10^8 M_\odot$ is assumed, the thin accretion disc and a hot corona failed to return a physical solution unless a warm Comptonization component was added (Section 6). The warm Comptonization component remained localized in the < 0.2 keV energy band. The results from broadband analyses thus support our finding (Section 8.6) that a warm Comptonizing corona is either absent in J0428−00 or if present, it is radiatively weak and with its spectrum not extending into the X-rays to manifest as the soft-excess.

8.8. Comparison to other AGNs and CLAGNs

We can compare the broadband spectral and variability properties of J0428−00 to those of normal Seyferts/quasars and CLAGNs. From the broad band spectral fit we estimate the values of $L_{2500\ \text{Å}}$ and $L_{2\ \text{keV}}$ to calculate the spectral index α_{OX} using the expression from Tananbaum et al. (1979) and Ruan et al. (2019):

$$\alpha_{\text{OX}} = -\frac{\log(\nu_{2500\text{Å}} L_{2500\text{Å}}) - \log(\nu_{2\text{keV}} L_{2\text{keV}})}{\log(\nu_{2500\text{Å}}) - \log(\nu_{2\text{keV}})} + 1 \quad (6)$$

The values of α_{OX} are calculated from the best-fitting AGNSED models and are found to be independent of the best-fitting model parameters. The values of α_{OX} vary from 1.4 to 1.1, averaging at ∼1.2, indicating that the value is rather static during our campaign. The scatter seen in α_{OX} is due to the short-term variability in the UV and especially the X-ray emission. These values of

α_{OX} are similar to those for X-ray-selected type-1 quasars at the same UV luminosity, as reported in Lusso et al. (2010).

The dependency of α_{OX} on Eddington ratio (λ_{edd}) in Lusso et al. (2010) and in Ruan et al. (2019) indicates a relation between properties of the global accretion flow structure and the spectral shape in both AGN/quasars and CLAGN. For CLAGN, Ruan et al. (2019) tracked the transitions of some selected CLAGN sources in the λ_{edd}–α_{OX} plane, with the implication that their transitions are analogous to that of state changes in accreting stellar-mass black hole binary systems, and associated with major changes in accretion disk structure. For J0428−00, however, we do not have a very strong constraint on the black hole mass. Hence the position of J0428−00 cannot be reliably constrained along the horizontal λ_{edd}-axis, and a straightforward conclusion on the accretion structure based solely on the α_{OX}–λ_{edd} diagram cannot be made.

However, arguments supporting a relatively stable accretion structure can be made based on observed timescales. The duration of the sharp flare in 2020 is only ∼80 days. The most relevant timescales associated with an outer thin disk, where optical emission originates, are the thermal, sound timescales, and viscous timescales (Section 8.9 for definition). At radii of hundreds of R_g, viscous timescales associated with a geometrically thin disk with mild viscosity (e.g., $H/R \sim 0.05$, $\alpha \sim 0.1$) are of order decades to millennia for the values of M_{BH} (Section 8.4 and 8.9) at play here (e.g. Treves et al. 1988). If the disk is geometrically thin, then it is unlikely that a new accretion flow structure could have formed via the accretion of new material solely in connection with the 2020 flare and/or the optical changing-look event. J0428−00 transitioned briefly into a type-1, and is currently reverting back to its previous type 1.9 state, with the broad Hβ weakening significantly by ∼2 years after the peak and the blue continuum weakening significantly within 1.5 years of the peak. This is unlike a systematic long-term accretion turn-on or shutdown. This notion is supported by the relatively stable and typical values of α_{OX} exhibited by the broadband spectrum of J0428−00 during both flare peak and its subsequent decay. The observations thus agree, with a short-lived temporary change in an existing accretion flow, which likely resulted in the multi-wavelength flare.

8.9. Transient variability in J0428−00: Possible origins for the flare

In this section, we discuss the temporal variability observed in J0428−00 in the context of accretion theory. As seen from the ATLAS difference light curves (Fig. 1), there is a slow rise lasting for about a few years until the 2020 flare, which starts to appear around ∼MJD 58810. The flux decays slowly after the 2020 flare over the next one year before the second, smaller flare appears, around MJD 59500. For the UV and the X-ray bands, we do not know the time for the occurrence of the main peak. However, after ∼MJD 58885, trends in optical, UV, and X-ray light curves are mostly of a decaying nature, and the light curves qualitatively are similar (Fig. 7d and 7e). The absence of observed UV and X-ray peaks does not allow us to infer any lags or leads between the X-ray, UV, and optical wavebands.

The dominant mechanism of X-ray production in radio-quiet Seyferts and quasars is upscattering of the UV and optical photons via Comptonization (Haardt & Maraschi 1993; Nandra et al. 2000) by thermal electrons in a hot corona. The general similarities in the optical/UV and X-ray light curves, as well as the X-ray photon index, are consistent with Compton upscattering, although our data sampling prevents any search for optical/UV-to-X-ray lags. Similarly, if there is any X-ray to optical/UV lag associated with thermal reprocessing in the disk (M^{c}Hardy et al. 2014) in addition to Comptonization, (e.g. Nandra et al. 2000), our data are not sensitive to it.

Stochastic variability in optical, UV, and X-ray on timescales from days to years has long been observed across Seyferts and blazars (e.g. Collier & Peterson 2001; Markowitz & Edelson 2004). The slow continuum flux rise preceding the 2020 flare is qualitatively consistent with such normal stochastic variability.

The relevant timescales associated with the variability in a black hole accretion flow at a given radius are the light-crossing, dynamic, thermal, and viscous timescales:

$$t_{lc} = \frac{R}{c} \tag{7a}$$

$$t_{dyn} \sim \sqrt{\frac{R^3}{GM_{BH}}} \tag{7b}$$

$$t_{th} \sim \frac{1}{\alpha} t_{dyn} \tag{7c}$$

$$t_{visc} \sim \left(\frac{H}{R}\right)^{-2} t_{th}. \tag{7d}$$

For a geometrically thin disk, the viscous timescale (Equation 7d) associated with change in the global accretion flow near the radii of optical continuum emission is in many cases quite long (e.g., centuries). It is thus incompatible with the short-term variability (days–weeks–months) seen in typical AGNs and CLAGNs, and incompatible with the ∼80 day-flare in J0428−00 in 2020.

The observed variability in J0428−00, in particular the sharp 2020 flare, can be better explained by disk instability models, such as the toy radiation pressure instability model developed by Śniegowska et al. (2020) and Śniegowska et al. (2023). In this model, an unstable annular region of the disk exists between a radiatively-inefficient inner region and the thin outer disk. When gas pressure exceeds radiation pressure, an instability builds at timescales shorter than the viscous timescale of the thin disk ($t_{SG} \sim t_{visc}\frac{\Delta r}{r}$). This is similar to a Lightman-Eardley instability, which is also triggered when the radiation pressure exceeds gas pressure at a given annulus. Such an instability builds up with a timescale of $t_{LE} \sim \left(\frac{\Delta r}{r}\right)^2 t_{visc}$ (Lightman & Eardley 1974) which is shorter than the viscous timescale (Kato et al. 2008). With $\frac{\Delta r}{r} > H/r \sim 0.05$, we have $0.05 \lesssim \frac{\Delta r}{r} \lesssim 1.0$ (see Lightman & Eardley 1974). Thus, the associated timescale of a LE instability is $0.0025 t_{visc} < t_{LE} < t_{visc}$. Thus, both the instability models described above can encompass a broad range of timescales shorter than t_{visc} of the thin disk (Fig. 3 and 4 of Śniegowska et al. 2020) and the flare timescale falls within the timescales that can be generated by this method .

The instability leads to the heating of the inner region of the disk, and the disk becomes geometrically thicker as a heat wave propagates from the inner disk towards outer radii. The local accretion rate drastically increases, leading to a multi-wavelength luminosity response which is dependent on the local temperature of the disk. This heating occurs on the thermal timescale. For a black hole of mass of $\sim 10^8 M_\odot$ and assuming a viscosity parameter of $\alpha = 0.1$, at a given radius of 50 R_g, we find that the thermal timescale is, t_{th} ∼60 days. The observed rise time of the flare is ∼40 days, which is consistent with the calculated value. Meanwhile, the UV seed photons both for X-ray production via Comptonization and for photoionized emission line production are enhanced. Thus, the broad line and the X-ray emitter

respond to the ionizing photons generated due to this variability at a timescale of $t_{\rm lc}$ but corresponding to different radii.

When the flare is peaking, the disk is geometrically thick, and the viscous timescale tends towards the thermal timescale. The observed duration of flaring is of order a few tens of days (Section 4) which is consistent with both $t_{\rm th}$ and the instability timescales ($t_{\rm SG}$ or $t_{\rm LE}$) when we assume $\Delta r/r \sim 0.1-0.01$. Later, as cooling becomes greater than heating and the flare subsequently fades, the cooling is dominated by the thermal timescale ($t_{\rm th}$ ~60 days).

Overall, a radiation-pressure driven instability can be a plausible explanation for the flare; we also note that the light curves calculated from the simulations of Śniegowska et al. (2020) and Śniegowska et al. (2023) resemble the observed light curves in J0428−00 in this manner.

8.10. IR variability

We find an evolution in $W1-W2$ color from an average of $\simeq$ 0.23 mag before MJD 58500 to an average of ~0.38 mag between ~MJD 58500 and ~MJD 59500. The maximum value, $W1-W2 = 0.52$, is reached around MJD 59100. The increase in the $W1-W2$ color indicates that this event, as seen in the optical–X-ray range, is not due to extrinsic factors like variable obscuration but due to an increase in accretion rate. We find a steady rise in IR flux that started much earlier (~400 days) than the 2020 optical flare and the IR peak occurs ~200 days after the optical flare in the *o*-, *c*-, *g*-, and, *r*-bands (Fig. 1b and 7a, 7b, and 7c). We find a similar steady rise in the optical light curves before the 2020 peak. In this Section, we discuss the implications of this observed phenomenon in the IR and its link to the optical or central engine variability.

Emission in the mid IR bands can originate in warm circumnuclear dust heated by the AGN. Consequently, one can model variability in the mid IR band as "dust echoes." Specifically, a ~parsec-scale dust structure is irradiated by the emission from the central engine, and this emission undergoes absorption and reprocessing, yielding a reverberation signature. The position and length scale of a distant dusty torus is dependent on the bolometric luminosity $L_{\rm bol}$ of the source. This length scale ($R_{\rm sub}$) is termed as the dust sublimation radius of the system, beyond which sublimation does not happen and dust grains survive the radiative heating. We use the following expression (Barvainis 1987; Netzer 2015) and the estimates of bolometric luminosity to estimate the dust sublimation radius ($R_{\rm sub}$) of the system:

$$R_{\rm sub} = 0.5 \text{ pc} \left(\frac{L_{\rm bol}}{10^{45} \text{ erg s}^{-1}}\right)^{1/2} \left(\frac{T_{\rm sub}}{1500 \text{ K}}\right)^{-2.6} f(\theta). \quad (8)$$

The value of $T_{\rm sub}$ depends on the content of the dust. For silicates and carbonaceous grains, the sublimation temperatures are $T_{\rm sub} = 1500$ K and $T_{\rm sub} = 1800$ K respectively (Barvainis 1987; Netzer 2015). The $f(\theta)$ function represents the anisotropy of the nuclear emission; where $f(\theta) = 1.0$ represents isotropic and $f(\theta) < 1$ represents anisotropic radiation. Assuming $T_{\rm sub} = 1650$ K, $L_{\rm bol} \sim 4 \times 10^{44}$ erg s^{-1}, and $f(\theta) = 1$, we get $R_{\rm sub} = 0.26$ pc. The corresponding light travel time, $R_{\rm sub}/c$, is 290 days. The light travel time is thus roughly consistent with the delay between the peaks of the optical and *WISE* light curves, considering that there is only one *WISE* flux point every six months.

We perform phenomenological modeling of the infrared echo to infer constraints on the geometry of the dusty material. We test several shapes for both the input optical light curve and for the dusty reprocessor. We describe the calculations in detail in Appendix F. First we consider a full-covering spherical shell. From the estimates in the previous paragraph, we find that the dust structure resides at radial distances greater than ~0.2 to 0.3 pc. Thus, we initially take the inner and outer radii of the shell to be $r_{\rm in} = 0.2$ pc and $r_{\rm out} = 1$ pc respectively. First, we consider as our input light curve a Gaussian flare of standard deviation ~20 days. We find that the echoed light-curve is asymmetrically smeared, as the rise is more abrupt compared to the decay; the width of the smearing is ~1000 days. We find that the peaks of the input and reprocessed light curves are delayed by ~42 days. When the values of $r_{\rm in}$ and $r_{\rm out}$ were increased to 0.4 pc and 2.0 pc respectively, the delay increases to ~60 days (Fig. 9a). Thus we cannot produce a delay signal similar to that observed in the IR in terms of IR smearing and optical-to-IR delay with a full spherical geometry.

However, if the shell was biconically cutout (as adopted in multiple AGN torus models; e.g. Ikeda et al. 2009), the delay between the peaks is affected by both the values of the inner and outer radii and the opening angle of the cutout region, denoted as θ_o. We assume for simplicity that the observer is located on the axial symmetry axis of the biconically cutout shell. As $\theta_{\rm o}$ increases, we find that the IR peaks become relatively more delayed (Fig. 9b). Thus for a biconically cutout shell it is possible to create delays of a few hundred days by varying θ_o. However, the output light curves have a smeared shape that is still highly asymmetric and does not directly resemble the observed *WISE* light curves. Consequently, varying only geometry in these simulations is insufficient to explain the observed $W1$ and $W2$ variability.

Additionally, in the dust-echo model, the IR emission from a parsec scale structure torus cannot lead the higher energy emission originating closer to the black hole. The advanced and slow rise in the observed infrared light curves indicates that the variability is not solely a response due to the 2020 optical flare. To have a slower rise in the IR response preceding the 2020 flare, there should exist a long-term variability component in the input light curve starting before the 2020 flare. The slow rise is also seen in the optical light curves.

Thus, we simulate reprocessed light curves for the case where the input light curve's sharp flare with $\sigma = 20$ days is superposed onto a broader Gaussian flare with $\sigma = 350$ days with both their maxima occurring at the same position. This input light curve can yield an output light curve with an initial rise before the main IR flare (Fig. 9c). Moreover, adopting values for $r_{\rm in} = 0.2$ pc, $r_{\rm out} = 1.0$ pc, and $\theta_{\rm o} \simeq 10°$, we find that the main IR peak occurs roughly 200 days after the main optical peak, similar to that observed, and with an output infrared light curve whose almost symmetric smearing lasts for ~1800 days, roughly similar to that observed. We stress that these are approximate values only, and that the model is relatively simple. However, in the context of the observed light curves, the simulated light curve consistently explains the trend when significant variability precedes the sharper flare, which we model using the underlying broad Gaussian profile.

In summary, we have demonstrated that variability in the infrared light curve for J0428−00 can qualitatively be explained by echoes from a parsec-scale structure extending from ~0.2 pc to ~1 pc, with a bi-conical cutout with an opening angle of 10°, and when the input light curve is a composite flare containing superposed short and long term variability trends. Additionally, this analysis using the phenomenological echo model supplements the statistical argument in favor of a slow rise in the optical light curves preceding the 2020 flare with a physical one. We caution,

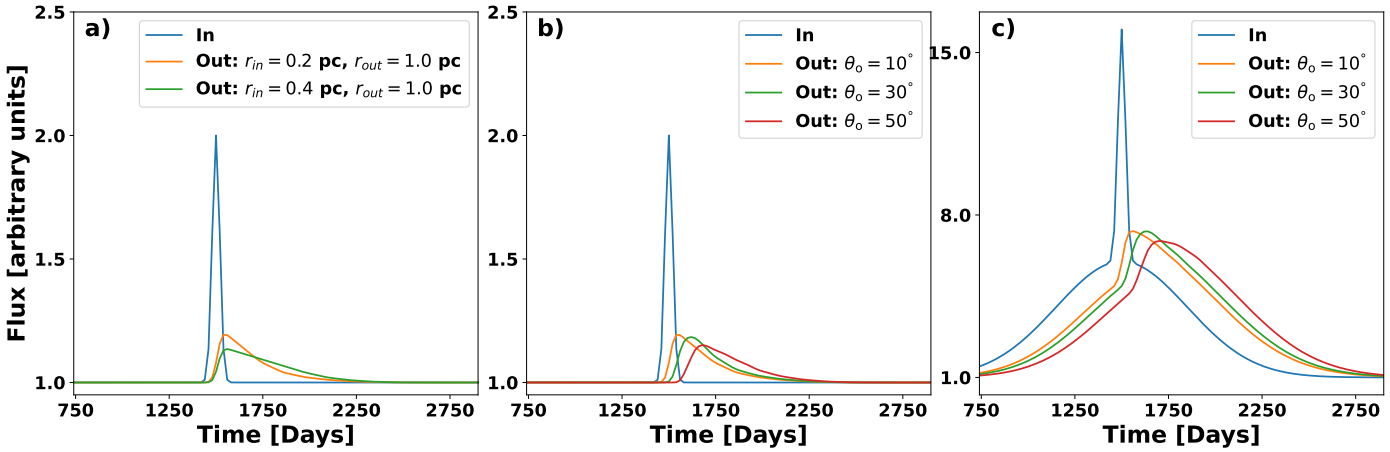

Fig. 9. The responses of a spherical shell and a spherical shell with a bi-conical cut out due to a sharp flare arising in the center of the system. When a single Gaussian flare of width $\sigma = 20$ days is considered as the input for a complete spherical shell (a), we find that with the change of the inner radius only the smearing out of the echo is affected, but no shift is found in the peaks. For a biconical cutout shell with inner radius $r_{\rm in} = 0.2$ pc and outer radius $r_{\rm out} = 1$ pc (b), the response to a single Gaussian flare is an abrupt rise and a slow decay. The delay between the peaks increases when the covering factor decreases (larger θ_o results in a lower covering factor). When the input signal consists of the superposition of a wide Gaussian and a narrow Gaussian (c), for the same radial extent of a bi-conical cutout shell, we find a much broader flare response with a much slower rise and decay, qualitatively similar to what has been observed.

however, that neither such a configuration nor these derived parameter values are definitive, given the simplicity of the model and likely model parameter degeneracies.

9. Summary

We report the detection of a new optical changing-look Seyfert: J0428−00 was originally a type-1.9 Seyfert, but in 2020 it exhibited a multi-wavelength flare captured in the optical by ZTF and in the X-ray by eROSITA's eRASS surveys. Tied to the extreme variability was a change in optical spectral classification from type 1.9 to 1, as broad Hβ emission had appeared by 2020. We initiated a three-year multi-wavelength follow-up campaign to track the source's emission as the flare gradually subsided, and to determine the nature of this transient event.

The continuum light curves and the recent X-ray spectra, combined with indications of historical AGN activity, argue against the event being due to the tidal disruption of a star by a supermassive black hole. Instead, the flare is more likely the result of a disk instability in a previously-existing accretion structure. Additional key findings include:

- J0428−00 exhibits persistent narrow emission lines of [O III], [N II], and [S II]. The BPT ratios indicate ongoing AGN activity for of order millennia (Section 8.2).
- J0428−00 exhibits double-peaked broad Balmer emission lines. Hα is relatively strong and persistent, even in the archival 6dF spectrum. Hβ appears only in 2020, consistent with being driven by the continuum flare, due to the increase in the flux of ionizing photons. However, the Balmer line fluxes overall track the continuum, i.e., Hβ slowly fades as the continuum flux subsides. The broad Balmer profiles' double peaks are fit well by models based on a disk-type geometry, extending from roughly a few hundred $R_{\rm g}$ to roughly a 1000 $R_{\rm g}$, though an additional broad Gaussian component was needed for optimum fits (Section 7.4). We also witness modest changes in broad line profiles over the course of the campaign, possibly due to azimuthal variations in emission.
- The optical spectrum exhibited a strong blue continuum during the initial phases of the 2020 event, but the source transitioned to a galaxy-dominated continuum in the later phases as the flare continuum faded (Fig. 4).
- The X-ray spectra are fit well by a power law with a flat photon index (∼1.9), typical for radio-quiet Seyferts. In addition, the X-ray and UV continuua decay in concert (Fig. 7d and e). The X-rays are thus consistent with thermal Comptonization of low-energy seed photons, though corona-to-disk thermal reprocessing cannot be excluded.
- Intriguingly, the soft X-ray excess, a near-ubiquitous feature of the X-ray spectra of nearby Seyferts, is absent in J0428−00. This could indicate the absence or extreme weakness of a warm corona, in the context of warm Comptonization models (Section 6). Alternatively, in the context of models of ionized disk reflection from the inner disk, the inner accretion disk could be truncated or radiatively inefficient.
- We also excluded the event as being due to a change in line-of-sight obscuration, as the X-ray spectra do not exhibit any signatures of obscuration (Section 5) beyond the Galactic column.
- The *WISE* lightcurves exhibit a broad flare, with the peak delayed by ∼200 days with respect to the main optical flare. Our analysis (Section 8.10) indicates that the infrared signal originates in a parsec-scale dust structure extending from ∼0.2 pc to ∼1 pc and is a response to both the 2020-flare and an underlying long term trend.

All these observations are consistent with a scenario where the main trigger of the events is a temporary instability in the accretion flow structure. A Lightman-Eardley instability triggered in the inner-disk (∼50 to 100$R_{\rm g}$) is consistent with the observed timescale of the main flare from 2020. Additionally, the continuum variability light curves of J0428−00 qualitatively resemble those theoretically calculated in Śniegowska et al. (2020) and Śniegowska et al. (2023).

Time-domain astronomy is yielding an ever-increasing accumulation of peculiar supermassive black hole transient events. The discovery of flaring activity in J0428−00 is part of this

multi-wavelength time domain effort, including eROSITA's new window into X-ray time domain studies. CLAGN and flaring-AGN are events that yield insight into major changes in accretion rate, though sometimes those changes are temporary. Nonetheless, it is critical to study them to fully understand AGNs' long-term, accumulated accretion histories and AGN's typical "duty cycles," as well as understanding parallels between AGN and black hole X-ray binary accretion modes. However, many of the recently-studied AGN yield insight beyond global transitions in accretion rate, as events such as J0428−00 and those reported in Frederick et al. (2019) and Frederick et al. (2021) may be driven by instabilities in the accretion disk. All this makes CLAGN and flaring AGN excellent test beds for theoretical instability models and for studying long-term black hole accretion.

Acknowledgements. The authors acknowledge insightful discussions with Prof. Chris Done. TS and AM acknowledge full or partial support from Polish Narodowym Centrum Nauki grants 2016/23/B/ST9/03123, 2018/31/G/ST9/03224, and 2019/35/B/ST9/03944. DH acknowledges support from DLR grant FKZ 50 OR 2003. MK is supported DLR grant FKZ 50 OR 2307. MG is supported by the EU Horizon 2020 research and innovation programme under grant agreement No 101004719. SH is supported by the German Science Foundation (DFG grant number WI 1860/14-1). This work is based on data from eROSITA, the soft X-ray instrument aboard SRG, a joint Russian-German science mission supported by the Russian Space Agency (Roskosmos), in the interests of the Russian Academy of Sciences represented by its Space Research Institute (IKI), and the Deutsches Zentrum für Luft- und Raumfahrt (DLR). The SRG spacecraft was built by Lavochkin Association (NPOL) and its subcontractors, and is operated by NPOL with support from the Max Planck Institute for Extraterrestrial Physics (MPE). The development and construction of the eROSITA X-ray instrument was led by MPE, with contributions from the Dr. Karl Remeis Observatory Bamberg & ECAP (FAU Erlangen-Nuernberg), the University of Hamburg Observatory, the Leibniz Institute for Astrophysics Potsdam (AIP), and the Institute for Astronomy and Astrophysics of the University of Tübingen, with the support of DLR and the Max Planck Society. The Argelander Institute for Astronomy of the University of Bonn and the Ludwig Maximilians Universität Munich also participated in the science preparation for eROSITA. The eROSITA data shown here were processed using the eSASS software system developed by the German eROSITA consortium. This work is based on observations obtained with XMM-Newton, an ESA science mission with instruments and contributions directly funded by ESA Member States and NASA. This research has made use of data and/or software provided by the High Energy Astrophysics Science Archive Research Center (HEASARC), which is a service of the Astrophysics Science Division at NASA/GSFC. This work has made use of data from the Asteroid Terrestrial-impact Last Alert System (ATLAS) project. The Asteroid Terrestrial-impact Last Alert System (ATLAS) project is primarily funded to search for near earth asteroids through NASA grants NN12AR55G, 80NSSC18K0284, and 80NSSC18K1575; byproducts of the NEO search include images and catalogs from the survey area. This work was partially funded by Kepler/K2 grant J1944/80NSSC19K0112 and HST GO-15889, and STFC grants ST/T000198/1 and ST/S006109/1. The ATLAS science products have been made possible through the contributions of the University of Hawaii Institute for Astronomy, the Queen's University Belfast, the Space Telescope Science Institute, the South African Astronomical Observatory, and The Millennium Institute of Astrophysics (MAS), Chile. Based on observations obtained with the Samuel Oschin Telescope 48-inch and the 60-inch Telescope at the Palomar Observatory as part of the Zwicky Transient Facility project. ZTF is supported by the National Science Foundation under Grant No. AST-1440341 and AST-2034437 and a collaboration including Caltech, IPAC, the Weizmann Institute for Science, the Oskar Klein Center at Stockholm University, the University of Maryland, the University of Washington, Deutsches Elektronen-Synchrotron and Humboldt University, Los Alamos National Laboratories, the TANGO Consortium of Taiwan, the University of Wisconsin at Milwaukee, Trinity College Dublin, Lawrence Berkeley National Laboratories, Lawrence Livermore National Laboratories, and IN2P3, France. Operations are conducted by COO, IPAC, and UW. This paper uses observations made from the South African Astronomical Observatory (SAAO). Some of the observations reported in this paper were obtained with the Southern African Large Telescope (SALT) under programs 2020-2-MLT-008 (PI: A. Markowitz) and 2021-2-LSP-001 (PI: D. Buckley). Polish participation in SALT is funded by grant No. MEiN nr 2021/WK/01. This publication makes use of data products from the Wide-field Infrared Survey Explorer, which is a joint project of the University of California, Los Angeles, and the Jet Propulsion Laboratory/California Institute of Technology, funded by the National Aeronautics and Space Administration. This publication also makes use of data products from NEOWISE, which is a project of the Jet Propulsion Laboratory/California Institute of Technology, funded by the Planetary Science Division of the National Aeronautics and Space Administration. This research has made use of the NASA/IPAC Extragalactic Database (NED), which is funded by the National Aeronautics and Space Administration and operated by the California Institute of Technology.

References

Akaike, H. 1974, IEEE Transactions on Automatic Control, 19, 716
Antonucci, R. 1993, ARA&A, 31, 473
Appenzeller, I., Fricke, K., Fürtig, W., et al. 1998, The Messenger, 94, 1
Auchettl, K., Ramirez-Ruiz, E., & Guillochon, J. 2018, ApJ, 852, 37
Balbus, S. A. & Hawley, J. F. 1991, ApJ, 376, 214
Baldwin, J. A., Phillips, M. M., & Terlevich, R. 1981a, PASP, 93, 5
Baldwin, J. A., Phillips, M. M., & Terlevich, R. 1981b, PASP, 93, 5
Barvainis, R. 1987, ApJ, 320, 537
Bellm, E. C., Kulkarni, S. R., Graham, M. J., et al. 2019, PASP, 131, 018002
Bentz, M. C., Peterson, B. M., Netzer, H., Pogge, R. W., & Vestergaard, M. 2009, ApJ, 697, 160
Brogan, R., Krumpe, M., Homan, D., et al. 2023, arXiv e-prints, arXiv:2307.14139
Bruhweiler, F. & Verner, E. 2008, ApJ, 675, 83
Brunner, H., Liu, T., Lamer, G., et al. 2022, A&A, 661, A1
Buchner, J. 2021, The Journal of Open Source Software, 6, 3001
Buchner, J., Georgakakis, A., Nandra, K., et al. 2014, A&A, 564, A125
Buckley, D. A. H., Swart, G. P., & Meiring, J. G. 2006, in Society of Photo-Optical Instrumentation Engineers (SPIE) Conference Series, Vol. 6267, Society of Photo-Optical Instrumentation Engineers (SPIE) Conference Series, ed. L. M. Stepp, 62670Z
Chen, K. & Halpern, J. P. 1989, ApJ, 344, 115
Chen, K., Halpern, J. P., & Filippenko, A. V. 1989, ApJ, 339, 742
Collier, S. & Peterson, B. M. 2001, ApJ, 555, 775
Crause, L. A., Gilbank, D., Gend, C. v., et al. 2019, Journal of Astronomical Telescopes, Instruments, and Systems, 5, 024007
Crummy, J., Fabian, A. C., Gallo, L., & Ross, R. R. 2006, MNRAS, 365, 1067
Denney, K. D., De Rosa, G., Croxall, K., et al. 2014, ApJ, 796, 134
Done, C., Davis, S. W., Jin, C., Blaes, O., & Ward, M. 2012, MNRAS, 420, 1848
Duras, F., Bongiorno, A., Ricci, F., et al. 2020, A&A, 636, A73
Elitzur, M. & Ho, L. C. 2009, ApJ, 701, L91
Elitzur, M., Ho, L. C., & Trump, J. R. 2014, MNRAS, 438, 3340
Evans, C. R. & Kochanek, C. S. 1989, ApJ, 346, L13
Frederick, S., Gezari, S., Graham, M. J., et al. 2019, ApJ, 883, 31
Frederick, S., Gezari, S., Graham, M. J., et al. 2021, ApJ, 920, 56
Frederick, S., Graham, M. J., Gezari, S., van Velzen, S., & Ward, C. 2020, The Astronomer's Telegram, 13460, 1
García, J., Dauser, T., Reynolds, C. S., et al. 2013, ApJ, 768, 146
Gehrels, N., Chincarini, G., Giommi, P., et al. 2004, ApJ, 611, 1005
Gezari, S. 2021, ARA&A, 59 [arXiv:2104.14580]
Gilli, R., Maiolino, R., Marconi, A., et al. 2000, A&A, 355, 485
Goodman, J. & Weare, J. 2010, Communications in Applied Mathematics and Computational Science, 5, 65
Graham, A. W. 2007, MNRAS, 379, 711
Graham, M. J., Ross, N. P., Stern, D., et al. 2020, MNRAS, 491, 4925
Greene, J. E., Peng, C. Y., Kim, M., et al. 2010, ApJ, 721, 26
Haardt, F. & Maraschi, L. 1991, ApJ, 380, L51
Haardt, F. & Maraschi, L. 1993, ApJ, 413, 507
Halpern, J. P. 1984, ApJ, 281, 90
Heckman, T. M., Ptak, A., Hornschemeier, A., & Kauffmann, G. 2005, ApJ, 634, 161
Homan, D., Krumpe, M., Markowitz, A., et al. 2023, A&A, 672, A167
Ikeda, S., Awaki, H., & Terashima, Y. 2009, ApJ, 692, 608
Ingram, A. & Done, C. 2011, MNRAS, 415, 2323
Jansen, F., Lumb, D., Altieri, B., et al. 2001, A&A, 365, L1
Jarrett, T. H., Cohen, M., Masci, F., et al. 2011, ApJ, 735, 112
Jones, D. H., Read, M. A., Saunders, W., et al. 2009, MNRAS, 399, 683
Jones, D. H., Saunders, W., Colless, M., et al. 2004, MNRAS, 355, 747
Kato, S., Fukue, J., & Mineshige, S. 2008, Black-Hole Accretion Disks — Towards a New Paradigm —
Kauffmann, G., Heckman, T. M., Tremonti, C., et al. 2003, MNRAS, 346, 1055
Kewley, L. J., Dopita, M. A., Sutherland, R. S., Heisler, C. A., & Trevena, J. 2001, ApJ, 556, 121
Kubota, A. & Done, C. 2018, MNRAS, 480, 1247
LaMassa, S. M., Cales, S., Moran, E. C., et al. 2015, ApJ, 800, 144
Lightman, A. P. & Eardley, D. M. 1974, ApJ, 187, L1
Lin, D., Godet, O., Webb, N. A., et al. 2022, ApJ, 924, L35
Lusso, E., Comastri, A., Vignali, C., et al. 2010, A&A, 512, A34
MacLeod, C. L., Ross, N. P., Lawrence, A., et al. 2016, MNRAS, 457, 389
Mannucci, F., Basile, F., Poggianti, B. M., et al. 2001, MNRAS, 326, 745
Markowitz, A. & Edelson, R. 2004, ApJ, 617, 939

Markowitz, A., Edelson, R., Vaughan, S., et al. 2003, ApJ, 593, 96
Mehdipour, M., Branduardi-Raymont, G., Kaastra, J. S., et al. 2011, A&A, 534, A39
Mehdipour, M., Kaastra, J. S., Kriss, G. A., et al. 2017, A&A, 607, A28
Miniutti, G., Sanfrutos, M., Beuchert, T., et al. 2014, MNRAS, 437, 1776
M^{c}Hardy, I. M., Cameron, D. T., Dwelly, T., et al. 2014, MNRAS, 444, 1469
Mushotzky, R. F., Done, C., & Pounds, K. A. 1993, ARA&A, 31, 717
Naddaf, M. H. & Czerny, B. 2022, A&A, 663, A77
Naddaf, M.-H., Czerny, B., & Szczerba, R. 2021, ApJ, 920, 30
Nandra, K., Le, T., George, I. M., et al. 2000, ApJ, 544, 734
Nelson, C. H. 2000, ApJ, 544, L91
Netzer, H. 2015, ARA&A, 53, 365
Nicholl, M., Wevers, T., Oates, S. R., et al. 2020, MNRAS, 499, 482
Oke, J. B., Cohen, J. G., Carr, M., et al. 1995, PASP, 107, 375
Osterbrock, D. E. & Koski, A. T. 1976, MNRAS, 176, 61P
Paturel, G., Vauglin, I., Petit, C., et al. 2005, A&A, 430, 751
Petrucci, P. O., Ursini, F., De Rosa, A., et al. 2018, A&A, 611, A59
Predehl, P., Andritschke, R., Arefiev, V., et al. 2021, A&A, 647, A1
Rees, M. J. 1988, Nature, 333, 523
Ricci, C., Kara, E., Loewenstein, M., et al. 2020, ApJ, 898, L1
Ricci, C., Loewenstein, M., Kara, E., et al. 2021, ApJS, 255, 7
Ross, N. P., Ford, K. E. S., Graham, M., et al. 2018, MNRAS, 480, 4468
Ruan, J. J., Anderson, S. F., Eracleous, M., et al. 2019, ApJ, 883, 76
Runnoe, J. C., Brotherton, M. S., & Shang, Z. 2012, MNRAS, 422, 478
Sazonov, S., Gilfanov, M., Medvedev, P., et al. 2021, MNRAS, 508, 3820
Scepi, N., Begelman, M. C., & Dexter, J. 2021, MNRAS, 502, L50
Schawinski, K., Thomas, D., Sarzi, M., et al. 2007, MNRAS, 382, 1415
Schimoia, J. S., Storchi-Bergmann, T., Nemmen, R. S., Winge, C., & Eracleous, M. 2012, ApJ, 748, 145
Schlafly, E. F. & Finkbeiner, D. P. 2011, ApJ, 737, 103
Shakura, N. I. & Sunyaev, R. A. 1973, A&A, 24, 337
Shappee, B. J., Prieto, J. L., Grupe, D., et al. 2014, ApJ, 788, 48
Shen, Y. 2021, ApJ, 921, 70
Shields, G. A. & McKee, C. F. 1981, ApJ, 246, L57
Sikora, M. & Begelman, M. C. 2013, ApJ, 764, L24
Śniegowska, M., Czerny, B., Bon, E., & Bon, N. 2020, A&A, 641, A167
Śniegowska, M., Grzędzielski, M., Czerny, B., & Janiuk, A. 2023, A&A, 672, A19
Sobolewska, M. A. & Done, C. 2007, MNRAS, 374, 150
Sołtan, A. 1982, MNRAS, 200, 115
Stern, J. & Laor, A. 2012, MNRAS, 426, 2703
Storchi-Bergmann, T., Schimoia, J. S., Peterson, B. M., et al. 2017, ApJ, 835, 236
Sunyaev, R., Arefiev, V., Babyshkin, V., et al. 2021, A&A, 656, A132
Tananbaum, H., Avni, Y., Branduardi, G., et al. 1979, ApJ, 234, L9
Tonry, J. L., Denneau, L., Heinze, A. N., et al. 2018, PASP, 130, 064505
Trakhtenbrot, B., Arcavi, I., Ricci, C., et al. 2019, Nature Astronomy, 3, 242
Treves, A., Maraschi, L., & Abramowicz, M. 1988, PASP, 100, 427
Trippe, M. L., Crenshaw, D. M., Deo, R., & Dietrich, M. 2008, AJ, 135, 2048
Tundo, E., Bernardi, M., Hyde, J. B., Sheth, R. K., & Pizzella, A. 2007, ApJ, 663, 53
Turner, T. J. & Pounds, K. A. 1989, MNRAS, 240, 833
Uttley, P., Edelson, R., McHardy, I. M., Peterson, B. M., & Markowitz, A. 2003, ApJ, 584, L53
van Groningen, E. & Wanders, I. 1992, PASP, 104, 700
van Velzen, S., Gezari, S., Hammerstein, E., et al. 2021, The Astrophysical Journal, 908, 4
Vanden Berk, D. E., Richards, G. T., Bauer, A., et al. 2001, AJ, 122, 549
Vestergaard, M. & Peterson, B. M. 2006, ApJ, 641, 689
Ward, C., Gezari, S., Nugent, P., et al. 2023, Panic at the ISCO: the visible accretion disks powering optical variability in ZTF AGN
Willingale, R., Starling, R. L. C., Beardmore, A. P., Tanvir, N. R., & O'Brien, P. T. 2013, MNRAS, 431, 394
Wright, E. L. 2006, PASP, 118, 1711
Wu, J., Wu, Q., Xue, H., Lei, W., & Lyu, B. 2023, arXiv e-prints, arXiv:2304.09435
Xiao, T., Barth, A. J., Greene, J. E., et al. 2011, ApJ, 739, 28
Zdziarski, A. A., Johnson, W. N., & Magdziarz, P. 1996, MNRAS, 283, 193
Zdziarski, A. A., Szanecki, M., Poutanen, J., Gierliński, M., & Biernacki, P. 2020, MNRAS, 492, 5234
Życki, P. T., Done, C., & Smith, D. A. 1999, MNRAS, 309, 561

Appendix A: Scaling the spectra using the [O III]λ5007 line

We scale all the optical spectra using the [O III]λ5007 narrow emission line using the method of van Groningen & Wanders (1992). We fit the [O III]λ5007 line profile of each spectrum to a selected reference spectrum, which in our case is the Keck spectrum. We smooth the reference spectrum to the lowest resolution among all the obtained spectra. We first select a window for the [O III]λ5007 line. Subsequently, in the selected region, we select a window for the fit which accounts for the line and the underlying continuum. To perform the fitting, we first select the [O III]λ5007 line region and the blueward and the redward continuum region. We then subtract the continuum baseline from the total flux in the selected wavelength region to obtain just the [O III]λ5007 line flux of the source. We use GW-MCMC (`emcee`, Goodman & Weare 2010) to fit the emission line in a target spectrum to the smoothed reference spectrum. We find that with the profile fitting, the discrepancy in the scaled flux of the target spectra to the reference can be upto 25%. This discrepancy can originate due to the degradation in the data quality during later phases of the monitoring. This methodology aligns the spectra by shifting the [O III]λ5007 line center to match the reference spectrum. Additionally, it calculates the scale factor to be multiplied with the spectra to obtain a similar line flux as the reference (Fig. A.1). We do not correct for different levels of host-galaxy contribution.

Appendix B: Modeling the optical spectrum

All the optical spectra are taken by different instruments and at different epochs hence the data have different data quality. The spectrum also exhibits significant evolution. Thus, our fitting methods and models vary for each spectrum. We summarize the spectral components in Table B.1. In the table, we use the following abbreviations: (a) power law: pl (b) galaxy: gal (c) linear component: lin (d) n number of Gaussian profiles used to model a given line: n-Gaussian. For the [S II] doublet we characterise them as: (a) 'resolved'–when each of the lines have visually equal width (b)'broad feature'–other case involving two artifacts of unequal width or just a single feature with the lines unresolved. We model the [S II] line region by using either one or two Gaussians profiles depending on which accounts for the total feature best. In all cases except for the Keck spectrum we see that the Hβ narrow emission line could not be identified. The flux of [O III]λ5007 and the broad Hβ and Hα is are reported in Table B.

We plot the data and the best fit model for rest of the optical spectra from: 6dF (Fig. B.1), LDT (Figures B.2, B.3, and B.4), SAAO (Fig. B.5), SALT (first spectrum Fig. B.6), VLT-FORS2 (Fig. B.7), NOT (Fig. B.8), DBSP (Fig. B.9), TNG (Fig. B.10), SALT (second spectrum Fig. B.11), SALT (third spectrum Fig. B.12), and VLT-FORS2 (second spectrum Fig. B.13).

Appendix C: Error calculation for the broad line fluxes

We calculate the flux errors on the emission lines from the root mean squared average residual:

$$\sigma_{\rm res} = \sqrt{\frac{\Sigma(d_{\rm i} - m_{\rm i})^2}{N-1}} \tag{C.1}$$

Here, $d_{\rm i}$ is the data, $m_{\rm i}$ is the model at a given wavelength and N is the number of data points. The quantity $\sigma_{\rm res}$ represents the average error on the flux density at any given wavelength. Thus, the error on a given emission line flux is thus, $e_{\rm flux} = \sigma_{\rm res}\Delta\lambda$ where $\Delta\lambda$ is the assumed extent of the emission line. For a line modeled by a single Gaussian the length $\Delta\lambda = 6\sigma_{,\lambda}$, which encloses the 3σ region on both sides of the peak, thus ensuring that 99.7% of the line region is accounted for. For a line modeled by double Gaussians the length is given by $\Delta\lambda = \lambda_R - \lambda_B + 3(\sigma_{\rm B} + \sigma_{\rm R})$, where ($\lambda_B$,$\sigma_B$) are parameters of the blue Gaussian and (λ_R,σ_R) are the parameters of the red Gaussian. In this case most of the line flux is enclosed within the $\lambda_{\rm R}-3\sigma_B$ and $\lambda_{\rm R}+3\sigma_R$ wavelength region.

Appendix D: FRADO profile plots

We modeled the broad-line profiles using the FRADO model. The plots were carried out under different conditions (Section 7.5) involving only a broadened FRADO profile and a FRADO+Gaussian profile. The results of the FRADO profile fitting are shown in Fig. D.1.

Appendix E: BPT Diagram methodology

In this section, we discuss the methodology and issues associated with the calculation of the narrow line ratios used to plot the BPT diagram (Fig. 8). We used the integrated narrow line fluxed to construct the BPT diagram. In most spectra, the narrow Hβ line had low S/N and could not be visually identified, with the Keck spectrum being the exception. Thus, to estimate the [O III]λ5007/Hβ flux ratio we used the flux of the narrow Hβ line from the Keck spectrum. For [S II], where the doublets are unresolved, we assumed that the flux of [S II]λ6716 is given by half of the integrated flux of the fit profile. We used the average flux of the [S II]λ6716 lines over all observations for estimating the BPT ratios, because of poor S/N. The only truly reliable estimates on line flux for the purpose of calculating BPT ratios are [O III]λ5007, [N II]λ6785, and Hα. Thus we could only get reliable estimates for the [N II]λ6785/Hα line ratio. Other ratio values can be considered as less reliable.

Appendix F: Infrared echo reprocessing simulation

To simulate the infrared continuum emission response from a dusty, ~parsec scale structure, we tested both a spherical shell and a biconically cutout spherical shell geometry, with the illuminating source placed at the center. The response from the later setup provided the best explanation to our data. The inner radius, outer radius, and the opening angle of the shell are $r_{\rm in}$, $r_{\rm out}$, and $\theta_{\rm o}$ respectively. The luminosity of the central source is $L_{\rm in}(t)$. For simplicity the observer lies on the axis of symmetry of the shell at an infinite distance.

Because of the delay due to light travel time, a volume element at (r,θ) responds to the radiation that originated at time $t - d(r,\theta)/c$, that is, the luminosity incident on this element is $L_{\rm in}(t - \frac{d(r,\theta)}{c})$, where $d(r,\theta) = r(1-\cos\theta)$. Other than delay, there are extinction effects. We apply a crude and parameterized model of extinction: light rays traveling through the medium undergo extinction following $f_1(r, r_{in}) = e^{-\beta(r-r_{\rm in})}$ up to a distance of r, after which the light ray is re-radiated towards the observer. Along the redirected path towards the observer, the extinction is given by $f_2(r,\theta,r_{\rm out}) = e^{-\beta(\sqrt{r_{\rm out}^2 - r^2\sin^2(\theta)} - r\cos\theta)}$. Here, β is an ad-hoc parameterization of absorption in the medium. The mathematical

Table B.1. The components that have been used to model the continuum and the line region for each optical spectra.

Time	Telescope	Global Continuum	Hβ-λ range	Hβ region continuum	Hα-λ range	Hα region continuum	[O III]-model	Hβ-model	[S II]-region
2005	6dF	-	(4500 Å, 5160 Å)	gal+lin	(6416 Å, 6780 Å)	gal+lin	1-Gaussian	2-Gaussian	broad feature
58871	KECK	pl+gal	(4500 Å, 5160 Å)	pl+gal	(6000 Å, 6750 Å)	pl+gal	3-Gaussian	2-Gaussian	resolved
58905	LDT	pl+gal	(4500 Å, 5160 Å)	pl+gal	(6350 Å, 6850 Å)	pl+gal+lin	3-Gaussian	2-Gaussian	broad feature
59105	LDT	pl+gal	(4500 Å, 5160 Å)	pl+gal	(6350 Å, 6850 Å)	pl+gal	2-Gaussian	2-Gaussian	resolved
59189	LDT	pl+gal	(4500 Å, 5160 Å)	pl+gal	(6000 Å, 6750 Å)	pl+gal	2-Gaussian	2-Gaussian	broad feature
59468	SAAO	gal	(4500 Å, 5160 Å)	gal	(6000 Å, 6750 Å)	gal+lin	2-Gaussian	1-Gaussian	resolved
59586	SALT-1	gal	(4500 Å, 5160 Å)	gal+lin	(6000 Å, 6750 Å)	gal+lin	2-Gaussian	1-Gaussian	broad feature
59660	FORS2	gal	(4500 Å, 5160 Å)	gal+lin	(6000 Å, 6750 Å)	gal+lin	2-Gaussian	2-Gaussian	resolved
59821	NOT	gal	(4500 Å, 5160 Å)	gal+lin	(6000 Å, 6750 Å)	gal+lin	2-Gaussian	2-Gaussian	broad feature
59828	DBSP	gal	(4500 Å, 5160 Å)	gal+lin	(6350 Å, 6850 Å)	gal+lin	2-Gaussian	1-Gaussian	broad feature
59853	TNG	gal	(4500 Å, 5160 Å)	gal+lin	(6350 Å, 6850 Å)	gal+lin	2-Gaussian	1-Gaussian	resolved
59881	SALT-2	gal	(4500 Å, 5160 Å)	gal+lin	(6350 Å, 6850 Å)	gal+lin	2-Gaussian	2-Gaussian	resolved
59883	SALT-3	gal	(4500 Å, 5160 Å)	gal+lin	(6350Å, 6850Å)	gal+lin	1-Gaussian	1-Gaussian	broad feature
60018	FORS2	gal	(4500 Å, 5160 Å)	gal+lin	(6000Å, 6750Å)	gal+lin	2-Gaussian	2-Gaussian	resolved

Notes. The difference in the modeling of the local continuum varies depending on the spectra. A power law component is required to model the first four spectra which were taken close to the flaring event. The spectra taken later did not require the power law component. All models required contributions from the host-galaxy. The modeling of the emission lines varied depending on spectral resolution and quality.

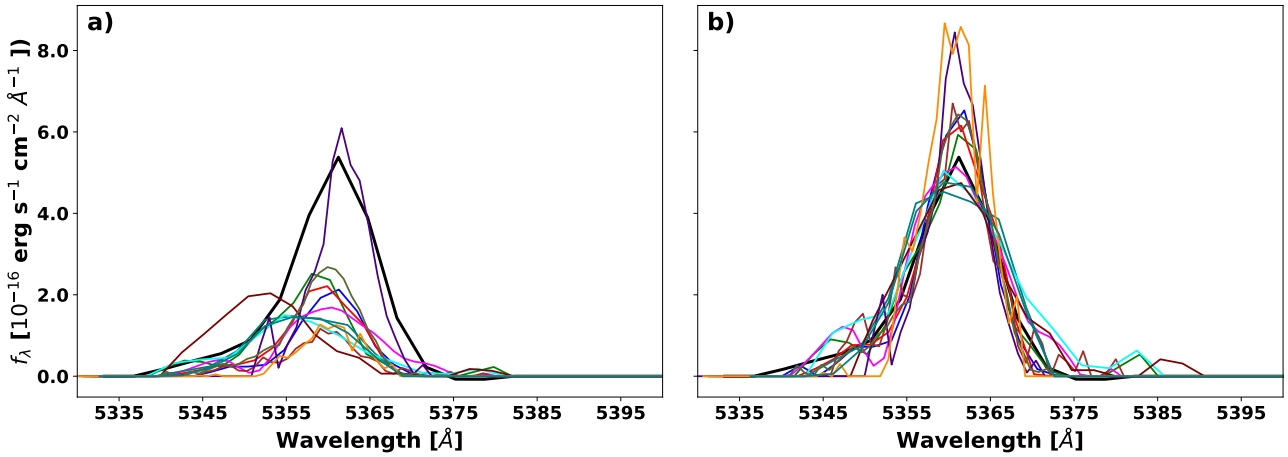

Fig. A.1. (a) The unscaled [O III] lines show the displacement of the line centers and the mismatch of the [O III] line flux across all the optical spectra. (b) After applying the scaling algorithm, the λ shifts were corrected and the flux scaling factors were determined and applied; the resulting flux-scaled and wavelength-corrected lines are plotted here.

Table B.2. The unscaled fluxes of the [O III]λ5007, Hβ broad and narrow, [N II]λ6585, and Hα broad and narrow emission lines.

Time	Telescope	Scale	F([O III]λ5007)	F(Hβ narrow)	F(Hβ broad)	F([N II]λ6585)	F(Hα narrow)	F(Hα broad)
58871	Keck	1.00	8.77 ± 0.39	0.2 ± 0.1	44.9 ± 6.8	3.88 ± 0.08	1.84 ± 0.09	119.0 ± 6.0
58905	LDT	3.07	3.70 ± 0.28	< 0.1	16.4 ± 2.9	1.39 ± 0.41	0.87 ± 0.48	51.1 ± 5.0
59105	LDT	2.36	4.17 ± 0.52	< 0.3	10.1 ± 3.7	0.96 ± 0.30	0.89 ± 0.29	41.5 ± 4.8
59189	LDT	2.78	3.56 ± 0.44	< 0.2	9.8 ± 3.8	2.36 ± 0.54	1.84 ± 0.54	36.1 ± 5.1
59468	SAAO	3.05	3.24 ± 0.70	< 1.5	< 16.5	1.87 ± 0.48	1.11 ± 0.48	17.5 ± 6.6
59586	SALT-1	5.75	1.26 ± 0.35	< 0.4	< 8.1	1.10 ± 0.34	0.50 ± 0.34	18.0 ± 4.0
59660	FORS2	3.07	3.10 ± 0.22	< 0.2	9.2 ± 2.4	0.76 ± 0.20	1.07 ± 0.20	32.7 ± 2.1
59821	NOT	3.36	2.24 ± 0.18	0.2 ± 0.1	4.0 ± 3.0	1.70 ± 0.40	1.36 ± 0.41	11.0 ± 2.5
59828	DBSP	2.33	4.45 ± 0.40	< 0.5	10.4 ± 9.0	1.92 ± 0.33	0.45 ± 0.32	43.0 ± 8.1
59853	TNG	1.38	2.94 ± 0.26	< 0.1	2.4 ± 1.5	3.27 ± 0.31	1.92 ± 0.33	22.6 ± 3.0
59881	SALT-2	2.40	3.07 ± 0.36	< 0.1	< 6.4	2.24 ± 0.07	< 0.5	15.0 ± 5.4
59883	SALT-3	6.82	1.28 ± 0.41	< 0.4	< 10.2	1.02 ± 0.35	0.55 ± 0.35	8.1 ± 4.6
60018	FORS2	3.28	3.09 ± 0.17	< 0.1	8.6 ± 2.8	0.44 ± 0.11	0.52 ± 0.13	26.5 ± 3.1

Notes. The broad line fluxes are estimated from the phenomenological Gaussian fitting. For the Hα emission line, the flux value is the integrated flux for the best-fitting double Gaussian model. For the Hβ emission line, most flux values are estimated from the double Gaussian fits, except those where we use a single Gaussian model due to the line having low intensity; in those cases we report fluxes estimated from the single Gaussian model. In order to estimate the scaled flux, any flux value in this table should be multiplied by the corresponding values in column 3.

expression multiplied by β is the corresponding path length. We then sum up the responses generated by each volume element (F) to estimate the total light-curve ($F_{\rm T}(t, r_{\rm in}, r_{\rm out}, \theta_o)$) at a given time. For the biconical cutout, the lower limit on θ is the opening angle (θ_o) of the parsec scale structure. The final profile is given by;

$$F_{\rm T}(t, r_{\rm in}, r_{\rm out}, \theta_o) = \int_{r_{\rm in}}^{r_{\rm out}} dr \int_{\theta_{\rm o}}^{\pi/2} \frac{L_{\rm inc}(t - \frac{d(r,\theta)}{c})}{2r^2} f_1(r, r_{in}) f_2(r, \theta, r_{\rm out}) \cos\theta \sin\theta d\theta \tag{F.1}$$

For all calculations we adopt $\alpha = 0.1$. We specify here that the scheme adopted here is to approximate the response of a $\sim$ parsec scale structure, solely due to the effect of light travel time delays. A proper detailed radiative transfer implementation is out of the scope of this paper.

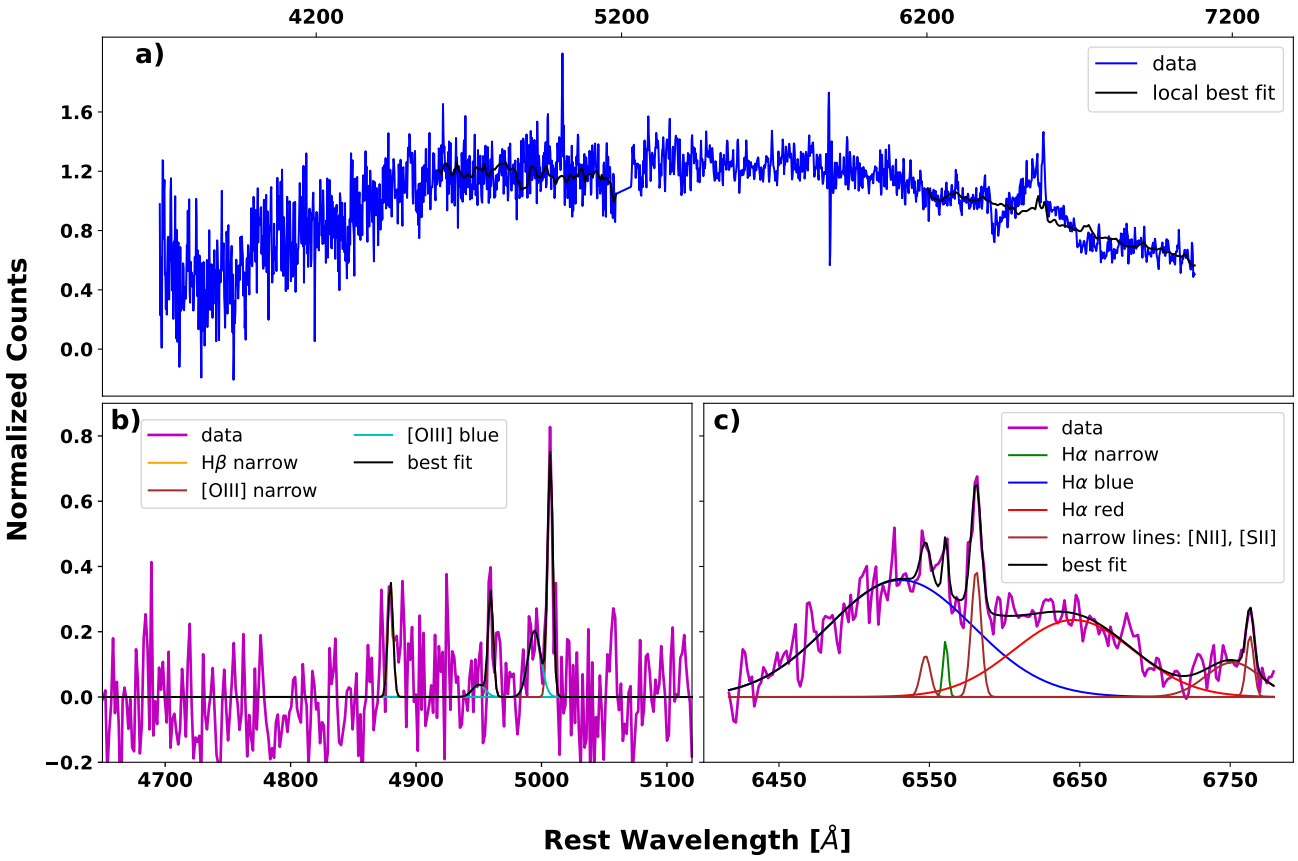

Fig. B.1. The piece-wise analysis of the archival 6dF spectrum taken on 7 February 2005. This spectrum is not flux calibrated. Including a broad Hβ component does not improve the fit. Thus, the best-fit model shows only the Hβ narrow line around 4832 Å.

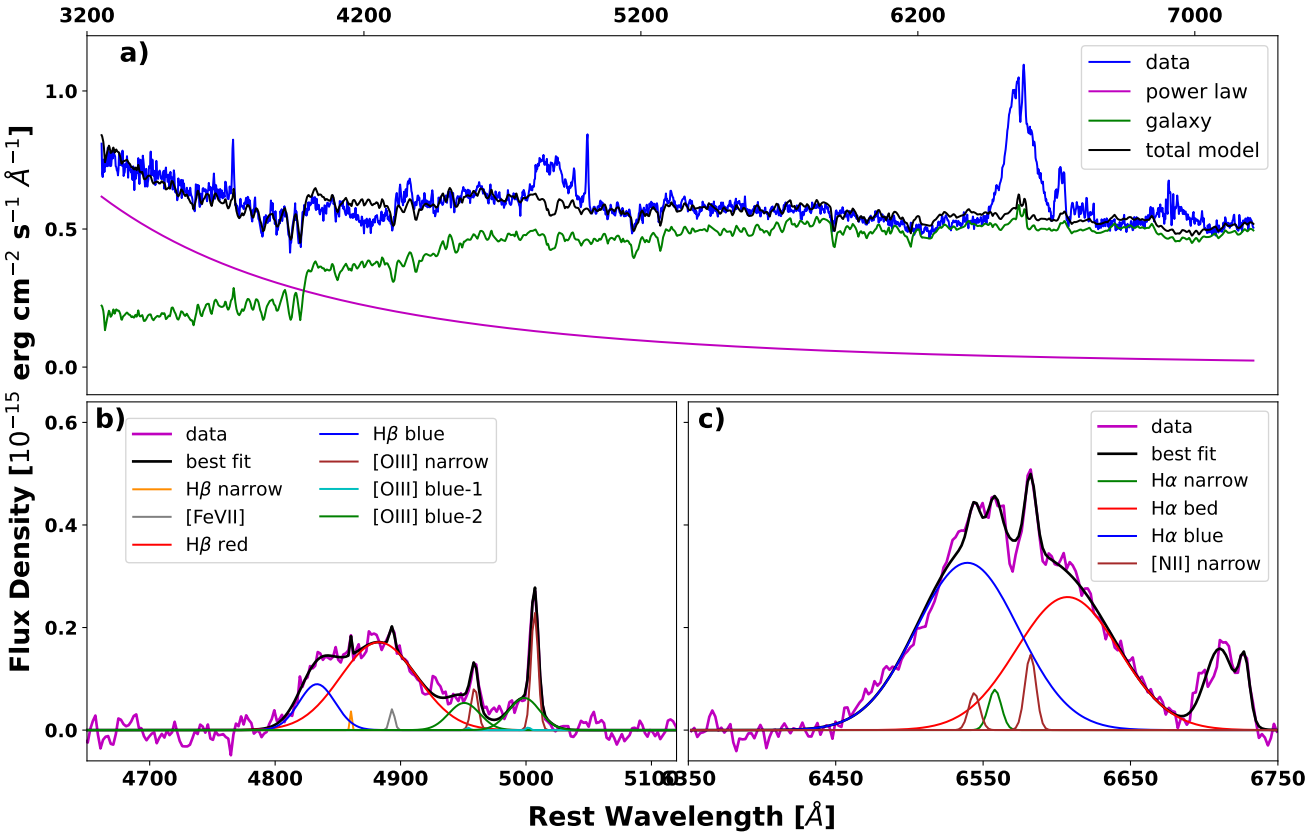

Fig. B.2. Same as Fig. 5 but for the first LDT spectrum taken on 26 February 2020.

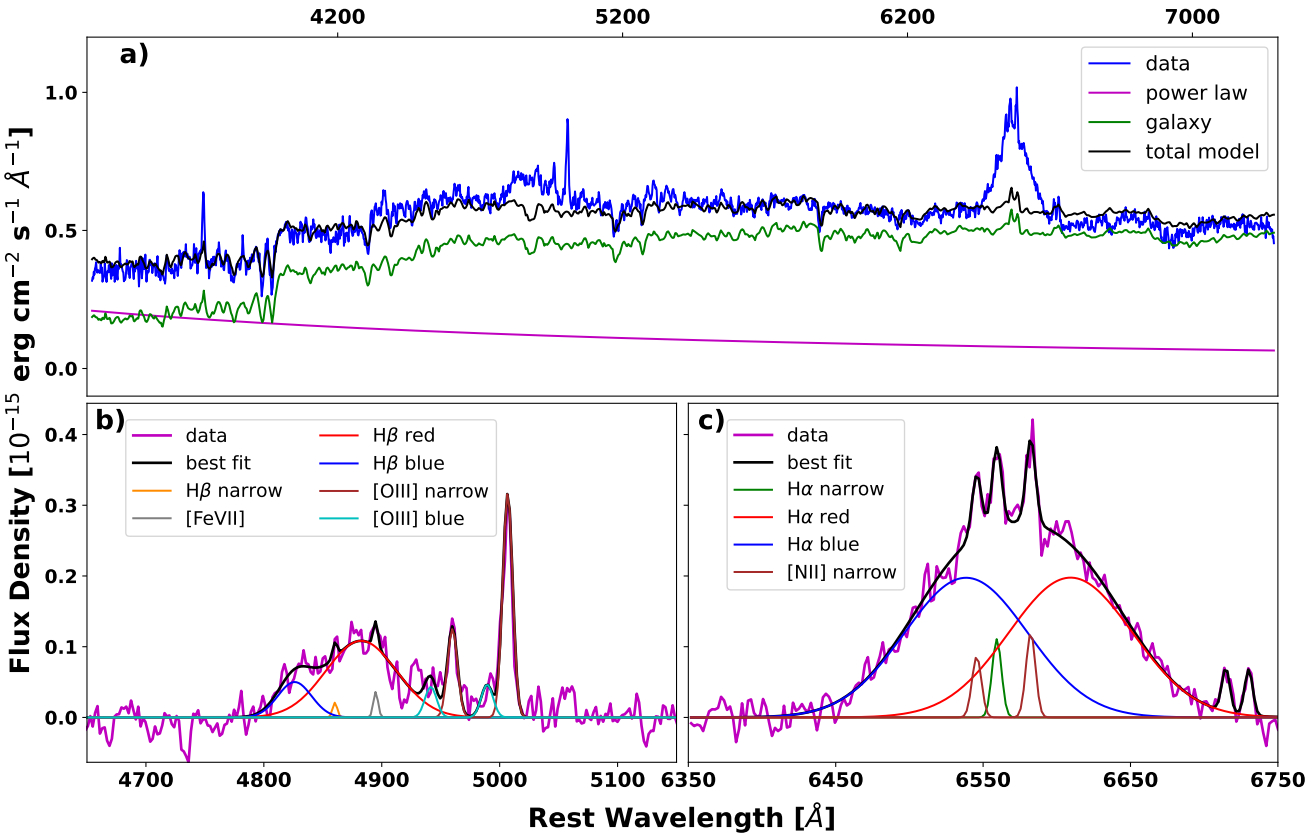

Fig. B.3. Same as Fig. 5 but for the second LDT spectrum taken on 13 February 2020.

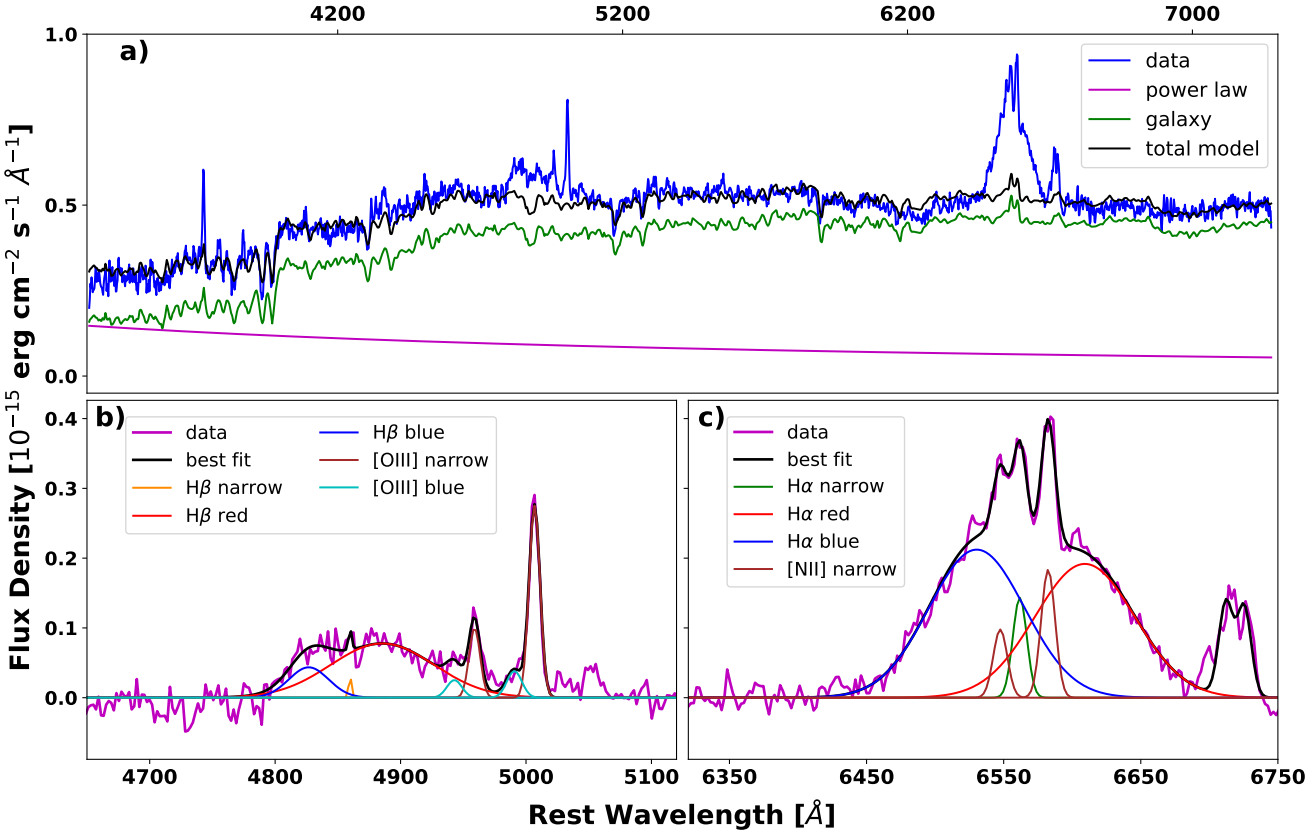

Fig. B.4. Same as Fig. 5 but for the third LDT spectrum taken on 6 January 2020.

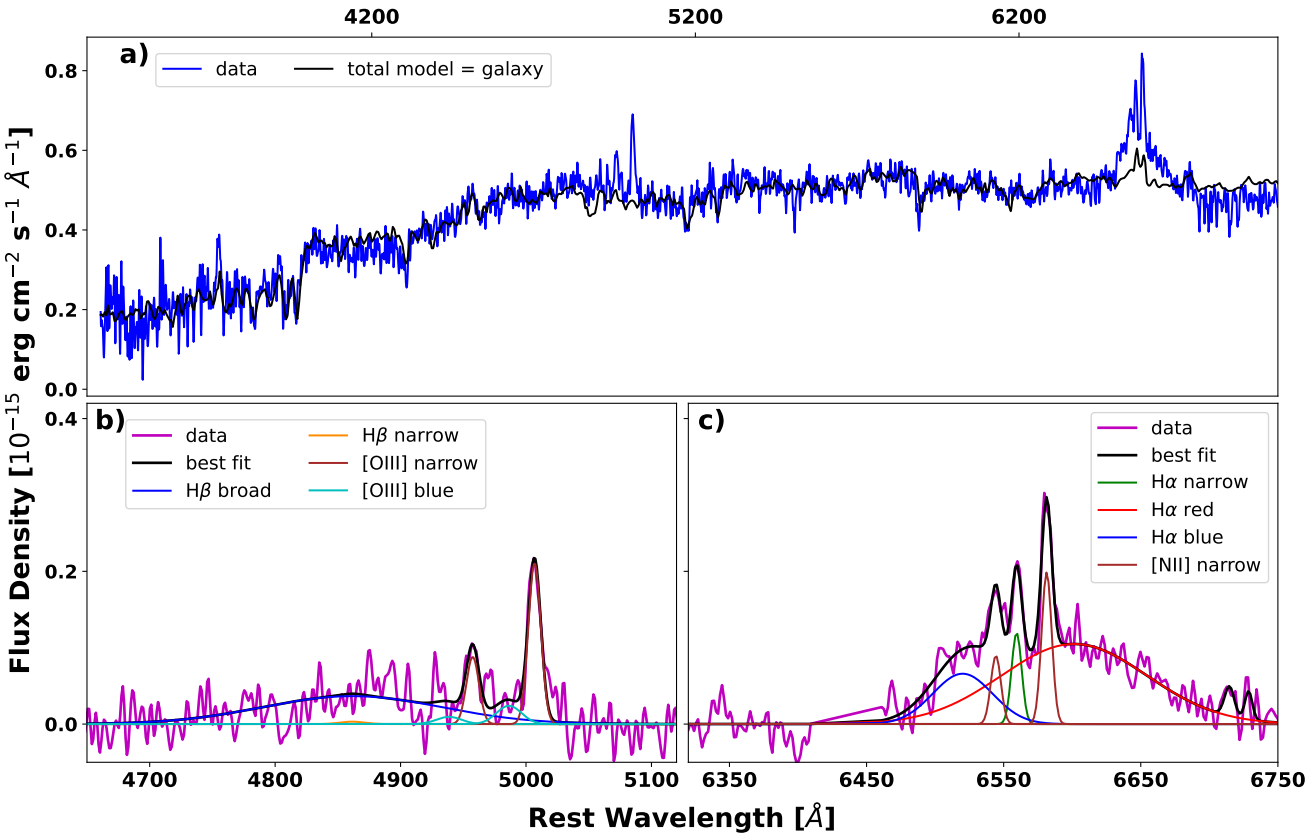

Fig. B.5. Same as Fig. 5 but for the SAAO spectrum taken on 11 September 2021.

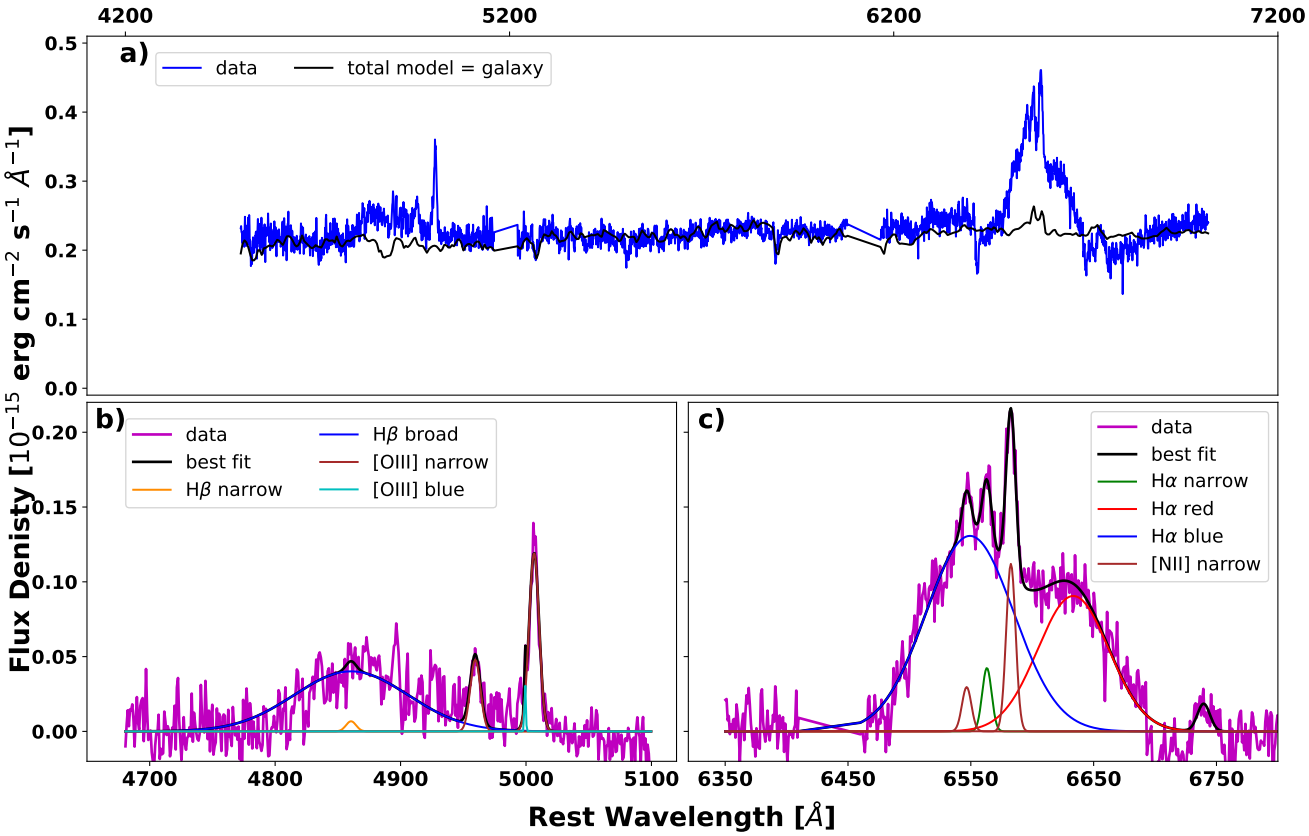

Fig. B.6. Same as Fig. 5 but for the SALT spectrum taken on 7 January 2022.

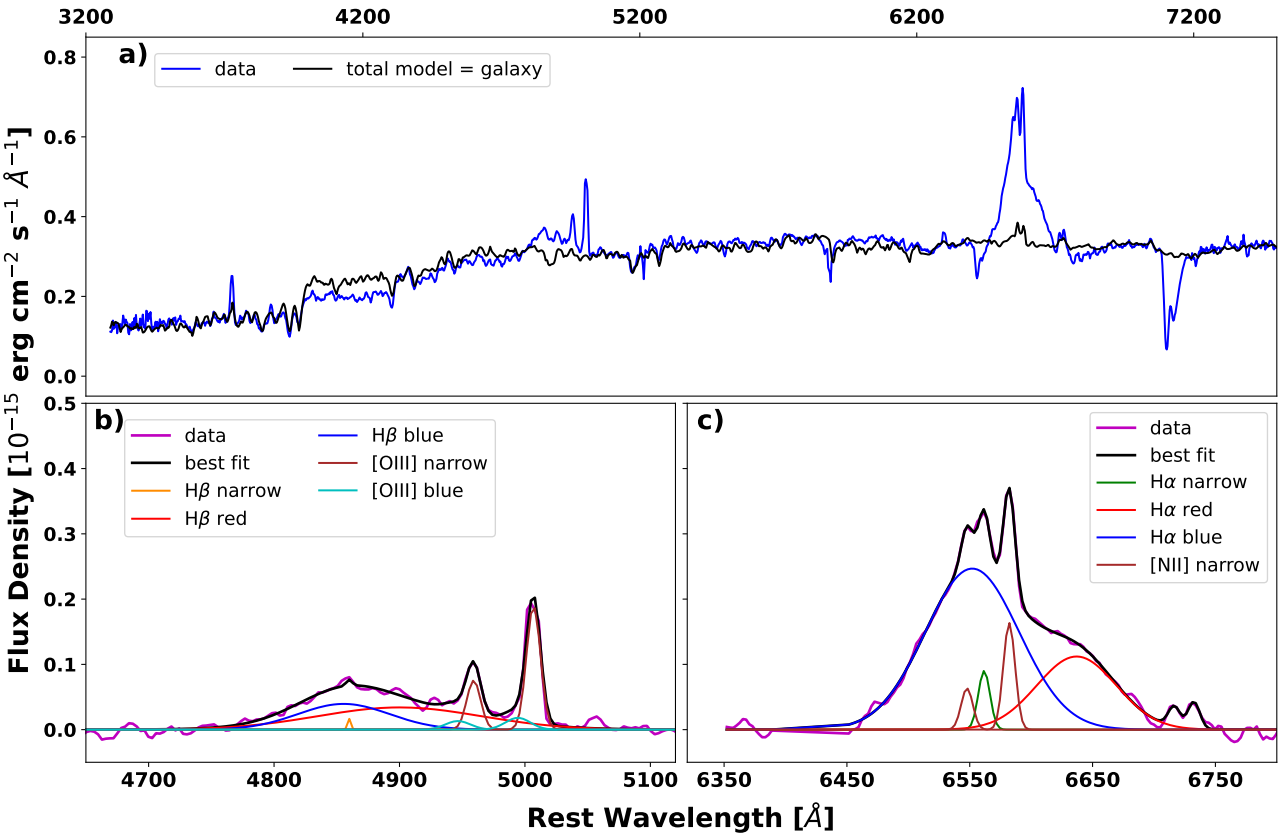

Fig. B.7. Same as Fig. 5 but for the FORS2 spectrum taken on 22 March 2022

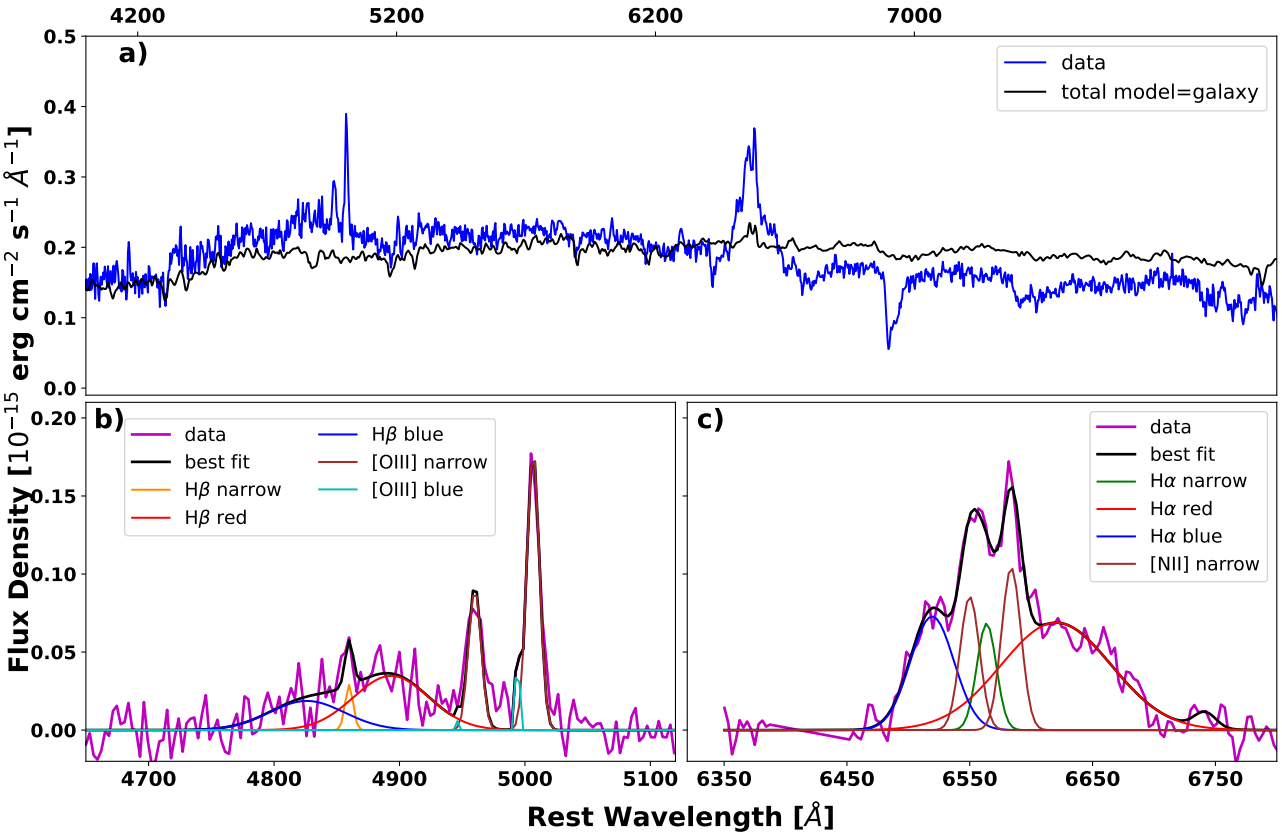

Fig. B.8. Same as Fig. 5 but for the NOT spectrum taken on 22 August 2022

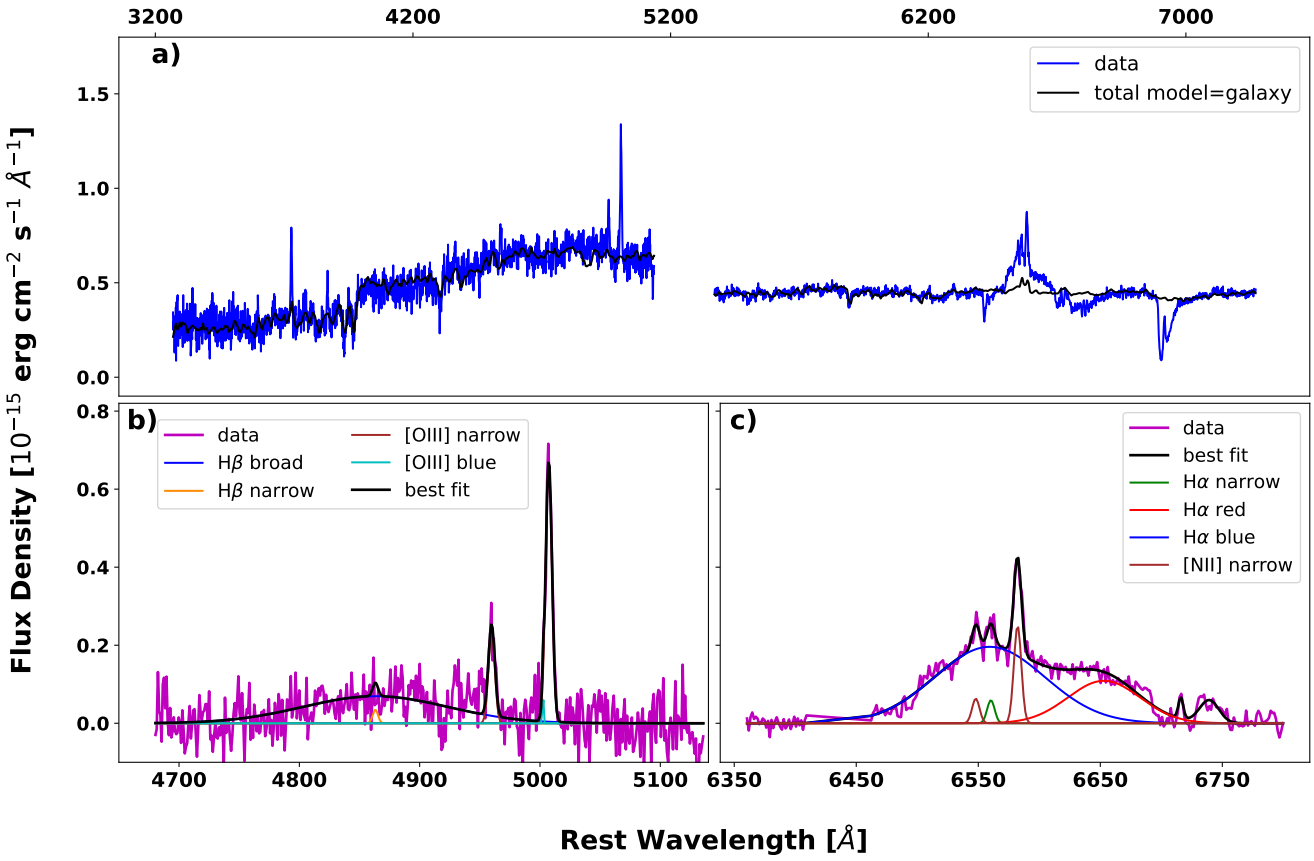

Fig. B.9. Same as Fig. 5 but for the DBSP spectrum taken on 6 September 2022

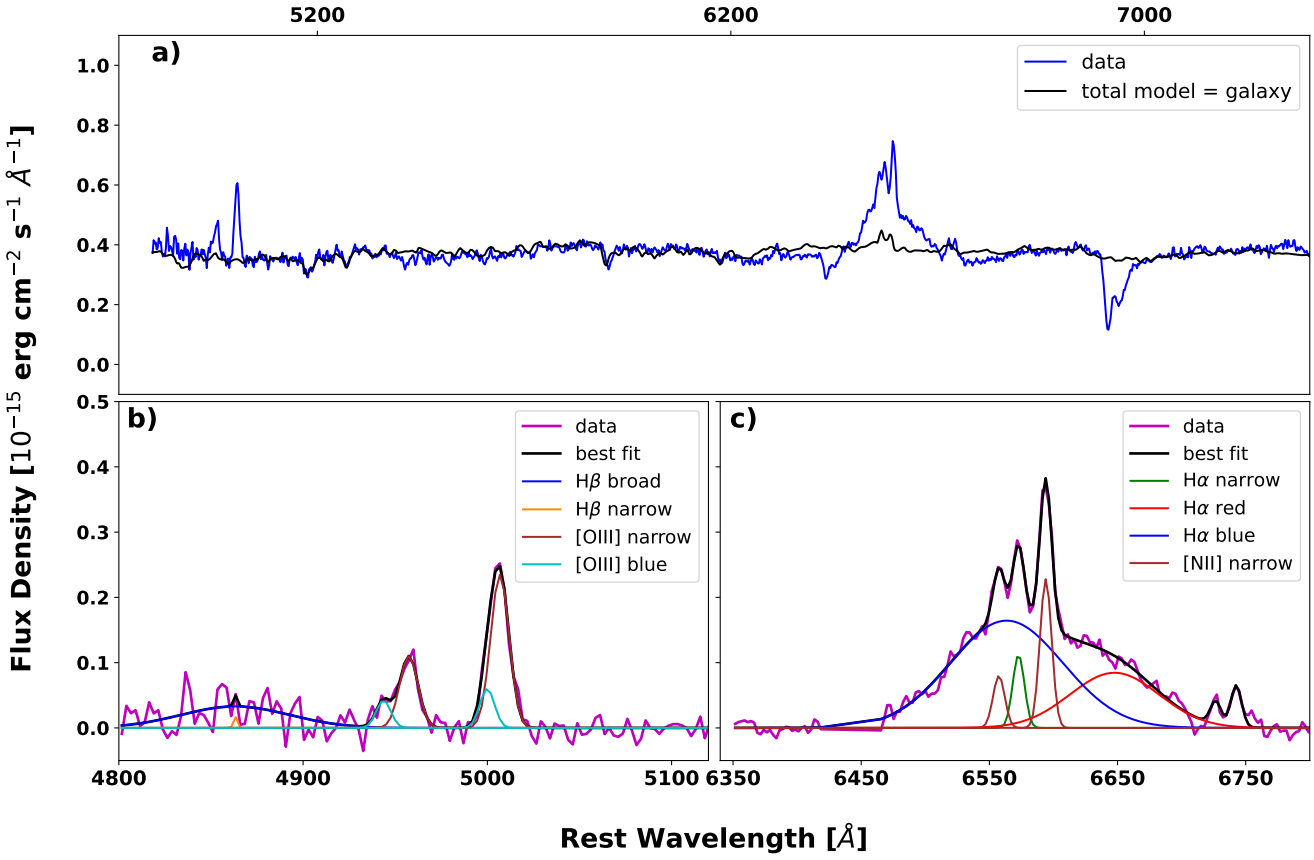

Fig. B.10. Same as Fig. 5 but for the TNG spectrum taken on 1 October 2022

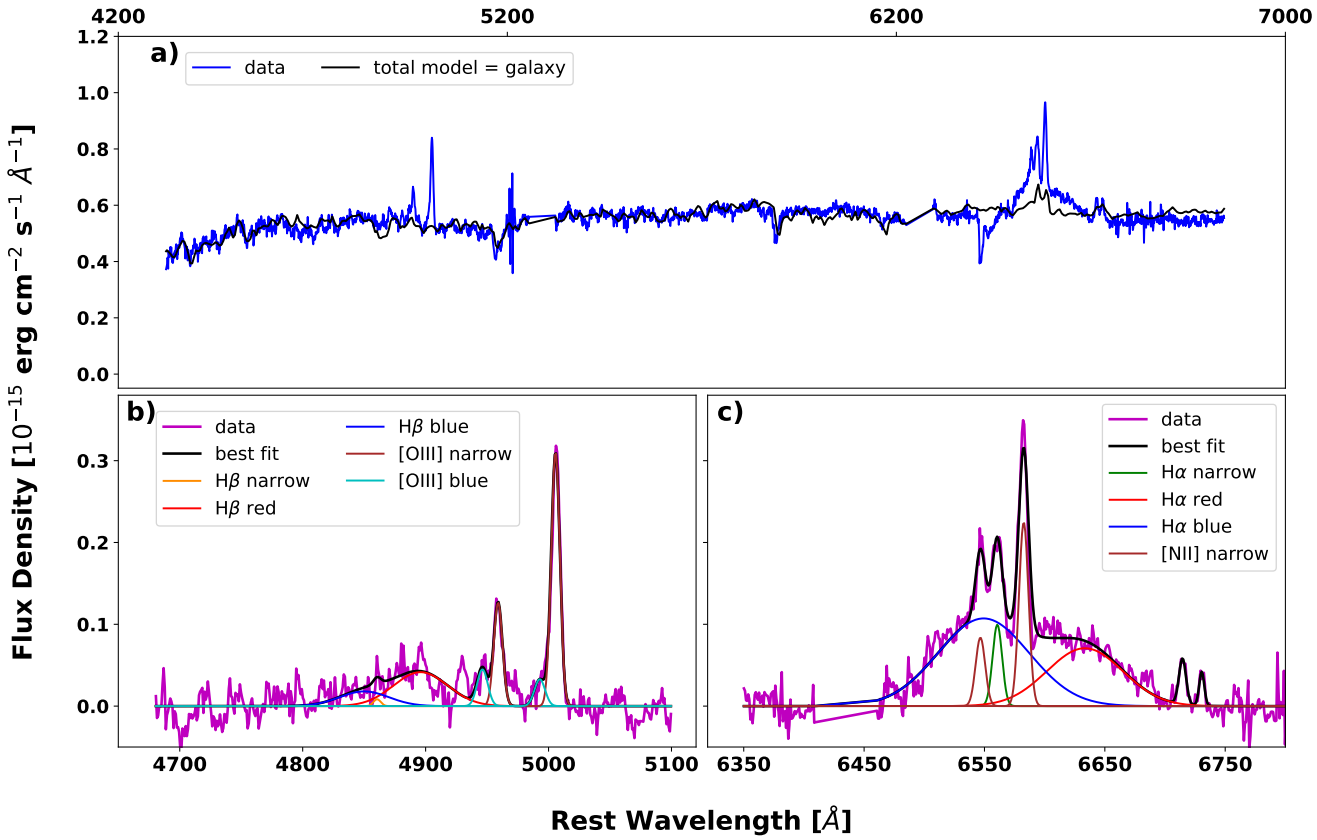

Fig. B.11. Same as Fig. 5 but for second SALT spectrum taken on 29 October 2022.

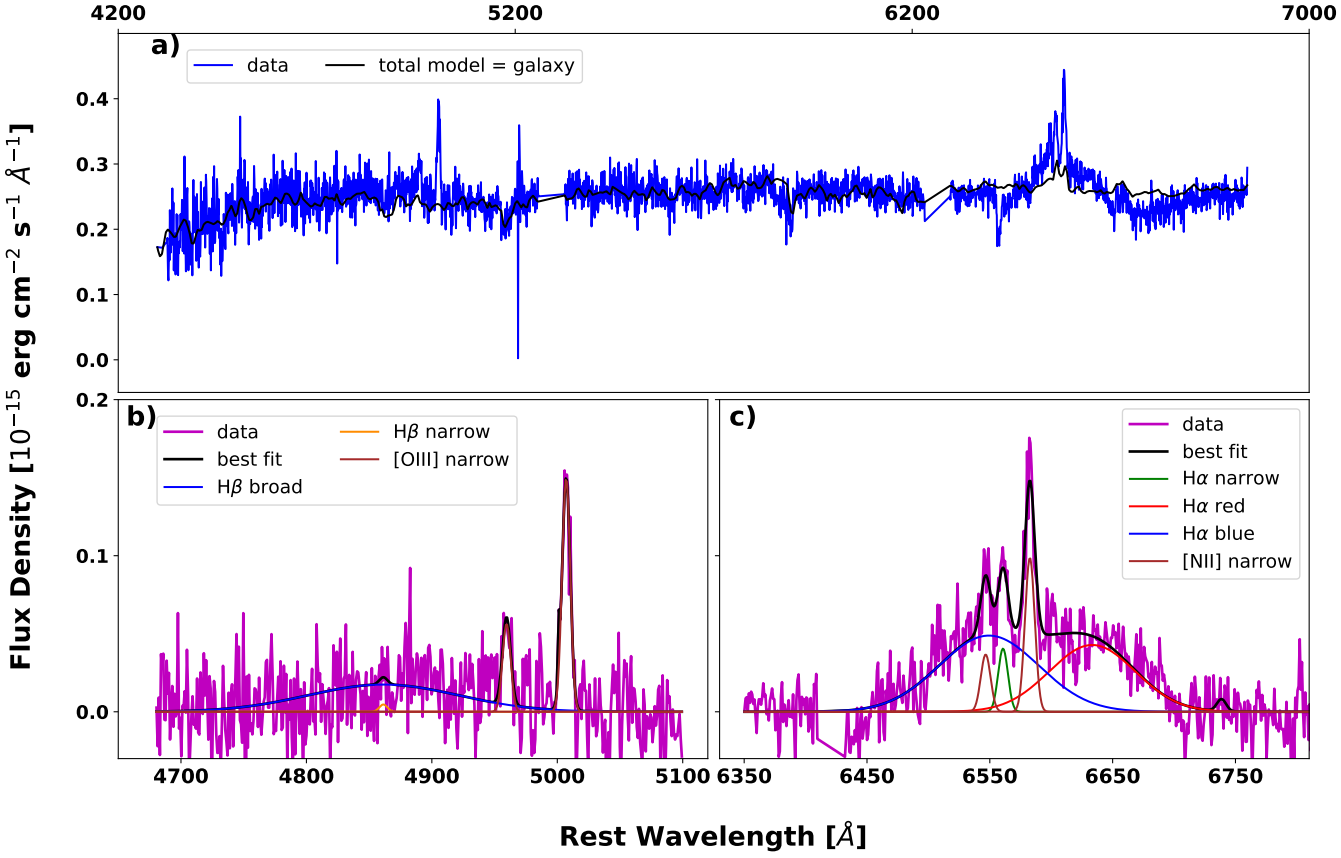

Fig. B.12. Same as Fig. 5 but for third SALT spectrum taken on 31 October 2022

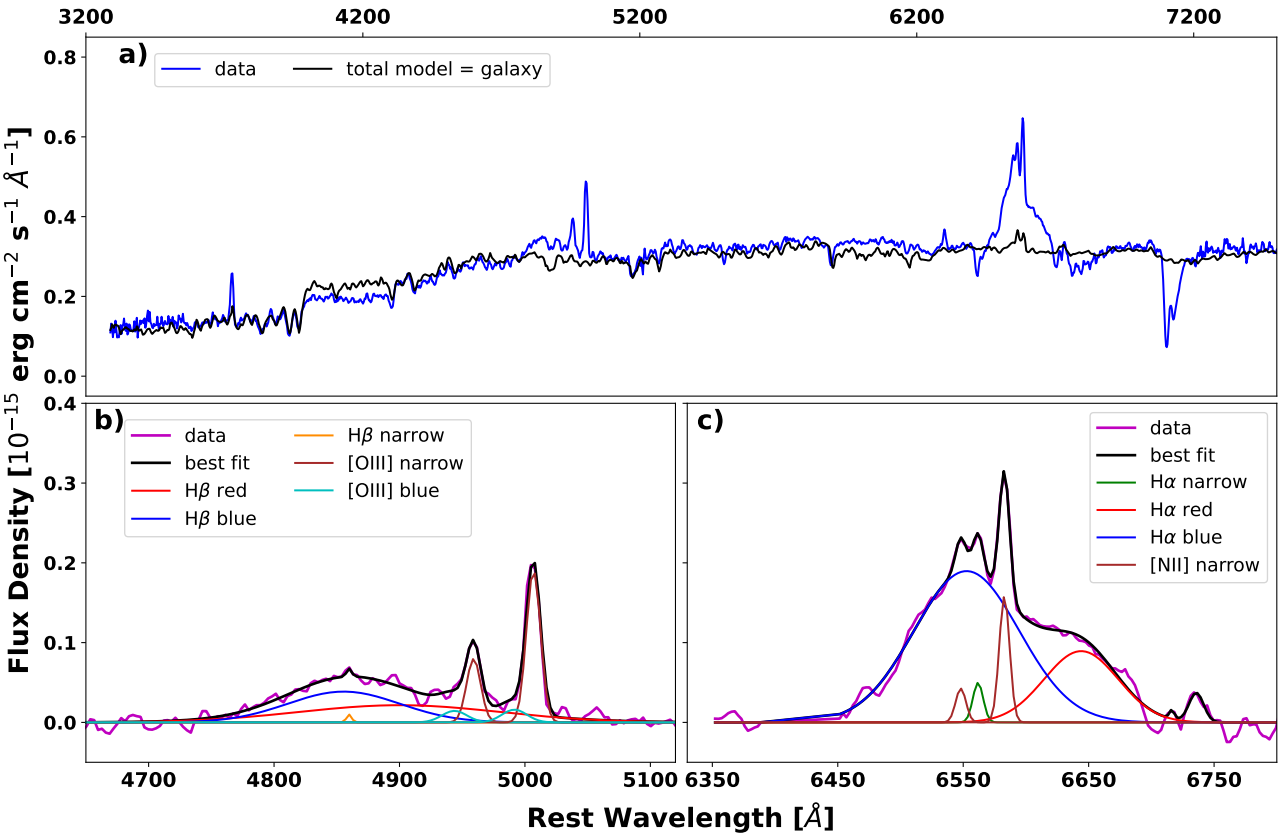

Fig. B.13. Same as Fig. 5 but for the second FORS2 spectrum taken on 15 May 2023

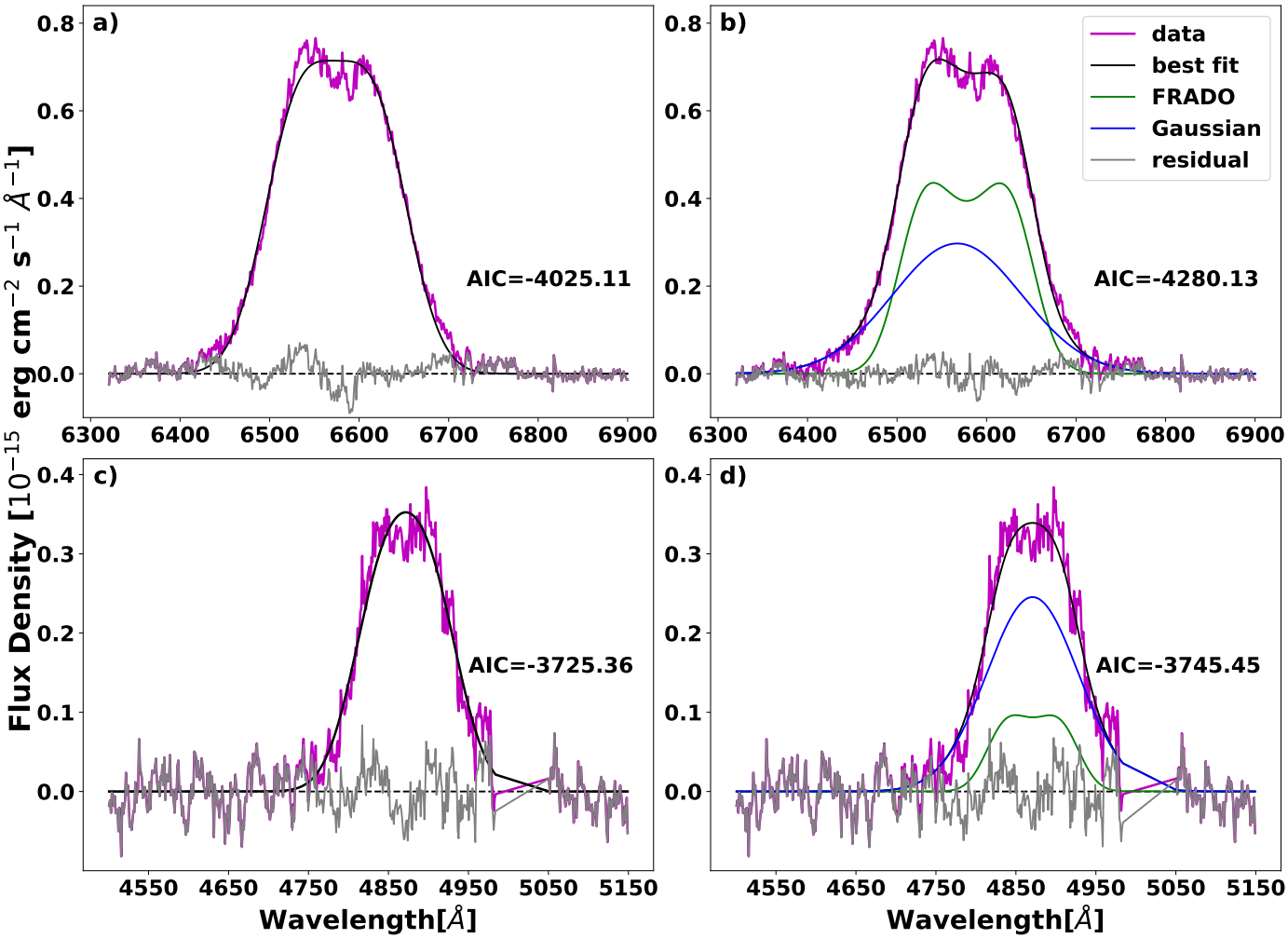

Fig. D.1. The phenomenological fits of the FRADO model, for black hole mass $M_{\rm BH} = 10^7 M_\odot$, metallicity $Z = 5$, $\lambda_{\rm Edd} = 0.01$ and inclination angle $\theta_i = 15.0°$. Plotted is the best-fitting model and the model components for the Hα line fit with (a) a single FRADO profile (b) a FRADO profile + broad Gaussian. Panels (c) and (d) show the best fitting single FRADO profile and FRADO profile + a broad Gaussian, respectively, for the Hβ line. Similar to the diskline profile fits, the addition of the Gaussian improves the fit considerably.

Chapter 4

Detection of changing obscuration AGNs with eROSITA

4.1 Introduction

Changing obscuration AGNs (Section 1.6.3 and Figure 1.2b) exhibit changes in the line of sight absorption ($N_{\rm H}$). Such a change is caused by the transit of discrete clouds across the line of sight to the central X-ray source. The phenomenon of changing obscuration has been reported for roughly two dozen Seyferts in multiple works as mentioned in Section 1.6.3.

eROSITA, the soft X-ray telescope (Predehl et al., 2021) onboard the Russian SRG spacecraft (Sunyaev et al., 2021) launched in mid-2019 is detecting multiple SMBH transient events. eROSITA has undertaken successive all-sky scans (eRASS) and detected multiple extreme X-ray variable transients. It is likely that there exists a statistically significant sample of changing obscuration events already in the archive generated by its all-sky scans. Analyzing the frequency of occurrence of these events in the archival dataset could provide insights into the statistics associated with CO transitions in a sample of Seyferts, including: (1) the prevalence of transitions into Compton-thin or Compton-thick obscuration from an unobscured source (or vice versa), and (2) the prevalence of transitions from Compton-thin to near Compton-thick obscuration (or vice versa). Additionally, successive follow-up campaigns of confirmed events with dense X-ray spectroscopic monitoring while the event is happening would help constrain the physical properties and possibly origins of individual clouds causing the obscuration. Specifically, we are interested in (1) the distance of the clouds from the central black hole, (2) the morphology of the cloud, and (3) the source of obscuration: torus, BLR, or an outflow. Several studies (Section 1.6.3) have revealed the nature of the obscuring clouds for a few individual objects. However, a statistical study of such events is required as it can potentially provide constraints on clumpy-torus model parameters such as the distributions of clouds (Nenkova et al., 2008; Markowitz, Krumpe, and Nikutta, 2014).

In this project, we aim to develop a code to assess our ability to detect a large, statistically significant sample of changing obscuration events using the repeated all-sky scans from a soft X-ray telescope, specifically eROSITA. Given the operational parameters of eROSITA during its all-sky scanning mode, there are anticipated challenges pertaining to the spectral counts. Low exposure times and vignetting resulting from the scanning pattern and strategy of eROSITA (Merloni et al., 2012) result in low spectral counts; hence there will be large uncertainties on measured counts. Consequently, we can only perform such a study on a subset of the soft X-ray brightest targets.Thus an effective detection strategy for COAGN transitions anticipating low photon counts is required. We intend to develop a reliable techniques for detection of these sources in eROSITA archives, and optimize the use of the real-time follow-up resources by ruling out false detections.

4.2 X-ray hardness ratio

A change in line of sight, lowly-ionized/neutral absorption modifies flux at different X-ray bands differently. With increasing absorption, the X-ray spectra undergoes a change in shape where the soft-X-rays undergo strong attenuation (Figure 4.1), inducing a low-energy cutoff which is dependent on the value of $N_{\rm H}$. The relative X-ray spectral shape due to changing absorption is measured mathematically by defining the quantity hardness ratio. The X-ray hardness ratio can be mathematically quantified through multiple expressions. In this work, we consider two different expressions of hardness ratio:

- HR1: A simple ratio of the counts in two bands:

$$HR1 = \frac{C_2}{C_1} \tag{4.1}$$

- HR2: The ratio of the counts difference between two bands to the total number of counts in the two bands:

$$HR2 = \frac{C_2 - C_1}{C_2 + C_1} \tag{4.2}$$

Here, C_2 is either the counts or flux in the high-energy band and, C_1 is the same in the low energy band. In this project, we check if such a change in hardness ratio induced by $N_{\rm H}$ transitions can be detected with eROSITA, by comparing hardness ratios in two adjacent eRASS scans, given eROSITA mission parameters.

4.3 Methodology

We aim to establish the particular transitions we can possibly detect from consecutive all sky scans from eROSITA (eRASS). This is done by simulations of spectra, using eROSITA instrument response files and backgrounds. Subsequently, hardness ratios values are calculated from the simulated spectra using the defined bands in the X-ray spectra. We adopt the following methodology to simulate the levels of absorption:

- A given level of flux for an initially unobscured spectrum is selected. We perform the simulations for three levels of 2–10 keV flux values: 10 mCrab, 1 mCrab, and 0.5 mCrab.
- For each level of fluxes we select twenty values of column density, spread uniformly between $\log N_{\rm H,min}$ and $\log N_{\rm H,max}$, where $N_{\rm H,min} = 0.07 \times 10^{22}$ cm^{-2} and $N_{\rm H,max} \simeq 70.0 \times 10^{22}$ cm^{-2}.
- We simulate $N_{\rm sim}$=400 spectra for each of these obscuration levels increase the levels of obscuration.

Our basic simulation model in generic notation of X-ray spectral analysis is:
Model = `tbabs`$\times$(soft-powerlaw + `ztbabs`*powerlaw).
Typically, AGN with a higher column density of circumnuclear gas distribution ($N_{\rm H}$ approaching 10^{24} cm^{-2}) would exhibit signatures of Compton reflection (Section 1.4.2) mostly dominant in the hard X-ray band ($E > 5$ keV). However, the eROSITA effective area drops by a factor of 10 above 2 keV, and hence is insufficient to detect the Compton reflection features.

Here, `tbabs` represent the Galactic absorption, the soft-power law is the component that originates from (Section 1.4.2 and e.g. Bianchi, Guainazzi, and Chiaberge, 2006) distant scattering,

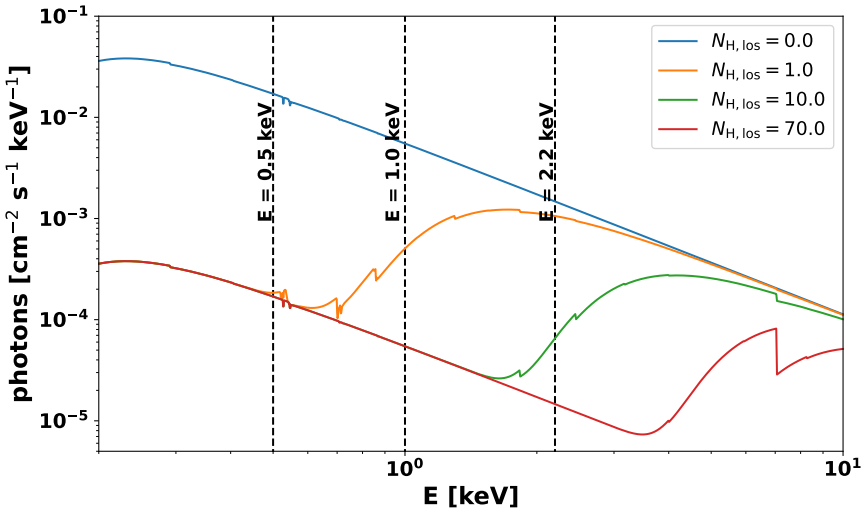

FIGURE 4.1: Model spectra of changing obscuration AGN: variation of the X-ray spectrum with changing N_H in the 2–10 keV energy range. The vertical dashed lines represents the boundaries of the energy bands that we use to calculate the hardness ratios.

the power law denotes the direct coronal emission, and `ztbabs` is the absorption from the intrinsic obscurer. For all simulations the Galactic absorption was kept fixed at $N_{H,Gal} = 10^{20}$ cm^{-2}. We assume a representative photon index value of $\Gamma = 1.7$ for both the the coronal and the scattered power laws. This value is lower than the typical value of $\Gamma = 1.9$, but it can potentially mimic the excess flux contributed by the Compton hump in the hard X-ray band. However, the normalization of the scattered power law was kept fixed at 10^{-2} times that of the coronal power law. We assume an on-axis exposure of 400 s unless stated otherwise. In real scenario the number of counts at a given exposure time can be also be effected by off-axis vignetting effects (Predehl et al., 2021), thus reducing the effective exposure time on the instrument. Thus, this exposure time should be considered to be a conservative upper limit for each *eROSITA* all-sky scan. However, optimistically higher exposure times (approaching ∼10 ks) are available for sources within a few degrees of the orbital pole. We use the Interactive Spectral Interpretation System (ISIS)[1] to simulate the datasets, using the heasoft function `fakeit()`. We use eROSITA backgrounds obtained from real all-sky scan observations to simulate the datasets.

4.3.1 Evaluation of counts

To estimate the hardness ratios of the source, we need to estimate the number of source counts in the bands of interest. This process involves the estimate the number originating from the source counts (C) in the spectrum. This process requires the subtraction of the background counts (B) from the total spectrum (S). Thus the source count in a given bin is given by $C_i = S_i - B_i$. However, in this case it is possible given the low exposure times and possibly low source flux that the counts are Poission-variable, thus each of S_i and B_i are Poisson variables. Thus the estimation of the error on the background subtracted spectrum is not straight-forward. Here we adopt the the approach of Buchner et al. (2022) to evaluate the error bar for the source and the background counts. For a given Poisson-distributed count value of C_0, the upper error bar is given by (Gehrels, 1986; Buchner et al., 2022)

$$\sigma_{C_0} = \sqrt{C_0 + 0.75} + 1 \tag{4.3}$$

[1] https://space.mit.edu/cxc/isis/

N_H	initial unobscured flux: 10 mCrab		initial unobscured flux: 0.5 mCrab	
	mean(N)	std. dev. of mean (σ_N)	mean(N)	std. dev. of mean (σ_N)
0.07	2.8×10^4	167	1381	40
11.1	940	30	47	9
69.5	422	22	24	7

TABLE 4.1: In this table we present the mean of the total counts (N) generated for 400 spectral simulations and the standard deviation (σ_N), for unobscured flux levels of 10 mCrab and 0.5 mCrab. For each of the initial unobscured flux level, we show the average counts and the standard deviations for three stages of obscuration.

The lower error bar is given by

$$\sigma_{C_0} = \sqrt{C_0 - 0.25} \tag{4.4}$$

However, we adopt the same approach of Buchner et al. (2022) and consider the value of the upper error bar as the symmetric error bar for all cases. This approximation over-estimates the error in all cases. Simultaneously, this also makes our detection estimate conservative, thus minimizing the possibility of wrongful detection of sources. Thus, for the background subtracted source spectrum, the error bar in the i-th bin is given by the source and the background error added in quadrature:

$$\sigma_{C_i} = \sqrt{\sigma_{S_i}^2 + \sigma_{B_i}^2} \tag{4.5}$$

For a given energy band extending from a lower energy E_l to a higher energy the energy E_h the counts in the individual bins are added: $C_{\rm band} = \Sigma_i C_i$. The error bars on the counts in the given band is given by

$$\sigma_{C_{band}} = \sqrt{\Sigma_i \sigma_{C_i}^2} \tag{4.6}$$

We selected four bands for the estimation of the hardness ratios. The counts in the bands are: C: 0.2–0.5 keV, D: 0.5–1.0 keV, F: 1.0–2.2 keV, and, N: 2.2–10.0 keV. These bands are used to calculate three hardness ratios. We define $HR1_{\rm DC} = D/C$, $HR1_{\rm FD} = F/D$, and $HR1_{\rm NF} = N/F$. The error bars of each of these bands are given by

$$\sigma 1_{\rm DC} = HR1_{\rm DC}\sqrt{(\sigma_D/D)^2 + (\sigma_C/C)^2} \tag{4.7}$$

and is defined similarly for the other bands.

We also calculate the hardness ratios according to the second definition:
$HR2_{\rm DC} = (D-C)/(D+C)$, $HR2_{\rm FD} = (F-D)/(F+D)$, and $HR2_{\rm NF} = (N-F)/(N+F)$. In this case the error on the hardness ratio is given by

$$\sigma 2_{\rm DC} = \frac{\sqrt{(\sigma_D)^2 + (\sigma_C)^2}}{(C+D)^2} \times C0 \tag{4.8}$$

where $C0 = C$ if $C > D$ and $C0 = D$ if $C < D$. A similar definition applies to the other bands.

4.3.2 Detection limits: a consequence of Poisson statistics

The data simulation process involves the generation of photon counts by applying a stochastic Poissonian process which is dependent on the characteristics of the detector (parameterized by the response and the effective area functions). This would invoke variations in the number of counts in a given bin, band, and spectrum at each instance of the spectral simulation. The variations are significant mostly when the intrinsic unobscured flux is low (Table 4.1). This type of

fluctuation in counts can also impact the hardness ratio values. Thus for multiple spectra simulated under the same conditions (exposure time, instrument, spectral model, etc.), the stochastic Poisson nature of the processes will produce a spread in the hardness ratio values and the uncertainties. For two spectra corresponding to a line of sight absorption with columns $N_{\rm H,i}$ and $N_{\rm H,j}$, we consider the two obscuration states distinguishable when the error bars between the corresponding hardness ratio values do not overlap. However, because of the spread in the values HR- and its uncertainty, multiple ($N_{\rm sim}$) instances of simulation of the same model under the same conditions might result in detection in one spectrum but a non-detection in another set of spectra. This effect would mostly dominate in the low-count regime. It is therefore important to ascertain that the change in observed hardness ratio is due to change in absorption levels and not an artefact of the photon statistics or the systematics associated with spectral fitting.

It is thus possible to assign a probability of a certain transition between one level of $N_{\rm H}$ and another taking into account the above-mentioned Poissonian effects. This can be accomplished by simulating spectra in bulk and subsequently counting the instances of successful detections. For a given spectral transition, T_{ij} : $N_{\rm H,i} \longrightarrow N_{\rm H,j}$, a positive detection means no overlap between the upper and the lower limits of the hardness ratios estimated for two obscuration states: $HR_i + \sigma_i < HR_j - \sigma_j$ or $HR_i - \sigma_i > HR_j + \sigma_j$. For a large number of simulated spectra, $N_{\rm sim}$, we count the number of instances $N_{\rm no-overlap,i,j}$ where no overlap happens between the hardness ratio ranges. Thus for a large number of simulations, we define the probability of detection as

$$P(T_{ij}) = \frac{N_{\rm no-overlap,i,j}}{N_{\rm sim}} \tag{4.9}$$

We plot these values in form of a map. We describe the methodology to read such a map in Figure 4.2.

We note that this probability is strongly dependent on the evaluation of the uncertainty on the hardness ratio values, which in turn depend on the correct error propagation, given a hardness ratio definition.

4.4 Results

4.4.1 The hardness ratios' dependence on $N_{\rm H}$

In this chapter, we discuss only the calculations of hardness ratio defined via Equation 4.2. The results from Equation 4.2 are discussed in Appendix A. However, both hardness ratio definitions yield qualitatively similar results. The hardness ratios calculated using the different bands are sensitive to different levels of line of sight absorption. The hardness ratio estimates using the bands in lower X-ray energies $E < 2.2$ keV (C, D, and F) are exhibit significant variation in the lower values of absorption ($N_{\rm H} \lesssim 10^{23}$ cm^{-2}, Figure 4.3b). However, for hardness ratios calculated using the higher energy bands, significant variations in the same is observed for higher values of absorption ($N_{\rm H} \gtrsim 5 \times 10^{22}$ cm^{-2}, Figure 4.3b). This variation in the sensitivity of the hardness ratio calculated from different energy bands indicates the importance of all of them to detect transitions across low and high $N_{\rm H}$ regimes.

4.4.2 Flux-dependent results

In this subsection, we describe the range of transitions that can be detected for a given flux level. The uncertainty in the hardness ratio increases with the decrease in count rates resulting from unobscured flux drops as shown in Figures 4.3b, 4.4b, and 4.5b, thus, decreasing likelihood of detecting transitions in $N_{\rm H}$. We discuss the results from each flux levels below:

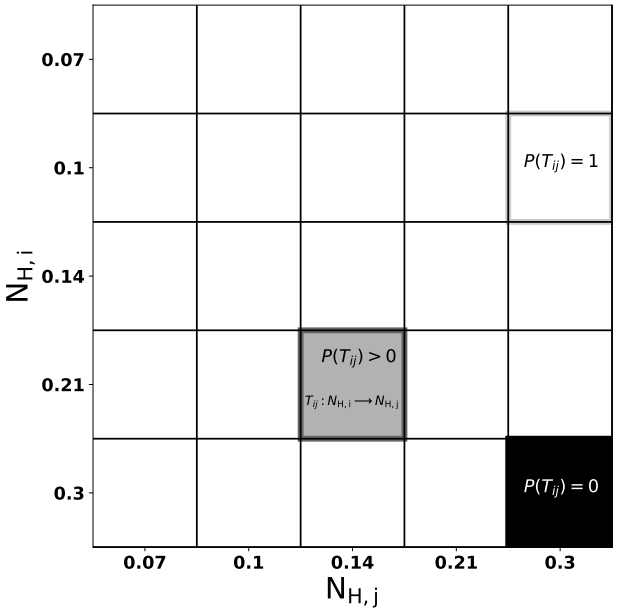

FIGURE 4.2: Probability map indicating likelihood of detection of a given obscuration transition. The line of sight values on the vertical axis, $N_{\rm H,i}$, represent the initial value of absorption. For a given value of $N_{\rm H,i}$, if we move horizontally in $N_{\rm H,j}$, the shade of the cell located at $(N_{\rm H,j}, N_{\rm H,i})$ is representative of the probability of detection of the transition $T_{ij} : N_{\rm H,i} \longrightarrow N_{\rm H,j}$. The colors of the cells vary from white to black via shades of grey. A white color of a cell implies $P(T_{ij}) = 1$ and black implies $P(T_{ij}) = 0$. The grey shades imply intermediate values of $0 < P(T_{ij}) < 1$.

- **F_{2-10} = 10 mCrab:** In general such a high unobscured flux is found only for a few nearby AGNs (e.g. Centaurus A, Beckmann et al., 2011). Thus, the results obtained using this flux level can be considered as either theoretically representative values or cases limited to only the highest-flux AGNs. Following the procedure of reading the probability maps described in Figure 4.2, we describe the physical implications. The maps are quite effective in demonstrating the importance of each sub-band hardness ratio definitions as each of these sub-band combinations allow us to explore different regions of the probability map, which is plotted in Fig. 4.6. The hardness ratio values involving the C & D bands – $HR1_{\rm DC}/HR2_{\rm DC}$ – are found to be effective in determining the transitions from mildly-obscured or unobscured states ($\sim 10^{20}$ cm^{-2}< $(N_{\rm H,i}, N_{\rm H,j}) \lesssim 10^{22}$ cm^{-2}) to other mildly-obscured (Compton-thin), states and to highly-obscured states approaching the Compton thick regime ($N_{\rm H} > 10^{23}$cm^{-2}). However, it is ineffective in determining transitions happening within the $\sim 10^{22}$ cm^{-2}< $(N_{\rm H,i}, N_{\rm H,j}) \lesssim 10^{24}$ cm^{-2} regime. Both $HR1_{\rm FD}/HR2_{\rm FD}$ and $HR1_{\rm NF}/HR2_{\rm NF}$ become effective in uncovering transitions in both the milder and the heavier-obscuration domains.

- **F_{2-10} = 1.0 mCrab:** Upon decrease of the flux by an order of magnitude to 1 mCrab, the increase in Poisson counts error increases the length of the error bars on the resulting hardness ratio values. We find that the $HR1_{\rm DC}$ value is unable to explore most parts of the parameter space, as plotted in Fig. 4.7(a). $HR1_{FD}$ can successfully detect transitions to the $N_{\rm H} > 5.5 \times 10^{22}$ cm^{-2} regime from the 4–10$\times 10^{21}$ cm^{-2} regime, and to the $N_{\rm H} < 1.3 \times 10^{22}$ cm^{-2} regime from all the mildly-obscured (<10^{21} cm^{-2}) states (Figure 4.7(b)). The transitions in these regions at the given flux levels are not detected by the $HR1_{DC}$ and $HR1_{NF}$ values. $HR1_{NF}$ can detect transitions from only the mildly-obscured ($\lesssim 9 \times 10^{21}$ cm^{-2}) to mostly the Compton-thin obscured states with $\sim 9 \times 10^{21} \lesssim N_{\rm H} \lesssim 5 \times 10^{22}$ cm^{-2}. This is incidentally the region that is not covered by $HR1_{\rm FD}$ and $HR1_{\rm DC}$.

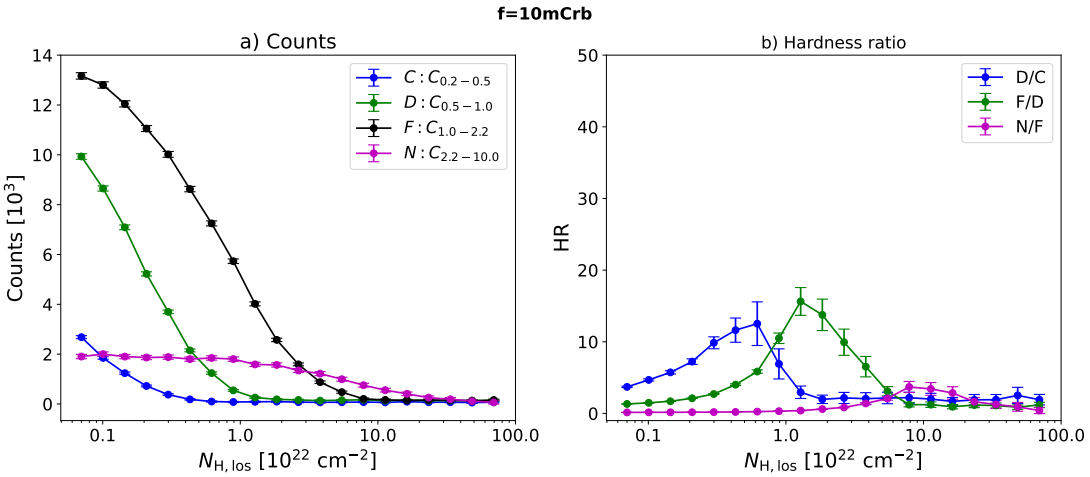

FIGURE 4.3: Simulated count rates in the different bands and the resultant hardness ratios as a function of N_H for a flux level of 10 mCrab. The hardness ratios are calculated using the expression in equation 4.2

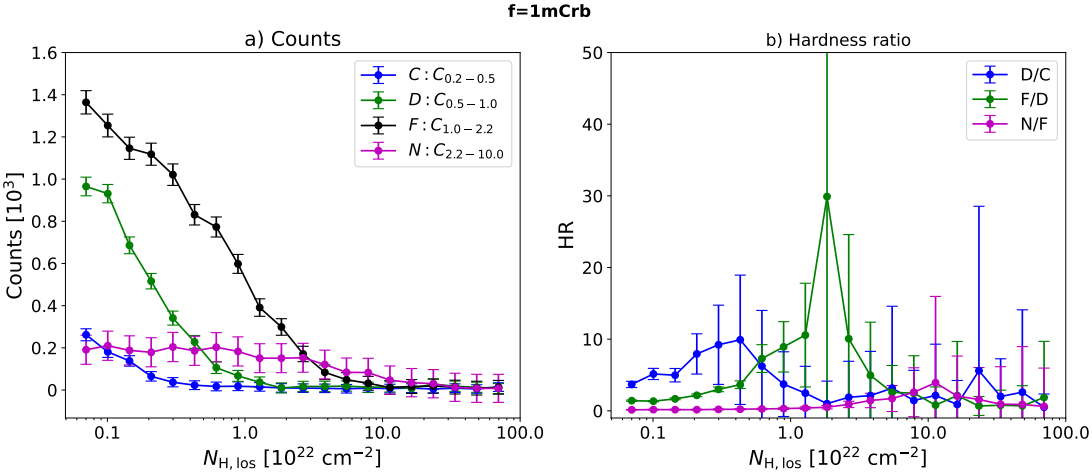

FIGURE 4.4: Same as figure 4.3 but for an unobscured flux of 1 mCrab.

- **F_{2-10} = 0.5 mCrab:** For a flux level of 0.5 mCrab, only the $HR1_{FD}$ band was able to detect N_H transitions, and limited only to the transitions starting and ending in the $N_H < 10^{22}$ cm^{-2} regime (Figure 4.5).

The simultaneous use of the different bands for calculating HR values become important for successful detection as they probe N_H transitions in different regions of the N_H space (as shown by Figures 4.6, 4.7, and 4.5)

4.5 Summary

- Different hardness ratio values utilizing different bands are needed to detect to cover all possible transitions in N_H.
- The Poisson stochastic process associated with data generation has been found to drastically vary the number of counts in the low count region. Thus, a hardness ratio / error estimation based on the counts is not reliable enough to ascertain a HR change due to N_H-variability.

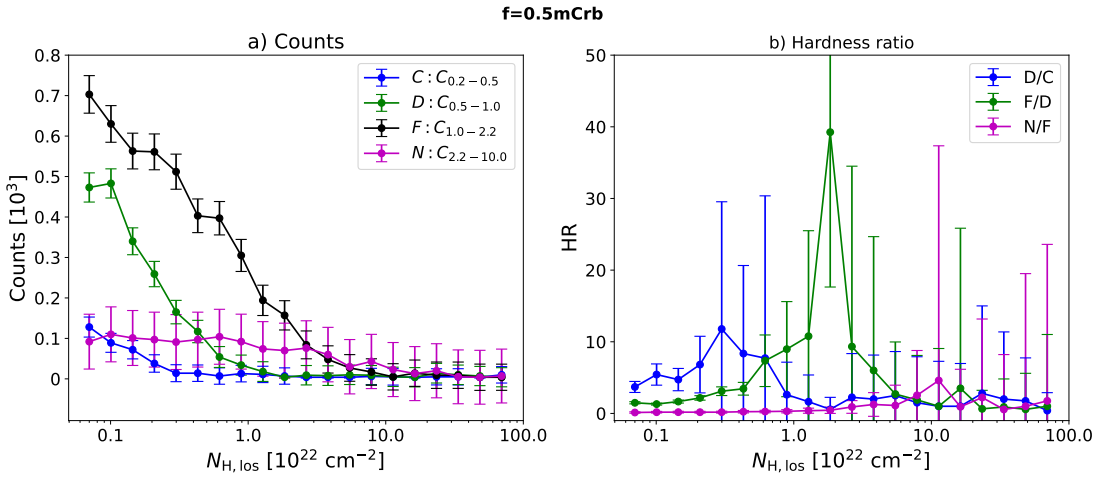

FIGURE 4.5: Same as figure 4.3 but for an unobscured flux of 0.5 mCrab.

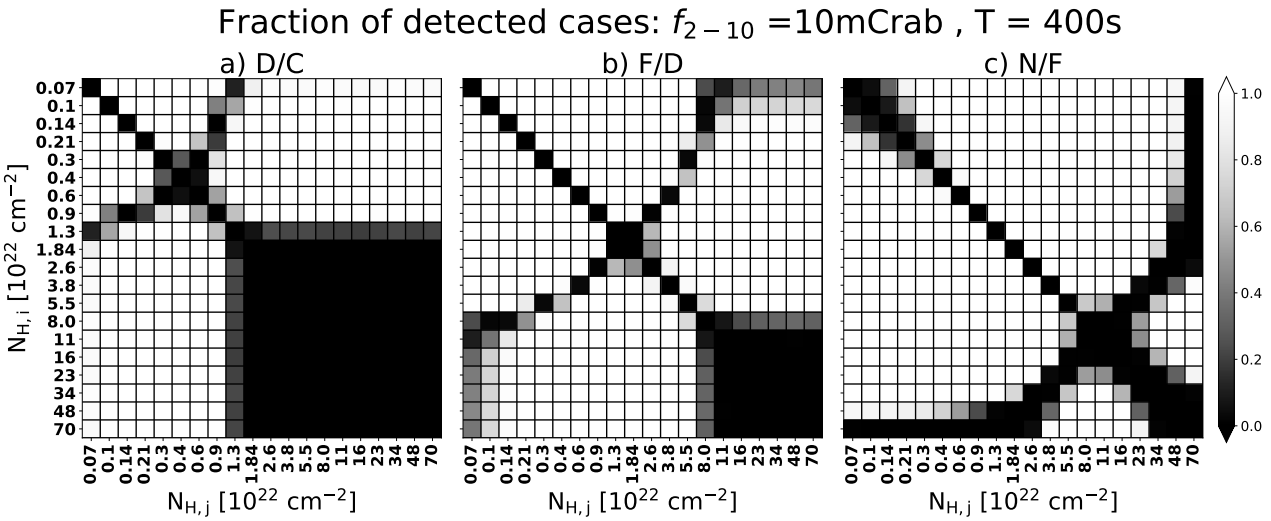

FIGURE 4.6: Map of the probability to detect particular transitions in line of sight absorption $N_{\rm H}$. Figure 4.2 explains the method to interpret this plot.

- We find that successful $N_{\rm H}$ transition detections are possible only when the unobscured flux of the source is above 1.0 mCrab.

4.6 Future plans

1. **Application to eROSITA archives:** Prior to its being placed into sleep mode in Feb. 2022, eROSITA had completed four all-sky scans, and was ∼1/3 through the fifth scan. We will exploit the AGN component of this archive as follows. We will compose a list of the Seyfert AGN whose fluxes are bright enough to detect potential transitions in $N_{\rm H}$. We will follow the log$N$–log$S$ number counts of Ajello et al. (2012), where N or $N(>S)$ is the number of sources with a source flux of S for all types of AGN per square degree. Ajello et al., 2012 obtained the following relation between the number and the limiting source flux:

$$\frac{dN}{dS} = A \times \left(\frac{S}{10^{-11}}\right)^{-\alpha} \tag{4.10}$$

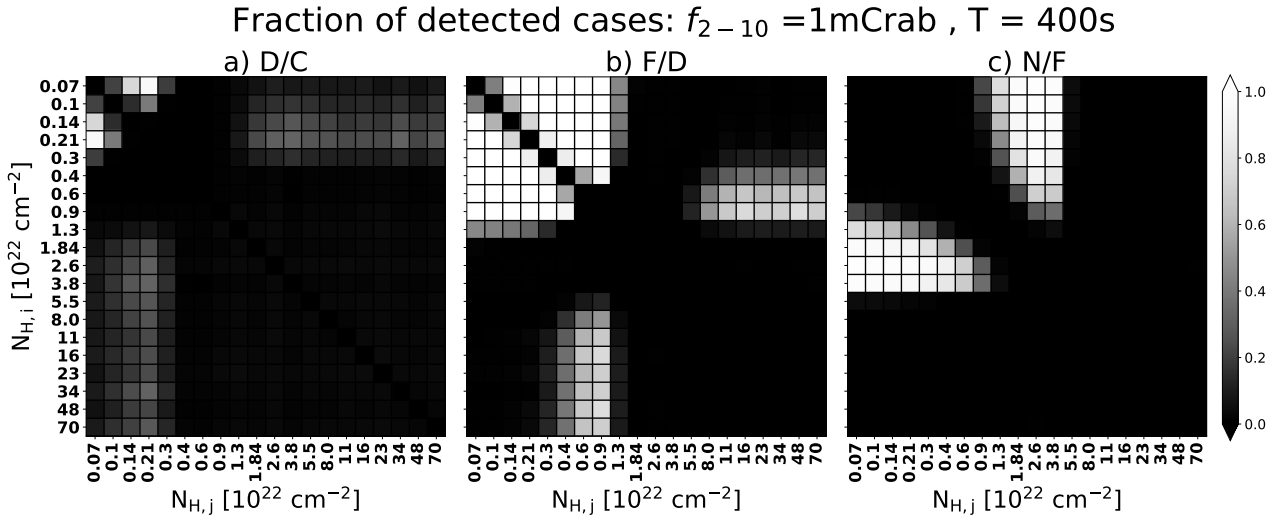

FIGURE 4.7: Same as figure 4.6, but for an unobscured flux level of 1 mCrab. The decrease in the detection fraction relative to the 10 mCrab case is evident from the greater prevalence of darker squares in the map.

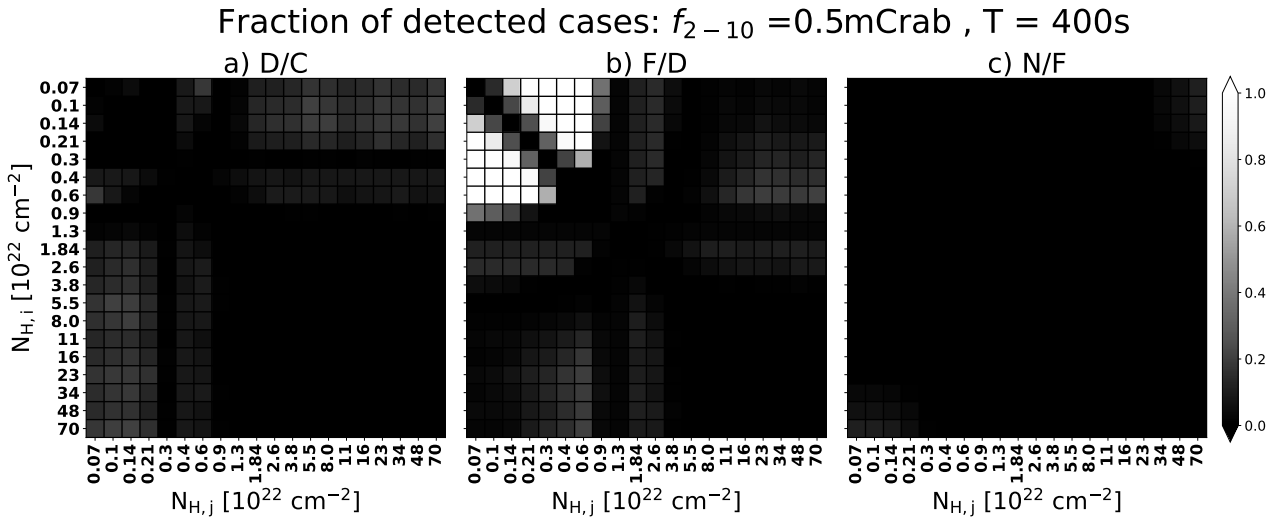

FIGURE 4.8: Same as figure 4.6, but for an unobscured flux level of 0.5 mCrab.

where, $\alpha = 2.49$, $A = 1.05 \times 10^{-9}$, and S is the source flux in 15–55 keV band. To calculate the number of sources that can be observed above a certain flux value, we integrate the above equation and obtain:

$$N(>S) = \frac{10^{-2}}{\alpha - 1} \left(\frac{S}{10^{-11}} \right)^{-\alpha+1} \text{deg}^{-2} \tag{4.11}$$

For an unobscured flux of $S > 1$ mCrab and $S > 0.5$ mCrab, we get $N(> 1 \text{ mCrab}) = 0.0047$ deg^{-2} and $N(> 0.5 \text{ mCrab}) = 0.013$ deg^{-2}. The area covered by eROSITA_DE corresponds to half of the sky which is 20627 deg^2. Thus, the number of sources that can potentially be observed for 1 mCrab and 0.5 mCrab flux levels are 96 and 270 respectively. Based on the *Swift* Burst Alert Transient all-sky survey, and we will assume that roughly 40% are Type 1 Seyferts and 30% are Compton-thin Seyferts. Thus, 70% of these sources are unobscured/Compton-thin. We predict that finally this list will approximately consist of ≤ 190 Seyferts which are likely to be mostly dominated by Type 1. We will then apply our hardness ratio selections to the eRASS catalog data for these Seyferts and comprise a list of candidate COAGN events. We will follow up such candidate transition events with BXA spectral fitting which will yield the posterior probability distribution of initial($N_{\rm H,i}$) and final($N_{\rm H,j}$) line of sight absorption: $p(N_{\rm H,i})$ and $p(N_{\rm H,j})$. Thus, to calculate the probability of detection, we will combine the posterior probabilities obtained from spectral fitting of with the hardness ratio estimated from simulations based on the fitting model. Thus, the real probability of detection $p_{\rm detection}$, is the convolution of the 'raw' transition probabilities ($P(T_{ij})$ from hardness ratio simulations with the statistical uncertainty associated with the line of sight $N_{\rm H}$ estimation. Mathematically, such an expression is given by:

$$p_{\rm detection} = \int \int P(T_{ij}|N_{\rm H,i}, N_{\rm H,j}) p(N_{\rm H,i}) p(N_{\rm H,i}) dN_{\rm H,i} dN_{\rm H,j} \tag{4.12}$$

We summarize the above process as follows: (1) raw spectral fitting: estimation of the values of absorption($N_{\rm H}$) and distinguish the transient event types using Bayesian evidence (2) hardness ratio: probability of detection for a given N_H transition ($P(T_{\rm ij})$) (3) estimate the probability of detection ($p_{\rm detection}$) by combining the uncertainty in the measurement of $N_{\rm H}$ and probability of detecting a given transition ($P(T_{\rm ij})$). The final probability estimate, thus, ascertains the probability of detection and estimates the feasibility of a follow-up.

2. **Application to future eRASS data:** Ideally, we would like to catch candidate transition events in-progress, and perform longer-exposure target-of-opportunity follow-up observations with X-ray missions such as *XMM-Newton* or *Chandra*. Thus, we could obtain X-ray spectra that could confirm a change in obscuration, precisely pinpoint $N_{\rm H}$, identify if the obscuration is full- or partial-covering, etc. We could also trigger target-of-opportunity observations for optical/UV continuum photometry (e.g., with *Swift* UVOT) and optical spectroscopy (e.g., SALT) to assess if the obscuration event is impacting our view of the accretion disk or BLR.

   For candidate events identified now (or in the near-future) from the eROSITA archive (2019–2022), there is a risk that the obscuration event has ended, e.g., if the obscuration was caused by a temporary disk wind, as observed in NGC 5548 (Mehdipour et al., 2022). Nonetheless, our hardness ratio selections will be incorporated via collaborative effort with Remeis Observatory into the eROSITA Near Real-Time Analysis (NRTA). When eRASS scans resume, the NRTA will be able to compare the latest eROSITA full- and subband count rates, automatically detect major changes in flux or hardness ratio compared to previous eRASS scans, and trigger alerts. These alerts will be manually vetted, and then follow-up observations can be triggered once vetting is complete and the candidate COAGN event is confirmed.

Hardness ratio changes can be influenced not just by varying $N_{\rm H}$. X-ray spectral hardening/softening might also result for change in Γ, resulting from extreme nuclear transients. We do not expect large variations in Γ to occur in the nearby, high-flux sources we focus on in the eROSITA archive. However, for real-time detections false positive alerts due to this degeneracy can result in wrong follow-up. Thus, it is required that the methodology is integrated with the system detecting extreme variability events and specific methodology is implemented to distinguish these events. The robust method to distinguish these events are Bayesian Evidence values generated via BXA fitting. Due to potential low counts this method requires a pre-computed repository of Bayesian evidence value distribution for competing models, which can indicate the probability of the statistically preferred transient event.

3. **Other spectral models:** Partial-covering absorption has been noted in multiple sources. Additionally, the reflection component can be taken into consideration while simulation of the spectra. We do not expect it to induce drastic variation to the counts which are mostly concentrated in the softer bands given eROSITA's effective area. However, it makes the estimates more precise. Other complexities in the X-ray spectra i.e. multiple soft band emission components can also influence counts.

Chapter 5

Conclusions

5.1 Project 1: Determination of AGN torus morphology using X-ray spectra

In an obscured Compton-thick AGN, the X-ray primary emission from the corona gets absorbed and reprocessed in the circumnuclear torus (Section 1.4.2). The resultant spectrum bears the signatures of the torus line of sight column density and morphology. Thus, an X-ray spectroscopic study is effective in principle, a channel for inferring the torus' properties (e.g. morphology). Several torus models encompassing smooth or clumpy distributions of matter and based on various physical properties such as radiation physics have been developed over the last decades (Chapter 2). They predict different X-ray spectral shapes for the torus spectrum, especially the Compton reflection hump. These models have been used for X-ray data analysis by the community over the years, to infer parameters of the torus both in spectra of individual Compton-thick targets and in spectral surveys. However, the current quality of X-ray spectral data and the commonly used techniques of X-ray spectral data analysis (e.g., χ^2-fitting) might influence parameter inference due to: (1) degeneracies between multiple model parameters, (2) the selection of a torus model for spectral fitting, and (3) the possibility/likelihood of the fit getting stuck in a local likelihood maxima due to the complex nature of the parameter space. In this project, we study the effectiveness of current X-ray data quality in determining torus properties. We performed extensive simulations of synthetic X-ray spectral data from XMM-Newton and NuSTAR representative of local Compton-thick AGNs, with six torus spectral models. We performed spectral fitting of the synthetic data with the same set of models using Bayesian nested sampling methods and studied the degeneracy between model parameters. We answered three specific questions in this project described in Chapter 2, and published at Saha, Markowitz, and Buchner (2022):

1. What is the status of parameter recovery and degeneracy for the parameters in a given model?
   Ans: To answer this, we simulated data under a given model and fit with the same. We termed these fits as intramodel (IM) fits. The parameters were recovered with varied degrees of accuracy. The photon index in IM fits was recovered accurately in general. The line of sight absorption ($N_{\rm H,los}$) was recovered accurately only in the medium Compton-thick regime (MCT; i.e., $N_{\rm H,los} < 2 \times 10^{24}$ cm^{-2}), using the transmitted component, which bears the main imprint of absorption. However, in the heavy Compton-thick regime (HCT; i.e., $N_{\rm H,los} > 2 \times 10^{24}$ cm^{-2}), the transmitted component is practically absent, resulting in poor constraints on the line of sight absorption ($N_{\rm H,los}$). Parameters of morphology (e.g., the distribution of clumps, number of clouds in the radial direction, covering fraction, etc.) are recovered better in the HCT regime as their signature is imprinted in the scattered reflection component, whose contribution to the overall flux dominates this regime. Thus, several parameters of morphology were poorly constrained, e.g., the posteriors of

clump distribution parameter(σ_0) of UXCLUMPY, the number of clouds in the radial direction in CTORUS, etc. Parameters also return asymmetric posterior distributions (e.g., σ_0 of UXCLUMPY), with asymmetric uncertainties, which can be overlooked in simple χ^2-fitting. We have also demonstrated the effectiveness of a given instrument in determining the constraints on a given parameter. This can prove useful while preparing for an observing proposal. For example, the constraints on the covering fraction of the Compton-thick ring in UXCLUMPY are mainly determined by the CRH properties, indicating that *NuSTAR* observations are required. In summary, our investigations employing Bayesian nested sampling techniques have unveiled the intricacies within the parameter space of the torus. Such intricacies are evident in the posterior distribution and the correlations among parameters. Furthermore, we have assessed the ability of a specific instrument to constrain these torus parameters effectively.

2. What is the status of parameter recovery when we fit data simulated under a given model with a wrong model?
   Ans: Here, we fit data to simulate data under a given model and fit with a different one. We refer to these fits as cross-model (CM) fits. In this case, the situation is more realistic because the actual fit is conducted on spectra obtained by an X-ray instrument. The X-ray instrument collects photon counts without the knowledge of the underlying physical model responsible for generating these counts. Several parameters that are common across different models were found to return discrepant values in a given fit. For example, photon indices were found to be significantly discrepant with $\Delta\Gamma > 0.1$ for many. The line of sight absorption is recovered with almost less than 20% discrepancy for the MCT cases ($N_{\rm H,los} < 2 \times 10^{24}$ cm^{-2}). However, the HCT ($N_{\rm H,los} < 2 \times 10^{24}$ cm^{-2}) regime the line of sight absorption yields a mismatch up to an order of magnitude with the input and is partially dependent on the CRH shape. At around $N_{\rm H,los} \simeq 5 \times 10^{24}$ cm^{-2}, we found severe systematic discrepancy involving the fitting of the Compton Reflection Hump, which can alter the physical interpretation of the fit. This phenomenon involved a case of the arbitrary variation of normalization or assuming a different $N_{\rm H,los}$ for the transmitted/photoelectric absorption component to fit the Compton-hump as shown in Chapter 2, Figure 15 and Figure 16c. Other cases involved irregular posteriors (Figure 10 in Saha, Markowitz, and Buchner, 2022), where for multiple parameters where the posterior distributions are not monomodal, a situation which is not discernable through a χ^2-fit. Thus, through the CM fitting exercise, we understood the implications of our model selections while fitting a given dataset. Overall, we confirm that the parameter values and the physical interpretation of the data are dependent on the systematics associated with model selection and setup.

3. Are models distinguishable given the current level of data quality?
   Ans: We used Bayes Factor values returned from the Bayesian fitting algorithm to check the distinguishability of the models. Bayesian evidence in nested sampling, which is the basis of calculation of the Bayes factor, systematically implements model preference based both on likelihood and optimal volume of the parameter space – the robust implementation of Occam's razor, making it one of the most effective tools for model distinction. We used Bayes factors to check the distinguishability of the best-fit models using different flux levels and band coverage implying two instruments are better than a single one. Bayes factor can distinguish models successfully and reliably, given that the photon counts are high enough as shown in Chapter 2 in Section 6 and Figure 17. The distinguishability is also affected by the band coverage of a given observation. In Chapter 2, we discussed the limitations of the Bayes Factor or Bayesian evidence values. We note the stochastic nature of the datasets generated, indicating the same getting induced in the Bayes Factor values. Thus, for datasets with low flux, exposure time, and lack of enough band coverage, in

general, low counts, the stochastic variations can lead to wrong model selection due to the fluctuations in the Bayesian evidence for a given instance of data simulation and fitting. This result has significant implications in the justification of requested observation time for preparing observation proposals. For real data analysis, data fits should be supplemented with the fitting of simulated spectra generated with the models being used, which can potentially demonstrate wrong model selection.

Through our simulation-based exercise in Chapter 2 and Saha, Markowitz, and Buchner (2022), we demonstrated the issues associated with the determination of AGN torus morphology using single epoch X-ray spectra from Compton-thick AGNs. Thus, Kammoun, Nardini, and Risaliti (2018) where the recovery of the spin parameter is tested, and Saha, Markowitz, and Buchner (2022), where the recovery of torus parameters are tested, in a broader context, encapsulate the degeneracy issues that are associated with X-ray spectral analysis in general, when measurable parameters of the central engine are concerned.

The AGN torus community is now proposing and building complicated models (e.g. Hönig et al., 2012; Wada, 2012; Buchner et al., 2021) for X-ray studies. Two factors are driving this effort: (a) the advancement in the understanding of the torus through infrared and imaging studies e.g. observation of NGC 1068 by (e.g. Gámez Rosas et al., 2022; García-Burillo et al., 2019) using observational facilities like VLT-GRAVITY, VLTI-MATISSE, and ALMA, and (b) the advancement of several generic radiative transfer and ray-tracing tools like XARS, REFLEX, and SKIRT is facilitating the simulation of these complicated models with the community currently using these models (e.g. Buchner, 2021). However, more careful distinguishing of complicated models would require better data quality. Future instruments like *ATHENA*, *XRISM*, *HEX-P* aim to provide higher effective area and importantly, higher energy resolutions, which results in an increased number of photon counts per channel, thereby enhancing spectral data quality. The enhanced data quality will be effective in resolving the Compton shoulders of the FeKα line, the kinematic components of the narrow Fe Kα core, the Fe K edge at 7.12 keV, the shape of the Compton hump, all of which are required for analysis of such complicated models. These simulations and methodology used in Saha, Markowitz, and Buchner (2022) can thus be used as an example to assess the instrument responses of future instruments like *ATHENA*, *XRISM*, *HEX-P* etc., in the context of complicated torus models in particular and other X-ray spectral models in general.

5.2 Project 2: Multiwavelength study of a flaring source with double-peaked Balmer emission lines

In this project, we study the properties of an extreme variability-flaring changing look AGN (LEDA 1154204), abbreviated as J0428−00, detected using the Zwicky Transient Facility and eROSITA through its all-sky surveys. The extreme flaring AGN was tied to a Seyfert-type change from 1.9 (in an archival spectrum obtained by the 6dF survey in 2005) to 1 (as seen in a recent spectrum taken in 2020 using the Keck telescope). A three-year multi-wavelength follow-up campaign was triggered to track the source's emission as the flare gradually subsided and to determine the nature of this transient event. We answer the following questions by analyzing diverse multi-wavelength spectral and variability datasets in our campaign.

1. What is the nature of the source and what is the mechanism that drove the extreme transient variability in the object?
   Ans: J0428−00 was found to exhibit persistent narrow forbidden emission lines of [OIII] $\lambda\lambda$5007,4959, [NII]$\lambda\lambda$6548,6585, and [SII]$\lambda\lambda$6716,6732 along with a broad Hα line in its optical spectra. Meanwhile, the following properties of the source, as described in Chapter 3, Section 8.3 of the submitted article indicate its inconsistency with a tidal disruption event:

(a) the lack of an abrupt rise and a $t^{-5/3}$-decay in the light curves, (b) the relative strength of the [OIII] narrow line luminosity with respect to the X-ray as $L_{[\mathrm{OIII}]}/L_{\mathrm{X-ray}} \lesssim 10^4$ (c) the absence of HeII emission lines and Bowen fluorescence emission lines (d) the relatively flat photon index ($\sim$ 1.9) of the X-ray emission compared to steeper photon indices seen in thermal tidal disruption events. The transient flare was rather found to be consistent with an instability in the accretion disk, which might be driven by radiation pressure instabilities as described in e.g. Lightman and Eardley, 1974; Sniegowska et al., 2020. Our timescale estimates indicate that the flaring, which lasts for $\sim$80 days as seen in the optical band, is consistent with thermal mechanisms dominating and wither the instability timescale associated with the radiation pressure instability for a representative black hole mass of $\sim 10^8 M_\odot$. Thus, the BPT ratios calculated from the narrow emission lines and multiple inconsistencies with a transient TDE indicate a persistent accretion driven AGN activity in J0428−00 for last $\sim 10^3$ years. This makes disk instability in a otherwise stable accretion flow, a viable mechanism driving the flare.

2. What is the morphology of the outer sub-parsec matter distribution i.e the BLR and distant dust structures?
Ans: J0428-00 exhibits double-peaked broad Balmer emission lines. Physical modeling of the broad Balmer Hβ and Hα emission lines using a diskline model (Chen and Halpern, 1989) was able to constrain the physical extent of the broad line emitter. The broad line emitter in J0428-00 extends from a few $100R_\mathrm{g}$ to $1000R_\mathrm{g}$. Modeling of the line profile using FRADO also indicates that the line emitter is consistent with a disk-type geometry, as the vertical height of the cloud trajectories is much lower compared to the corresponding radius where they originate ($H/R \sim 0.01$).

   The source also exhibits a broad infrared echo that lasted for $\sim$ 1000 days with its peak being delayed by $\sim$200 days with respect to the optical flare. This infrared flare is thought to originate due to reverberation from the dust structures in the vicinity of the central engine. Assuming a phenomenological model of reverberation in a distant dusty structure, we show that the infrared variability in the WISE-$W1$ and WISE-$W2$ bands is a result of both an underlying long-term trend and the sharp flare from 2020 superposed on it. We were able to estimate the extent of the dust distribution using our phenomenological model. The inner boundary that was determined here from $\sim$ 0.2 pc is consistent with the dust-sublimation radius. The outer boundary is found to be $\sim$ 1 pc.

3. What are the properties of the inner accretion flow and its relation to the evolving continuum spectral properties?
Ans: The X-ray spectra in the sources is consistent with Comptonization in a hot corona. Additionally, from the X-ray and broadband spectral analyses we find that the source does not exhibit the soft-X-ray excess that is seen in multiple unobscured AGNs. This indicates that the flow lacks a warm corona in the context of models of warm Comptonization, the warm corona is not present or emits negligible soft X-ray emission. If instead, reflection from the ionized inner disk is considered, this missing soft excess hints at an inner disk that is truncated or radiatively inefficient. The X-ray spectra are unobscured throughout the entire period of our monitoring and exhibit a single flat power-law component.

   The optical emission exhibited a blue AGN continuum which subsides as the flare decays and in the later phases of our monitoring, the continuum is dominated by the host galaxy. From the optical photometric data from Swift and XMM-Newton, we find that all wavebands vary in sync indicating a radiative response from multiple substructures to the flaring that resulted from the disk instability.

We summarize the whole sequence of events associated with the transient variability as follows: a disk instability caused a local increase in accretion in inner disk, causing a flaring output via thermal optical/UV continuum emission. This flaring continuum (a) drove X-rays via Comptonization in the hot corona (b) drove the Balmer line activity (appearance of Hβ) via reverberation and photoionization in the disk-type BLR resulting in the appearance of the broad double-peaked emission line; and (c) drove the infrared dust echo.

This multi-wavelength study of J0428-00 is one of the most detailed follow-up campaigns of a flaring changing-look AGN observed as the event was happening. Systematic detection and instantaneous follow-up campaigns of these sources are now possible because of X-ray and optical survey facilities like eROSITA and ZTF, thus, indicating significant progress in Time-domain astronomy from the view point of detection. The community is now accumulating a statistically significant sample of peculiar supermassive black hole transient events. The detection of these events can now yield a significant amount of multi-wavelength spectroscopic and timing follow-up resulting in a comprehensive understanding of the variations in accretion flow in diverse classes of flaring Seyferts and/or CLAGNs. Hence a more integrated and systematic follow-up campaign is required to observe these sources as early as possible.

5.3 Project 3: Detection of changing obscuration AGNs in eROSITA

As described in Section 1.6.3 and 4.1, observations of changes in AGNs' line-of-sight obscuring column density provide key insight into the geometry and position of circumnuclear matter in the vicinity of supermassive black holes. This project initiates the development of a robust COAGN detection pipeline as applied to eROSITA's all-sky scans, the most systematic and regular monitoring X-ray survey currently available in X-ray astronomy. The eROSITA archive results in a large starting sample of $\gtrsim 10^5$ AGNs, several dozens of which are X-ray bright enough for us to potentially detect changing-obscuration events occurring in them between eRASS scans. The immediate goal of this project is to detect these events in the already-existing eROSITA archive and construct a catalog of such events. Additionally, when eROSITA all-sky surveys resume, those real-time all-sky surveys will help us detect additional obsucration events in real-time. For real-time detections, we intend to perform a dense follow-up spectral and timing observing campaign to study the size and profile of the clump causing the obscuration. This study will require follow-up observations with X-ray telescopes like NICER or NuSTAR. Ideally, if a sufficient number of COAGN events are found, we can derive statistical constraints on clumpy-torus model parameters. The methodology is also extendable to future upcoming survey missions that can potentially generate a repository of big data.

Appendix A

Additional information for chapter 4

In this Appendix, we present the results when hardness ratios is defined according to equation 4.2. These maps can be read following the description in Figure 4.2.

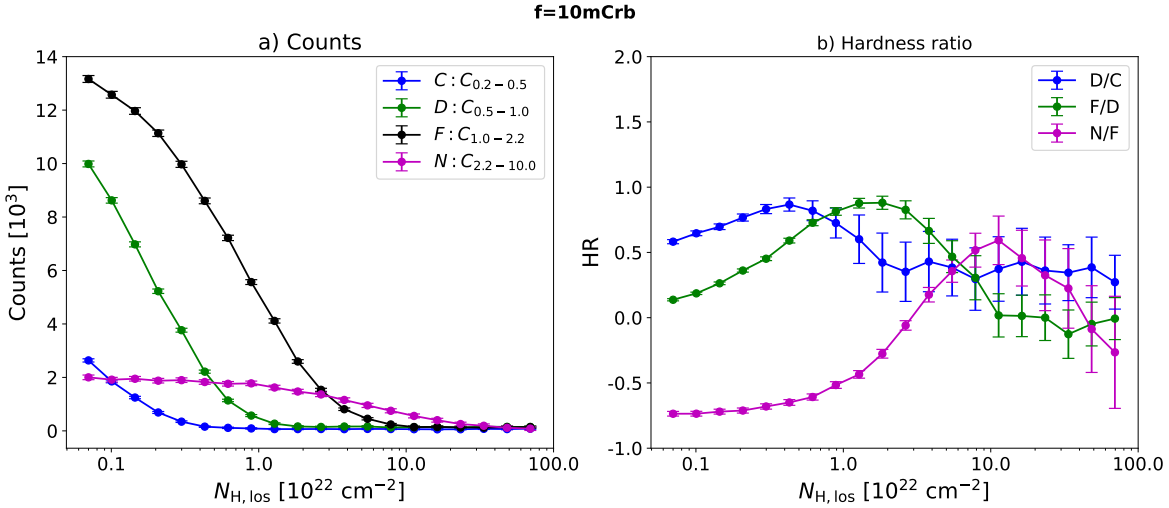

FIGURE A.1: The figures show the simulated count rates in the different band and the resultant hardness ratio for a flux level of 10 mCrab, for hardness ratio defined according to equation 4.2.

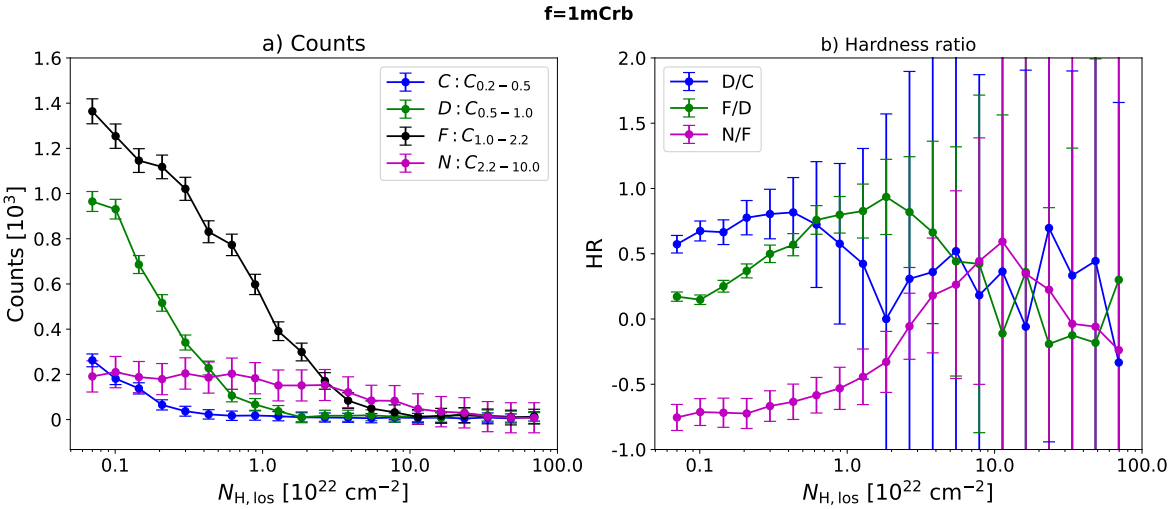

FIGURE A.2: Same as figure A.1 but for 1 mCrb flux level.

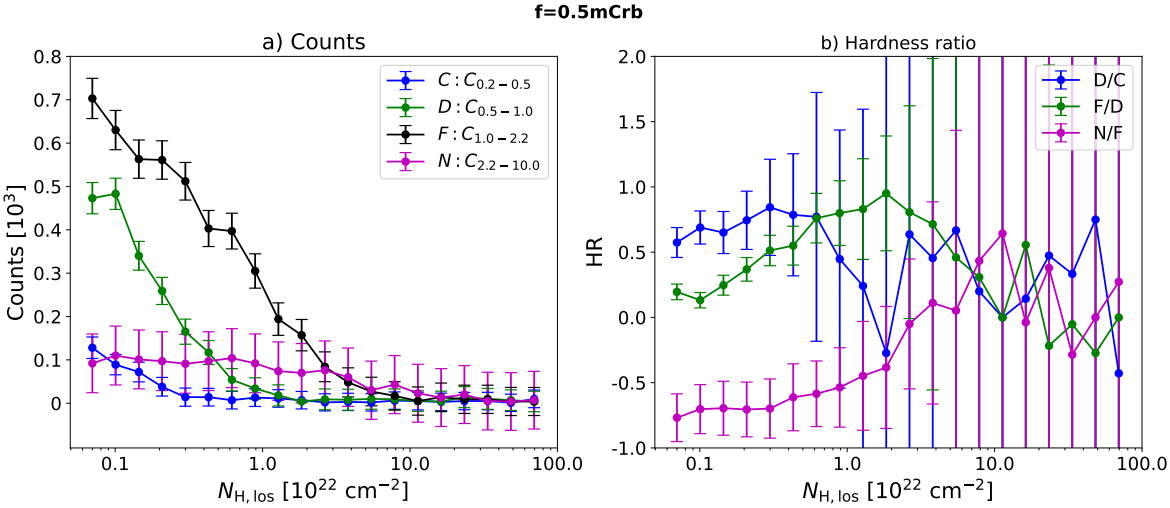

FIGURE A.3: Same as figure A.1 but for 0.5 mCrb flux level.

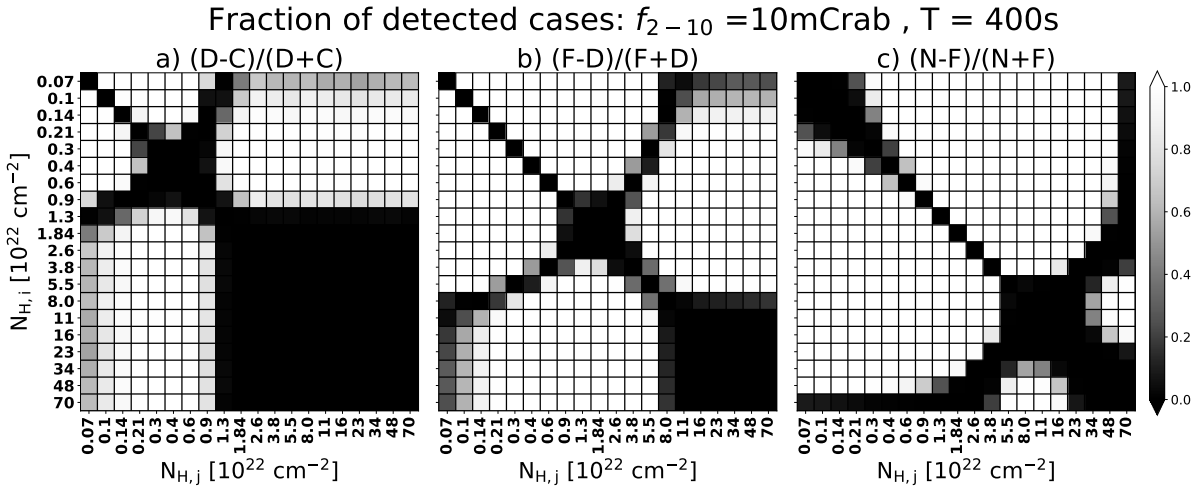

FIGURE A.4: In this figure we present a map of the probability to detect particular transitions in line of sight absorption $N_{\rm H}$ according to the definition of hardness ratio in equation 4.2. Figure 4.2 explains the method to interpret this plot.

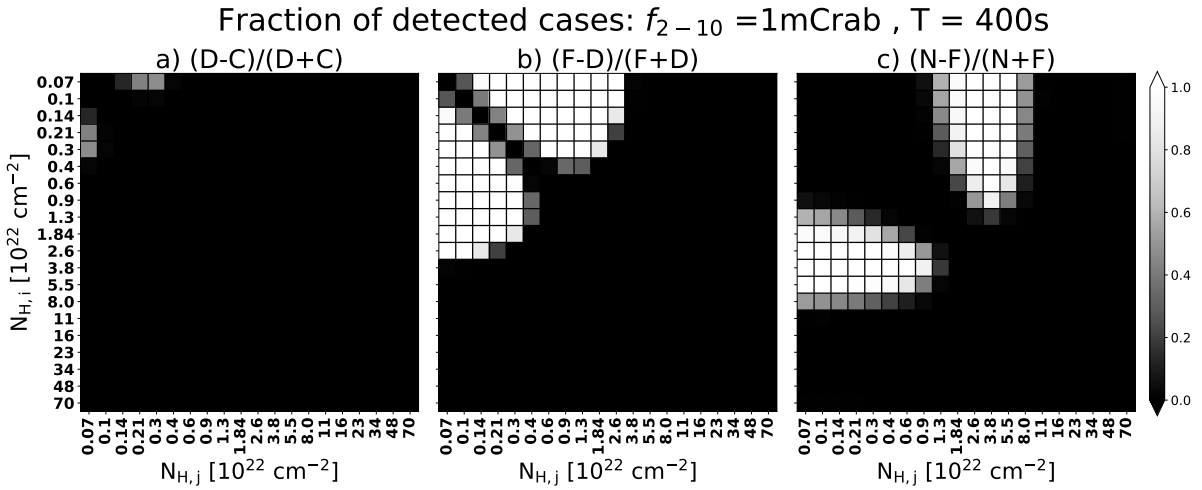

FIGURE A.5: Same as figure A.4 but for a flux level of 1 mCrab.

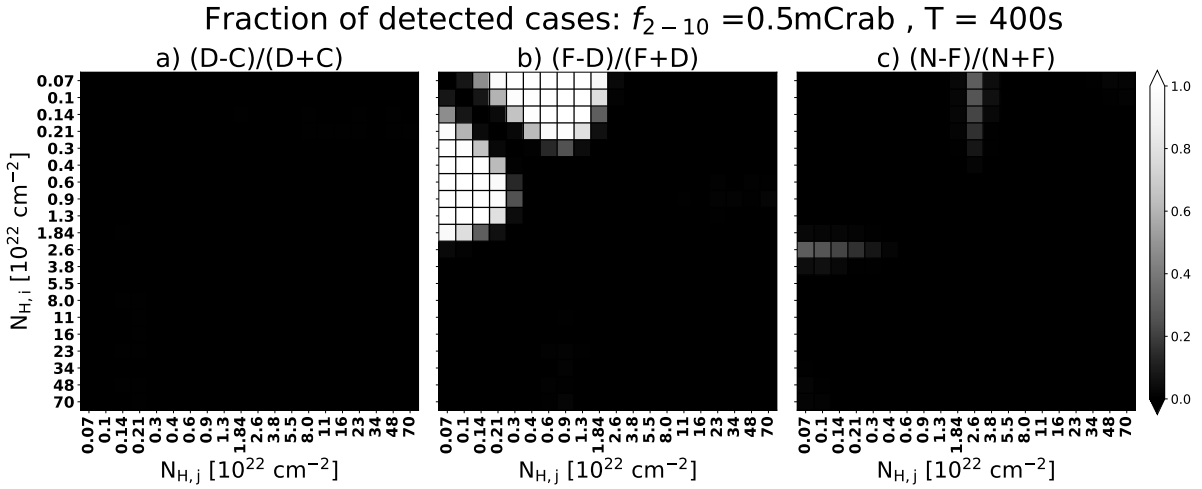

FIGURE A.6: Same as figure A.4 but for a flux level of 0.5 mCrab.

Bibliography

Abbott, B. P. et al. (Oct. 2016). "Binary Black Hole Mergers in the First Advanced LIGO Observing Run". In: *Physical Review X* 6.4, 041015, p. 041015. DOI: 10.1103/PhysRevX.6.041015. arXiv: 1606.04856 [gr-qc].

Abramowicz, M. A. et al. (Sept. 1988). "Slim Accretion Disks". In: *The Astrophysical Journal* 332, p. 646. DOI: 10.1086/166683.

Ajello, M. et al. (Apr. 2012). "The 60 Month All-sky Burst Alert Telescope Survey of Active Galactic Nucleus and the Anisotropy of nearby AGNs". In: *The Astrophysical Journal* 749.1, 21, p. 21. DOI: 10.1088/0004-637X/749/1/21. arXiv: 1202.3137 [astro-ph.CO].

Akiyama, Masayuki et al. (Oct. 2003). "Optical Identification of the ASCA Medium Sensitivity Survey in the Northern Sky: Nature of Hard X-Ray-Selected Luminous Active Galactic Nuclei". In: *The Astrophysical Journal Supplement* 148.2, pp. 275–315. DOI: 10.1086/376441. arXiv: astro-ph/0307164 [astro-ph].

Ananna, Tonima Tasnim et al. (Feb. 2019). "The Accretion History of AGNs. I. Supermassive Black Hole Population Synthesis Model". In: *The Astrophysical Journal* 871.2, 240, p. 240. DOI: 10.3847/1538-4357/aafb77. arXiv: 1810.02298 [astro-ph.GA].

Andonie, Carolina et al. (Aug. 2022). "Localizing narrow Fe Kα emission within bright AGN". In: *Astronomy and Astrophysics* 664, A46, A46. DOI: 10.1051/0004-6361/202142473. arXiv: 2204.09469 [astro-ph.HE].

Antonucci, R. R. J. and J. S. Miller (Oct. 1985). "Spectropolarimetry and the nature of NGC 1068." In: *The Astrophysical Journal* 297, pp. 621–632. DOI: 10.1086/163559.

Antonucci, Robert (Jan. 1993). "Unified models for active galactic nuclei and quasars." In: *Annual Review of Astronomy and Astrophysics* 31, pp. 473–521. DOI: 10.1146/annurev.aa.31.090193.002353.

Arbeiter, C., M. Pohl, and R. Schlickeiser (July 2005). "Synchrotron Self-Comptonization in a Relativistic Collision Front Model". In: *The Astrophysical Journal* 627.1, pp. 62–74. DOI: 10.1086/430118.

Arévalo, P. et al. (Aug. 2014). "The 2-79 keV X-Ray Spectrum of the Circinus Galaxy with NuSTAR, XMM-Newton, and Chandra: A Fully Compton-thick Active Galactic Nucleus". In: *The Astrophysical Journal* 791.2, 81, p. 81. DOI: 10.1088/0004-637X/791/2/81. arXiv: 1406.3345 [astro-ph.HE].

Awaki, Hisamitsu et al. (Apr. 1991a). "X-Ray Implications of a Unified Model of Seyfert Galaxies". In: *Publications of the Astrophysical Society of Japan* 43, pp. 195–212.

– (Apr. 1991b). "X-Ray Implications of a Unified Model of Seyfert Galaxies". In: *Publications of the Astrophysical Society of Japan* 43, pp. 195–212.

Balbus, Steven A. and John F. Hawley (July 1991). "A Powerful Local Shear Instability in Weakly Magnetized Disks. I. Linear Analysis". In: *The Astrophysical Journal* 376, p. 214. DOI: 10.1086/170270.

– (Dec. 1992). "A Powerful Local Shear Instability in Weakly Magnetized Disks. IV. Nonaxisymmetric Perturbations". In: *The Astrophysical Journal* 400, pp. 610–621. DOI: 10.1086/172022.

Baldwin, J. A., M. M. Phillips, and R. Terlevich (Feb. 1981). "Classification parameters for the emission-line spectra of extragalactic objects." In: *Publications of the Astronomical Society of the Pacific* 93, pp. 5–19. DOI: 10.1086/130766.

Baloković, M. et al. (Feb. 2018). "New Spectral Model for Constraining Torus Covering Factors from Broadband X-Ray Spectra of Active Galactic Nuclei". In: *The Astrophysical Journal* 854.1, 42, p. 42. DOI: 10.3847/1538-4357/aaa7eb. arXiv: 1801.04938 [astro-ph.HE].

Barvainis, Richard (Sept. 1987). "Hot Dust and the Near-Infrared Bump in the Continuum Spectra of Quasars and Active Galactic Nuclei". In: *The Astrophysical Journal* 320, p. 537. DOI: 10.1086/165571.

Bauer, Franz E. et al. (Oct. 2015). "NuSTAR Spectroscopy of Multi-component X-Ray Reflection from NGC 1068". In: *The Astrophysical Journal* 812.2, 116, p. 116. DOI: 10.1088/0004-637X/812/2/116. arXiv: 1411.0670 [astro-ph.HE].

Baum, Stefi A., Esther L. Zirbel, and Christopher P. O'Dea (Sept. 1995). "Toward Understanding the Fanaroff-Riley Dichotomy in Radio Source Morphology and Power". In: *The Astrophysical Journal* 451, p. 88. DOI: 10.1086/176202.

Beckmann, V. et al. (July 2011). "The hard X-ray emission of Centaurus A". In: *Astronomy and Astrophysics* 531, A70, A70. DOI: 10.1051/0004-6361/201016020. arXiv: 1104.4253 [astro-ph.CO].

Beckmann, Volker and Chris R. Shrader (2012). *Active Galactic Nuclei*.

Bellm, Eric C. et al. (Jan. 2019). "The Zwicky Transient Facility: System Overview, Performance, and First Results". In: *Publications of the Astronomical Society of the Pacific* 131.995, p. 018002. DOI: 10.1088/1538-3873/aaecbe. arXiv: 1902.01932 [astro-ph.IM].

Beuchert, T. et al. (Dec. 2015). "A variable-density absorption event in NGC 3227 mapped with Suzaku and Swift". In: *Astronomy and Astrophysics* 584, A82, A82. DOI: 10.1051/0004-6361/201526790. arXiv: 1508.04565 [astro-ph.GA].

Bianchi, S., M. Guainazzi, and M. Chiaberge (Mar. 2006). "The soft X-ray/NLR connection: a single photoionized medium?" In: *Astronomy and Astrophysics* 448.2, pp. 499–511. DOI: 10.1051/0004-6361:20054091. arXiv: astro-ph/0511216 [astro-ph].

Bianchi, S. et al. (Mar. 2008). "NGC 3147: a 'true' type 2 Seyfert galaxy without the broad-line region". In: *Monthly Notices of the Royal Astronomical Society* 385.1, pp. 195–199. DOI: 10.1111/j.1365-2966.2007.12625.x. arXiv: 0710.4226 [astro-ph].

Bianchi, Stefano et al. (June 2005). "The XMM-Newton view of Mrk 3 and IXO 30". In: *Monthly Notices of the Royal Astronomical Society* 360.1, pp. 380–389. DOI: 10.1111/j.1365-2966.2005.09048.x. arXiv: astro-ph/0503623 [astro-ph].

Blandford, R. D. and M. J. Rees (Dec. 1974). "A "twin-exhaust" model for double radio sources." In: *Monthly Notices of the Royal Astronomical Society* 169, pp. 395–415. DOI: 10.1093/mnras/169.3.395.

Blandford, R. D. and R. L. Znajek (May 1977). "Electromagnetic extraction of energy from Kerr black holes." In: *Monthly Notices of the Royal Astronomical Society* 179, pp. 433–456. DOI: 10.1093/mnras/179.3.433.

Boella, G. et al. (Apr. 1997). "BeppoSAX, the wide band mission for X-ray astronomy". In: *Astronomy and Astrophysics Supplement* 122, pp. 299–307. DOI: 10.1051/aas:1997136.

Bondi, H. (Jan. 1952). "On spherically symmetrical accretion". In: *Monthly Notices of the Royal Astronomical Society* 112, p. 195. DOI: 10.1093/mnras/112.2.195.

Boroson, Todd A. and Richard F. Green (May 1992). "The Emission-Line Properties of Low-Redshift Quasi-stellar Objects". In: *The Astrophysical Journal Supplement* 80, p. 109. DOI: 10.1086/191661.

Brightman, Murray and Kirpal Nandra (Nov. 2008). "On the nature of unabsorbed Seyfert 2 galaxies". In: *Monthly Notices of the Royal Astronomical Society* 390.3, pp. 1241–1249. DOI: 10.1111/j.1365-2966.2008.13841.x. arXiv: 0808.2385 [astro-ph].

Brightman, Murray et al. (Sept. 2014). "Compton thick active galactic nuclei in Chandra surveys". In: *Monthly Notices of the Royal Astronomical Society* 443.3, pp. 1999–2017. DOI: 10.1093/mnras/stu1175. arXiv: 1406.4502 [astro-ph.HE].

Bruhweiler, F. and E. Verner (Mar. 2008). "Modeling Fe II Emission and Revised Fe II (UV) Empirical Templates for the Seyfert 1 Galaxy I Zw 1". In: *The Astrophysical Journal* 675.1, pp. 83–95. DOI: 10.1086/525557.

Buchner, Johannes (Apr. 2021). "UltraNest - a robust, general purpose Bayesian inference engine". In: *The Journal of Open Source Software* 6.60, 3001, p. 3001. DOI: 10.21105/joss.03001. arXiv: 2101.09604 [stat.CO].

Buchner, Johannes et al. (Sept. 2019). "X-ray spectral and eclipsing model of the clumpy obscurer in active galactic nuclei". In: *Astronomy and Astrophysics* 629, A16, A16. DOI: 10.1051/0004-6361/201834771. arXiv: 1907.13137 [astro-ph.HE].

Buchner, Johannes et al. (July 2021). "Physically motivated X-ray obscurer models". In: *Astronomy and Astrophysics* 651, A58, A58. DOI: 10.1051/0004-6361/201834963. arXiv: 2106.08331 [astro-ph.HE].

Buchner, Johannes et al. (May 2022). "Systematic evaluation of variability detection methods for eROSITA". In: *Astronomy and Astrophysics* 661, A18, A18. DOI: 10.1051/0004-6361/202141099. arXiv: 2106.14529 [astro-ph.HE].

Chen, Kaiyou and Jules P. Halpern (Sept. 1989). "Structure of Line-emitting Accretion Disks in Active Galactic Nuclei: ARP 102B". In: *The Astrophysical Journal* 344, p. 115. DOI: 10.1086/167782.

Comastri, A. (Aug. 2004). "Compton-Thick AGN: The Dark Side of the X-Ray Background". In: *Supermassive Black Holes in the Distant Universe*. Ed. by A. J. Barger. Vol. 308. Astrophysics and Space Science Library, p. 245. DOI: 10.1007/978-1-4020-2471-9_8. arXiv: astro-ph/0403693 [astro-ph].

Crummy, J. et al. (Feb. 2006). "An explanation for the soft X-ray excess in active galactic nuclei". In: *Monthly Notices of the Royal Astronomical Society* 365.4, pp. 1067–1081. DOI: 10.1111/j.1365-2966.2005.09844.x. arXiv: astro-ph/0511457 [astro-ph].

Czerny, B. and K. Hryniewicz (Jan. 2011). "The origin of the broad line region in active galactic nuclei". In: *Astronomy and Astrophysics* 525, L8, p. L8. DOI: 10.1051/0004-6361/201016025. arXiv: 1010.6201 [astro-ph.CO].

Czerny, Bozena and Martin Elvis (Oct. 1987). "Constraints on Quasar Accretion Disks from the Optical/Ultraviolet/Soft X-Ray Big Bump". In: *The Astrophysical Journal* 321, p. 305. DOI: 10.1086/165630.

Dauser, T. et al. (Dec. 2010). "Broad emission lines for a negatively spinning black hole". In: *Monthly Notices of the Royal Astronomical Society* 409.4, pp. 1534–1540. DOI: 10.1111/j.1365-2966.2010.17393.x. arXiv: 1007.4937 [astro-ph.HE].

Dauser, T. et al. (Oct. 2014). "The role of the reflection fraction in constraining black hole spin." In: *Monthly Notices of the Royal Astronomical Society* 444, pp. L100–L104. DOI: 10.1093/mnrasl/slu125. arXiv: 1408.2347 [astro-ph.HE].

de Marco, B. et al. (Oct. 2011). "PG 1211+143: probing high-frequency lags in a high-mass active galactic nucleus". In: *Monthly Notices of the Royal Astronomical Society* 417.1, pp. L98–L102. DOI: 10.1111/j.1745-3933.2011.01129.x. arXiv: 1108.3503 [astro-ph.HE].

Denney, K. D. et al. (Dec. 2014). "The Typecasting of Active Galactic Nuclei: Mrk 590 no Longer Fits the Role". In: *The Astrophysical Journal* 796.2, 134, p. 134. DOI: 10.1088/0004-637X/796/2/134. arXiv: 1404.4879 [astro-ph.GA].

Done, Chris et al. (Mar. 2012). "Intrinsic disc emission and the soft X-ray excess in active galactic nuclei". In: *Monthly Notices of the Royal Astronomical Society* 420.3, pp. 1848–1860. DOI: 10.1111/j.1365-2966.2011.19779.x. arXiv: 1107.5429 [astro-ph.HE].

Draine, B. T. (Dec. 2003). "Scattering by Interstellar Dust Grains. II. X-Rays". In: *The Astrophysical Journal* 598.2, pp. 1026–1037. DOI: 10.1086/379123. arXiv: astro-ph/0308251 [astro-ph].

Duras, F. et al. (Apr. 2020). "Universal bolometric corrections for active galactic nuclei over seven luminosity decades". In: *Astronomy and Astrophysics* 636, A73, A73. DOI: 10.1051/0004-6361/201936817. arXiv: 2001.09984 [astro-ph.GA].

Elitzur, Moshe and Luis C. Ho (Aug. 2009). "On the Disappearance of the Broad-Line Region in Low-Luminosity Active Galactic Nuclei". In: *The Astrophysical Journal Letters* 701.2, pp. L91–L94. DOI: 10.1088/0004-637X/701/2/L91. arXiv: 0907.3752 [astro-ph.CO].

Elitzur, Moshe, Luis C. Ho, and Jonathan R. Trump (Mar. 2014). "Evolution of broad-line emission from active galactic nuclei". In: *Monthly Notices of the Royal Astronomical Society* 438.4, pp. 3340–3351. DOI: 10.1093/mnras/stt2445. arXiv: 1312.4922 [astro-ph.GA].

Elvis, Martin et al. (Nov. 2004). "An Unveiling Event in the Type 2 Active Galactic Nucleus NGC 4388:A Challenge for a Parsec-Scale Absorber". In: *The Astrophysical Journal Letters* 615.1, pp. L25–L28. DOI: 10.1086/424380. arXiv: astro-ph/0407291 [astro-ph].

Esin, Ann A., Jeffrey E. McClintock, and Ramesh Narayan (Nov. 1997). "Advection-Dominated Accretion and the Spectral States of Black Hole X-Ray Binaries: Application to Nova Muscae 1991". In: *The Astrophysical Journal* 489.2, pp. 865–889. DOI: 10.1086/304829. arXiv: astro-ph/9705237 [astro-ph].

Event Horizon Telescope Collaboration et al. (Apr. 2019). "First M87 Event Horizon Telescope Results. IV. Imaging the Central Supermassive Black Hole". In: *The Astrophysical Journal Letters* 875.1, L4, p. L4. DOI: 10.3847/2041-8213/ab0e85. arXiv: 1906.11241 [astro-ph.GA].

Event Horizon Telescope Collaboration et al. (May 2022). "First Sagittarius A* Event Horizon Telescope Results. VI. Testing the Black Hole Metric". In: *The Astrophysical Journal Letters* 930.2, L17, p. L17. DOI: 10.3847/2041-8213/ac6756.

Fabian, A. C. (Dec. 2006). "A short introduction to broad and variable iron lines around black holes". In: *Astronomische Nachrichten* 327.10, p. 943. DOI: 10.1002/asna.200610669.

Fabian, A. C. et al. (May 1989). "X-ray fluorescence from the inner disc in Cygnus X-1." In: *Monthly Notices of the Royal Astronomical Society* 238, pp. 729–736. DOI: 10.1093/mnras/238.3.729.

Fabian, A. C. et al. (May 2009). "Broad line emission from iron K- and L-shell transitions in the active galaxy 1H0707-495". In: *Nature* 459.7246, pp. 540–542. DOI: 10.1038/nature08007.

Fabian, A. C. et al. (Aug. 2015). "Properties of AGN coronae in the NuSTAR era". In: *Monthly Notices of the Royal Astronomical Society* 451.4, pp. 4375–4383. DOI: 10.1093/mnras/stv1218. arXiv: 1505.07603 [astro-ph.HE].

Fanaroff, B. L. and J. M. Riley (May 1974). "The morphology of extragalactic radio sources of high and low luminosity". In: *Monthly Notices of the Royal Astronomical Society* 167, 31P–36P. DOI: 10.1093/mnras/167.1.31P.

Fath, Edward Arthur (Jan. 1909). "The spectra of some spiral nebulae and globular star clusters". In: *Lick Observatory Bulletin* 149, pp. 71–77. DOI: 10.5479/ADS/bib/1909LicOB.5.71F.

Ferland, Gary J. et al. (Apr. 1996). "High Metal Enrichments in Luminous Quasars". In: *The Astrophysical Journal* 461, p. 683. DOI: 10.1086/177094.

Frank, Juhan, Andrew King, and Derek J. Raine (2002). *Accretion Power in Astrophysics: Third Edition*.

Frederick, Sara et al. (Sept. 2019). "A New Class of Changing-look LINERs". In: *The Astrophysical Journal* 883.1, 31, p. 31. DOI: 10.3847/1538-4357/ab3a38. arXiv: 1904.10973 [astro-ph.HE].

Frederick, Sara et al. (Oct. 2021). "A Family Tree of Optical Transients from Narrow-line Seyfert 1 Galaxies". In: *The Astrophysical Journal* 920.1, 56, p. 56. DOI: 10.3847/1538-4357/ac110f. arXiv: 2010.08554 [astro-ph.HE].

Gámez Rosas, Violeta et al. (Feb. 2022). "Thermal imaging of dust hiding the black hole in NGC 1068". In: *Nature* 602.7897, pp. 403–407. DOI: 10.1038/s41586-021-04311-7. arXiv: 2112.13694 [astro-ph.GA].

García, J. et al. (May 2013). "X-Ray Reflected Spectra from Accretion Disk Models. III. A Complete Grid of Ionized Reflection Calculations". In: *The Astrophysical Journal* 768.2, 146, p. 146. DOI: 10.1088/0004-637X/768/2/146. arXiv: 1303.2112 [astro-ph.HE].

García, J. et al. (Feb. 2014). "Improved Reflection Models of Black Hole Accretion Disks: Treating the Angular Distribution of X-Rays". In: *The Astrophysical Journal* 782.2, 76, p. 76. DOI: 10.1088/0004-637X/782/2/76. arXiv: 1312.3231 [astro-ph.HE].

García-Burillo, S. et al. (Dec. 2019). "ALMA images the many faces of the <ASTROBJ>NGC 1068</ASTROBJ> torus and its surroundings". In: *Astronomy and Astrophysics* 632, A61, A61. DOI: 10.1051/0004-6361/201936606. arXiv: 1909.00675 [astro-ph.GA].

Gehrels, N. (Apr. 1986). "Confidence Limits for Small Numbers of Events in Astrophysical Data". In: *The Astrophysical Journal* 303, p. 336. DOI: 10.1086/164079.

Ghez, A. M. et al. (Feb. 2005). "Stellar Orbits around the Galactic Center Black Hole". In: *The Astrphysical Journal* 620.2, pp. 744–757. DOI: 10.1086/427175. arXiv: astro-ph/0306130 [astro-ph].

Ghisellini, G., F. Haardt, and G. Matt (Apr. 1994). "The contribution of the obscuring torus to the X-ray spectrum of Seyfert galaxies: a test for the unification model." In: *Monthly Notices of the Royal Astronomical Society* 267, pp. 743–754. DOI: 10.1093/mnras/267.3.743. arXiv: astro-ph/9401044 [astro-ph].

Gilli, R., M. Salvati, and G. Hasinger (Feb. 2001). "Testing current synthesis models of the X-ray background". In: *Astronomy and Astrophysics* 366, pp. 407–417. DOI: 10.1051/0004-6361:20000105. arXiv: astro-ph/0011341 [astro-ph].

Goulding, A. D. et al. (Aug. 2012). "Deep Silicate Absorption Features in Compton-thick Active Galactic Nuclei Predominantly Arise due to Dust in the Host Galaxy". In: *The Astrophysical Journal* 755.1, 5, p. 5. DOI: 10.1088/0004-637X/755/1/5. arXiv: 1205.1800 [astro-ph.GA].

Gravity Collaboration et al. (Nov. 2018). "Spatially resolved rotation of the broad-line region of a quasar at sub-parsec scale". In: *Nature* 563.7733, pp. 657–660. DOI: 10.1038/s41586-018-0731-9. arXiv: 1811.11195 [astro-ph.GA].

Greenstein, Jesse L. and Maarten Schmidt (July 1964). "The Quasi-Stellar Radio Sources 3C 48 and 3C 273." In: *The Astrophysical Journal* 140, p. 1. DOI: 10.1086/147889.

Grier, C. J. et al. (Jan. 2012). "A Reverberation Lag for the High-ionization Component of the Broad-line Region in the Narrow-line Seyfert 1 Mrk 335". In: *The Astrophysical Journal Letters* 744.1, L4, p. L4. DOI: 10.1088/2041-8205/744/1/L4. arXiv: 1110.6179 [astro-ph.CO].

Haardt, Francesco and Laura Maraschi (Aug. 1993). "X-Ray Spectra from Two-Phase Accretion Disks". In: *The Astrophysical Journal* 413, p. 507. DOI: 10.1086/173020.

Halpern, J. P. (June 1984). "Variable X-ray absorption in the QSO MR 2251-178." In: *The Astrophysical Journal* 281, pp. 90–94. DOI: 10.1086/162077.

Hao, Lei et al. (Feb. 2007). "The Distribution of Silicate Strength in Spitzer Spectra of AGNs and ULIRGs". In: *The Astrophysical Journal Letters* 655.2, pp. L77–L80. DOI: 10.1086/511973. arXiv: astro-ph/0612509 [astro-ph].

Harrison, Fiona A. et al. (June 2013). "The Nuclear Spectroscopic Telescope Array (NuSTAR) High-energy X-Ray Mission". In: *The Astrophysical Journal* 770.2, 103, p. 103. DOI: 10.1088/0004-637X/770/2/103. arXiv: 1301.7307 [astro-ph.IM].

Hatziminaoglou, E. et al. (Apr. 2015). "A Complete Census of Silicate Features in the Mid-infrared Spectra of Active Galaxies". In: *The Astrophysical Journal* 803.2, 110, p. 110. DOI: 10.1088/0004-637X/803/2/110. arXiv: 1502.05823 [astro-ph.GA].

Henri, Gilles and Guy Pelletier (Dec. 1991). "Relativistic Electron-Positron Beam Formation in the Framework of the Two-Flow Model for Active Galactic Nuclei". In: *The Astrophysical Journal Letters* 383, p. L7. DOI: 10.1086/186228.

Herrnstein, J. R. et al. (Aug. 1999). "A geometric distance to the galaxy NGC4258 from orbital motions in a nuclear gas disk". In: *Nature* 400.6744, pp. 539–541. DOI: 10.1038/22972. arXiv: astro-ph/9907013 [astro-ph].

Hickox, Ryan C. and David M. Alexander (Sept. 2018). "Obscured Active Galactic Nuclei". In: *Annual Review of Astronomy and Astrophysics* 56, pp. 625–671. DOI: 10.1146/annurev-astro-081817-051803. arXiv: 1806.04680 [astro-ph.GA].

Homan, D. et al. (Apr. 2023). "Discovery of the luminous X-ray ignition eRASSt J234402.9−352640. I. Tidal disruption event or a rapid increase in accretion in an active galactic nucleus?" In: *Astronomy and Astrophysics* 672, A167, A167. DOI: 10.1051/0004-6361/202245078. arXiv: 2302.06989 [astro-ph.HE].

Hönig, S. F. et al. (Aug. 2012). "Parsec-scale Dust Emission from the Polar Region in the Type 2 Nucleus of NGC 424". In: *The Astrophysical Journal* 755.2, 149, p. 149. DOI: 10.1088/0004-637X/755/2/149. arXiv: 1206.4307 [astro-ph.CO].

Hopkins, Philip F. et al. (Sept. 2005). "Black Holes in Galaxy Mergers: Evolution of Quasars". In: *The Astrophysical Journal* 630.2, pp. 705–715. DOI: 10.1086/432438. arXiv: astro-ph/0504190 [astro-ph].

Hoyle, F. and W. A. Fowler (Jan. 1963a). "On the nature of strong radio sources". In: *Monthly Notices of the Royal Astronomical Society* 125, p. 169. DOI: 10.1093/mnras/125.2.169.

Hoyle, F. and William A. Fowler (Feb. 1963b). "Nature of Strong Radio Sources". In: *Nature* 197.4867, pp. 533–535. DOI: 10.1038/197533a0.

Hubble, E. P. (Dec. 1926). "Extragalactic nebulae." In: *The Astrophysical Journal* 64, pp. 321–369. DOI: 10.1086/143018.

Ichimaru, S. (June 1977). "Bimodal behavior of accretion disks: theory and application to Cygnus X-1 transitions." In: *The Astrophysical Journal* 214, pp. 840–855. DOI: 10.1086/155314.

Ikeda, Shinya, Hisamitu Awaki, and Yuichi Terashima (Feb. 2009). "Study on X-Ray Spectra of Obscured Active Galactic Nuclei Based on Monte Carlo Simulation—An Interpretation of Observed Wide-Band Spectra". In: *The Astrophysical Journal* 692.1, pp. 608–617. DOI: 10.1088/0004-637X/692/1/608. arXiv: 0810.3950 [astro-ph].

Ilić, Dragana et al. (Nov. 2010). "Physical properties of the broad line region in active galactic nuclei". In: *Journal of Physics Conference Series*. Vol. 257. Journal of Physics Conference Series, p. 012034. DOI: 10.1088/1742-6596/257/1/012034.

Imanishi, Masatoshi et al. (Oct. 2020). "ALMA 0"02 Resolution Observations Reveal HCN-abundance-enhanced Counter-rotating and Outflowing Dense Molecular Gas at the NGC 1068 Nucleus". In: *The Astrophysical Journal* 902.2, 99, p. 99. DOI: 10.3847/1538-4357/abaf50. arXiv: 2008.08101 [astro-ph.GA].

Ingram, Adam and Chris Done (Aug. 2011). "A physical model for the continuum variability and quasi-periodic oscillation in accreting black holes". In: *Monthly Notices of the Royal Astronomical Society* 415.3, pp. 2323–2335. DOI: 10.1111/j.1365-2966.2011.18860.x. arXiv: 1101.2336 [astro-ph.SR].

Jansen, F. et al. (Jan. 2001). "XMM-Newton observatory. I. The spacecraft and operations". In: *Astronomy and Astrophysics* 365, pp. L1–L6. DOI: 10.1051/0004-6361:20000036.

Jiang, Yan-Fei, Shane W. Davis, and James M. Stone (Aug. 2016). "Iron Opacity Bump Changes the Stability and Structure of Accretion Disks in Active Galactic Nuclei". In: *The Astrophysical Journal* 827.1, 10, p. 10. DOI: 10.3847/0004-637X/827/1/10. arXiv: 1601.06836 [astro-ph.HE].

Kammoun, E. S., E. Nardini, and G. Risaliti (June 2018). "Testing the accuracy of reflection-based supermassive black hole spin measurements in AGN". In: *Astronomy and Astrophysics* 614, A44, A44. DOI: 10.1051/0004-6361/201732377. arXiv: 1802.06800 [astro-ph.HE].

Kayal, Abhijit et al. (July 2023). "Multi-epoch hard X-ray view of Compton-thick AGN Circinus Galaxy". In: *Monthly Notices of the Royal Astronomical Society* 522.3, pp. 4098–4115. DOI: 10.1093/mnras/stad1216. arXiv: 2304.10972 [astro-ph.GA].

Khachikian, E. Y. and D. W. Weedman (Sept. 1974). "An atlas of Seyfert galaxies." In: *The Astrophysical Journal* 192, pp. 581–589. DOI: 10.1086/153093.

Kishimoto, Makoto, Robert Antonucci, and Omer Blaes (Oct. 2003). "A first close look at the Balmer-edge behaviour of the quasar big blue bump". In: *Monthly Notices of the Royal Astronomical Society* 345.1, pp. 253–260. DOI: 10.1046/j.1365-8711.2003.06934.x. arXiv: astro-ph/0212259 [astro-ph].

Kollatschny, W. et al. (Nov. 2001). "Short-term emission line and continuum variations in Mrk 110". In: *Astronomy and Astrophysics* 379, pp. 125–135. DOI: 10.1051/0004-6361:20011323. arXiv: astro-ph/0109470 [astro-ph].

Korista, Kirk, Gary Ferland, and Jack Baldwin (Oct. 1997). "Do the Broad Emission Line Clouds See the Same Continuum That We See?" In: *The Astrophysical Journal* 487.2, pp. 555–559. DOI: 10.1086/304659. arXiv: astro-ph/9704262 [astro-ph].

Korista, Kirk et al. (Jan. 1997). "An Atlas of Computed Equivalent Widths of Quasar Broad Emission Lines". In: *The Astrophysical Journal Supplements* 108.2, pp. 401–415. DOI: 10.1086/312966. arXiv: astro-ph/9611220 [astro-ph].

Krolik, J. H. (Apr. 1999). "Magnetized Accretion inside the Marginally Stable Orbit around a Black Hole". In: *The Astrophysical Journal Letter* 515.2, pp. L73–L76. DOI: 10.1086/311979. arXiv: astro-ph/9902267 [astro-ph].

Krolik, Julian H. and Mitchell C. Begelman (June 1988). "Molecular Tori in Seyfert Galaxies: Feeding the Monster and Hiding It". In: *The Astrophysical Journal* 329, p. 702. DOI: 10.1086/166414.

Kubota, Aya and Chris Done (Oct. 2018). "A physical model of the broad-band continuum of AGN and its implications for the UV/X relation and optical variability". In: *Monthly Notices of the Royal Astronomical Society* 480.1, pp. 1247–1262. DOI: 10.1093/mnras/sty1890. arXiv: 1804.00171 [astro-ph.HE].

Laha, Sibasish et al. (July 2020). "The Variable and Non-variable X-Ray Absorbers in Compton-thin Type II Active Galactic Nuclei". In: *The Astrophysical Journal* 897.1, 66, p. 66. DOI: 10.3847/1538-4357/ab92ab. arXiv: 2005.06079 [astro-ph.GA].

LaMassa, Stephanie M. et al. (Feb. 2015). "The Discovery of the First "Changing Look" Quasar: New Insights Into the Physics and Phenomenology of Active Galactic Nucleus". In: *The Astrophysical Journal* 800.2, 144, p. 144. DOI: 10.1088/0004-637X/800/2/144. arXiv: 1412.2136 [astro-ph.GA].

Lančová, Debora et al. (Oct. 2019). "Puffy Accretion Disks: Sub-Eddington, Optically Thick, and Stable". In: *The Astrophysical Journal Letters* 884.2, L37, p. L37. DOI: 10.3847/2041-8213/ab48f5. arXiv: 1908.08396 [astro-ph.HE].

Leung, Gene C. K. et al. (Nov. 2019). "The MOSDEF Survey: A Census of AGN-driven Ionized Outflows at z = 1.4-3.8". In: *The Astrophysical Journal* 886.1, 11, p. 11. DOI: 10.3847/1538-4357/ab4a7c. arXiv: 1905.13338 [astro-ph.GA].

Lightman, Alan P. and Douglas M. Eardley (Jan. 1974). "Black Holes in Binary Systems: Instability of Disk Accretion". In: *The Astrophysical Journal Letters* 187, p. L1. DOI: 10.1086/181377.

Lin, D. N. C. and G. A. Shields (June 1986). "Accretion Disks and Periodic Outbursts of Active Galaxies Nuclei". In: *The Astrophysical Journal* 305, p. 28. DOI: 10.1086/164225.

Liu, Jiren et al. (Dec. 2019). "X-ray signatures of the polar dusty gas in AGN". In: *Monthly Notices of the Royal Astronomical Society* 490.3, pp. 4344–4352. DOI: 10.1093/mnras/stz2908. arXiv: 1910.05476 [astro-ph.HE].

Liu, Yuan and Xiaobo Li (May 2014). "An X-Ray Spectral Model for Clumpy Tori in Active Galactic Nuclei". In: *The Astrophysical Journal* 787.1, 52, p. 52. DOI: 10.1088/0004-637X/787/1/52. arXiv: 1405.0687 [astro-ph.HE].

Lynden-Bell, D. (Aug. 1969). "Galactic Nuclei as Collapsed Old Quasars". In: *Nature* 223.5207, pp. 690–694. DOI: 10.1038/223690a0.

Lyubarskii, Yu. E. (Dec. 1997). "Flicker noise in accretion discs". In: *Monthly Notices of the Royal Astronomical Society* 292.3, pp. 679–685. DOI: 10.1093/mnras/292.3.679.

MacLeod, Chelsea L. et al. (Mar. 2016). "A systematic search for changing-look quasars in SDSS". In: *Monthly Notices of the Royal Astronomical Society* 457.1, pp. 389–404. DOI: 10.1093/mnras/stv2997. arXiv: 1509.08393 [astro-ph.GA].

MacLeod, Chelsea L. et al. (Mar. 2019). "Changing-look Quasar Candidates: First Results from Follow-up Spectroscopy of Highly Optically Variable Quasars". In: *The Astrophysical Journal* 874.1, 8, p. 8. DOI: 10.3847/1538-4357/ab05e2. arXiv: 1810.00087 [astro-ph.GA].

Magdziarz, Pawel and Andrzej A. Zdziarski (Apr. 1995). "Angle-dependent Compton reflection of X-rays and gamma-rays". In: *Monthly Notices of the Royal Astronomical Society* 273.3, pp. 837–848. DOI: 10.1093/mnras/273.3.837.

Maiolino, R. et al. (Oct. 1998). "Heavy obscuration in X-ray weak AGNs". In: *Astronomy and Astrophysics* 338, pp. 781–794. DOI: 10.48550/arXiv.astro-ph/9806055. arXiv: astro-ph/9806055 [astro-ph].

Maiolino, R. et al. (July 2010). ""Comets" orbiting a black hole". In: *Astronomy and Astrophysics* 517, A47, A47. DOI: 10.1051/0004-6361/200913985. arXiv: 1005.3365 [astro-ph.HE].

Malkan, M. A. (May 1983). "The ultraviolet excess of luminous quasars. II. Evidence for massive accretion disks." In: *The Astrophysical Journal* 268, pp. 582–590. DOI: 10.1086/160981.

Malkan, M. A. and W. L. W. Sargent (Mar. 1982). "The ultraviolet excess of Seyfert 1 galaxies and quasars." In: *The Astrophysical Journal* 254, pp. 22–37. DOI: 10.1086/159701.

Malkan, Matthew A., Varoujan Gorjian, and Raymond Tam (July 1998). "A Hubble Space Telescope Imaging Survey of Nearby Active Galactic Nuclei". In: *Astrophysical Journal Supplement Series* 117.1, pp. 25–88. DOI: 10.1086/313110. arXiv: astro-ph/9803123 [astro-ph].

Maraschi, L. and F. Haardt (Jan. 1997). "Disk-Corona Models and X-Ray Emission from Seyfert Galaxies". In: *IAU Colloq. 163: Accretion Phenomena and Related Outflows*. Ed. by D. T. Wickramasinghe, G. V. Bicknell, and L. Ferrario. Vol. 121. Astronomical Society of the Pacific Conference Series, p. 101. DOI: 10.48550/arXiv.astro-ph/9611048. arXiv: astro-ph/9611048 [astro-ph].

Marchesi, S. et al. (Aug. 2022). "Compton-thick AGN in the NuSTAR Era. VIII. A joint NuSTAR-XMM-Newton Monitoring of the Changing-look Compton-thick AGN NGC 1358". In: *The Astrophysical Journal* 935.2, 114, p. 114. DOI: 10.3847/1538-4357/ac80be. arXiv: 2207.06734 [astro-ph.GA].

Marinucci, A. et al. (Dec. 2013). "A Chandra view of the clumpy reflector at the heart of the Circinus galaxy". In: *Monthly Notices of the Royal Astronomical Society* 436.3, pp. 2500–2504. DOI: 10.1093/mnras/stt1759. arXiv: 1309.4456 [astro-ph.CO].

Markoff, Sera, Michael A. Nowak, and Jörn Wilms (Dec. 2005). "Going with the Flow: Can the Base of Jets Subsume the Role of Compact Accretion Disk Coronae?" In: *The Astrophysical Journal* 635.2, pp. 1203–1216. DOI: 10.1086/497628. arXiv: astro-ph/0509028 [astro-ph].

Markowitz, A. and R. Edelson (Dec. 2004). "An Expanded Rossi X-Ray Timing Explorer Survey of X-Ray Variability in Seyfert 1 Galaxies". In: *The Astrophysical Journal* 617.2, pp. 939–965. DOI: 10.1086/425559. arXiv: astro-ph/0409045 [astro-ph].

Markowitz, A., R. Edelson, and S. Vaughan (Dec. 2003). "Long-Term X-Ray Spectral Variability in Seyfert 1 Galaxies". In: *The Astrophysical Journal* 598.2, pp. 935–955. DOI: 10.1086/379103. arXiv: astro-ph/0308312 [astro-ph].

Markowitz, A. G., M. Krumpe, and R. Nikutta (Apr. 2014). "First X-ray-based statistical tests for clumpy-torus models: eclipse events from 230 years of monitoring of Seyfert AGN". In: *Monthly Notices of the Royal Astronomical Society* 439.2, pp. 1403–1458. DOI: 10.1093/mnras/stt2492. arXiv: 1402.2779 [astro-ph.GA].

Martínez-Aldama, Mary Loli et al. (Mar. 2015). "O I and Ca II Observations in Intermediate Redshift Quasars". In: *The Astrophysical Journal Supplement* 217.1, 3, p. 3. DOI: 10.1088/0067-0049/217/1/3. arXiv: 1501.04718 [astro-ph.GA].

Matt, G. (Mar. 2000). "Dust lanes, thick absorbers, and the unification model for Seyfert galaxies". In: *Astronomy and Astrophysics* 355, pp. L31–L33. DOI: 10.48550/arXiv.astro-ph/0002427. arXiv: astro-ph/0002427 [astro-ph].

Matt, G. et al. (Aug. 1996). "A reflection-dominated X-ray spectrum discovered by ASCA in the Circinus galaxy". In: *Monthly Notices of the Royal Astronomical Society* 281.4, pp. L69–L73. DOI: 10.1093/mnras/281.4.L69.

Mehdipour, M. et al. (Oct. 2011). "Multiwavelength campaign on Mrk 509. IV. Optical-UV-X-ray variability and the nature of the soft X-ray excess". In: *Astronomy and Astrophysics* 534, A39, A39. DOI: 10.1051/0004-6361/201116875. arXiv: 1107.0659 [astro-ph.CO].

Mehdipour, M. et al. (Oct. 2017). "Chasing obscuration in type-I AGN: discovery of an eclipsing clumpy wind at the outer broad-line region of NGC 3783". In: *Astronomy and Astrophysics* 607, A28, A28. DOI: 10.1051/0004-6361/201731175. arXiv: 1707.04671 [astro-ph.HE].

Mehdipour, M. et al. (Aug. 2021). "Transient obscuration event captured in NGC 3227. I. Continuum model for the broadband spectral energy distribution". In: *Astronomy and Astrophysics* 652, A150, A150. DOI: 10.1051/0004-6361/202141324. arXiv: 2106.14957 [astro-ph.HE].

Mehdipour, Missagh et al. (Aug. 2022). "10 Yr Transformation of the Obscuring Wind in NGC 5548". In: *The Astrophysical Journal Letters* 934.2, L24, p. L24. DOI: 10.3847/2041-8213/ac822f. arXiv: 2207.09464 [astro-ph.HE].

Merloni, A. et al. (Sept. 2012). "eROSITA Science Book: Mapping the Structure of the Energetic Universe". In: *arXiv e-prints*, arXiv:1209.3114, arXiv:1209.3114. DOI: 10.48550/arXiv.1209.3114. arXiv: 1209.3114 [astro-ph.HE].

Miller, J. S. and R. R. J. Antonucci (Aug. 1983). "Evidence for a highly polarized continuum in the nucleus of NGC 1068." In: *The Astrophysical Journal Letters* 271, pp. L7–L11. DOI: 10.1086/184082.

Miller, J. S. and R. W. Goodrich (June 1990). "Spectropolarimetry of High-Polarization Seyfert 2 Galaxies and Unified Seyfert Theories". In: *The Astrophysical Journal* 355, p. 456. DOI: 10.1086/168780.

Miniutti, G. et al. (Jan. 2014). "The properties of the clumpy torus and BLR in the polar-scattered Seyfert 1 galaxy ESO 323-G77 through X-ray absorption variability". In: *Monthly Notices of the Royal Astronomical Society* 437.2, pp. 1776–1790. DOI: 10.1093/mnras/stt2005. arXiv: 1310.7701 [astro-ph.HE].

Mishra, Bhupendra et al. (Feb. 2020). "Strongly magnetized accretion discs: structure and accretion from global magnetohydrodynamic simulations". In: *Monthly Notices of the Royal Astronomical Society* 492.2, pp. 1855–1868. DOI: 10.1093/mnras/stz3572. arXiv: 1907.08995 [astro-ph.HE].

Misner, Charles W., Kip S. Thorne, and John Archibald Wheeler (1973). *Gravitation*.

Miyoshi, Makoto et al. (Jan. 1995). "Evidence for a black hole from high rotation velocities in a sub-parsec region of NGC4258". In: *Nature* 373.6510, pp. 127–129. DOI: 10.1038/373127a0.

Mulchaey, John S. et al. (Dec. 1994). "Multiwavelength Tests of the Dusty Torus Model for Seyfert Galaxies". In: *The Astrophysical Journal* 436, p. 586. DOI: 10.1086/174933.

Müller-Sánchez, F. et al. (Oct. 2011). "Outflows from Active Galactic Nuclei: Kinematics of the Narrow-line and Coronal-line Regions in Seyfert Galaxies". In: *The Astrophysical Journal* 739.2, 69, p. 69. DOI: 10.1088/0004-637X/739/2/69. arXiv: 1107.3140 [astro-ph.CO].

Murphy, Kendrah D. and Tahir Yaqoob (Aug. 2009). "An X-ray spectral model for Compton-thick toroidal reprocessors". In: *Monthly Notices of the Royal Astronomical Society* 397.3, pp. 1549–1562. DOI: 10.1111/j.1365-2966.2009.15025.x. arXiv: 0905.3188 [astro-ph.HE].

Mushotzky, Richard F., Christine Done, and Kenneth A. Pounds (Jan. 1993). "X-ray spectra and time variability of active galactic nuclei." In: *Annual Review of Astronomy and Astrophysics* 31, pp. 717–717. DOI: 10.1146/annurev.aa.31.090193.003441.

Naddaf, M. H. and B. Czerny (July 2022). "Radiation pressure on dust explaining the low ionized broad emission lines in active galactic nuclei. Dust as an important driver of line shape". In: *Astronomy and Astrophysics* 663, A77, A77. DOI: 10.1051/0004-6361/202142806. arXiv: 2111.14963 [astro-ph.GA].

Narayan, Ramesh and Insu Yi (June 1994). "Advection-dominated Accretion: A Self-similar Solution". In: *The Astrophysical Journal Letters* 428, p. L13. DOI: 10.1086/187381. arXiv: astro-ph/9403052 [astro-ph].

Nenkova, Maia et al. (Sept. 2008). "AGN Dusty Tori. II. Observational Implications of Clumpiness". In: *The Astrophysical Journal* 685.1, pp. 160–180. DOI: 10.1086/590483. arXiv: 0806.0512 [astro-ph].

Netzer, Hagai (2013). *The Physics and Evolution of Active Galactic Nuclei*.

– (Aug. 2015). "Revisiting the Unified Model of Active Galactic Nuclei". In: *Annu. Rev. Astron. Astrophys.* 53, pp. 365–408. DOI: 10.1146/annurev-astro-082214-122302. arXiv: 1505.00811 [astro-ph.GA].

Noda, Hirofumi and Chris Done (Nov. 2018). "Explaining changing-look AGN with state transition triggered by rapid mass accretion rate drop". In: *Monthly Notices of the Royal Astronomical Society* 480.3, pp. 3898–3906. DOI: 10.1093/mnras/sty2032. arXiv: 1805.07873 [astro-ph.GA].

Ogawa, Shoji et al. (Jan. 2021). "Systematic Study of AGN Clumpy Tori with Broadband X-Ray Spectroscopy: Updated Unified Picture of AGN Structure". In: *The Astrophysical Journal* 906.2, 84, p. 84. DOI: 10.3847/1538-4357/abccce. arXiv: 2011.13931 [astro-ph.HE].

Osterbrock, D. E. (Aug. 1977). "Spectrophotometry of Seyfert 1 galaxies." In: *The Astrophysical Journal* 215, pp. 733–745. DOI: 10.1086/155407.

– (Oct. 1981). "Seyfert galaxies with weak broad H alpha emission lines". In: *The Astrophysical Journal* 249, pp. 462–470. DOI: 10.1086/159306.

Osterbrock, D. E. and A. T. Koski (Aug. 1976). "NGC 4151 and Markarian 6 - two intermediate-type Seyfert galaxies". In: *Monthly Notices of the Royal Astronomical Society* 176, 61P–66P. DOI: 10.1093/mnras/176.1.61P.

Paltani, S. and C. Ricci (Nov. 2017). "RefleX: X-ray absorption and reflection in active galactic nuclei for arbitrary geometries". In: *Astronomy and Astrophysics* 607, A31, A31. DOI: 10.1051/0004-6361/201629623. arXiv: 1906.08824 [astro-ph.HE].

Pancoast, Anna, Brendon J. Brewer, and Tommaso Treu (Dec. 2014). "Modelling reverberation mapping data - I. Improved geometric and dynamical models and comparison with cross-correlation results". In: *Monthly Notices of the Royal Astronomical Society* 445.3, pp. 3055–3072. DOI: 10.1093/mnras/stu1809. arXiv: 1407.2941 [astro-ph.GA].

Pancoast, Anna et al. (Dec. 2014). "Modelling reverberation mapping data - II. Dynamical modelling of the Lick AGN Monitoring Project 2008 data set". In: *Monthly Notices of the Royal Astronomical Society* 445.3, pp. 3073–3091. DOI: 10.1093/mnras/stu1419. arXiv: 1311.6475 [astro-ph.CO].

Panda, Swayamtrupta (June 2021). "The CaFe project: Optical Fe II and near-infrared Ca II triplet emission in active galaxies: simulated EWs and the co-dependence of cloud size and metal content". In: *Astronomy and Astrophysics* 650, A154, A154. DOI: 10.1051/0004-6361/202140393. arXiv: 2004.13113 [astro-ph.GA].

Panda, Swayamtrupta et al. (Oct. 2020). "The CaFe Project: Optical Fe II and Near-infrared Ca II Triplet Emission in Active Galaxies. I. Photoionization Modeling". In: *The Astrophysical Journal* 902.1, 76, p. 76. DOI: 10.3847/1538-4357/abb5b8. arXiv: 2004.05201 [astro-ph.HE].

Petrucci, P. O. et al. (Mar. 2018). "Testing warm Comptonization models for the origin of the soft X-ray excess in AGNs". In: *Astronomy and Astrophysics* 611, A59, A59. DOI: 10.1051/0004-6361/201731580. arXiv: 1710.04940 [astro-ph.HE].

Pier, Edward A. and Julian H. Krolik (Dec. 1992). "Infrared Spectra of Obscuring Dust Tori around Active Galactic Nuclei. I. Calculational Method and Basic Trends". In: *The Astrophysical Journal* 401, p. 99. DOI: 10.1086/172042.

– (Dec. 1993). "Infrared Spectra of Obscuring Dust Tori around Active Galactic Nuclei. II. Comparison with Observations". In: *The Astrophysical Journal* 418, p. 673. DOI: 10.1086/173427.

Predehl, P. et al. (Mar. 2021). "The eROSITA X-ray telescope on SRG". In: *Astronomy and Astrophysics* 647, A1, A1. DOI: 10.1051/0004-6361/202039313. arXiv: 2010.03477 [astro-ph.HE].

Ramos Almeida, C. et al. (Apr. 2011). "Testing the Unification Model for Active Galactic Nuclei in the Infrared: Are the Obscuring Tori of Type 1 and 2 Seyferts Different?" In: *The Astrophysical Journal* 731.2, 92, p. 92. DOI: 10.1088/0004-637X/731/2/92. arXiv: 1101.3335 [astro-ph.CO].

Ramos Almeida, Cristina and Claudio Ricci (Oct. 2017). "Nuclear obscuration in active galactic nuclei". In: *Nature Astronomy* 1, pp. 679–689. DOI: 10.1038/s41550-017-0232-z. arXiv: 1709.00019 [astro-ph.GA].

Rees, Martin J. (June 1988). "Tidal disruption of stars by black holes of 10^6-10^8 solar masses in nearby galaxies". In: *Nature* 333.6173, pp. 523–528. DOI: 10.1038/333523a0.

Remillard, Ronald A. and Jeffrey E. McClintock (Sept. 2006). "X-Ray Properties of Black-Hole Binaries". In: *Annual Review of Astronomy and Astrophysics* 44.1, pp. 49–92. DOI: 10.1146/annurev.astro.44.051905.092532. arXiv: astro-ph/0606352 [astro-ph].

Ricci, C. et al. (July 2020). "The Destruction and Recreation of the X-Ray Corona in a Changing-look Active Galactic Nucleus". In: *The Astrophysical Journal Letters* 898.1, L1, p. L1. DOI: 10.3847/2041-8213/ab91a1. arXiv: 2007.07275 [astro-ph.HE].

Ricci, Claudio and Stéphane Paltani (Mar. 2023). "Ray-tracing Simulations and Spectral Models of X-Ray Radiation in Dusty Media". In: *The Astrophysical Journal* 945.1, 55, p. 55. DOI: 10.3847/1538-4357/acb5a6. arXiv: 2301.10268 [astro-ph.HE].

Risaliti, G., R. Maiolino, and M. Salvati (Sept. 1999). "The Distribution of Absorbing Column Densities among Seyfert 2 Galaxies". In: *The Astrophysical Journal* 522.1, pp. 157–164. DOI: 10.1086/307623. arXiv: astro-ph/9902377 [astro-ph].

Risaliti, G. et al. (Apr. 2007). "Occultation Measurement of the Size of the X-Ray-emitting Region in the Active Galactic Nucleus of NGC 1365". In: *The Astrophysical Journal Letters* 659.2, pp. L111–L114. DOI: 10.1086/517884. arXiv: astro-ph/0703173 [astro-ph].

Rivers, Elizabeth, Alex Markowitz, and Richard Rothschild (Mar. 2011). "Spectral Survey of X-ray Bright Active Galactic Nuclei from the Rossi X-ray Timing Explorer". In: *The Astrophysical Journal Supplement* 193.1, 3, p. 3. DOI: 10.1088/0067-0049/193/1/3. arXiv: 1101.1545 [astro-ph.HE].

Ross, Nicholas P. et al. (Nov. 2018). "A new physical interpretation of optical and infrared variability in quasars". In: *Monthly Notices of the Royal Astronomical Society* 480.4, pp. 4468–4479. DOI: 10.1093/mnras/sty2002. arXiv: 1805.06921 [astro-ph.GA].

Ruan, John J. et al. (Sept. 2019). "The Analogous Structure of Accretion Flows in Supermassive and Stellar Mass Black Holes: New Insights from Faded Changing-look Quasars". In: *The Astrophysical Journal* 883.1, 76, p. 76. DOI: 10.3847/1538-4357/ab3c1a. arXiv: 1903.02553 [astro-ph.HE].

Saha, T. et al. (Sept. 2023). "Multiwavelength study of extreme variability in LEDA 1154204: A changing-look event in a type 1.9 Seyfert". In: *arXiv e-prints*, arXiv:2309.08956, arXiv:2309.08956. DOI: 10.48550/arXiv.2309.08956. arXiv: 2309.08956 [astro-ph.HE].

Saha, Tathagata, Alex G. Markowitz, and Johannes Buchner (Feb. 2022). "Inferring the morphology of AGN torus using X-ray spectra: a reliability study". In: *Monthly Notices of the Royal Astronomical Society* 509.4, pp. 5485–5510. DOI: 10.1093/mnras/stab3250. arXiv: 2112.07393 [astro-ph.HE].

Salpeter, E. E. (Aug. 1964). "Accretion of Interstellar Matter by Massive Objects." In: *ApJ* 140, pp. 796–800. DOI: 10.1086/147973.

Scepi, Nicolas, Mitchell C. Begelman, and Jason Dexter (Mar. 2021). "Magnetic flux inversion in a peculiar changing look AGN". In: *Monthly Notices of the Royal Astronomical Society* 502.1, pp. L50–L54. DOI: 10.1093/mnrasl/slab002. arXiv: 2011.01954 [astro-ph.HE].

Schmidt, M. (Mar. 1963). "3C 273 : A Star-Like Object with Large Red-Shift". In: *Nature* 197.4872, p. 1040. DOI: 10.1038/1971040a0.

Setti, G. and L. Woltjer (Oct. 1989). "Active galactic nuclei and the spectrum of the X-ray background." In: *Astronomy and Astrophysics* 224, pp. L21–L23.

Seyfert, Carl K. (Jan. 1943). "Nuclear Emission in Spiral Nebulae." In: *The Astrophysical Journal* 97, p. 28. DOI: 10.1086/144488.

Shakura, N. I. and R. A. Sunyaev (Jan. 1973). "Black holes in binary systems. Observational appearance." In: *Astronomy and Astrophysics* 24, pp. 337–355.

Shappee, B. J. et al. (June 2014). "The Man behind the Curtain: X-Rays Drive the UV through NIR Variability in the 2013 Active Galactic Nucleus Outburst in NGC 2617". In: *The Astrophysical Journal* 788.1, 48, p. 48. DOI: 10.1088/0004-637X/788/1/48. arXiv: 1310.2241 [astro-ph.HE].

Shen, Yue (Nov. 2021). "Extreme Variability and Episodic Lifetime of Quasars". In: *The Astrophysical Journal* 921.1, 70, p. 70. DOI: 10.3847/1538-4357/ac1ce4. arXiv: 2108.05381 [astro-ph.GA].

Shi, Yong et al. (May 2010). "Unobscured Type 2 Active Galactic Nuclei". In: *The Astrophysical Journal* 714.1, pp. 115–129. DOI: 10.1088/0004-637X/714/1/115. arXiv: 1004.2077 [astro-ph.CO].

Shields, G. A. (Apr. 1978). "Thermal continuum from accretion disks in quasars". In: *Nature* 272.5655, pp. 706–708. DOI: 10.1038/272706a0.

Sikora, Marek and Mitchell C. Begelman (Feb. 2013). "Magnetic Flux Paradigm for Radio Loudness of Active Galactic Nuclei". In: *The Astrophysical Journal Letters* 764.2, L24, p. L24. DOI: 10.1088/2041-8205/764/2/L24. arXiv: 1301.5638 [astro-ph.HE].

Sikora, Marek, Mitchell C. Begelman, and Martin J. Rees (Jan. 1994). "Comptonization of Diffuse Ambient Radiation by a Relativistic Jet: The Source of Gamma Rays from Blazars?" In: *The Astrophysical Journal* 421, p. 153. DOI: 10.1086/173633.

Silverman, John D. et al. (July 2023). "Resolving Galactic-scale Obscuration of X-Ray AGNs at $z \gtrsim 1$ with COSMOS-Web". In: *The Astrophysical Journal Letters* 951.2, L41, p. L41. DOI: 10.3847/2041-8213/acdef4. arXiv: 2306.03205 [astro-ph.GA].

Sniegowska, M. et al. (Sept. 2020). "Possible mechanism for multiple changing-look phenomena in active galactic nuclei". In: *Astronomy and Astrophysics* 641, A167, A167. DOI: 10.1051/0004-6361/202038575. arXiv: 2007.06441 [astro-ph.GA].

Soltan, A. (July 1982). "Masses of quasars." In: *Monthly Notices of the Royal Astronomical Society* 200, pp. 115–122. DOI: 10.1093/mnras/200.1.115.

Stalevski, Marko, Daniel Asmus, and Konrad R. W. Tristram (Dec. 2017). "Dissecting the active galactic nucleus in Circinus - I. Peculiar mid-IR morphology explained by a dusty hollow cone". In: *Monthly Notices of the Royal Astronomical Society* 472.4, pp. 3854–3870. DOI: 10.1093/mnras/stx2227. arXiv: 1708.07838 [astro-ph.GA].

Stalevski, Marko, Konrad R. W. Tristram, and Daniel Asmus (Apr. 2019). "Dissecting the active galactic nucleus in Circinus - II. A thin dusty disc and a polar outflow on parsec scales". In: *Monthly Notices of the Royal Astronomical Society* 484.3, pp. 3334–3355. DOI: 10.1093/mnras/stz220. arXiv: 1901.05488 [astro-ph.GA].

Sunyaev, R. et al. (Dec. 2021). "SRG X-ray orbital observatory. Its telescopes and first scientific results". In: *Astronomy and Astrophysics* 656, A132, A132. DOI: 10.1051/0004-6361/202141179. arXiv: 2104.13267 [astro-ph.HE].

Tanimoto, Atsushi et al. (June 2019). "XCLUMPY: X-Ray Spectral Model from Clumpy Torus and Its Application to the Circinus Galaxy". In: *The Astrophysical Journal* 877.2, 95, p. 95. DOI: 10.3847/1538-4357/ab1b20. arXiv: 1904.08945 [astro-ph.HE].

Tchekhovskoy, Alexander, Jonathan C. McKinney, and Ramesh Narayan (July 2012). "General Relativistic Modeling of Magnetized Jets from Accreting Black Holes". In: *Journal of Physics Conference Series*. Vol. 372. Journal of Physics Conference Series, p. 012040. DOI: 10.1088/1742-6596/372/1/012040. arXiv: 1202.2864 [astro-ph.HE].

Temple, Matthew J. et al. (July 2023). "Testing AGN outflow and accretion models with C IV and He II emission line demographics in $z \approx 2$ quasars". In: *Monthly Notices of the Royal*

Astronomical Society 523.1, pp. 646–666. DOI: 10.1093/mnras/stad1448. arXiv: 2301.02675 [astro-ph.GA].

Thatte, N. et al. (Nov. 1997). "The Nuclear Stellar Core, the Hot Dust Source, and the Location of the Nucleus of NGC 1068". In: *The Astrophysical Journal* 490.1, pp. 238–246. DOI: 10.1086/304848.

Torres-Albà, N. et al. (Jan. 2023). "Hydrogen Column Density Variability in a Sample of Local Compton-Thin AGN". In: *arXiv e-prints*, arXiv:2301.07138, arXiv:2301.07138. DOI: 10.48550/arXiv.2301.07138. arXiv: 2301.07138 [astro-ph.GA].

Tortosa, A. et al. (June 2018). "A NuSTAR census of coronal parameters in Seyfert galaxies". In: *Astronomy and Astrophysics* 614, A37, A37. DOI: 10.1051/0004-6361/201732382. arXiv: 1801.04456 [astro-ph.GA].

Trakhtenbrot, Benny et al. (Sept. 2019). "1ES 1927+654: An AGN Caught Changing Look on a Timescale of Months". In: *The Astrophysical Journal* 883.1, 94, p. 94. DOI: 10.3847/1538-4357/ab39e4. arXiv: 1903.11084 [astro-ph.GA].

Tran, Hien D. (Feb. 2003). "The Unified Model and Evolution of Active Galaxies: Implications from a Spectropolarimetric Study". In: *The Astrophysical Journal* 583.2, pp. 632–648. DOI: 10.1086/345473. arXiv: astro-ph/0210262 [astro-ph].

Tristram, K. R. W. et al. (Nov. 2007). "Resolving the complex structure of the dust torus in the active nucleus of the Circinus galaxy". In: *Astronomy and Astrophysics* 474.3, pp. 837–850. DOI: 10.1051/0004-6361:20078369. arXiv: 0709.0209 [astro-ph].

Tristram, Konrad R. W. et al. (Mar. 2014). "The dusty torus in the Circinus galaxy: a dense disk and the torus funnel". In: *Astronomy and Astrophysics* 563, A82, A82. DOI: 10.1051/0004-6361/201322698. arXiv: 1312.4534 [astro-ph.GA].

Turner, T. J. and K. A. Pounds (Oct. 1989). "The EXOSAT spectral survey of AGN." In: *Monthly Notices of the Royal Astronomical Society* 240, pp. 833–880. DOI: 10.1093/mnras/240.4.833.

Urry, C. Megan and Paolo Padovani (Sept. 1995). "Unified Schemes for Radio-Loud Active Galactic Nuclei". In: *Publications of the Astronomical Society of the Pacific* 107, p. 803. DOI: 10.1086/133630. arXiv: astro-ph/9506063 [astro-ph].

Uttley, Philip et al. (Feb. 2003). "Correlated Long-Term Optical and X-Ray Variations in NGC 5548". In: *The Astrophysical Journal Letters* 584.2, pp. L53–L56. DOI: 10.1086/373887. arXiv: astro-ph/0301216 [astro-ph].

Vander Meulen, Bert et al. (June 2023). "X-ray radiative transfer in full 3D with SKIRT". In: *Astronomy and Astrophysics* 674, A123, A123. DOI: 10.1051/0004-6361/202245783. arXiv: 2304.10563 [astro-ph.HE].

Verner, E. M. et al. (Jan. 1999). "Numerical Simulations of Fe II Emission Spectra". In: *The Astrophysical Journal Supplements* 120.1, pp. 101–112. DOI: 10.1086/313171.

Villafaña, Lizvette et al. (May 2022). "The Lick AGN Monitoring Project 2016: Dynamical Modeling of Velocity-resolved Hβ Lags in Luminous Seyfert Galaxies". In: *The Astrophysical Journal* 930.1, 52, p. 52. DOI: 10.3847/1538-4357/ac6171. arXiv: 2203.15000 [astro-ph.GA].

Volonteri, Marta and Martin J. Rees (Nov. 2005). "Rapid Growth of High-Redshift Black Holes". In: *The Astrophysical Journal* 633.2, pp. 624–629. DOI: 10.1086/466521. arXiv: astro-ph/0506040 [astro-ph].

Wada, Keiichi (Oct. 2012). "Radiation-driven Fountain and Origin of Torus around Active Galactic Nuclei". In: *The Astrophysical Journal* 758.1, 66, p. 66. DOI: 10.1088/0004-637X/758/1/66. arXiv: 1208.5272 [astro-ph.GA].

Weisskopf, Martin C. et al. (July 2000). "Chandra X-ray Observatory (CXO): overview". In: *X-Ray Optics, Instruments, and Missions III*. Ed. by Joachim E. Truemper and Bernd Aschenbach. Vol. 4012. Society of Photo-Optical Instrumentation Engineers (SPIE) Conference Series, pp. 2–16. DOI: 10.1117/12.391545. arXiv: astro-ph/0004127 [astro-ph].

Wielgus, Maciek et al. (July 2022). "Observational properties of puffy discs: radiative GRMHD spectra of mildly sub-Eddington accretion". In: *Monthly Notices of the Royal Astronomical Society* 514.1, pp. 780–789. DOI: 10.1093/mnras/stac1317. arXiv: 2202.08831 [astro-ph.HE].

Wołowska, Aleksandra et al. (June 2021). "Caltech-NRAO Stripe 82 Survey (CNSS). V. AGNs That Transitioned to Radio-loud State". In: *The Astrophysical Journal* 914.1, 22, p. 22. DOI: 10.3847/1538-4357/abe62d. arXiv: 2103.08422 [astro-ph.GA].

Zaino, A. et al. (Mar. 2020). "Probing the circumnuclear absorbing medium of the buried AGN in NGC 1068 through NuSTAR observations". In: *Monthly Notices of the Royal Astronomical Society* 492.3, pp. 3872–3884. DOI: 10.1093/mnras/staa107. arXiv: 2001.05499 [astro-ph.GA].

Zdziarski, Andrzej A. et al. (Mar. 2020). "Spectral and temporal properties of Compton scattering by mildly relativistic thermal electrons". In: *Monthly Notices of the Royal Astronomical Society* 492.4, pp. 5234–5246. DOI: 10.1093/mnras/staa159. arXiv: 1910.04535 [astro-ph.HE].

Zheng, Wei et al. (Feb. 1997). "A Composite HST Spectrum of Quasars". In: *The Astrophysical Journal* 475.2, pp. 469–478. DOI: 10.1086/303560. arXiv: astro-ph/9608198 [astro-ph].